Table of Contents

Overview

1 Introduction

KEKB is an asymmetric electron-positron collider at 8×3.5 GeV, which aims to provide electron-positron collisions at a center-of-mass energy of 10.58 GeV. Its mission is to support high energy physics research programs on CP-violation and other topcis in B-meson decays. Its luminosity goal is $10^{34}\mathrm{cm}^{-2}\mathrm{s}^{-1}$. With approval by the Japanese government as a five-year project, the construction of KEKB formally began in April of 1994. The two rings of KEKB (the low-energy ring LER for positrons at 3.5 GeV, and the high-energy ring HER for electrons at 8 GeV) will be built in the existing TRISTAN tunnel, which has a circumference of 3 km. Maximum use will be made of the infrastructure of TRISTAN. Taking advantage of the large tunnel width, the two rings of KEKB will be built side by side. Since vertical bending of the beam trajectory tends to increase the vertical beam emittance, its use is minimized.

Figure 1 illustrates the layout of the two rings. KEKB has only one interaction point (IP) in the Tsukuba experimental hall, where the electron and positron beams collide at a finite angle of ±11 mrad. The BELLE detector will be installed in this interaction region. The straight section at Fuji will be used for injecting beams from the linac, and also for installing RF cavities of the LER. The RF cavities of the HER will be installed in the straight sections of Nikko and Oho. These straight sections are also reserved for wigglers for the LER. They will reduce the longitudinal damping time of the LER from 43 ms to 23 ms, i.e. the same damping time as the HER. In order to make the circumference of the two rings precisely equal, a cross-over will be built at the Fuji area. The HER and LER are located at the outer and inner sides inside the tunnel in the Tsukuba-Oho-Fuji part. The relative positions of the two rings are reversed in the Fuji-Nikko-Tsukuba part of the tunnel.

To facilitate full-energy injection into the KEKB rings, and thus to eliminate the need for accelerating high-current beams in the rings, the existing 2.5 GeV electron linac will be upgraded to 8 GeV. The upgrade program includes the following modifications to the injector configuration: combine the main linac with the positron production

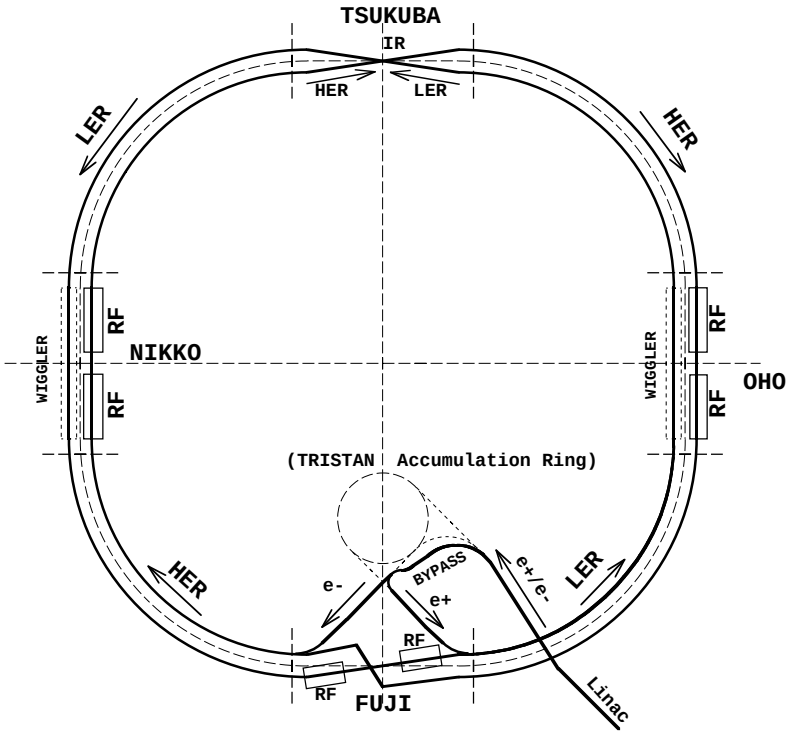

Figure 1: Configuration of the KEKB accelerator system.

linac, increase the number of accelerating structures, replace the klystrons with higher-power types, and compress the RF pulse power by using a SLED scheme. With this upgrade the energy of electrons impinging on the positron production target will be increased from 250 MeV to 4 GeV. This will increase the available positron intensity by 16. With this improvement the injection time of positrons to the LER from zero to the full current is expected to be 900 s.

A new bypass tunnel, which is 130 m long, will be excavated for building transport lines between the linac and KEKB. This new beam transport functionally separates the TRISTAN accumulation ring (AR) from KEKB. This will be an advantage to both KEKB and AR programs, since the upgrade work of either accelerator can be carried out without significantly affecting the other. The tunnel will be built in JFY 1996 and 1997.

2 Basic Design

A Beam Parameters

Table 1 summarizes the main parameters of KEKB. The HER and LER have the same circumference, beam emittance, and beta-function values at IP ($\beta*$). The large current, small $\beta*$, and finite-angle crossing of beams are salient features of KEKB.

Table 1: Main Parameters of KEKB

Ring		LER	HER	
Energy	E	3.5	8.0	GeV
Circumference	C	3016.26		m
Luminosity	$\mathcal{L}$	1×10^{34}		$\mathrm{cm^{-2}s^{-1}}$
Crossing angle	θ_x	±11		mrad
Tune shifts	ξ_x/ξ_y	0.039/0.052		
Beta function at IP	β_x^*/β_y^*	0.33/0.01		m
Beam current	I	2.6	1.1	A
Natural bunch length	σ_z	0.4		cm
Energy spread	σ_ε	7.1×10^{-4}	6.7×10^{-4}	
Bunch spacing	s_b	0.59		m
Particles/bunch	N	3.3×10^{10}	1.4×10^{10}	
Emittance	$\varepsilon_x/\varepsilon_y$	$1.8\times10^{-8}/3.6\times10^{-10}$		m
Synchrotron tune	ν_s	$0.01 \sim 0.02$		
Betatron tune	ν_x/ν_y	45.52/45.08	47.52/43.08	
Momentum compaction factor	α_p	$1\times10^{-4} \sim 2\times10^{-4}$		
Energy loss/turn	U_o	0.81†/1.5††	3.5	MeV
RF voltage	V_c	$5 \sim 10$	$10 \sim 20$	MV
RF frequency	f_{RF}	508.887		MHz
Harmonic number	h	5120		
Longitudinal damping time	τ_ε	43†/23††	23	ms
Total beam power	P_b	2.7†/4.5††	4.0	MW
Radiation power	P_{SR}	2.1†/4.0††	3.8	MW
HOM power	P_{HOM}	0.57	0.15	MW
Bending radius	ρ	16.3	104.5	m
Length of bending magnet	ℓ_B	0.915	5.86	m

†: without wigglers, ††: with wigglers

B Noninterleaved Chromaticity Correction and 2.5π Lattice

For efficient operation it is highly desirable to be able to inject beams into KEKB without having to modify the lattice optics from the collision time. This calls for a design which maximizes the dynamic aperture. A large dynamic aperture is also preferred for increasing the beam lifetime. For this goal, a noninterleaved sextupole chromaticity correction scheme has been adopted for the arc sections. In this scheme sextupole magnets are paired into a large number of families. Two sextupole magnets in each pair are placed π apart in both the horizontal and vertical phases. No other sextupole magnets are installed within a pair. This arrangement cancels out geometric aberrations of the sextupole magnets through a "$-I$" transformation between each member of the sextupole pair.

One unit cell of the arc lattice has a phase advance of 2.5π. It includes two pairs of sextupole magnets, SF and SD. With the introduction of an extra $\pi/2$ phase advance on the 2π structure, chromatic kicks by the lattice magnet components are very efficiently corrected, and it significantly improves the dynamic aperture.

The lattice design includes a mechanism that makes it possible to change the momentum compaction in the range from -1$\times 10^{-4}$ to 4$\times 10^{-4}$. By adding two quadrupole magnets in a cell the emittance is also made tunable from 50% to 200% of the nominal value. The flexibility for choosing such critical parameters will be a strong asset for optimizing the operating condition of KEKB.

In addition, a local chromaticity correction scheme will be implemented for the LER in order to correct the large vertical chromaticity that is produced by the final focus quadrupole magnets near the IP. A few dipole magnets will be introduced in the IR straight section to create a dispersion at each side of the IP. A $-I$ sextupole magnet pair will be arranged in this area for each side of the IP to correct the vertical chromaticity. In the HER, since the chromaticity correction by sextupole magnets in the arc sections can guarantee sufficient large apertures, this local correction scheme will not be applied.

C Finite-Angle Crossing of Beams

A finite-angle crossing scheme of ± 11 mrad has been adopted for the IP of KEKB. With this scheme, parasitic collisions will not be a concern, even when every bucket is filled by bunches. Since the need for separation bend magnets is eliminated, it allows a much less complex design of synchrotron light masks and a round vertex vacuum chamber at the IP. This choice is expected to improve the optimization of vertex detection and particle tracking devices of the experimental facility.

Superconducting final-focus quadrupole magnets will be used at KEKB for better flexibility of tuning. The use of a finite crossing angle scheme has created room for implementing superconducting compensation solenoid magnets. One superconducting solenoid and one final-focus quadrupole are contained in a single cryostat. The compensation solenoids help reduce the coupling effects due to the detector solenoid, and consequently, improve the dynamic aperture and emittance coupling.

Computer simulation work has found that the finite-angle crossing somewhat reduces usable areas in the ν_x-ν_y plane. This effect comes from synchro-betatron resonances. However, if the synchrotron tune (ν_s) is kept smaller than 0.02, a fair amount of area in the ν_x-ν_y plane will be still free from reduction of luminosity due to resonances.

D Impedance Budget and Beam Instabilities

The total inductive impedance and loss factor in the LER are estimated to be 0.014 Ω and 42.2 V/pC. They correspond to a HOM power of 570 kW. Since the HER has more RF cavities than the LER does, its total loss factor is larger, 60 V/pC. The total HOM power in the HER will be 150 kW.

According to calculations, neither bunch lengthening nor the transverse mode-coupling instability will impose a significant limitation on the stored bunch current. The design current has a factor of two margin for the threshold of the microwave instability. With the design intensity, the magnitude of bunch lengthening will be 20%.

Although a large vacuum chamber (diameter = 94 mm) is to be used in the LER, the growth time of the transverse coupled-bunch instability due to resistive wall of vacuum ducts is estimated to be 5 ms. This instability must be cured by a fast feedback system.

Recent studies indicate that two other types of transverse coupled bunch instabilities may be encountered at KEKB. One is caused by ions that are temporarily trapped around the electron beam orbit in the HER. The ions excite a vertical betatron oscillation with a typical growth time of 1 ms. It will be accompanied by a vertical emittance growth. Although this phenomenon has been neither fully understood nor observed in any storage ring, we should prepare tactical plans for the worst case. A simulation shows that instability oscillations of successive bunches have a similar phase, and hence it can be controlled by using a narrow-band feedback system. It is considered that this instability can be damped by an adequate use of the feedback system

Another is related to photoelectrons coming off synchrotron radiation onto the inner wall of the vacuum chamber. This phenomenon is expected to appear in positron storage rings, e.g. the LER. A simulation shows that the photoelectrons excite a coupled bunch oscillation with a growth time shorter than the damping time. While the photoelectrons have been recently suspected of exciting coupled bunch instabilities in

CESR and the KEK Photon Factory, the proposed conjecture is still controversial. Since the phase difference of the instability oscillations of the bunches is again predicted to be small, we will be able to suppress the photoelectron instability with a powerful narrow-band feedback system.

3 Hardware Systems

A RF System

The RF cavity for KEKB should have a structure that damps higher-order modes (HOMs) in the cavity. The growth time of coupled-bunch instabilities excited by HOMs must be comparable to or longer than the damping time. The cavity should have a sufficient amount of stored energy, so that the detuning frequency due to beam loading is brought below revolution frequency of the ring. Otherwise, a strong coupled-bunch instability will be excited by the fundamental mode of the cavity. For KEKB, two types of accelerating cavities are currently under development: a normal conducting cavity, called ARES, and a single-cell superconducting cavity.

B ARES

Extensive R&D work is under way for ARES (accelerator resonantly coupled with energy storage). It has been shown that the amount of the detuning frequency of the accelerator cell can be dramatically decreased by attaching a low-loss energy storage cell with a large volume. For practical applications at KEKB a 3-cell structure has been proposed, where an accelerating and an energy storage cells are joined via a coupling cell. The system uses a $\pi/2$ mode, which excites an almost pure TM010 mode in the accelerating cell and an almost pure TE015(013) mode in the energy storage cell. In this configuration the field excitation in the coupling cell is negligibly small. Two parasitic modes (0 and π modes) excite a field in the coupling cell. However, they can be damped relatively easily by using a coupler attached to the coupling cell.

In order to suppress HOMs in the accelerating cavity, a choke-mode structure is adopted. While the fundamental mode is confined within the accelerating volume by the choke, HOMs are extracted and absorbed by SiC absorbers. The first prototype of the choke-mode cavity has been successfully tested up to a wall loss power of 110 kW, which corresponds to a gap voltage of 0.73 MV.

C Superconducting RF Cavity

A superconducting cavity has a large stored energy because of its high field gradient. Consequently, it is less sensitive to beam-loading than standard normal-conducting cavities. The superconducting cavity for KEKB is a single-cell cavity with two large-aperture beam pipes attached to the cell. HOMs propagate toward the beam pipes, because their frequencies are above the cut-off frequencies of the pipes. The iris between the cell and the larger beam pipe prevents the fundamental mode from propagating toward the beam pipe. HOMs are absorbed by ferrite absorbers.

A full-size niobium model has been built and tested in a vertical cryostat. The maximum accelerating field of 14.4 MV/m with a Q value of 10^9 have been obtained. Another prototype cavity is under construction for beam tests at the TRISTAN AR. HOM dampers are made by using the hot isostatic pressing (HIP) method. There, ferrite powder is sintered and bonded on the vacuum pipe surface under a high temperature and high pressure environment. Two HOM damper modules built this way have been successfully tested at 508 MHz. The outgassing rate was found to be sufficiently low. No damages to the ferrite was observed. A beam test of these dampers is in preparation.

D Crab Cavity

In a case where some unexpected problems are encountered with finite-angle collisions at the interaction point (IP), a crab crossing scheme will be introduced. The beam line design around the IP includes adequate spaces for crab cavities, which can effectively restore the head-on collision condition with a finite orbit crossing angle.

The TM110 mode field of 1.4 MV at 508.9 MHz will be used to create time-dependent horizontal rotational kicks to beam bunches. Designs of the crab cavity shape and a coaxial beam pipe together with a notch filter have been developed. The required TM110 mode is trapped within the cavity, while other modes that are not required are extracted from the cavity module.

A one-third niobium model has been built for measuring the RF characteristics. The kick voltage required for KEKB has been achieved with a sufficiently high Q-value. Full scale niobium crab cavities for KEKB will be built within three years.

E Vacuum System

Copper will be used as the material for vacuum ducts for its low photo-desorption coefficient, high thermal conductivity, and capability of shielding X-ray. The maximum

heat load due to synchrotron light will be 14.8 kW/m for the LER, and 5.8 kW/m for the HER.

The LER duct has a circular cross section with an inner diameter of 94 mm for reducing resistive wall instabilities. With this large duct size and dipole magnets having a short length, the use of a non-distributed pumping system is allowed for the LER. NEG cartridges will be used as the main pumps for the LER.

In the HER, since the resistive wall instabilities are not strong, a duct with a race-track shape will be used. This will minimize the gap size of the dipole magnets. However, because of the long dipole magnets to be used at the HER, a distributed pumping system with NEG strips will be used there.

F Magnets and Power Supplies

The specifications for magnets and power supplies have been nearly finalized. They are based on an optimization of the lattice design, and studies of the sensitivities of the ring performance with respect to various construction errors. Experience with TRISTAN indicates that those specifications will be satisfied by using a conventional technique.

A large number of magnets from the TRISTAN Main Ring will be recycled for the HER and LER, in as much as they do not compromise the performance of KEKB. The HER will re-use magnets from TRISTAN, except for some quadrupole magnets and defocusing sextupole magnets. For the LER new dipole and quadrupole magnets will be fabricated. This is because the LER requires quadrupole magnets with a larger bore aperture size, and short dipole magnets for obtaining a short damping time.

Some of the large power supplies from TRISTAN will be also used for cost-saving. A main issue in constructing the power supply system is that a large number of medium and small-size power supplies with good stability need to be prepared for sextupole magnets and steering correction magnets. R&D work is under way for building new power supplies to meet the specifications, while minimizing the manufacturing cost.

G Beam Instrumentation

The performance of the KEKB optics will be sensitive to various magnet errors and to the beam orbit at coupling elements, such as sextupole magnets. In order to recover the ideal optics by correcting these errors, beam-based error measurement techniques will be used. The beam position monitor (BPM) system at KEKB will be built to provide beam orbit data for these purposes. The BPM read-out at KEKB is based on a "slow system" in the sense that the beam positions averaged over many turns will be extracted. This allows the beam position data to be obtained with good stability and

precision. The minimum read-out time is approximately 1 second. The signal detection is done with a narrow-band filter circuit together with a synchronous detector. The same detection system has been working at TRISTAN.

Synchrotron light monitors are being prepared for observing the beam profile and for measuring the bunch length. Weak dipole magnets will be installed as the light source. For further precise profile measurement we plan to use another system with lasers, which is now under study.

Feedback systems are being developed to damp the coupled-bunch oscillations of the beam. Since the number of bunches is large ($\sim$ 5000), and the bunch spacing is short (2 ns), the signal processing part of the system is a technological challenge. A 2-tap FIR digital filter system is being developed as the kernel of the signal processing unit. Since this filter requires only subtraction operations in the arithmetic unit (no multiplication operations are necessary), the circuit can be built with memory chips and simple CMOS logic ICs, without relying on digital signal processing (DSP) chips. This signal processing scheme is used for both the longitudinal and transverse feedback systems. Prototype units have been completed for transverse and longitudinal pick-ups that can detect bunch oscillations for the 500 MHz bunch frequency. Feedback kickers are also being developed.

H Control System

Efforts will be made to maximally utilize the existing software toolbox, libraries and the framework for efficient development of a reliable control system for KEKB.

The lowest level hardware control will be done by either CAMAC, GPIB or VME. The software to control such devices and to handle low level data manipulation will be built with the EPICS toolbox system, which has been developed by a collaboration of several high energy physics laboratories. The data acquisition and the control signal transmission are to be handled by I/O processors that operate in the framework of the EPICS system.

Fast network loops with FDDI or ethernet, wherever appropriate, will be implemented to provide a sufficient bandwidth for the data traffic. The man-machine interface layer will be built on the X-windows system which will be running on Unix workstations. A sophisticated accelerator model code will be integrated with the control system for improved efficiency in understanding the machine behavior.

4 Schedule

A three-month long beam experiment is planned for 1996 at AR. The existing RF cavities will be temporarily removed from the ring, and an ARES cavity and a single-cell superconducting cavity for KEKB will be installed for testing. The goal is to store a 500 mA electron beam at 2.5 GeV in a multi bunch mode. Transverse and longitudinal feedback systems will also be installed and tested.

The main components of the LER, such as the magnets and vacuum elements, will be fabricated in JFY 1995 and 1996, whereas those for HER will be fabricated in JFY 1996 and 1997. Operation of the TRISTAN Main Ring will be discontinued near the end of 1995. Its components will be dismantled, starting January, 1996. By the end of 1996 the TRISTAN tunnel will be ready for installing the magnets. The commissioning of KEKB is scheduled to begin within JFY 1998.

Table 2 summarizes the budget profile of the project. The total budget amounts to 354×10^8 yen. From JFY1998, the last year of construction, we expect 32×10^8 yen for operational money.

Table 2: Budget Profile of KEKB

Fiscal year	Accelerator and linac	Detector	Operational	Total
1994	14.61	5.37		19.98
1995	30.41	11.61		42.02
1996	76.53	18.63		95.16
1997	98.49	16.29		114.78
1998	73.96	8.10	32.00	114.06
Total	294.00	60.00	32.00	386.00

Unit: 10^8yen

Chapter 1

Physics Requirements

1.1 Energy Asymmetry

The required energy asymmetry at KEKB is derived from considerations on the physics program. The major part of the research topic is a study on CP violation in decays of neutral B mesons, where decay modes such as $B \to J/\psi K_S$ need to be reconstructed. The magnitude of CP violation is expected to be $O(10\%)$ according to the Standard Model. For this study, B mesons with finite momenta have to be produced so that the time evolution of their decay pattern can be measured. The B mesons produced in decays of $\Upsilon(4s)$ at rest do not suit this purpose, because in this condition the B mesons will have only a small fixed momentum of 300 MeV in the laboratory frame. An e^+e^- collider with an asymmetric energy collision is required to produce $\Upsilon(4s)$s which are moving along the beam axis in the laboratory frame.

The energy asymmetry is characterized by the motion of the center of mass of the $B\bar{B}$ system in the laboratory frame. Its Lorentz boost parameter is written as

$$\beta\gamma = \frac{E_- - E_+}{\sqrt{s}}. \tag{1.1}$$

Here, the E_- and E_+ are the energies of the electron and positron beams, respectively. The $\sqrt{s}$ is the center-of-mass energy, which can be written as $\sqrt{s} = \sqrt{4E_-E_+}$. It is equal to the rest mass of $\Upsilon(4s)$, 10.58 GeV.

With a larger energy asymmetry, time evolution measurements can be done with better accuracy. However, the effective acceptance of the detector with a fixed geometry will be reduced. The optimum value of the asymmetry must be found by taking into account these two factors. Figure 1.1 shows the total integrated luminosity that is required to observe CP violation as a 3 standard deviation signal as a function of $\beta\gamma$.

It is seen that the asymmetry values between $\beta\gamma$=0.4 and 0.8 result in a similar sensitivity for this measurement.

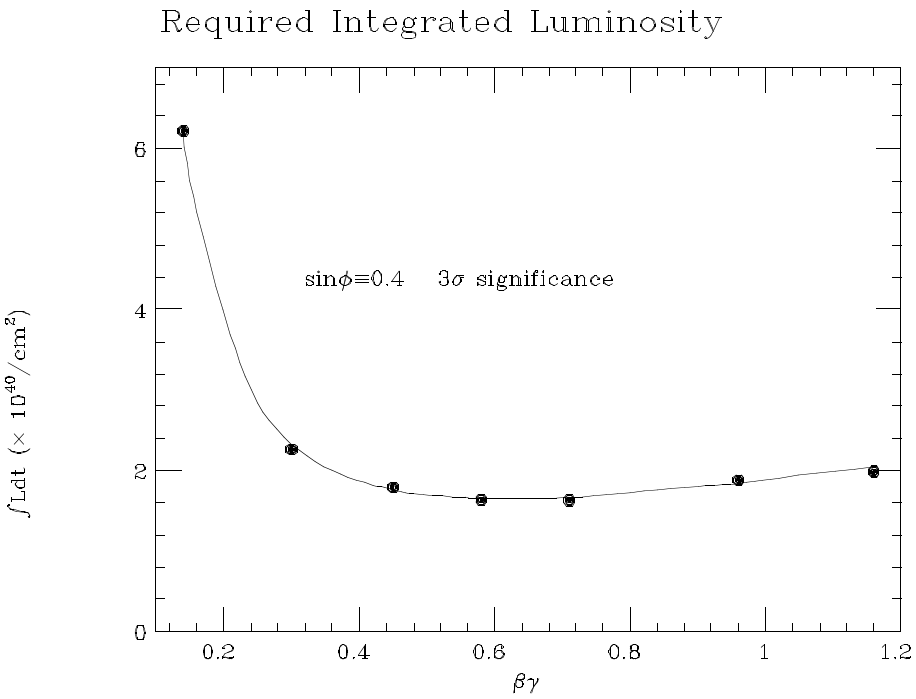

Figure 1.1: Required integrated luminosity for observing CP violation, as a function of energy asymmetry ($\beta\gamma$).

On the other hand, it should be pointed out that there are a number of other physics topics involving B meson decays, where studies of the decay time evolution are not required. For these processes, a smaller asymmetry is preferred for a larger acceptance and for a better event reconstruction efficiency [1].

Combining these considerations, the energy asymmetry has been chosen as $\beta\gamma$=0.42, which is obtained by

$$E_- = 8.00\ GeV \tag{1.2}$$

$$E_+ = 3.50\ GeV \tag{1.3}$$

1.2 Luminosity

For measuring the CP violation in the decay $B \to J/\psi K_S$, the required integrated luminosity is estimated to be between 30 and 100 fb^{-1}. The uncertainty of this estimate arises from quoted errors in the experimental data and their theoretical interpretations.

Other channels to measure CP violation have been also studied. It is estimated that at least 100 fb^{-1} of the integrated luminosity is necessary to measure other important parameters in the Standard Model.

The CLEO-II experiment at CESR is presently collecting data with a world-record high luminosity of a few $\times 10^{32}$ cm^{-2}s^{-1}. They are expected to collect 20 fb^{-1} by the time KEKB starts data taking. Studies on a variety of rare decay modes of B mesons will have been conducted by then. A desire to go beyond the statistical sensitivity available at CLEO-II adds another reason why KEKB should collect more than 100 fb^{-1}.

From these considerations, it is concluded that the target luminosity for the first few years of the experiment should be 100 fb^{-1}. To achieve this in a timely manner, the target peak luminosity for KEKB should be 1.0×10^{34} cm^{-2}s^{-1}.

1.3 Energy Range

Three Υ resonances are known to exist below the $B\bar{B}$ threshold, while the first resonance above the $B\bar{B}$ threshold is Υ(4s) at 10.58 GeV. The Υ(4s) decays almost exclusively into $B\bar{B}$ (either B_u or B_d), and it is at this resonance that the bulk of data should be collected at KEKB.

However, some data need to be collected at different center-of-mass energies for the following reasons.

- An energy scan is required to find the peak of $\Upsilon(4s)$. This is to ensure that the data taking is conducted at the most efficient energy. Since the mass and width of Υ(4s) is well known from measurements by CLEO, it also serves the purpose of cross-calibration of the machine configuration at KEKB. The width of the energy scan can be as small as 30 MeV, and the number of the data points will be at most 10.

- Off-resonance data have to be collected to understand $q\bar{q}$ continuum events. This is important for some data analyses where the continuum background has to be statistically subtracted. An integrated luminosity of more than 10% of the on-resonance data will be required for this purpose. The energy of the off-resonance run should be 10.50 GeV, where the cross section of the $B\bar{B}$ pair-production is negligibly small. At KEKB this determines the lowest center of mass energy for the required run.

- It has been pointed out that studies of B_s should provide additional information on b-quark decays. For this purpose it is necessary to go to Υ(5s) (10.87 GeV) to produce B_s mesons. However, its production rate is expected to be $O(\frac{1}{10})$ of the $B_{u,d}$ production rate at Υ(4s). The present perspective is that the measurement of B_s will be done only after a significant amount of data is collected for $B_{u,d}$ at

Υ(4s). At KEKB this specifies the highest center of mass energy for the required run.

It is concluded that the energy coverage by KEKB should be between 10.4 and 11.0 GeV, which includes a small margin on the higher and lower ends.

$$\sqrt{4E_{-}E_{+}} = 10.4 \sim 11.0\ GeV \tag{1.4}$$

Throughout these runs, the energy asymmetry should be kept at $\beta\gamma$=0.42.

1.4 Beam Energy Spread

In the experiment at KEKB, rare decays of B mesons need to be reconstructed, where the combinatorial background from continuum events can be significant. In many of those decay modes, a reduction of this background is equivalent to an increase of the effective luminosity from the viewpoint of statistical significance.

It has been shown by simulation studies that the signal-to-noise ratio S/N of the B decay reconstruction is approximately inversely proportional to the beam energy spread [2]. By applying an adequate Lorentz boost according to the beam energy, the measured momentum vectors of B meson decay products can be brought into the rest frame of Υ(4). The momentum of the B in this frame will have a fixed value of 300 MeV. This can be used as a powerful constraint for finding B. The effectiveness of this technique depends on the magnitude of the energy spread of the accelerator.

For example, in the reconstruction of B_d decays into $\pi^+\pi^-$, the signal-to-noise ratio is expected to be approximately 1:1 with a beam energy spread of 7.8×10^{-4}. It will be worsened to 1:2, if the energy spread increases by a factor of two. This is equivalent to a factor of 1.7 reduction of the luminosity.

The energy spread should, therefore, be chosen to be the smallest possible that is allowed by machine design considerations.

1.5 Beam background

As the previous sections have shown, high luminosity is required to study the CP violation and rare decays. Naturally, the KEKB machine must store an extremely high beam current. Also, a beam pipe with a small radius needs to be used at the interaction point (IP) for precise vertex measurements. Therefore, the reduction of beam background is a critical issue. It is essential to design the machine, especially the interaction region (IR), so as to reduce the beam background.

If bend magnets are used near the collision point to separate two beams, the synchrotron radiation emitted by particles passing through these magnets have to be handled with utmost care. This condition can be significantly relaxed if no separation bend magnets are used, because synchrotron radiation from other magnets will have a significantly reduced critical energy.

However, it will still be necessary to have movable masks in the straight section to absorb photons that are emitted by the beams when they go through the magnets far from the interaction point. Also, the location and size of the magnets near the IP have to be designed while taking into account the synchrotron radiation background. The aperture of beam pipe vacuum chambers needs to be allocated with sufficient margins to allow the synchrotron radiation to pass, as well as the beam during injection conditions.

The particle background due to beam-gas scattering is potentially more harmful than the synchrotron radiation in KEKB. The vacuum pressure in the IP straight section must be kept at less than 10^{-9} torr. This is required for reducing the rate of off-momentum particles directed toward the beam pipe to an acceptable level.

A set of movable masks in the arc or non-IR straight sections needs to be implemented, in order to clip the beam tail, because the long beam tail might hit the IR masks and cause severe background.

The beam background during the injection time is another important issue, considering radiation damage to the silicon vertex detector, the CsI calorimeter, and their electronics circuit. These issues have to be considered in the design of the injection scheme and the shielding of detector components.

Bibliography

[1] The BELLE Collaboration, KEK Report 94-2.

[2] "Progress Report on Physics and Detector at KEK Asymmetric B Factory", B Physics Task Force, May 1992, KEK Report 92-3.

Chapter 2

Machine Parameters

2.1 Luminosity, tune shift, beam intensity

KEKB is a double-ring asymmetric e^+e^- collider at 3.5 GeV×8 GeV. Its target peak luminosity is $\mathcal{L} = 10^{34}$ cm^{-2}s^{-1}. To determine basic machine parameters, we begin with the most fundamental equations for the luminosity and vertical beam-beam tune shift:

$$\mathcal{L} = \frac{N_1 N_2 f}{4\pi\sigma_x^*\sigma_y^*} R_{\mathcal{L}} \left(\theta_x, \beta_x^*, \beta_y^*, \varepsilon_x, \varepsilon_y, \sigma_z\right) \ , \tag{2.1}$$

$$\xi_{yk} = \frac{N_{3-k} r_e \beta_{yk}^*}{2\pi\gamma_k \left(\sigma_x^* + \sigma_y^*\right)\sigma_y^*} R_{\xi y} \left(\theta_x, \beta_x^*, \varepsilon_x, \varepsilon_y, \beta_y^*, \sigma_z\right) \ . \tag{2.2}$$

Here, $N_{1,2}$ is the number of particles per bunch, and f is the bunch collision frequency. The suffix $k = 1, 2$ specifies each beam in the low energy ring (LER) and high energy ring (HER). The θ_x is the half crossing angle at the interaction point (IP). The functions $R_{\mathcal{L}}$ and $R_{\xi y}$ represent reduction factors for the luminosity and the vertical tune shift, which arise from the crossing angle and the hour-glass effect. Since there is no obvious reason for choosing unequal beam parameters, except for the number of particles per bunch, we simply set ξ_y, $\beta_{x,y}^*$, $\varepsilon_{x,y}$, and σ_z to be equal for the two beams. This implies that $N_1\gamma_1 = N_2\gamma_2$.

The possibility of a round-beam collision has been excluded. With a round beam with small β^* in two planes, so far no consistent design solutions have been found with an acceptable dynamic aperture and with a feasible two beam separation at the IP. We thus combine Equations 2.1 and 2.2, and by assuming equal beam-parameters and flat beams ($\sigma_x^* \gg \sigma_y^*$),

$$\mathcal{L} = \frac{\gamma_k I_k \xi_y}{2e r_e \beta_y^*} \frac{R_{\mathcal{L}}}{R_{\xi y}} \ , \tag{2.3}$$

where $I_k = N_k e f$ is the current for each beam, with $k = 1, 2$. It should be pointed out that if the relation $\beta_y^* \gg \sigma_z$ holds (*i.e.* if the hour-glass effect is small), the ratio of the reduction factors above becomes close to a unity,

$$\frac{R_{\mathcal{L}}}{R_{\xi y}} \approx 1 \ . \tag{2.4}$$

This means that Equation 2.3 can be rewritten in a form that is nearly independent of the choice of the crossing angle. Thus, to a good approximation,

$$\mathcal{L} \approx \frac{\gamma_k I_k \xi_y}{2 e r_e \beta_y^*} \ . \tag{2.5}$$

Equations 2.3, 2.4 and 2.5 state that while the luminosity may be reduced due to the crossing angle, the beam-beam interaction is also reduced by approximately the same ratio. Therefore, if the dynamics of the beam-beam interaction with the crossing angle allows the same value of ξ_y as for the head-on collision, there is no loss of the luminosity for a fixed total beam current. Figure 2.1 shows the calculated reduction factors and the ratio $R_{\mathcal{L}}/R_{\xi y}$ as functions of the half crossing angle θ_x. Note that the reduction factors above simply involve geometric effects due to the crossing angle and the hour-glass effect. No effects due to the dynamics of the beam-beam interactions are included.

In the design of KEKB, we assume $\xi_y \approx 0.05$ and $\beta_y^* = 1$ cm. Then, the beam intensities required for $\mathcal{L} = 10^{34}$ cm^{-2}s^{-1} are $I = 2.6$ A for the LER and $I = 1.1$ A for the HER. Exactly how much luminosity will be actually available at KEKB can be answered only after operating the machine and after examining where the performance limitations come from. Re-optimization of operating parameters will naturally follow studies during operation. An important issue concerning the design of KEKB at this stage is to allocate some flexibility in the parameter space, so that such changes in the future can be easily accommodated. Details of some of the specific issues are discussed in subsequent chapters.

2.2 Crossing angle

Near the IP a rapid two beam separation is necessary in order to maintain optimized focusing of the LER and the HER beams without significantly increasing the chromaticity. Suppression of emerging parasitic crossing effects also calls for a good beam separation, except the designated IP.

Several beam separation schemes based on horizontal bend magnets, a finite beam crossing angle, and their mixed combinations have been examined for KEKB. For

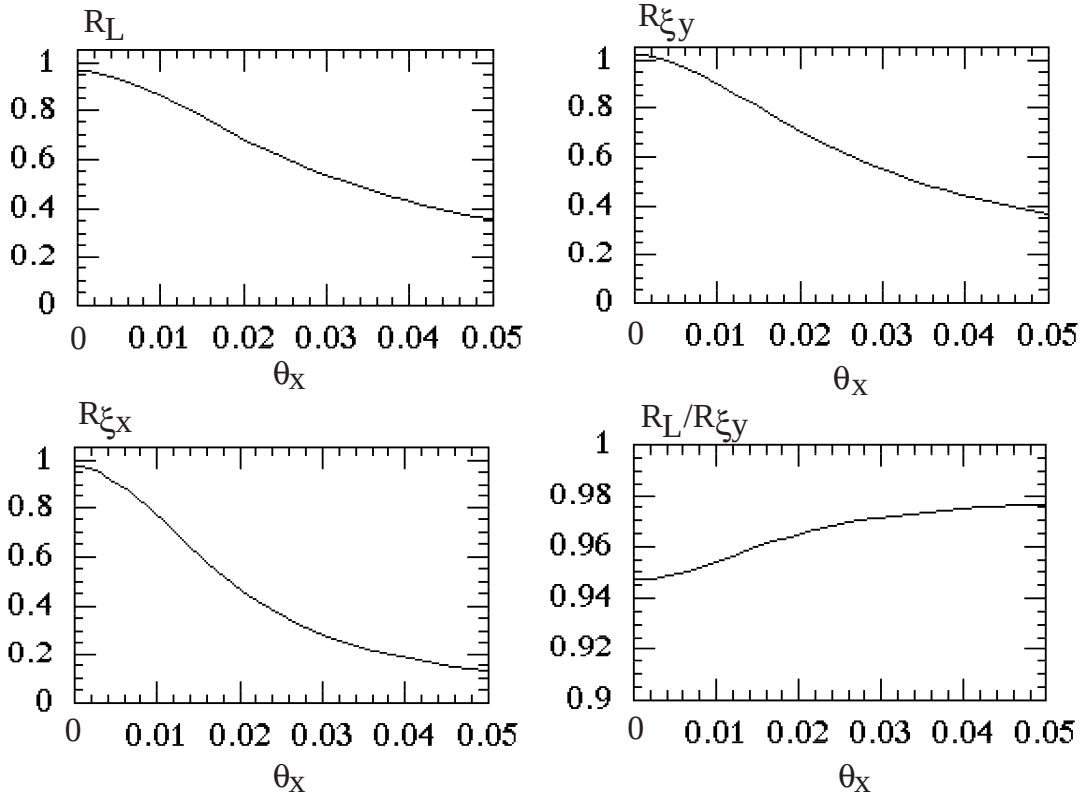

Figure 2.1: Reduction factors of the luminosity and tune shifts as functions of the half crossing angle θ_x. Other parameters are KEKB's. The ratio $R_{\mathcal{L}}/R_{\xi y}$ is always close to unity.

example, it has been found that to allow more than a $20\sigma_x$ beam separation at the first parasitic crossing point, it will be very difficult to accommodate a bunch spacing s_b below 3 m if a small or zero crossing angle at the IP ($\theta_x \leq 3$ mrad) is to be maintained. The reasons include:

- The separation bend magnets will have to be strong (> 0.6 T) compared to the standard bend magnets in the arc sections, leading to significant problems in handling synchrotron radiation in the vicinity of the IP.
- There is a severe limitation of geometrical space available for separation bends very close to the IP (*i.e.* a distance comparable to a half of the bunch spacing).

However, the situation can change significantly when a larger beam crossing angle is allowed. A brief summary of the hardware and beam-dynamics issues involved in the beam separation of varying crossing angle choices is given in Table 2.1.

Crossing angle	Hardware	Beam dynamics
0 mrad	Very compact separation bend magnets (such as permanent magnets) are necessary.	Rapid beam separation is critical for staying away from parasitic crossing effects
2 mrad	Superconducting separation bend is feasible with a reasonable field strength (< 0.7 T).	Synchro-betatron resonance OK?
5 mrad		Comfortable for parasitic crossing effects with $s_b \approx 0.6$ m.
8 mrad	Separation bend magnets are no longer necessary.	
10 mrad		Synchro-betatron resonances OK? Need to be checked.
20 mrad	Use of common quadrupole magnet for two opposing beams per side becomes painful.	Increased need for Crab-crossing.

Table 2.1: Possible choices of the crossing angle, and their implications to the hardware design and beam dynamics.

The big advantage of a moderately large crossing angle of $\theta_x \geq 10$ mrad is that although it eliminates the need for separation bend magnets, it allows final focusing with superconducting quadrupole magnets with reasonable inner aperture sizes. It also offers a flexible configuration that permits a wide range of combinations of the bunch intensity vs. bunch spacing for varying center-of-mass energies. The scheme allows us to safely stay away from potential problems due to parasitic crossing effects. The critical energy of synchrotron radiation that passes through the IP is also significantly reduced by not using separation bend magnets.

It has been estimated that with a crossing angle of $\simeq 3$ mrad or less, the maximum achievable luminosity, with its inevitably large bunch spacing ($\simeq 3$ m), is roughly 3×10^{33} cm^{-2}s^{-1}. Therefore, assuming that full-bunch operation with $s_b = 0.6$ m is eventually possible from RF and multi-bunch stability viewpoints, a scheme with a crossing angle of $\simeq 10$ mrad brings big advantages, if the beam-beam parameter can be maintained at $\xi_y \geq 0.015$. Thus, the critical question is how the beam dynamics behavior will be with finite crossing angles. To investigate this issue, we have conducted extensive simulation studies on the beam-beam interaction with finite crossing angles. The results, as detailed in later chapters, demonstrate an absence of serious degradations at many operating points.

From these considerations and from practical evaluations of the accelerator layout near the IP, we have chosen the half-crossing angle θ_x to be 11 mrad. As a fall-back position, the use of a crab-crossing scheme with superconducting cavities is also being considered. It will serve as a cure to reduce the remaining luminosity degradation, or to extend the acceptable combinations of operating parameters. It should be noted that a crossing angle 11 mrad is close to the minimum that allows us to eliminate the IP separation bend magnets. It is also nearly the maximum crossing angle that allows final focusing of both beams at the IP with common quadrupole magnets. If separate quadrupole magnets are to be used for the two beams, hardware design constraints will force us to use a crossing angle larger than 40 mrad. In that case, the field strength of the crab cavities will have to be increased four-fold, and their reliable operation can be problematic. Up to now the 11 mrad value for the half crossing angle is the most preferred one.

2.3 Bunch length

A shorter bunch length is preferred for reduced intrinsic synchrotron-betatron coupling in the beam-beam interaction. It is also preferred for reduced hour-glass and reduced crossing-angle effects. The lower limit of the bunch length is given by the single-bunch

longitudinal instability, Touschek lifetime, and the required accelerating voltage. We have chosen the bunch length to be $\sigma_z \geq 4$ mm, which is close to the minimum possible value. Here, the bunch-lengthening due to a potential-well distortion needs to be taken into account. The target value of 4 mm includes this bunch-lengthening effect of 20% in the LER. As detailed in subsequent chapters, the lattice design of KEKB will allow us to tune the momentum compaction over a wide range, so that the actual bunch length can be optimized by looking at the beam behavior.

2.4 Bunch spacing

The bunch spacing is the next parameter to be determined. First, the accelerating RF frequency should be $\sim$ 508 MHz, because the RF resources at TRISTAN, which will be reused at KEKB, are based on this frequency. Therefore, the allowed bunch spacing will be an integer multiple of $\sim$ 0.59 m. Since the total beam current has been determined to be 2.6 A for the LER and 1.1 A for the HER, the number of particles per bunch is proportional to the bunch spacing. The hardest limit on the number of particles per bunch comes from the longitudinal single-bunch threshold for the LER. At KEKB, the threshold bunch intensity is about 2.5 times the bunch intensity for the minimum bunch spacing of $s_b = 0.6$ m. Therefore, either $s_b = 0.6$ m or $s_b = 1.2$ m is a possible choice.

Second, we examine the relation between the required bunch intensity and emittance. The vertical beam-beam tune shift given by Equation 2.2 can be rewritten as

$$\xi_{yk} = \frac{N_{3-k} r_e}{2\pi\gamma_k} R_{\xi y} \sqrt{\frac{\beta_y^*}{\kappa\beta_x^*}} \frac{1}{\varepsilon_x} \ , \tag{2.6}$$

where $\kappa = \varepsilon_y/\varepsilon_x$ is the ratio of the horizontal and vertical emittance. We thus obtain the relation

$$\varepsilon_x \propto \frac{N}{\sqrt{\kappa\beta_x^*}} \ . \tag{2.7}$$

Consequently, if the emittance ratio κ and β_x^* are kept constant, the required horizontal emittance is proportional to the bunch spacing, because $N \propto s_b$. Another reason for increasing the emittance, besides Equation 2.7, is the need for maintaining a sufficiently long Touschek beam lifetime for an increased bunch intensity when the bunch spacing is increased.

However, design considerations concerning the interaction region limit the practical maximum beam emittance. This is because when the beam emittance is increased for a fixed β_x^* at IP, the angular divergence there is also increased, resulting in an increased

synchrotron radiation background to the detector. Although a smaller emittance coupling ratio may allow a larger emittance without increasing the angular divergence, it will be problematic to rely on delicate operating conditions of this sort.

In conclusion, at KEKB we have chosen s_b=0.6 m as the standard value. Consequently, the number of particles per bunch with $s_b = 0.6$ m is set as $N = 3.3 \times 10^{10}$ for the LER and $N = 1.4 \times 10^{10}$ for the HER.

2.5 Emittance

When the bunch spacing is chosen, and once the β_x and κ are given, the horizontal emittance is determined by Equation 2.7. As stated earlier, although a smaller β_x^* is preferred for a larger κ, there is a limit given by the angular divergence limit at IP. The horizontal beam-beam tune shift, which can be written as

$$\xi_{xk} = \frac{N_{3-k} r_e}{2\pi\gamma_k \varepsilon_x} R_{\xi x}\left(\theta_x, \beta_x^*, \beta_y^*, \varepsilon_x, \varepsilon_y, \sigma_z\right) \ , \tag{2.8}$$

also speaks for reduced horizontal emittance. The horizontal tune shift does not have to be equal to the vertical value. However, it should not be significantly larger than 0.05, which corresponds to $\varepsilon_x = 1.4 \times 10^{-8}$ m. We have chosen the horizontal emittance so that the luminosity given by the strong-weak beam-beam simulation is maximized in the allowable range. The results are $\beta_x^* = 33$ cm, $\kappa = 2.4\%$, and $\varepsilon_x = 1.8 \times 10^{-8}$. With this choice, the bunch diagonal angle at the IP σ_x^*/σ_z will be 19 mrad, nearly equal to the total beam crossing angle. The reduction ratios, luminosity, and tune shifts are summarized in Table 2.2.

The lattice design (discussed in detail in Chapter 6) will incorporate quadrupole magnet "knobs" so that it can vary the horizontal emittance in the range of $1.0 \times 10^{-8} \leq \varepsilon_x \leq 3.6 \times 10^{-8}$ m. This is to manage possible changes of the bunch spacing, angular divergence, beam intensity, and emittance ratio under actual operating conditions. For instance, full-current operation with $s_b = 1.2$ m instead of 0.6 m will be possible by using this measure.

2.6 Momentum spread and synchrotron tune

The momentum spread of the beam is set to be $\sim 0.07\%$, which is close to the upper limit value from a high energy physics experiment viewpoint, which prefers a small energy spread. From accelerator design considerations, it is hard to reduce the energy spread much below 0.07% without decreasing the radiation damping rate.

The last issue among the choice of basic parameters is the synchrotron tune ν_s, and the momentum compaction factor α_p. Since the bunch length and the momentum spread σ_δ have been determined, ν_s and α_p are not independent. They are related as

$$\sigma_z = \frac{c\alpha_p}{\omega_s}\sigma_\delta \ , \tag{2.9}$$

where $\omega_s = 2\pi\nu_s/T_0$ is the synchrotron frequency. Generally speaking, a large ν_s induces pronounced synchro-betatron resonances, due to lattice nonlinearity effects and beam-beam interactions. It also causes an anomalous emittance growth at synchro-betatron resonance lines. A small value of $\nu_s \leq 0.02$ is necessary to have a sufficiently large tune space as the possible operational parameter space.

On the other hand, a small ν_s decreases the threshold for single-bunch instabilities. Also, higher-order momentum compaction can be more harmful with a small α_p for synchrotron motions with large amplitudes.

Our choice is $\nu_s = 0.015$ for both the LER and the HER. However, the lattice design of KEKB will incorporate another set of quadrupole strength "knobs," so that it can vary the momentum compaction in the range $-1 \times 10^{-4} \leq \alpha_p \leq 4 \times 10^{-4}$, without affecting the horizontal beam emittance.

2.7 Other Issues

The particles in the LER have been chosen to be positrons, so as to reduce the effects of the ion trapping phenomenon of residual gas molecules in the vacuum chamber. In the HER (*i.e.* electron ring), 100–500 of RF buckets need to be left vacant in order to avoid ion trapping. Even if ions are not trapped, transient ions created by the bunch train may interact with the trailing bunches, and a beam break-up phenomenon may result, as has been observed in linear accelerators. Studies of these phenomena are in progress.

The radiation damping time of the LER is longer than that of the HER's by a factor of 2, if the sole source of radiation is bending due to dipole magnets in the lattice. A room will be allocated in straight sections of the LER to implement damping wiggler magnets, if it is found necessary to change the LER damping time.

The machine parameters are listed in Table 2.2.

		LER	HER	
Beam Energy	E	3.5	8.0	GeV
Luminosity	$\mathcal{L}$	1.0×10^{34}		$\mathrm{cm}^{-2}\mathrm{s}^{-1}$
Luminosity Reduction Factor	$R_{\mathcal{L}}$	0.845		
Half crossing angle	θ_x	11		mrad
Tune shifts	ξ_x/ξ_y	0.039/0.052		
Tune shift reductions	$R_{\xi x}/R_{\xi y}$	0.737/0.885		
Beta functions	β_x^*/β_y^*	0.33/0.01		m
Beam current	I	2.6	1.1	A
Bunch spacing	s_b	0.59		m
Particles/bunch	N	3.3×10^{10}	1.4×10^{10}	
Number of bunches/ring	N_B	5000		
Emittance	$\varepsilon_x/\varepsilon_y$	$1.8 \times 10^{-8}/3.6 \times 10^{-10}$		m
Bunch length	σ_z	4		mm
Momentum spread	σ_δ	7.1×10^{-4}	6.7×10^{-4}	
Synchrotron tune	ν_s	0.01∼0.02		
Momentum compaction factor	α_p	$1 \times 10^{-4} \sim 2 \times 10^{-4}$		
Betatron tunes	ν_x/ν_y	45.52/46.08	47.52/43.08	
Circumference	C	3016.26		m
Damping time	τ_E	44.9	22.5	ms

Table 2.2: Machine Parameters of KEKB.

Chapter 3

Beam-Beam Interactions

3.1 Introduction

As Chapter 2 has shown, a beam separation scheme with a relatively large crossing angle (2×11 mrad) has been chosen for KEKB. The expected benefits are as follows:

1. It makes it possible to accommodate a wide range of combinations of the bunch intensity vs. bunch spacing (minimum 0.6 m).

2. It makes it possible to use superconducting final focusing quadrupole magnets, and the system can provide collisions at $E_{CM} = 10.4 \sim 11.0$ GeV without modifying the hardware layout of the beam line.

3. The absence of separation bend magnets leads to a significant reduction of synchrotron radiation near the interaction point.

4. Compensation solenoid magnets can be implemented near the interaction point.

5. An extremely large beam separation is provided, even at the first parasitic collision point.

How this scheme is realistically adequate at KEKB depends on whether the behavior of the beams should be stable and satisfactory under finite angle crossing. The purpose of this chapter is to document the results of studies that have been carried out for KEKB in an effort to answer this question.

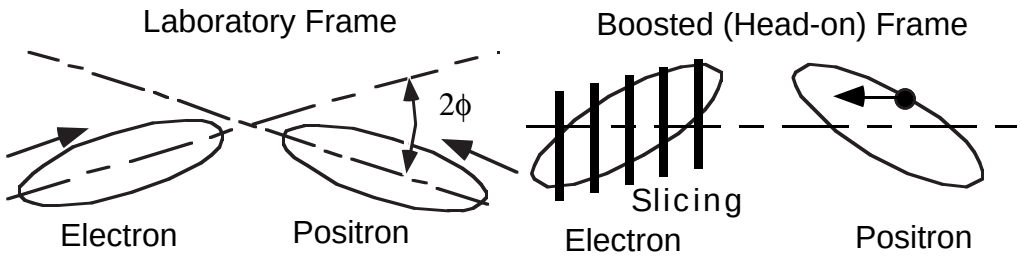

Figure 3.1: Lorentz transformation from the laboratory frame to the "head-on" frame, which is used for applying synchro-beam mapping to calculate beam-beam interactions with finite crossing angles.

3.2 Simulation of a Beam Collision with Finite Crossing Angles

A new modelling algorithm has been developed to simulate beam-beam collisions under finite crossing angles. In the algorithm, as indicated in Figure 3.1, the bunches that are colliding at the crossing angle are first Lorentz-transformed into a frame in which their momentum vectors are parallel. In this "head-on" frame a symplectic synchro-beam mapping is applied, and the beam-beam forces and their effects on the bunches are calculated. When the mapping is finished, the two bunches are Lorentz-transformed back to the laboratory frame, where the beam tracking code takes over the rest of the simulation.

This beam-beam code incorporates all known effects, including: (a) the energy loss due to the fact that a particle traverses the transverse electric fields at an angle, (b) energy loss due to longitudinal electric fields, and (c) effects due to the variation of β along the bunch length during a collision (hourglass effect).

Full descriptions of this code and its preliminary results are given in [1] and the references therein. To date, this is the only code known to us to be fully symplectic in the 6-dimensional phase space with the hourglass and crossing angle effects taken into account. The symplecticity in the 3-dimensional sense, and correct treatment of Lorentz-covariance and bunch slicing there are considered to be important in our application. This is because the planned total crossing angle (22 mrad) is comparable to the geometric angle of bunches at the IP of KEKB, *i.e.* $\sigma_x/\sigma_z = 19$ mrad.

3.3 Beam-Beam Simulation with Linear Lattice Functions

A series of beam-beam simulations has been conducted based on a simplified lattice model, where the beam transfer through the ring is represented by a one-turn matrix and a diffusion matrix [5]. Although the interaction between the beam-beam and non-linear lattice effects cannot be studied using this method, it allows us to quickly compare the luminosity performance in various beam parameter and tune conditions. This simulation is also necessary to compare the luminosity between linear and non-linear lattices.

In this simulation the beam-beam effect is calculated according to the prescriptions given in the previous section. A weak-strong formalism is used. Typically the strong bunch is longitudinally sliced in 5 slices, and the weak bunch is represented by 50 super-particles. The effects of radiation damping and diffusion are included in the calculation. Its details are given in [1]. Parameters such as the initial beam emittance, coupling, bunch intensity, β^*, orbit errors at the IP and the machine tunes are specified as initial conditions. Then, the beam-beam collision and revolutions through the ring are simulated for up to 10 radiation damping times. The resultant beam size is examined. The strong beam is given a specified Gaussian distribution. The weak beam has a distribution function given as the sum of δ-functions, which represent the ensemble of particles. The expected luminosity is calculated as a convolution of the distribution functions of the two beams.

The initial beam parameters in the simulation are specified in such a way that they would give the design luminosity value of 1×10^{34} cm^{2}s^{-1} or somewhat higher values, with collisions of 5120 bunches per ring in the absence of aberrations and beam blow-up. Figure 3.2 shows an example of the results from this simulation. In this case, the crossing angle at the IP is set to zero. The synchrotron tune ν_s is assumed to be 0.017. The figure shows a contour diagram of the expected luminosity as a function of the transverse tune (ν_x and ν_y) in the range $0 < \nu_x, \nu_y < 0.25$. The contour spacing is 10^{33} cm^{-2}s^{-1}. Pronounced luminosity reduction due to the coupling resonance is seen. Also, traces of $\nu_y = 2\nu_x$, $4\nu_x + 2\nu_y = 1$ and the synchro-betatron resonance $\nu_s = 2\nu_y$ are seen.

Figure 3.3 shows a similar luminosity contour plot in the ν_x-ν_y plane, but for the case with a crossing angle of 2×10 mrad. The beam intensity was changed from that of Figure 3.2 in order to adjust the geometric luminosity, while keeping the other parameters unchanged. An additional luminosity reduction due to the synchro-betatron resonance line $\nu_s = 2\nu_x$ is evident. Also, resonance lines such as $\nu_x = 2\nu_y$, $3\nu_x = 5\nu_y$,

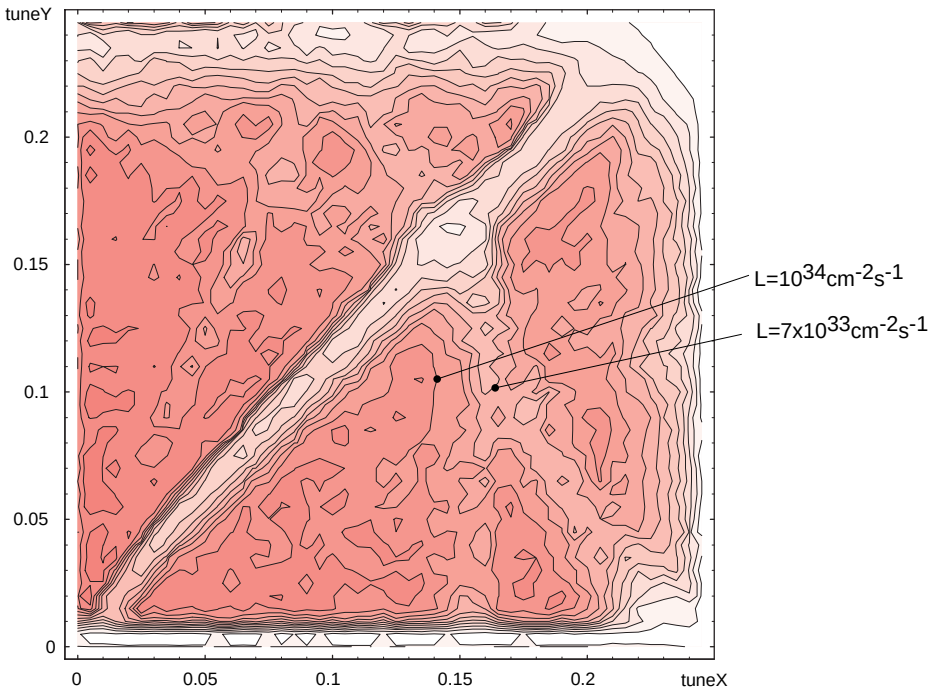

Figure 3.2: Result from a beam-beam simulation with a linear lattice model. In this case, the crossing angle is set to zero. The expected luminosity in the ν_x-ν_y plane is shown. The contour spacing is 10^{33} cm^{-2}s^{-1}.

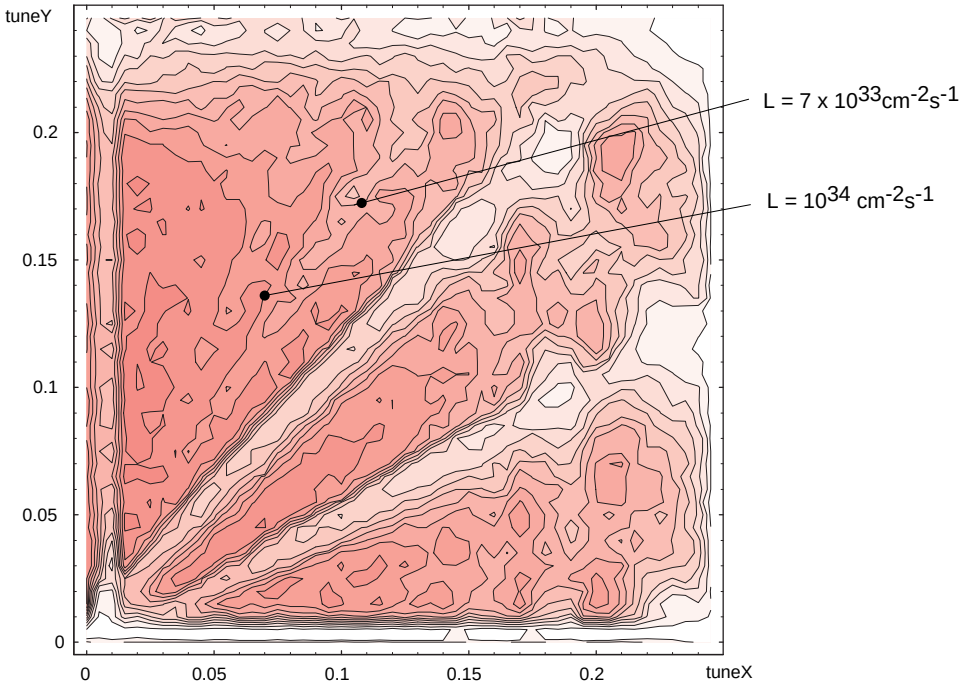

Figure 3.3: Calculated luminosity contour diagram in the case of a crossing angle of 2×10 mrad. The expected luminosity in the ν_x-ν_y plane is shown. The contour spacing is 10^{33} cm^{-2}s^{-1}.

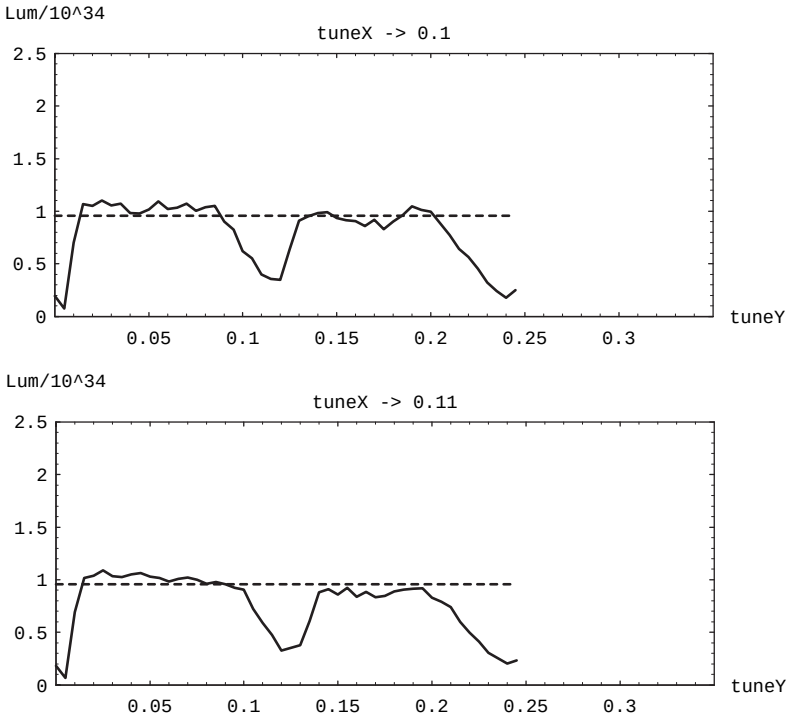

Figure 3.4: Two slices from the luminosity contour plot for the zero crossing angle case. The expected luminosity as a function of ν_y is shown for $\nu_x = 0.1$ and 0.11.

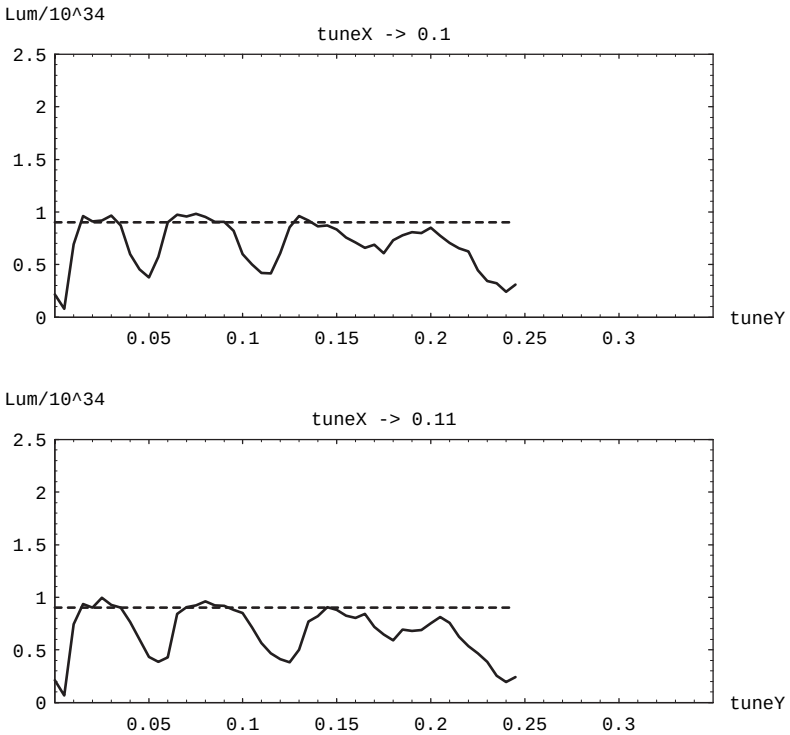

Figure 3.5: Two slices from the luminosity contour plot for a crossing angle of 2×10 mrad. The expected luminosity as a function of ν_y is shown for $\nu_x = 0.1$ and 0.11.

$3\nu_x = \nu_y$, and $4\nu_y - 4\nu_s = 1$ are causing a luminosity reduction. Those resonances did not cause a luminosity reduction in the case of the zero crossing angle. However, a sizeable amount of areas in the ν_x-ν_y plane appear to be intact.

Figure 3.4 shows two slices of the contour plot in Figure 3.2. The expected luminosity as a function of ν_y is shown for $\nu_x = 0.1$ and 0.11. Likewise, Figure 3.5 shows two slices of Figure 3.3 for a comparison.

Some notable observations are summarized as follows:

1. Introducing a finite crossing angle at the IP certainly causes a reduction of usable ν_x-ν_y combinations, because of synchro-betatron and other resonances. The effects are larger for a larger synchrotron tune ν_s, particularly when $\nu_s > 0.03$ holds.

2. However, when ν_s is kept small *i.e.* below 0.02, a fair amount of regions in the ν_x-ν_y plane is still free from synchro-betatron resonances, and thus they appear to be usable. Such regions exist as well-connected zones, rather than many isolated islands. Some of the acceptable ν_x-ν_y regions are compatible with the conditions preferred in dynamic aperture considerations.

3. For the beam intensity of a few $\times 10^{10}$ per bunch or below, no intensity-dependent beam blow-up is predicted with finite crossing angles, as far as this simulation using the simplified lattice model is concerned.

4. When the synchrotron tune (ν_s) is small, and when a resonance-free condition of ν_x-ν_y is chosen, the expected luminosity there is roughly consistent with naive expectations based on the geometric and linear effects, as discussed in Chapter 2.

5. The luminosity calculated with an ideal linear lattice, in some cases, can become larger than a naive expectation, which only considers geometric factors. This is because of effects of the dynamic beta [3] and dynamic emittance [4]. As an example, Figure 3.6 shows correction factors for the β and ϵ calculated for $0 < \nu_y < 0.1$.

The results from this study have been reviewed in conjunction with investigations on the tune-dependence of the dynamic aperture and other aspects of the KEKB design. It has been found that beam dynamics considerations in the lattice design favor a horizontal tune (ν_x) slightly above the half integer resonance. From studies on the engineering design required for magnets in the interaction region, a crossing angle of 2×11 mrad has been chosen. Figures 3.7 and 3.8 show the calculated luminosity tune

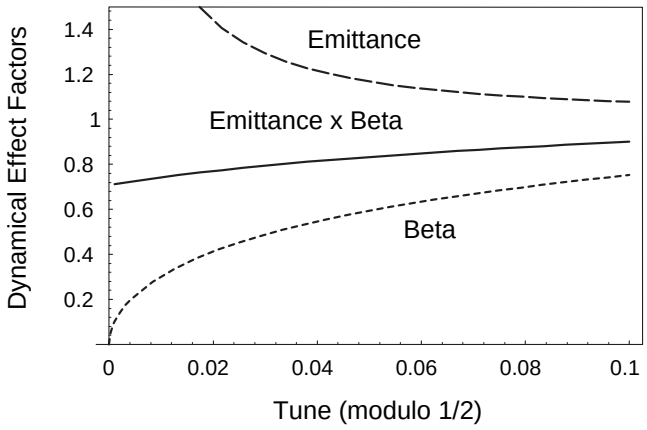

Figure 3.6: Dynamic beta and dynamic emittance effects: the dotted line indicates β, dashed line is ϵ and the solid line is $\beta\epsilon$. The horizontal axis is the tune (modulo 1/2). All of these are normalized by their nominal values.

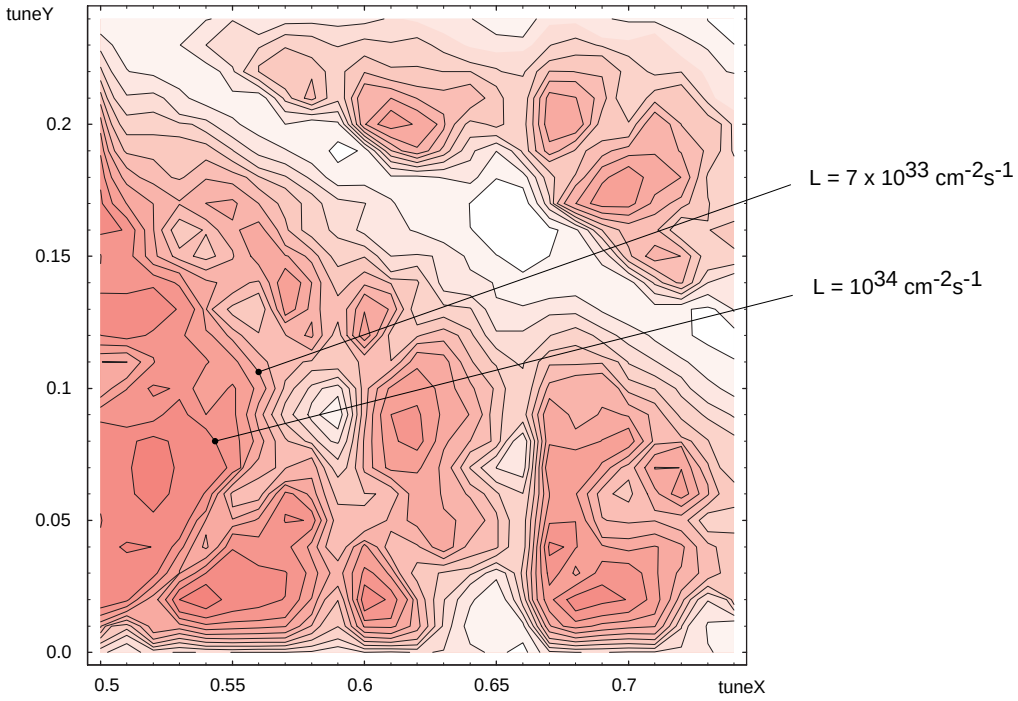

Figure 3.7: Result from a beam-beam simulation with simplified particle tracking. In this case, the crossing angle is set to 2×10 mrad. The expected luminosity in the ν_x-ν_y plane is shown. The contour spacing is 10^{33} cm^{-2}s^{-1}.

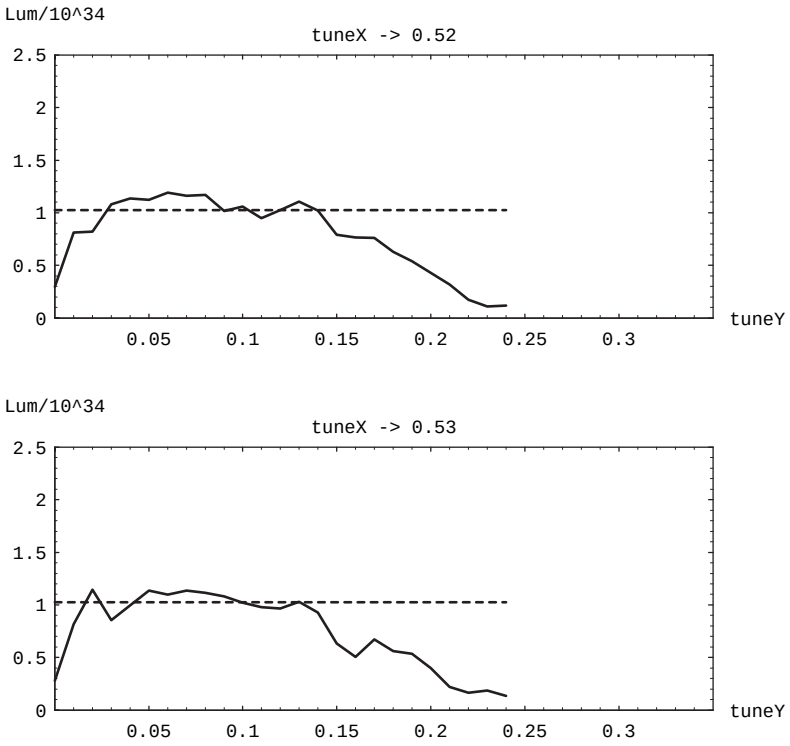

Figure 3.8: Two slices from the luminosity contour plot of for the region $0.5 < \nu_x < 0.75$ and $0 < \nu_y < 0.25$ as shown in Figure 3.7. Expected luminosity as function of ν_y is shown for $\nu_x = 0.52$ and 0.53.

diagram for $0.5 < \nu_x < 0.75$ and $0 < \nu_y < 0.25$. The final working parameters for the detailed design work have been determined as Table 3.1. The effective beam-beam parameter for this set of parameters is $\xi_{x,y} = (0.04, 0.05)$, which takes account of the dynamical reduction factors, as discussed in Chapter 1. Figure 3.9 shows the luminosity tune diagram, which gives a magnified view of the vicinity of the working parameter set.

Surveys have also been made on how the luminosity is affected by the bunch length. Let us call the bunch length of the weak beam σ_z^w and that of the strong beam σ_z^s. Figure 3.10 shows the expected luminosity as a function of σ_z^w and σ_z^s. The plot on the right side shows the expected luminosity (solid line) when the condition $\sigma_z^w = \sigma_z^s$ is imposed. The broken line in the plot shows the luminosity expected from a consideration of only the geometry. It is seen that a shorter bunch gives a higher luminosity. It is also seen that there is no reasons for choosing different bunch lengths for the two beams; each bunch should have the bunch length as short as possible. From a consideration of the necessary RF voltages, it was decided to use 4 mm for the bunch length.

β_x at the IP	0.33	m
β_y at the IP	0.01	m
ϵ_x	1.8×10^{-8}	m
ϵ_y	3.6×10^{-10}	m
σ_z	0.004	m
(ν_x, ν_y, ν_s)	(0.52,0.08,0.017)	
Bunch population	1.4×10^{10}	electrons / bunch
	3.2×10^{10}	positrons / bunch
Total number of bunches	5120 max.	per ring

Table 3.1: Working parameter set for the half crossing angle θ_x of 11 mrad, determined from considerations on beam-beam effects, dynamic apertures and others.

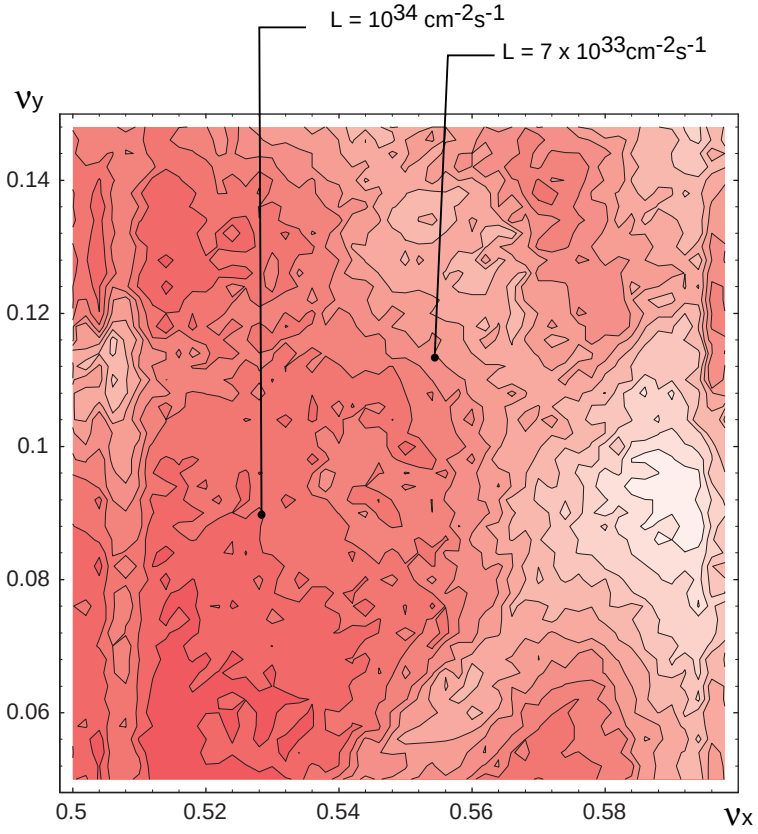

Figure 3.9: Luminosity contour diagram near the operating point.

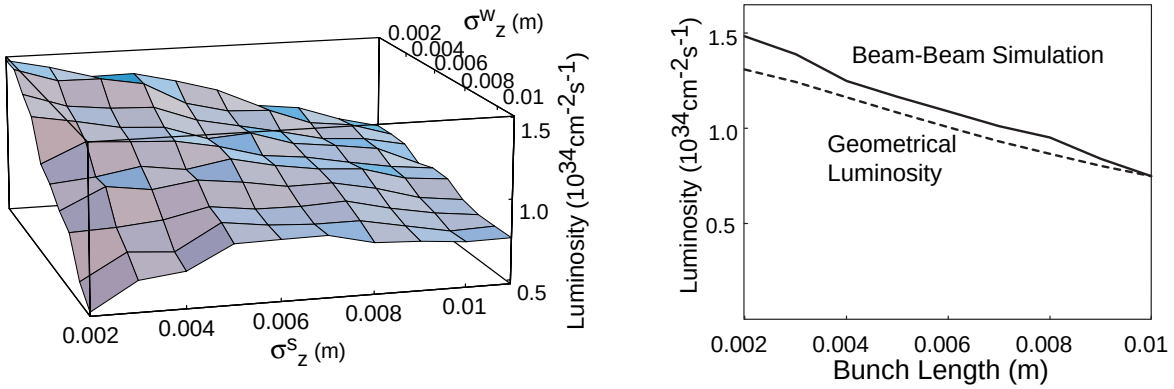

Figure 3.10: Left: Expected luminosity as a function of the bunch length (in m) of the strong bunch (σ_z^s) and the weak bunch (σ_z^w). Right: The same figure for the case with $\sigma_z^w = \sigma_z^s$.

3.4 Simulations with the Lattice Which Includes Nonlinearity and Errors

The beam-beam simulation algorithm based on the weak-strong model has been incorporated in the computer code SAD at KEK (SAD stands for"Strategic Accelerator Design" code). This facilitates a tool to study the effects of finite crossing angles at the IP, combined with the nonlinearity of the lattice and its possible errors.

3.4.1 With Quadrupole Rotation Errors Only

To create finite vertical emittance in the tracking procedure, it is necessary to assume some x-y coupling sources in the ring. As a simplified case, we first examine a nonlinear lattice where rotation errors of the quadrupole (Q) magnets are considered to be the sole source of coupling. We rotate all of the Q magnets randomly, according to

$$\text{rotation angle} = f \times \hat{r}_3,$$

where $\hat{r}_3$ is the Gaussian random variable around zero with a unit standard deviation. The distribution is cut off at 3 standard deviations. For each series of errors, we adjust f so that the σ_y equals the assumed vertical beam size at the IP. (Without errors, the vertical beam size vanishes.) A typical value of f is 5×10^{-4} rad.

Calculations of the beam-beam collision and particle tracking, now with SAD, have been conducted for up to 90,000 turns. Then, the expected luminosity is calculated. Parallel to these calculations, with the given rotation errors of the Q magnets, the single-turn beam transfer matrix with radiation damping and the single-turn diffusion

matrix of the ring are extracted[5]. These matrices are used in a beam-beam simulation with the linear ring-lattice as discussed in the previous section. The difference between the luminosity values obtained in these two methods is considered to give some information about the effects of nonlinearity in the lattice including sextupole magnets and skew fields.

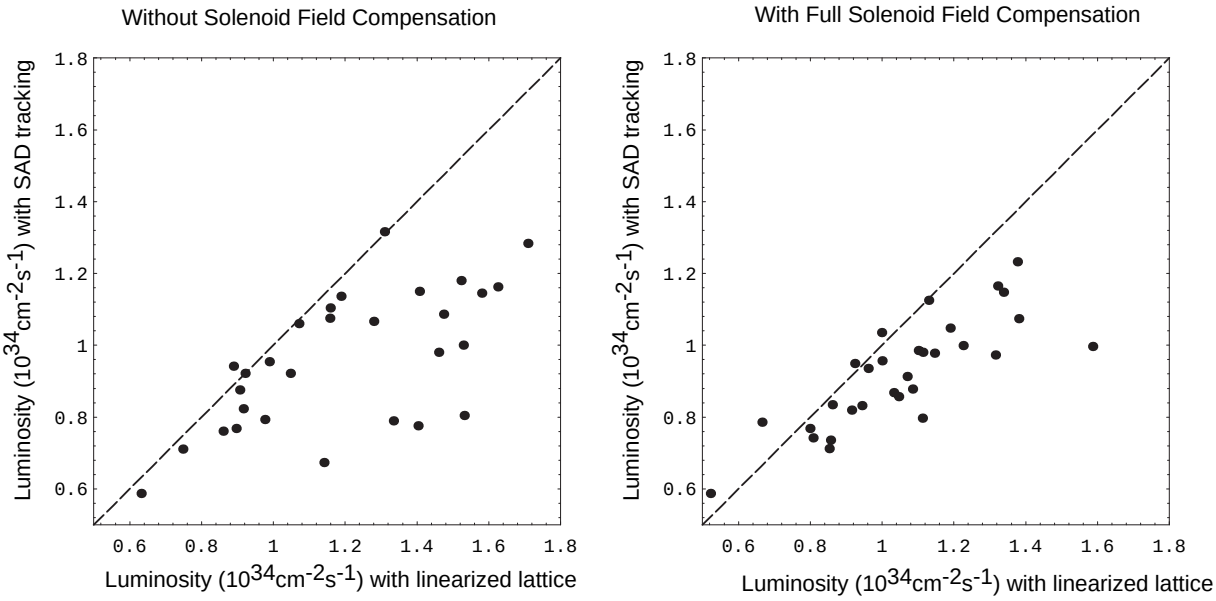

Figure 3.11: Expected luminosity in the weak-strong model calculations of beam-beam interactions, which are combined with tracking through the ring. The two diagrams show the cases where the detector solenoid field is compensated in situ at the IP (right) and without (direct) solenoid field compensations (left); the solenoid field is compensated by skew quadrupole magnets sitting at other locations.

Furthermore, to investigate the effects of the presence of a solenoid field from the experimental facility at the IP, those calculations have been repeated for two versions of the lattice design. In the first case, no explicit solenoid field compensation is made at the IP, and all of the coupling corrections are made with skew quadrupole magnets distributed in the interaction region. In the lattice case, the field compensation is achieved with counter-acting solenoid magnets.

Figure 3.11 shows the results of this study. For each data point in the scatter diagram, the horizontal coordinate gives the expected luminosity from calculations based on the linear lattice matrix. The vertical coordinate gives the luminosity expected from full SAD tracking. The diagram on the left shows the result with a lattice design which assumes no solenoid field compensation at the IP. The diagram on the right is from a lattice design with full solenoid field compensation.

The expected luminosity has been found in the range of $(0.938 \pm 0.185) \times 10^{34} \mathrm{cm}^{-2}\mathrm{s}^{-1}$, depending on the random number seed that is used to create rotation errors of quadrupole magnets. Figure 3.11 indicates that compensation of the detector solenoid field by counter-acting solenoid magnets is favored over coupling corrections with skew quadrupole magnets. The field compensation scheme at the interaction point is designed to use compensation solenoid magnets.

3.4.2 With Realistic Lattice Errors

Simulations with SAD have been repeated with a more advanced model of lattice errors. Here, finite alignment and excitation errors of the bend (B), quadrupole (Q) and sextupole (S) magnets are simultaneously considered, together with offset errors of the beam position monitors (BPMs). The typical magnitudes of the assumed errors, which we consider realistic, are summarized as follows:

type of element	BPM	B	Q	S	Steering correctors
horizontal shift (μm)	75	0	100	100	0
vertical shift (μm)	75	100	100	100	0
x-y rotation (mrad)	0	0.1	0.1	0.1	0.1
strength error	0	10^{-4}	10^{-3}	10^{-3}	0

$\times f$,

Gaussian errors ($\hat{r}_3$) are produced according to the rms values given in the table above. For each series of generated errors, orbit and tune corrections are made in the tracking code as if it were in an actual operation. Then, the scale of the assumed errors is re-normalized so that the expected vertical spot size σ_y agrees with the design value. We call this normalization factor f. With those renormalized errors in the machine, the orbit and tune corrections are, once again, performed. The expected luminosity is evaluated by using the beam-beam code, plus the tracking with SAD. Different random seeds used for generating lattice errors result in different values of f (error normalization factor) and different expected luminosity values. Some of the obtained results are:

$$\mathrm{luminosity}/10^{34}\mathrm{cm}^{-2}\mathrm{s}^{-1} = \begin{cases} 1.21 & f = 1.4 \\ 0.9 & f = 0.8 \\ 1.34 & f = 0.5 \end{cases}$$

This result indicates that the lattice nonlinearity and possible machine errors do not lead to fatal degradations of the estimated luminosity.

3.5 Quasi Strong-Strong Simulation

The results presented so far are based on a strong-weak model, where typically the HER beam (electron) is assumed to be strong, and the LER beam (positron) to be weak. To address the issues which may be overlooked in this treatment, a quasi strong-strong formalism has been developed. In this scheme, once every 500 turns of revolution the average electron and positron bunch sizes are "registered." During the next 500 turns, weak-strong model calculations are performed, while this "registered" electron (positron) bunch size is used as the "strong bunch size" for calculating the development of the positron (electron) bunch size. Then the "strong bunch sizes" are updated again, and the simulation continues.

Figure 3.12 shows the expected luminosity as a function of the revolutions. A linear lattice is used to represent the lattice beam transfer. No indications of a bunch core blow-up is seen. Figure 3.13 shows that the horizontal beam size obtained in the simulation is $\sigma_x = 6.2 \times 10^{-5}$ m. It is somewhat smaller than the nominal value 7.56×10^{-5} m. This is consistent with the dynamic beta and dynamic emittance effects.

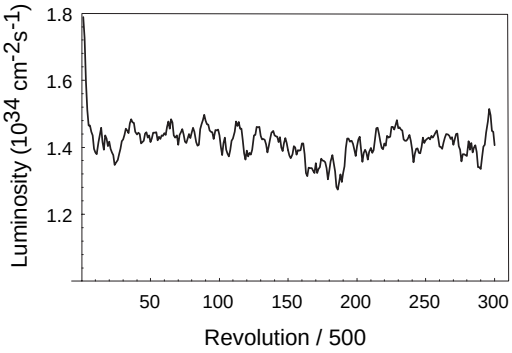

Figure 3.12: The expected luminosity as a function of the revolution number in the quasi strong-strong model calculation.

However, it has been found that unequal damping times between the LER and HER could result in unequal blow-up of the vertical tails of the two beams. This phenomenon is illustrated in Figure 3.14. There, the time development of the rms bunch size in the vertical direction for the electron (positron) is shown by solid (broken) lines. The left side represents the case where equal damping times are assumed for the LER and HER.

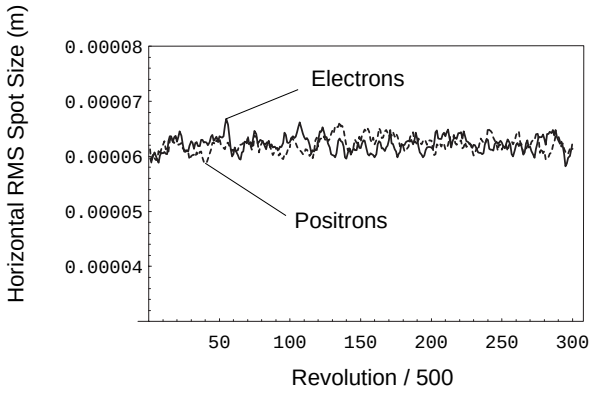

Figure 3.13: Behavior of σ_x as a function of the revolution number. The solid line shows the electron bunch size. The broken line shows the positron bunch size.

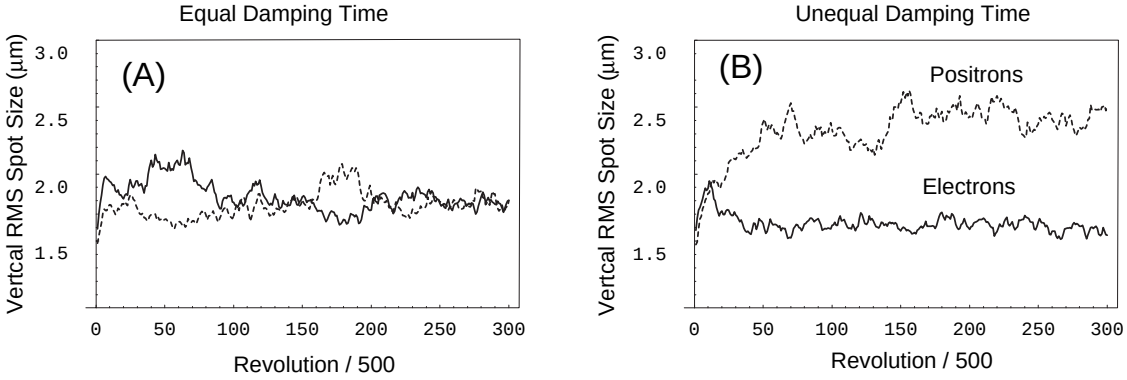

Figure 3.14: Behavior of σ_y as a function of the revolution number. The design value is $\sigma_y = 1.66 \times 10^{-6}$ m. The solid lines show the HER beam size and the broken lines show the LER beam size. The figure on the left (A) is for the case when both beams have equal damping times. Figure on the right (B) shows the case where the LER has a damping time longer by factor 2.

The right side of Figure 3.14 shows the case with unequal damping times between the LER and HER ($\tau_{\rm LER} = 2\tau_{\rm HER}$). A factor 1.5 blow-up of the positron rms size is seen. Note that the spot sizes plotted here are based on the rms of particle distributions. On the other hand, calculations of the luminosity based on the convolution of the particle distributions show no significant difference for the two cases: *i.e.* with and without equal damping times. This signature is consistent with a growth of the vertical tail. Thus, it appears desirable to maintain similar damping times for the LER and HER. This can be accomplished by using damping wigglers in the LER; it will be part of the lattice design goals.

3.6 Bunch Tails Excited by Beam-Beam Interactions

The presence of non-Gaussian bunch tails causes an extra synchrotron radiation (SR) background to the detector facility, which is harmful to its data collection and data analysis. The fractional bunch tail population should be kept less than 10^{-5} for $> 10\sigma_x$ and 10^{-5} for $> 30\sigma_y$, according to design considerations on SR masks near the interaction point.

The development of bunch tails due to beam-beam interactions has been studied with a long-term strong-weak calculation with a linear lattice model. Typically the simulation is done by tracking 50 super particles over 10^8 turns of revolution. This means 1000 seconds for 50 particles, and 14 hours for a single particle in the actual machine.

Figure 3.15 shows the calculated particle distribution as a function of the action variable I_y in the vertical coordinate,

$$I_y = \frac{1}{2}\left[y^2/(\sigma_y)^2 + p_y^2/(\sigma_{p_y})^2\right]. \tag{3.1}$$

The particle distribution function $\rho(I_y)$ is normalized to unity. In Figure 3.15 the vertical axis indicates $\log_{10}(\rho(I_y))$. The core part is identical with the nominal Gaussian distribution. Non-gaussian tails in the particle distribution are seen. In this case the function $\rho(I_y)$ can be fitted with a sum of

$$\rho(I_y) \lesssim e^{-I_y} + 5.2\times 10^{-3} e^{-0.15 I_y} + 3\times 10^{-6} e^{-0.04 I_y}. \tag{3.2}$$

We define the normalized vertical amplitude A_y as

$$A_y = \sqrt{2I_y}.$$

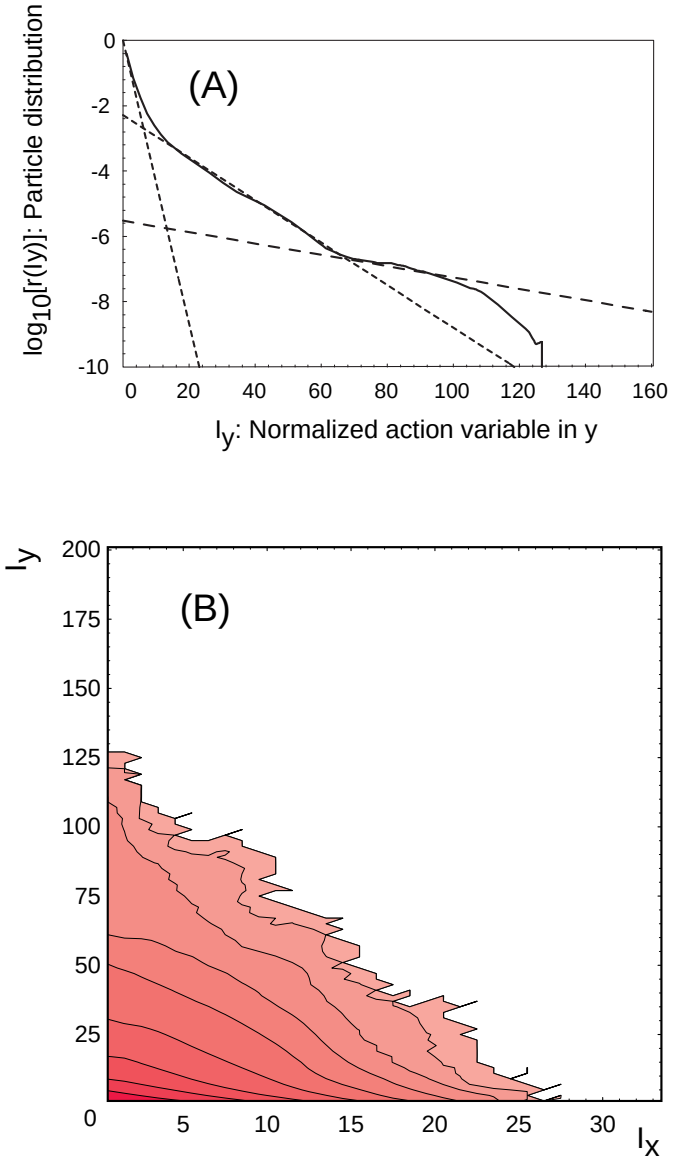

Figure 3.15: (A) Tail distribution for an ideal linear lattice as a function of the normalized nominal action I_y. (B) The same distribution in the (I_x, I_y) space. The contour lines are drawn for each factor step of 10.

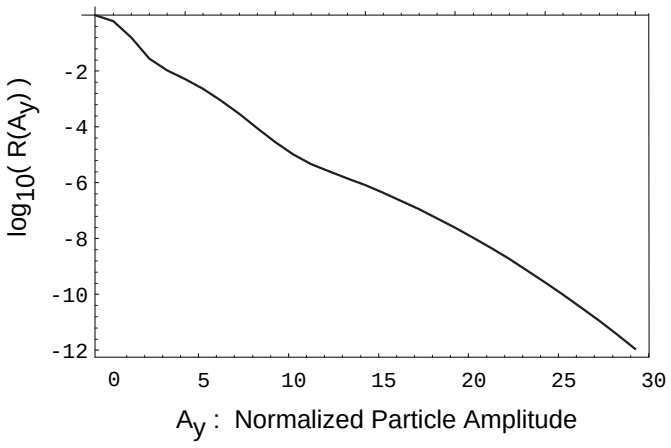

Figure 3.16: Probability of a particle having the amplitude larger than A_y.

Then the probability of finding a particle whose amplitude exceeds A_y is calculated as

$$R[A_y] = \int_{A_y}^{\infty} \rho(I_y) A_y dA_y.$$

Figure 3.16 shows $\log_{10}(R[A_y])$ as a function of A_y, based on the calculations shown in Figure 3.15.

It can be seen that the probability that a particle has a vertical amplitude larger than $30\sigma_y$, where σ_y is the design bunch size, is approximately 10^{-12}. Since the bunch population is on the order of 10^{10}, no particle is likely to have such a large vertical amplitude. Tails in the horizontal direction have been also studied. It has been found that the development of horizontal bunch tails is much slower than in the vertical direction. The limit imposed by requirements on the small synchrotron radiation background to the detector facility is satisfied without problems. Preparations are under way to evaluate bunch tails by using tracking calculations which include non-linear effects of the lattice and possible machine errors.

3.7 Tail, Luminosity and Longitudinal Tilt

The dependence of the tail behaviors on the tunes have been studied. To characterize the size of bunch tails the largest amplitude (a_x, a_y) among 50 super-particles during several damping times is picked up. The part (A) and (B) of Figure 3.17 show luminosity contour plots for the region $0.5 < \nu_x < 1.0$ and $0 < \nu_y < 0.5$ along with the maximum particle amplitude in the vertical direction. They show that luminosity reduction is frequently associated with a growth of vertical tails, but not necessarily so all the time.

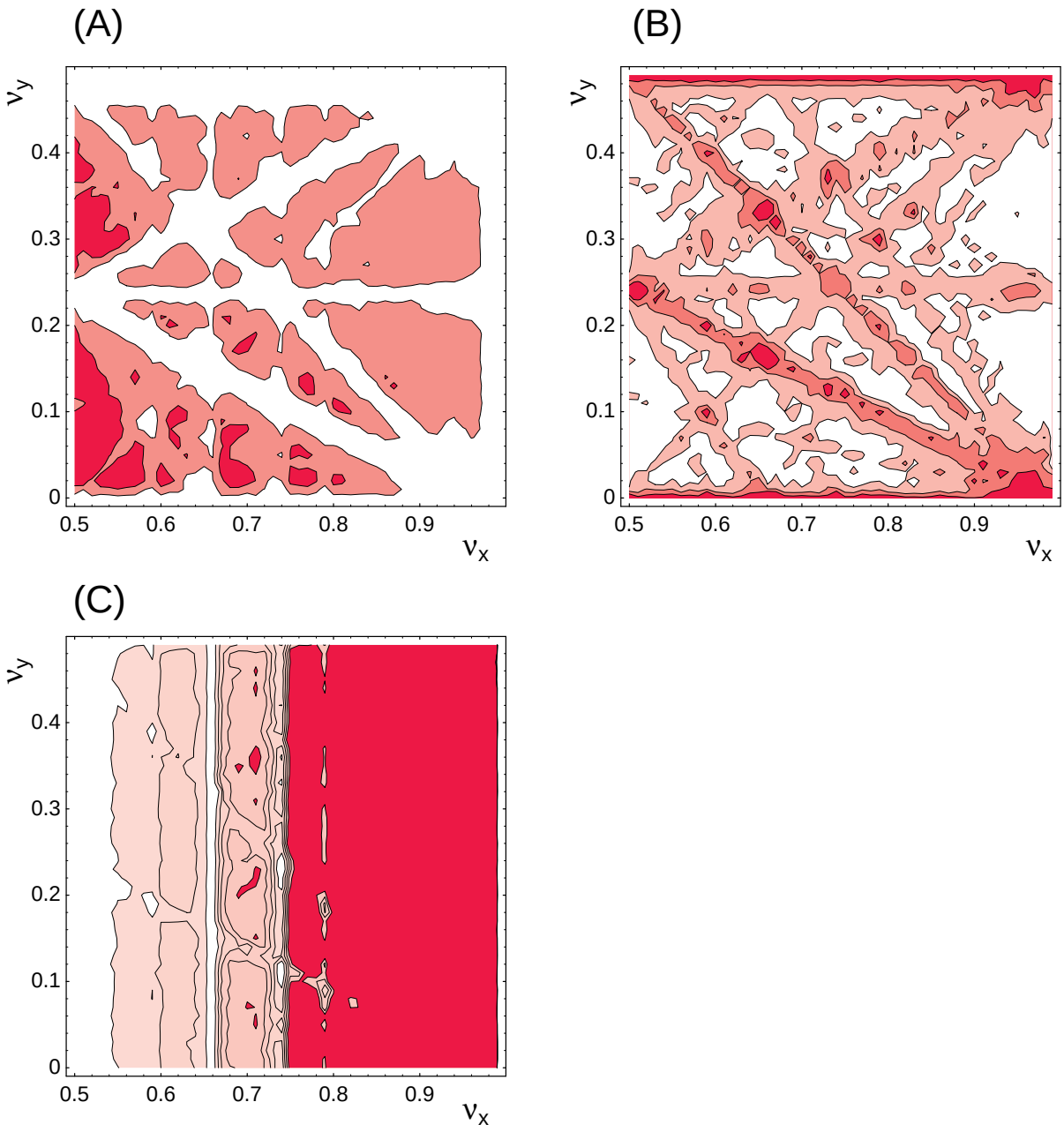

Figure 3.17: (A) Luminosity contour diagram in the ν_x-ν_y plane. The contour lines are drawn for luminosity values of 10^{34} and 0.5×10^{34} cm^{-2}s^{-1}. (B) Contour diagram of the maximum vertical amplitude of bunch particles. Contour lines are drawn for $30\sigma_{0y}$, $20\sigma_{0y}$ and $10\sigma_{0y}$, where σ_{0y} is the nominal vertcal beam size. (C) The longitudinal tilt angle ϕ_{xz} is shown. The contour lines are drawn for 1, 0.8, 0.6, 0.4,and 0.2 mrad.

The angle of the beam envelope relative to the longitudinal coordinate has been also calculated at the same time. The crossing angle in the collision introduces a coupling between the transverse and longitudinal coordinates. Consequently, the principal axes of the bunch may tilt not only transversely, but also longitudinally. We calculate the longitudinal tilt angle in the head-on frame as

$$\phi_{xz} = \frac{1}{2}\arctan\left\{\frac{2\langle xz\rangle}{\langle zz\rangle - \langle xx\rangle}\right\} - \theta_x.$$

Here, $\langle xz\rangle$ represents the long term (three damping times) average of xz. Similar definitions hold for $\langle xz\rangle$ and $\langle xx\rangle$. To be more precise, evaluation should be made with a strong-strong model simulation. However, the weak-strong results can indicate how serious the effect is.

Part (C) of Figure 3.17 shows a contour diagram of the calculated ϕ_{xy}. The longitudinal tilt angle increases as ν_x approaches the integral value from below. It exceeds 1 mrad for $\nu_x > 0.75$.

3.8 Summary of Beam-Beam Simulations with Finite Crossing Angles

The estimated values of the luminosity in the simulations presented so far are summarized in Table 3.2. The assumed beam parameters are set as in Table 3.1.

Method	Luminosity ($\times 10^{34}$)	Legend
1	1.16	Geometrical
2	1.24	Ideal linear lattice
3	0.938±0.185	Nonlinear lattice
4	0.9 to 1.34	Nonlinear lattice with realistic errors and corrections
5	1.4	Quasi strong-strong (equal damping)

Table 3.2: Comparison of the expected luminosity values evaluated by various simulations.

Brief descriptions of individual cases in Table 3.2 are given bellow:

1. Expected luminosity with the 2×11 mrad crossing angle, where only the geometric effects are considered. Dynamical effects, such as the dynamic beta and dynamic emittance, are not considered.

2. Weak-strong beam-beam simulation, combined with a linear, error-free lattice.

3. Weak-strong beam-beam simulation, combined with a nonlinear lattice. Rotation errors of the Q magnets are used to create the finite luminosity coupling. The variations are due to the difference in the seed used to generate the rotation errors. Full compensation of the detector solenoid field is assumed.

4. Weak-strong beam-beam simulation, combined with the nonlinear lattice model. Excitation and alignment errors of bend, quadrupole and sextupole magnets are considered. Orbit and coupling corrections are performed in the tracking code, mimicking the actual operation.

5. Quasi strong-strong simulation with a linear, error-free lattice. Equal damping times for the HER and LER are assumed.

It is seen that within the simulation studies conducted so far, the luminosity in the design goal can be achieved with a finite angle crossing of 2×11 mrad at the interaction point. Unfortunately, this performance cannot be fully experimentally tested until operating the real-life KEKB machine. As a back-up safety measure, the use of crab crossing scheme to combine with the finite angle collision is being considered. The status of its R&D efforts is presented in Chapter 8. Meanwhile, more elaborate studies of beam-beam effects will be continued:

- In a tail simulation, nonlinear effects in the lattice should be included in the calculation.

- In a weak-strong simulation with a nonlinear lattice, error correction schemes from the beam-beam point of view will be examined.

- The strong-strong simulation will be updated so that it can evaluate the beam envelopes in each turn, using a Gaussian approximation to calculate the beam-beam forces.

- A more ambitious strong-strong simulation which does not rely on the Gaussian approximation to calculate the beam-beam force is being developed.

One example of storage rings which implemented a finite crossing angle in the past is DORIS at DESY. It has been known that difficulties were encountered in its operation. According to a report [2]:

"Although the width of these satellite resonances (due to synchro-betatron resonances) is very small (< 0.001) as compared to the distance between the resonances,

they limit the luminosity of the storage ring DORIS. The reasons are the decoupling transmitter and the rf-quadrupole, which are needed to suppress instabilities. The decoupling transmitter gives to different bunches different synchrotron frequencies, with a spread of $\Delta Q_s = \pm 0.006$. The rf-quadrupole produces a spread in betatron frequencies of $\Delta Q_\beta = \pm 0.005$. At the present operating point between 6.24 and 6.15, there are always some bunches on a resonance."

"The theoretical and experimental investigations have shown that the satellite resonances are weaker for Q_β-values closer to an integer. We therefore expect that shifting the operating point into a region near 6.1 will permit higher currents and thus increase the luminosity."

Attention has been paid in the KEKB design so that those conditions which could lead to serious operational difficulties will be avoided. For instance, a fairly low synchrotron tune ($0.01 < \nu_s < 0.02$) will be used. The coupled-bunch instabilities will be addressed by careful design of the RF cavities, feedback systems and an optimized choice of operating parameters, and by not introducing a tune spread.

3.9 Comments on Parasitic Crossing Effects

When the half crossing angle is small ($\sim$ a few mrad or less), the issue of parasitic crossing is quite difficult to study theoretically. This is because both the focussing effects and shifts of bunch centroid need to be considered in a multi-bunch, multi-crossing condition in a 3-dimensional way. Studies have been carried out with simulation calculations for a bunch spacing as small as 0.6 m:

1. A strong-strong model simulation based on the Rigid Gaussian Model has been conducted. Closed orbit effects due to parasitic collisions have been analyzed. It was observed that the closed orbits of individual bunches will differ from each other for a smaller (a few mrad or less) crossing angle. In extreme cases, a closed orbit may not exist at all. Chaotic behaviors of clusters of bunches can result, having orbit deviations exceeding $10\sigma_x$.

2. A 2-dimensional weak-strong model simulation to analyze the beam size during injection and collision conditions has been performed. It was found that for small crossing angles, the injected beam can rapidly blow up, exceeding the dynamic aperture limit, and may never become damped to acceptable sizes.

However, it should be pointed out that the validity of the results for small crossing angles ($<$ a few mrad) with a small bunch spacing ($<$ 1 m) are limited by the approxi-

mation which is used in the simulation. With the present-day capabilities of computing facilities, it appears to be very difficult to obtain reliable results in a realistic computation time. Thus, for a crossing angle $< 2 \times 2.5$ mrad, exact statements cannot be made, except that the acceptable bunch spacing is likely to be limited to roughly 3 m or larger.

Fortunately, the choice of a 11×2 mrad crossing allows us to evaluate the effects of parasitic collisions with an approximation that is based on the simplified Gaussian model with adequate accuracies. This is because the beam separation at the first and subsequent parasitic crossing points will be large (> 6 mm), and the forces between opposing bunches in parasitic crossing will be quite weak. No fatal effects have been observed for a half crossing angle near 10 mrad in weak-strong or strong-strong simulations. We consider that it is safe to conclude that the effects of parasitic collisions at KEKB with a crossing angle of 2×11 mrad are negligible.

Bibliography

[1] For a treatment of the beam-beam interaction, see K. Hirata, H. Moshammer and F. Ruggiero, Particle Accelerators **40**, 205 (1993); K. Hirata, Phys. Rev. Lett., **74** 2228(1995); N. Toge and K. Hirata, *Study on Beam-Beam Interactions for KEKB*, KEK Preprint 94-160 (1994).

[2] A. Piwinski, IEEE Trans. on Nucl. Sci. **24** 1408 (1977).

[3] B. Richter, Proc. Int. Sym. Electron and Positron Storage Rings, Saclay, 1966.

[4] K. Hirata and F. Ruggiero, Particle Accelerators **28**, 137 (1990). (Proceedings of XIV Int. Conf. on High Energy Accel. 1989 Tsukuba.)

[5] K. Ohmi, K. Hirata and K. Oide, Phys. Rev. **E49**751(1994).

Chapter 4

RF Parameters

4.1 Introduction

This chapter discusses the requirements for the KEKB RF system, coupled-bunch instabilities caused by RF cavities and our solutions, and a consistent set of RF design parameters. Detailed descriptions of the cavities and other RF hardware components are given in chapter 8.

Coupled-bunch instabilities arising from the higher-order modes (HOM's) of cavities must be sufficiently suppressed. Since the stored current at KEKB is much higher than that at any existing storage rings, the Q-values of HOM's must be sufficiently lowered, typically much below 100 for dangerous modes, by effectively extracting the field energy out of the cavity. A number of HOM-damped cavity structures have been proposed and studied around the world.

In addition, the accelerating mode itself can give rise to a longitudinal coupled-bunch instability in a large electron/positron storage ring with an extremely high beam current, such as KEKB or other high-luminosity factory machines. If we use conventional normal-conducting damped cavities in KEKB, several modes of coupled-bunch instabilities can be excited. The growth rate will be extremely high due to the high impedance of the accelerating mode.

In order to solve this problem, a new normal-conducting RF structure, referred to as an accelerator resonantly coupled with an energy storage (ARES) [1], was proposed. It employs an energy storage cavity operating in a high-Q mode. Another candidate is a superconducting cavity (SCC), which is fairly immune against this instability. Extensive R&D work is in progress at KEK on both the ARES and the superconducting cavity.

The design parameters of the RF system have been determined by taking the followings into consideration: required accelerating voltage and beam power, growth rates of

the coupled-bunch instabilities, RF properties of the proposed cavities, and the power handling capability of high power components.

4.2 Requirements

4.2.1 RF Voltage

The total RF voltage is determined by requirements to provide: (1) a short bunch length ($\sigma_z = 4$ mm) and (2) the desired synchrotron tune. The required RF voltage (V_c) is given by

$$V_c \sin\phi_s = \frac{cC\alpha_p E\sigma_\varepsilon^2}{e\omega_{RF}\sigma_z^2}, \tag{4.1}$$

where c is the velocity of light, C the ring circumference, α_p the momentum compaction factor, E the beam energy, σ_ε the relative energy spread, σ_z the rms bunch length, ω_{RF} the RF angular frequency and ϕ_s the synchronous phase. In general, a short bunch length requires a high accelerating voltage. The synchrotron tune (ν_s) is given by

$$\nu_s = \frac{C\alpha_p\sigma_\varepsilon}{2\pi\sigma_z}. \tag{4.2}$$

It is seen from Equations (4.1) and (4.2) that when σ_ε and σ_z are given, $V_c \sin\phi_s$ and α_p are proportional to ν_s. Since σ_ε is given by the bending radius, V_c and α_p are determined uniquely by giving σ_z and ν_s.

From beam dynamics considerations the synchrotron tune should be variable in order to find the best operation point, while avoiding synchrotron-betatron coupling resonances. It is considered that the synchrotron tune should be variable from 0.01 to 0.02, while keeping the bunch length constant. For this purpose both the momentum compaction factor and the total RF voltage need to be able to be varied in proportion to each other. Thus the RF voltage should be variable over a range of 4.9∼9.4 MV (LER) and 8.7∼16.2 MV (HER), respectively.

4.2.2 Beam Power

The radiation power loss of the beam at bending magnets is 2.1 MW for the LER and 3.8 MW for the HER. An additional beam power loss is caused by wake potentials due to the ring impedance (HOM loss) and by radiation at wiggler magnets. The total ring impedance is estimated to give a loss factor of about 42 V/pC in the LER and 60 V/pC in the HER, which causes a HOM loss of about 0.57 MW and 0.14 MW, respectively. Wiggler magnets may be optionally installed in the LER in the future for reducing the

Table 4.1: RF-related machine parameters.

Ring	LER	HER	
Particle	positron	electron	
Beam energy	3.5	8.0	GeV
Beam current	2.6	1.1	A
Bunch length	0.4		cm
Energy spread	7.4×10^{-4}	6.7×10^{-4}	
Bunch spacing	0.59		m
Synchrotron tune	0.01∼0.02	0.01∼0.02	
Momentum compaction	$0.93 \sim 1.9 \times 10^{-4}$	$1.2 \sim 2.5 \times 10^{-4}$	
Energy loss/turn	$0.81^{\dagger}/1.5^{\dagger\dagger}$	3.5	MeV
RF voltage	4.9∼9.4	8.7∼16.2	MV
RF frequency	508.887		MHz
Harmonic number	5120		
Damping time	$43^{\dagger}/23^{\dagger\dagger}$	23	msec
Radiation Power	$2.1^{\dagger}/4.0^{\dagger\dagger}$	3.8	MW
HOM Power	0.57	0.14	MW
Total Beam power	$2.7^{\dagger}/4.5^{\dagger\dagger}$	4.0	MW

† — without wiggler

†† — with wiggler

damping time from 43 ms to 23 ms, and also to control the emittance. The total beam power loss in the LER is 2.7 MW without the wiggler, and about 4.5 MW with the wiggler. The total beam power loss in the HER is 4.0 MW. These and other RF-related ring parameters are summarized in Table 4.1.

4.3 Cavity-Related Instabilities

The radiation damping time of KEKB is 23 ms (HER) and 43 ms (LER), respectively. (If the wiggler magnets are installed in the LER, the damping time is reduced to 23 ms.) The growth time of any coupled-bunch instabilities must be longer than the radiation damping time, or at least longer than several milliseconds, so that the instability can be suppressed by a bunch-by-bunch feedback system or by an RF feedback system.

4.3.1 Coupled-Bunch Instability due to the Accelerating Mode

In storage rings, the cavity tuning is usually set to minimize the input power to the cavity. The resonant frequency is detuned toward the lower side to compensate for the reactive component of the beam loading. Without this detuning, a large amount of RF power is reflected from the cavity. The amount of detuning frequency for an optimum operation is given by

$$\Delta f = -\frac{I \sin \phi_s}{2V_c} \times \frac{R_s}{Q_0} \times f_{RF} = -\frac{P_b \tan \phi_s}{4\pi U}, \tag{4.3}$$

where I is the beam current, ϕ_s the synchronous phase, V_c the voltage per cavity, R_s the shunt impedance, Q_0 the Q-value, f_{RF} the RF frequency, P_b the beam power and U the stored energy.

If a high beam current is stored in a large storage ring, the detuning frequency can be comparable to, or even exceed the revolution frequency (f_{rev}). The coupling impedance of the accelerating mode at the upper synchrotron sidebands of the revolution harmonic frequencies f becomes significantly high. Here the f is given by $f = f_{rev}(h + m + \nu_s)$, where h is the harmonic number and $m = -1, -2, \ldots$. If we use conventional normal-conducting cavities in KEKB, the detuning frequency would be several times the revolution frequency. It will excite several modes of the coupled-bunch instability with a growth time on the order of 100 μsec, which is much faster than the radiation damping time.

In order to reduce the growth rate of this instability, the detuning frequency should be decreased. As seen in Equation 4.3, a direct solution is to increase the stored energy compared to the beam power. In other words, we need to decrease R/Q, while keeping a high shunt impedance and V_c.

By employing an energy storage cavity operating in a high-Q mode that is coupled to an accelerating cavity,the stored energy is increased and the growth rate is lowered. This was first pointed out by T. Shintake [2]. In order to put this idea into practical use, Y. Yamazaki and T. Kageyama devised the ARES scheme [1]. A schematic view of ARES is shown in Figure 4.1. The accelerating cavity couples with the energy storage cavity through a coupling cavity in between. With the additional coupling cavity, ARES has advantages in the stability of the accelerating mode and in the damping of parasitic modes associated with the accelerating mode. A more detailed description of ARES is given in chapter 8.

The use of a superconducting cavity (SCC) is another possible solution, since its R/Q value is usually lower than that of conventional normal-conducting cavities, and it can be operated at a higher accelerating voltage. The R&D work is in progress at KEK on both the ARES normal-conducting cavity and the superconducting cavity.

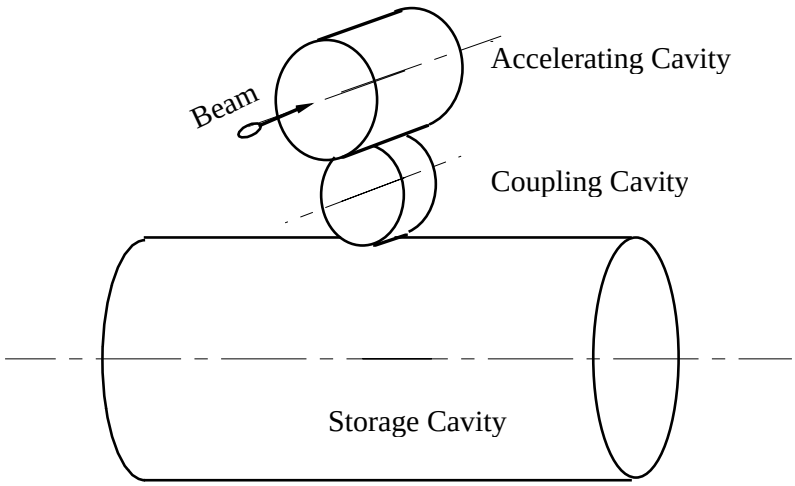

Figure 4.1: Schematic view of the ARES normal-conducting cavity system.

The growth time is quantitatively discussed in the next section in connection with the RF parameters.

Another approach to avoid this instability is to introduce an RF cavity feedback system. This feedback reduces the coupling impedance at the upper synchrotron sidebands of the revolution harmonic frequencies. Along with the development of the cavities, we are developing an RF feedback system with parallel comb filters. It will be applied for providing additional damping, when necessary.

4.3.2 Coupled-Bunch Instability due to HOM's of the RF Cavities

Detailed descriptions on the HOM properties of ARES and SCC are given in chapter 8. This section summarizes the estimated growth time.

Naturally, the accelerating cavity itself that is employed in the ARES scheme must be a HOM-damped structure. The HOM-damping method applied to the accelerating cavity of ARES is to employ a coaxial wave guide which is equipped with a notch filter [3], [4] (see, section 8.1). The R/Q and Q values of the HOM's in the accelerating cavity of ARES was calculated using a computer code MAFIA. The number of cavities is estimated in the next section (20 cavities for the LER and 36 for the HER). The growth time of the fastest growing mode in the LER (HER) is then about 60 msec (150 msec) in the longitudinal case and 30 msec (80 msec) in the transverse case.

In the ARES, since the accelerating cavity is connected to the storage cavity via the coupling cavity, we must be careful concerning the following facts.

- The coupling impedance can be different if the HOM of the accelerating cavity is coupled to other cavities. The impedance of the whole ARES system needs to be accurately estimated.

- Since ARES is a three-cell cavity, the system has 0, $\pi/2$ and π modes which couple to the accelerating mode. The $\pi/2$ mode is the operating mode. The 0 and π modes are parasitic modes; their frequencies are close to the operating RF. The parasitic modes (0 and π) can be damped by a damper attached to the coupling cavity, and the growth time of the coupled bunch instability due to these modes is expected to be longer than 10 msec.

In the case of superconducting cavity, the HOM's are extracted through beam pipes with a large diameter, and are absorbed by ferrite material attached toe the beam pipes. The R/Q values of HOM's have been calculated using a computer code URMEL. The frequency and the Q value of each HOM have been measured with a full-size model cavity made of copper. According to the result shown in section 8.2, when 10 SC cavities are used in the HER, the growth time of the fastest growing mode is about 420 msec for longitudinal and 110 msec for transverse instabilities. They are much slower than the damping time.

4.3.3 Static Robinson Limit

The static Robinson limit gives a maximum stored current of

$$I_{max} = \frac{2V_c \sin\phi_s}{\sin 2(\phi_s - \alpha_L)} \times \frac{1}{\frac{R_s}{Q_0} \times Q_L}, \tag{4.4}$$

where ϕ_s is the synchronous phase, α_L the tuning-offset angle, and Q_L the loaded-Q value. It should be pointed out that if superconducting cavities are operated with the optimum input coupling to the design beam current (I_d) and with the optimum tuning ($\alpha_L = 0$) to compensate for the reactive component of beam loading, the stability condition becomes marginal at the design current. This is because the input coupling is much larger than unity in the case of SCC and the loaded-Q is represented by

$$Q_L = \frac{Q_0}{1+\beta} \approx \frac{Q_0}{\frac{P_b}{P_c}} = \frac{V_c Q_0}{I_d R_s \cos\phi_s}. \tag{4.5}$$

Here, P_b, P_c, β, and Q_0 are the beam power, cavity wall loss, input coupling, and intrinsic Q-value, respectively. It is seen that I_d in Equation (4.5) is equal to I_{max} in Equation (4.4) when $\alpha_L = 0$. In order to avoid an instability, an artificial offset from the optimum tuning should be introduced at the expense of extra RF power. For

this purpose, 10∼20 degrees of the tuning offset (α_L) will be sufficient, which requires 3∼13% extra input power. This will be taken into account in the RF parameters discussed in the next section.

4.4 RF Parameters

The RF operation parameters have been optimized by taking the following into account:

- The required RF voltage should be provided. (It should be variable to change ν_s from 0.01 to 0.02)
- The expected beam power should be supplied.
- The growth time of the instability due to the accelerating mode should be longer than the damping time.
- It should also meet the full wiggler option in the LER.
- The high power system should be stably operated.

It should be noted that in KEKB the beam power is rather high, while the required RF voltage is relatively low. In ordinary storage rings where the beam loading is moderate, the number of cavities is determined by the total RF voltage. On the other hand, in a storage ring where the beam power is significantly large, the number of cavities is determined by the cavity input power, which may be limited by the performance of the input couplers, high power source or others. In the latter case, since the cavities are operated with a lower field gradient, and hence with a larger detuning frequency, the growth rate of the coupled-bunch instability due to the accelerating mode is increased. This is in contrast with the growth rate of the coupled-bunch instability due to HOM's, which is simply proportional to the number of cavities. In the following, we quantify the feasibility for both cases of ARES and SCC, operated in the LER and HER, with the full design beam current and the full wiggler option in the LER. The cavity performance, power handling capability, and the growth rate of the instability are taken into account. The RF properties of the accelerating mode of these cavities are listed in Table 4.2.

4.4.1 ARES Normal-conducting Cavity

The maximum cavity voltage is expected to be 0.5∼0.6 MV/cavity, which corresponds to a permissible wall loss of 150 kW. (This wall loss is distributed to the accelerating

Table 4.2: Accelerating mode of the cavities.

	ARES	SCC	
R/Q	12.8	93	Ω/cavity
Q_0	1.33×10^5	$> 1 \times 10^9$	

cavity and the storage cavity of ARES.) The maximum input power to the cavity depends on the technology available for the input coupler. The input couplers for the APS normal-conducting cavities in TRISTAN have been successfully operated up to 200 kW. The R&D work is in progress to develop an input coupler that can handle a much higher power. In addition, since we will feed the power through the storage cavity, two input couplers can be installed for each ARES system. This scheme doubles the power transfer capability.

Figure 4.2 shows the input power, wall loss, and reflection power in each cavity of the HER as a function of the RF voltage. The input coupling was set to give the optimum coupling at 13.2 MV (ν_s=0.016). The maximum required RF voltage of 16.2 MV can be provided by 36 ARES cavities with an input power of 233 kW. The growth time of the coupled-bunch instability due to the accelerating mode is much longer than the damping time. Thus the required range of the RF voltage from 8.7 MV to 16.2 MV can be covered with these cavities without changing the input coupling or the number of cavities. The parameters at 8.7 MV and 16.2 MV are listed in Table 4.3.

In the LER, the input coupling and the number of cavities should be optimized depending on the total RF voltage. As an example, the parameters optimized at 4.9 MV (ν_s=0.01) and 9.4 MV (ν_s=0.02) are listed in Table 4.3. The maximum required RF voltage of 9.4 MV can be provided with 20 ARES cavities, with the input RF power to each ARES being 355 kW. If the operating voltage is 4.9 MV, we need to decrease the number of cavities; otherwise the growth time becomes faster than the damping time. In this low voltage case 10$\sim$12 ARES cavities will be operated, each of which is powered by one klystron. The growth time will be longer than 30 msec in either case. Thus, the required voltage range can be covered by optimizing the input coupling and the number of cavities.

4.4.2 Superconducting Cavity

An accelerating gradient of 10 MV/m can be easily achieved in a bench test with the present technology for 508 MHz superconducting cavities at KEK. The design gap voltage of the KEKB cavity is set to 1.5 MV/cavity, which corresponds to a gradient

Table 4.3: RF Operation Parameters for the ARES Cavity.

		LER		HER	
Beam energy	GeV	3.5		8.0	
Beam current	A	2.6		1.1	
Beam power	MW	4.5		4.0	
RF voltage	MV	4.9	9.4	8.7	16.2
Synchrotron tune		0.01	0.02	0.01	0.02
# of Cavities		10	20	36	
R/Q	Ω/cav.	12.8		12.8	
Q_0		1.33×10^5		1.33×10^5	
Q_L	$\times 10^4$	2.6	3.6	3.9	
Input β		4.19	2.73	2.41	
Voltage	MV/cav.	0.49	0.47	0.24	0.45
Input power	kW/cav.	591	355	157	233
Wall loss	kW/cav.	141	130	34	119
Detuning freq.	kHz	16.2	17.7	13.5	7.8
Growth time†	msec	49	30	100	180
# of Klystrons		10†††	10	18	
Klystron power††	kW	640	760	340	500

Wiggler magnets are included in the LER.

† — Coupled-bunch instability due to the accelerating mode.

†† — 7% loss at the wave guide, circulator, magic tee etc. is taken into account.

††† — In this case one klystron feeds one cavity.

of 6 MV/m. It is expected to have a sufficient margin for stable operation with high beam currents.

The number of SC cavities for KEKB is determined by the capability of power transfer into the cavity, rather than by an available field gradient. This is because the required RF power to the beam is high, while the required RF voltage is low. If sufficient power cannot be transferred to each cavity, a larger number of cavities should be operated at a lower operating gradient than the design value. In this case, the growth rate of the coupled-bunch instability due to the accelerating mode becomes larger, since the detuning frequency increases.

Figure 4.3 shows the input power and reflection power in each cavity in the HER as a function of the RF voltage in the two cases of 10 and 12 cavities. The input coupling was set at 5×10^4, and a tuning offset of -20 degrees was introduced in order to have a sufficient margin for the static Robinson stability criterion. Figure 4.4 shows the growth rate of the coupled-bunch instability due to the accelerating mode. Using ten SC cavities seems to be a good solution; the growth rate is lower than the damping rate, even if the RF voltage is decreased to 8.7 MV. The necessary input power is 450 $\sim$ 550 kW, depending on the RF voltage. Bench tests of the input couplers, which are of the same type as those used in the SC cavities in TRISTAN, have achieved 850 kW CW power transfer. Thus the required range of the RF voltage from 8.7 MV

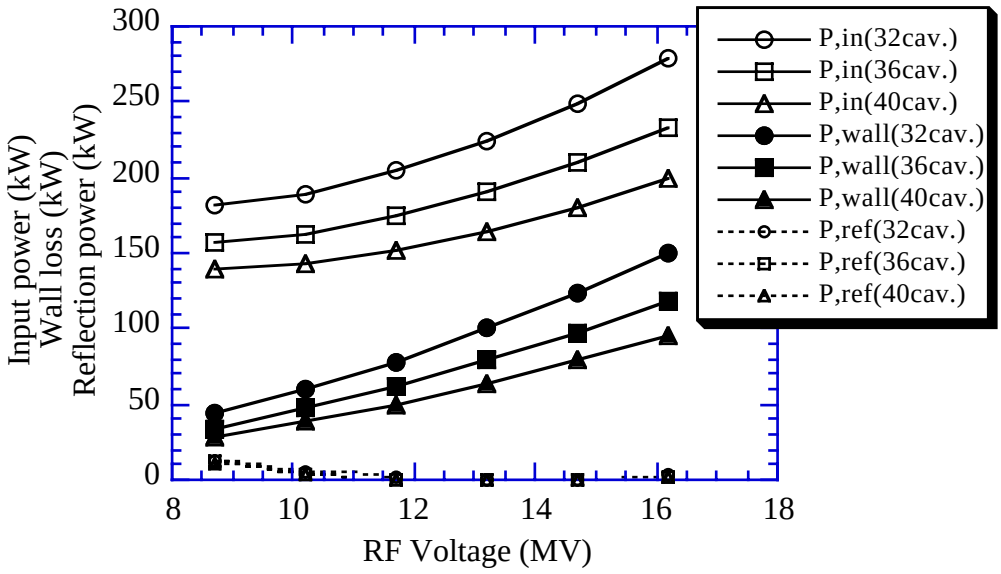

Figure 4.2: ARES in the HER. Input power, cavity wall loss, and reflection power as functions of the RF voltage.

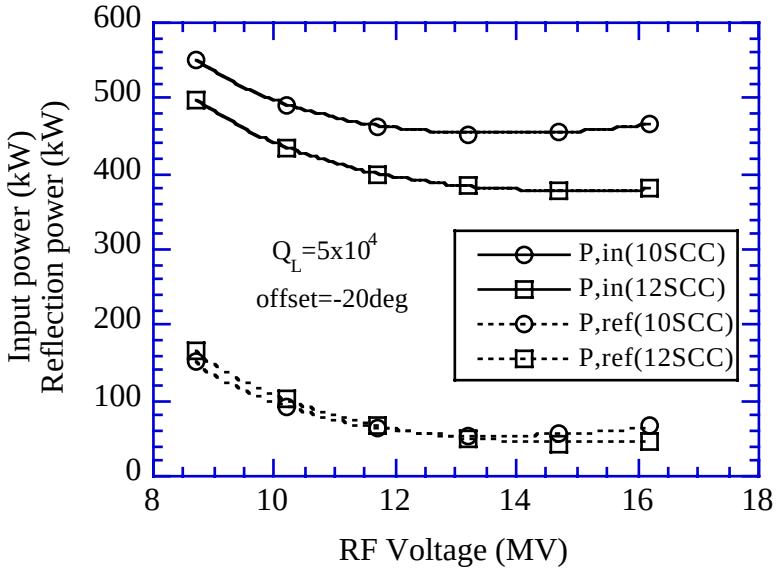

Figure 4.3: SCC in the HER. Input power and reflection power as functions of the RF voltage.

to 16.2 MV can be covered with these cavities.

In the LER, since the beam loading is very heavy and the required RF voltage is low, the detuning frequency is significantly large, even with the SC cavities. An example of the operation parameters is shown in Table 4.4. Even when an input power of 500 kW is fed into the cavity, and even without the wiggler, the growth time is faster than the damping time. If the wiggler magnets are installed, the detuning frequency will exceed the revolution frequency, and the growth time will become on the order of 0.1 msec. If we insist on applying SC cavities in the LER, the impedance seen by the beam must be reduced by 40 dB, for example, by the RF feedback system. This totally defeats the major advantage of SC cavities over the conventional normal-conducting cavities. Thus, the SC cavities are not presently being considered for the LER.

4.4.3 High Power System

As seen from Table 4.3 and Figure 4.3, the klystron output power required in a normal operation is less than 800 kW. However, some margin is needed for the case when one RF unit is down because of a trip or other reason. Thus the maximum power requirement is set to be about 900 kW in the LER with the full wiggler option.

The existing high power systems will be re-used at KEKB, including: the klystrons, power supply systems and cooling systems for the klystrons, and wave guide components, such as the magic tees and circulators. The long-term operation of TRISTAN

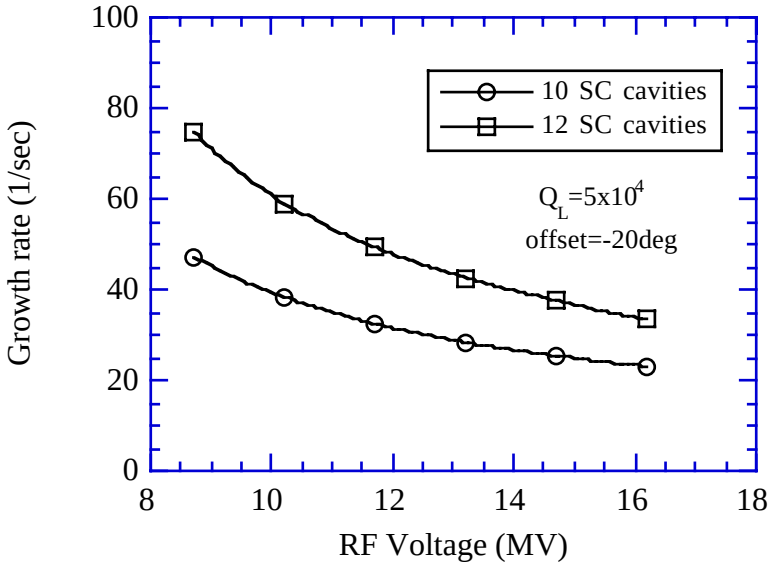

Figure 4.4: SCC in the HER. Growth rate of the instability arising from the accelerating mode.

Table 4.4: RF operation parameters for the superconducting cavity.

	LER		HER	
Beam energy	3.5		8.0	GeV
Beam current	2.6		1.1	A
Synchrotron tune	$0.01 \sim 0.02$		$0.01 \sim 0.02$	MV
Total RF voltage	$4.9 \sim 9.4$		$8.7 \sim 16.2$	MV
	(no wiggler)	(with wigglers)		
Beam power	2.7	4.5	4.0	MW
Number of cavities	6	10	10	
R/Q	93		93	Ω
Unloaded Q	1×10^9		1×10^9	
Gap voltage	$0.8 \sim 1.6$	$0.5 \sim 0.9$	$0.9 \sim 1.6$	MV/cell
Coupler power	450		$500 \sim 400$	kW/coupler
External Q	1.6×10^4	6×10^3	5×10^4	
	$\sim 6 \times 10^4$	$\sim 2 \times 10^4$		
Growth time	$1.2 \sim 14$	$0.3 \sim 0.5$	$23 \sim 54$	msec

has proven the reliability and stability of our high power system. Furthermore, some R&D efforts will be made to improve the performance.

4.5 Summary

We have studied the RF operating parameters by taking into account the requirements for the RF system, the power handling capability of the cavities and the high power systems, and the growth rate of the coupled-bunch instabilities. A consistent set of RF parameters which satisfies these requirements has been obtained for ARES for both the LER and HER, and for SCC in the HER. Using SCC in the LER will require a very sophisticated RF feedback system.

The growth time of any coupled-bunch instabilities caused by the cavities (arising from the accelerating mode and the higher order modes) is expected to be longer than the radiation damping time, or at least, longer than several milliseconds. Even if the growth time of some modes might be faster than the radiation damping time, it is expected to be cured by a bunch-by-bunch feedback system or the RF cavity feedback system.

Bibliography

[1] Y. Yamazaki and T. Kageyama, *Particle Accelerators* **44** 107 (1994).

[2] T. Shintake, *Particle Accelerators* **44** 131 (1994).

[3] K. Akai, J. Kirchgessner, D. Moffat, H. Padamsee, J. Sears, T. Stowe and M. Tigner, *Proc. B Factories* **SLAC-400** 181 Apr. 6-10 SLAC (1992), and *Proc. 15th Int. Conf. on High Energy Accel.* 757 (1992).

[4] T. Shintake, *Jpn. J. Appl. Phys.*, **31** L1567 (1992).

Chapter 5

Impedance and Beam Instabilities

This chapter focuses on the beam instabilities due to single-beam collective effects, impedance contributions from various beamline elements, ion trapping, and other issues in KEKB. We also discuss the power deposition generated by a beam in the form of the higher order mode (HOM) losses by interacting with its surroundings.

The dominant issues at KEKB in terms of beam instabilities are the very high beam current (2.6 A in the LER and 1.1 A in the HER) to achieve the high luminosity goal of $10^{34}\mathrm{cm}^{-2}\mathrm{s}^{-1}$, and a short bunch length (σ_z =4 mm) to avoid degradation of the luminosity by the hour-glass effect and a finite angle crossing. However, since the charges are distributed over many (up to 5120) bunches, the bunch current is not unusually high. As a consequence, single-bunch effects are expected to be relatively moderate; they are well below the stability limits with comfortable margins. The main concern, in turn, is coupled-bunch instabilities due to high-Q resonant structures such as RF cavities and the transverse resistive-wall instability at very low frequency (lower than the revolution frequency). The short bunch can pick up impedance at a very high frequency ($f \sim 20$ GHz), which can lead to an enormous heat deposition by the HOM. The deposited power is likely to be localized at places where wake fields can be trapped by small discontinuities in the beam chamber such as BPMs, or in regions partitioned by two objects inserted inside the beam chamber, such as masks at the interaction region (IR). This heating problem requires serious efforts to (i) reduce the impedance of various beam components or (ii) eliminate structures in the vacuum system which can trap higher order modes.

Other classes of issues include multi-bunch instabilities that may be caused by the effects of ionized gas molecules and photo-electrons in the ring. Some theoretical investigations have been made. They are also discussed in this chapter.

5.1 Impedance

In this section, we summarize our estimate of impedance contributions from various beamline components. Most of them are small discontinuities in the vacuum chamber wall which produce inductive impedance. Their wake potentials are almost a derivative of the delta-function, and therefore, their loss factors are mostly negligible. Among the impedance-generating elements in the rings, the largest contributors are RF cavities, the resistive wall, the IR chamber (including two recombination chambers at both ends), bellows (because of their large numbers), and their protection masks in the arc sections. The impedance of normal-conducting ARES and superconducting cavities will be described in detail in Chapter 8. We only show their loss factors at a bunch length σ_z of 4 mm for later use in the loss factor budget.

5.1.1 ARES RF cavities

When the ARES system is implemented at KEKB, the number of ARES cavities required is 20 for the LER and 40 for the HER. These numbers have been derived to compensate for the synchrotron radiation and HOM power losses, as well as to satisfy the requirement for the short bunch length. Using the program ABCI [1], we have estimated that the main body of the ARES cavity produces a loss factor of 0.529 V/pC for a bunch length of 4 mm. If this cavity is connected to the beam chamber (diameter=100 mm) at both ends with 100 mm long tapers,[1] the additional loss factor will be 0.363 V/pC [2]. In total, the loss factor of one cell of the ARES cavity is 0.892 V/pC.

5.1.2 Resistive-Wall

The material of the KEKB beam chamber was chosen to be copper because of its low photon-induced gas desorption coefficient, its high thermal conductivity, and its large photon absorption coefficient. Its high electrical conductivity also helps to reduce the resistive-wall impedance. Nevertheless, this is still the dominant source of transverse impedance for the coupled-bunch instability. The total transverse resistive-wall impedance of the circular pipe with an inner radius b is given by

$$Z_{RW}(\omega) = Z_0(\mathrm{sgn}(\omega) - i)\frac{\delta R}{b^3}, \tag{5.1}$$

[1]There is a possibility of not using tapers (the vacuum chamber with a diameter of 145 mm may run all the way through the straight section). The quote loss factor quoted will then represent the worst-case scenario.

where Z_0 ($\cong 377\Omega$) is the characteristic impedance of the vacuum, δ the skin depth, R the average radius of the ring, and sgn(ω) the sign of ω. For the LER vacuum chamber ($b \cong 50$ mm), Eq. (5.1) gives the resistive-wall impedance of 0.3 MΩ/m at the revolution frequency 100 kHz, while the impedance decreases to 2 kΩ/m at the cutoff frequency 2.3 GHz of the chamber. The HER vacuum chamber, which has a racetrack cross section shape, may be approximated by a circular one with a radius of 25 mm.

5.1.3 Masks at Arc

Each bellows has a mask (5 mm high) located at its front side so that it is shielded from the synchrotron radiation from a nearby bending magnet. There are about 1000 bellows (one bellows on both sides of each quadrupole magnet. There will be no mask for the BPMs). The cross section of the mask in the medium plane is shown in Fig. 5.1.

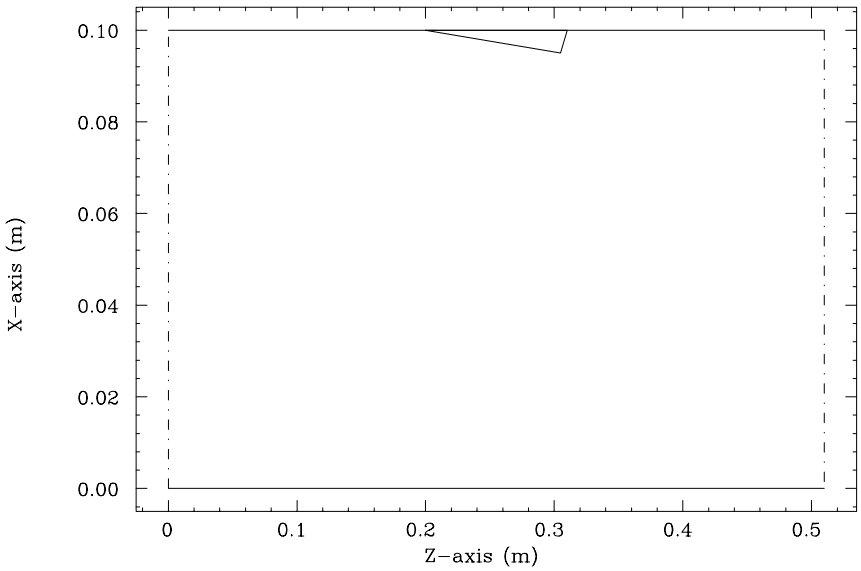

Figure 5.1: Mask at arc

For accurate calculations of the wake potentials and loss factors, a 3-D program called MASK30 has been developed to solve the Maxwell equations directly in the time domain. Using this code, we have found that the total longitudinal impedance of 1000 masks is

$$\mathrm{Im}[\frac{Z(\omega)}{n}] = 2.8 \times 10^{-3} \ \ \Omega, \tag{5.2}$$

where n expresses the frequency ω divided by the revolution frequency ω_0, $n = \omega/\omega_0$. The total loss factor is

$$k_{\mathrm{L}} = 4.6 \ \ \mathrm{V/pC}, \tag{5.3}$$

which corresponds to a total HOM power of 62 kW in the LER.

5.1.4 Pumping Slots

The current design of the pumping slots adopts a so-called "hidden holes" structure, which is similar to those of HERA and PEP-II. A slot has a rectangular shape with rounded edges, which is long in the beam-axis direction (100 mm long, 4 mm wide). The slot is patched on the pumping chamber side by a rectangular grid. They help to prevent microwave power generated somewhere else from penetrating through the slots to the pumping chamber, and then depositing the energy in the NEG pumps. Analytic formulae exist for calculating impedance and loss factor of such a narrow slot with length l and width w by Kurennoy and Chin[3]. The formula for the inductive impedance can be written at low frequency (until the wavelength becomes comparable to the slot width) as

$$\mathrm{Im}[Z(\omega)] \approx -0.1334\ Z_0 \frac{\omega}{c} \cdot \frac{w^3}{4\pi^2 b^2}, \tag{5.4}$$

where c is the speed of light. The thickness correction to the above formula was studied by Gluckstern[4]. It tends to reduce the impedance by 44% compared with that for the zero-thickness case. The total impedance of the pumping slots at arc (there are 10 slots per port and there are 1800 ports in total) with a thickness correction is

$$\mathrm{Im}[\frac{Z(\omega)}{n}] = 1.1 \times 10^{-3}\ \ \Omega. \tag{5.5}$$

The total loss factor was calculated to be

$$k_{\mathrm{L}} = 0.37\ \ \mathrm{V/pC}. \tag{5.6}$$

There will be additional contributions from pumping slots in the straight section. Among them, only those at the wiggler section have been designed. A rough estimate shows that they will increase the above values for the impedance and the loss factor by about 10%.

5.1.5 BPMs

The annular gap (or groove) in a BPM between the button electrode and the supporting beam chamber can be approximated by a regular octagon. The impedance of a BPM can thus be calculated with the same formula for a narrow slot, by considering it as a combination of eight narrow slots (two transverse, two longitudinal, and four tilted)[5]. If we neglect small contributions from the longitudinal slots, and consider four tilted

slots as two transverse ones, the impedance of the BPM becomes equivalent to that of the four transverse slots. For a transverse slot, equation (5.4) is replaced by

$$\mathrm{Im}[Z(\omega)] \approx -Z_0 \frac{\omega}{c} \frac{\alpha_m}{4\pi^2 b^2}, \tag{5.7}$$

where

$$\alpha_m = \frac{2}{3}(\frac{\pi}{4})^2 \frac{a^3}{\ln \frac{2\pi a}{w} + \frac{\pi t}{2w} - \frac{7}{3}} \tag{5.8}$$

is the longitudinal magnetic polarizability. The other parameters are: a, the radius of the annular gap; w , the width of the gap; and t, the thickness of the chamber wall. In our case, they are numerically, $a = 6.5$ mm, $w = 1$ mm, and $t = 1$ mm. For 400 four-button BPMs, the total inductive impedance is

$$\mathrm{Im}[\frac{Z(\omega)}{n}] = 1.3 \times 10^{-4} \ \ \Omega. \tag{5.9}$$

The total loss factor of the BPMs has been computed using the T3 code of MAFIA, and found to be

$$k_{\mathrm{L}} = 0.79 \ \ \mathrm{V/pC}. \tag{5.10}$$

There is a theory [6] which predicts that small holes or slots in the beam chamber can create localized trapped modes in their vicinity. These trapped modes can give rise to sharply peaked behavior of the impedance slightly below the cutoff frequencies of the corresponding propagating modes in the beam chamber. These narrow resonances may drive coupled-bunch instabilities. We have estimated the shunt impedance and the Q-value of such a trapped mode created by the gap in the BPM at the first cutoff frequency of the LER chamber (2.3 GHz) according to Kurennoy-Stupakov's formulae. In this calculation, we assumed that the radiated fields through the gap in the outer space (=inside the BPM) will propagate away freely, and will not resonate in the BPM. Our BPMs have been designed to satisfy this condition. The resulting shunt impedance is

$$R = 1.56 \times 10^{-6} \ \ \Omega \tag{5.11}$$

per one button of the BPM. The Q-value is 0.7×10^5, and the resonant frequency is only by 1.8 Hz below the cutoff frequency. Thus, this mode is likely to propagate away quickly by coupling with the TM mode of the beam chamber. Besides, the shunt impedance given by (5.11) is completely negligible compared with those of HOMs in the cavity.

5.1.6 Mask at IP

There are four masks (two large and two small) on both sides of the beryllium chamber at the interaction point (IP) to shield it from direct synchrotron radiation. Figure 5.2 shows their geometry.

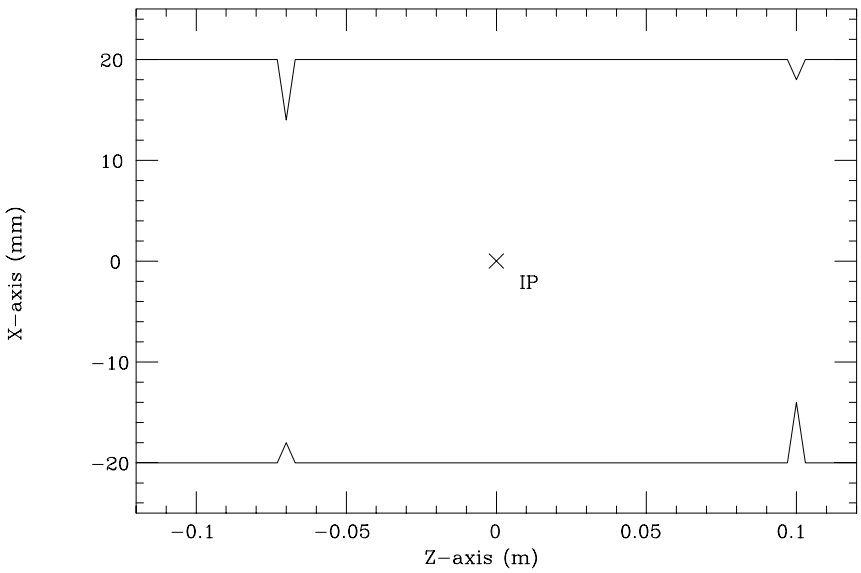

Figure 5.2: Mask at the IP.

The loss factor due to these masks has been calculated using the code MASK30, and was found to be

$$k_{\mathrm{L}} = 0.08 \ \ \mathrm{V/pC}. \tag{5.12}$$

This value is about one-fourth that obtained by ABCI using the axially symmetrical model. The ratio of the two loss factors agrees with the ratio of the opening angle of the IP mask from the beam axis (about 90 degrees) to that of an entire circle. It is seen that a rough estimate of the loss factor can be obtained by multiplying the result for an axially-symmetric model by a factor that corresponds to the solid angle covered by the asymmetric model of interest.

Not all of the power generated at the IP will be deposited there. This depends on the Q-values of modes excited between the masks. The beam chamber at the IP has a cutoff frequency at 6.36 GHz, and the tips of the taller masks create another cutoff frequency at 8.20 GHz. It was estimated using the MASK30 code that if the wake fields between these two frequencies are trapped, the deposited power by two (an electron and a positron) bunches at the IP will be

$$\mathrm{P} = 0.0084 \ \mathrm{V/pC} \times (2.6 + 1.1) \ \mathrm{A} \times (5.23 + 2.22) \ \mathrm{nC} = 240 \ \ \mathrm{W}, \tag{5.13}$$

which is 20% more than the design tolerance of 200 W for a beryllium chamber. However, a careful examination using an axially symmetric model for the IP masks showed that the actual Q-values of the modes between 6.36 - 8.20 GHz are at most 70, which is much smaller than Q $\sim 1.4 \times 10^4$ based on the finite conductivity of the beryllium chamber. This is because the radius of the beam chamber remains the same inside and outside of the IP region separated by the masks, and therefore, the modes can escape to the outside region by making a bridge over the masks. Consequently, less than 0.5%(= $70/(1.4 \times 10^4)$) of the HOM power created at the IP is deposited there (P$\leq$ 1.2W). Even if these modes are resonant with the bunch spacing causing a build-up of wake fields, the maximum enhancement factor for a mode on the resonance is only

$$\mathrm{D_{max}} = \frac{4Qc}{\omega_m s_b} \sim 3.5, \tag{5.14}$$

where ω_m is a typical mode frequency and s_b is the bunch spacing. Therefore, the maximum power deposition is $\mathrm{D_{max}}$P $\leq$ 4.2W. The actual 3-D masks at the IP have a more open structure than the axially symmetric model, and thus the power deposition might be even smaller.

A more serious problem may be a dissipation of the HOM power generated at other parts of the IR chamber, which propagates to the IP region. As will be seen in the next two subsections, a HOM power of about 26 kW will be created in the entire IR region. If the same factor (0.5%) found above can be used as the efficiency for the power deposition at the IP, we can estimate that a power of about 130 W will be deposited at the IP out of 26 kW.

5.1.7 IR Chamber

The vacuum chamber inside the experimental facility makes two large shallow tapers. Its layout is sketched in Fig. 5.3. Its impedance has been calculated using ABCI and was found to be mostly inductive,

$$\mathrm{Im}[\frac{Z(\omega)}{n}] = 1.0 \times 10^{-3} \ \ \Omega. \tag{5.15}$$

The loss factor without any contribution from the IP masks is

$$k_L = 0.29 \ \ \mathrm{V/pC}, \tag{5.16}$$

which corresponds to a HOM power loss of 4 kW. This power deposition as well as the power generated at the recombination chambers must be taken care of by e.g., putting an absorber in the chambers.

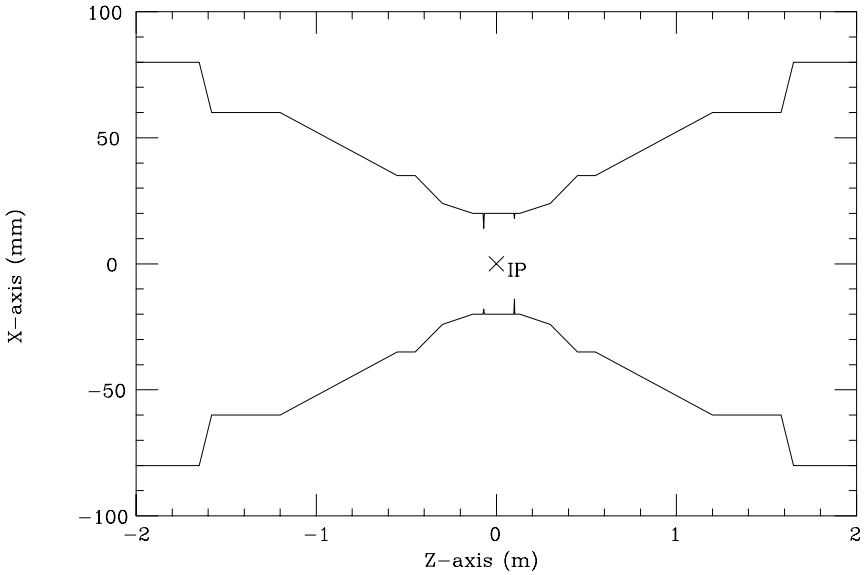

Figure 5.3: Layout of the IR chamber.

5.1.8 Y-shaped recombination chambers

The LER and HER chambers are combined to make a single chamber on both sides of the IP (about 3 m away). The impedance and loss factors of two recombination chambers were modeled as axially symmetric structures, and the results by ABCI were then averaged in proportion to the azimuthal filling factors. It is found to give a large loss factor, almost equivalent to that of two ARES cavities,

$$k_{\rm L} = 1.6 \ \ {\rm V/pC}, \tag{5.17}$$

which corresponds to a HOM power loss of 22 kW due to the low energy beam.

5.1.9 Bellows

As explained in the subsection for the masks at arc, there are about 1000 shielded bellows in both rings (one bellows on both sides of every quadrupole). We have adopted the so-called sliding-finger structure for bellows. Their layout in the LER is sketched in Fig. 5.4. The bellows in the HER have a similar structure. These bellows produce predominantly inductive impedance. Their impedance has been calculated using ABCI. The imaginary part of the total impedance and the total loss factor for 1000 bellows in the LER ring are

$$\mathrm{Im}[\frac{Z(\omega)}{n}] = 4.23 \times 10^{-3} \ \ \Omega \tag{5.18}$$

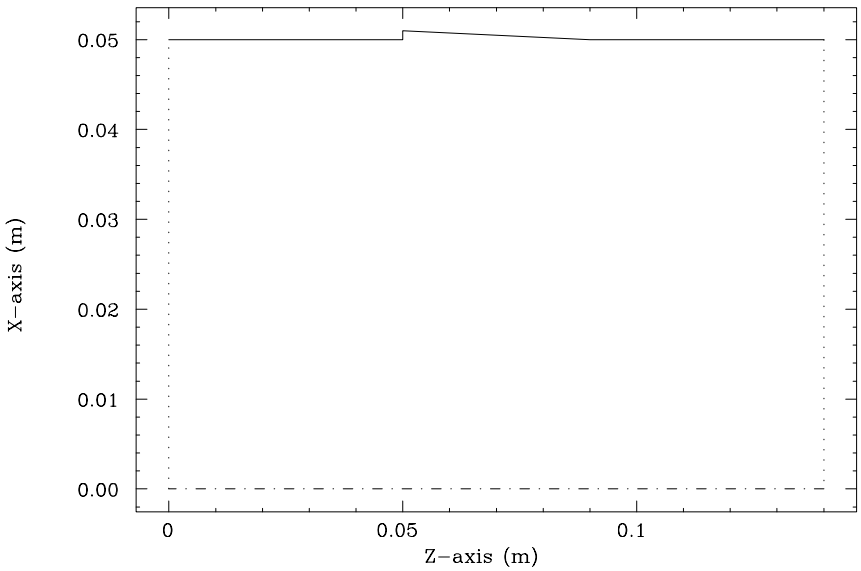

Figure 5.4: Bellows in the LER.

and

$$k_{\rm L} = 2.5 \ \ {\rm V/pC}. \tag{5.19}$$

They are ${\rm Im}[Z/n] = 0.8 \times 10^{-2}\ \Omega$ and $k_{\rm L} = 5.0$ V/pC in the HER.

Additional impedance is generated by the slits between the sliding fingers of the bellows. Using the same formula for a narrow slot, we found that their contributions are negligible.

5.1.10 Summary of Impedance Section

The inductive impedance and the loss factors of the individual elements in the LER are tabulated in Table 1.1. The total longitudinal wake potential for the LER is plotted in Fig. 5.5. The total HOM power deposition in the LER (corresponding to the loss factor of 32.1 V/pC) is P=440 kW. Without tapers for the ARES cavities, it is reduced to 330 kW. In the HER, the total inductive impedance would be comparable to that of the LER. The total loss factor in the HER is larger than that of the LER by 18 V/pC (10.6 V/pC without tapers) due to additional 20 RF cavities, leading to 50 V/pC (36.3 V/pC without tapers). The corresponding total HOM power deposition is 120 kW (90 kW without tapers). These numbers should be used in designing RF parameters.

Table 5.1: LER inductive impedance and HOM power loss budgets. The values in brackets are those without tapers for ARES cavities.

Component	Number of items	Inductive impedance Im[Z/n] (Ω)	Loss factor (V/pC)	HOM power (kW)
Cavities	20	—	17.8 (10.6)	243 (144)
Resistive-wall	3016 m	5.2×10^{-3} at 2.3 GHz	4.0	54
Masks at arc	1000	2.8×10^{-3}	4.6	62
Pumping slots	10×1800	1.1×10^{-3}	0.37	5.5
BPMs	4×400	1.3×10^{-4}	0.79	10.7
Mask at IP	1	negligible	0.08	1.1
IR chamber	1	1.0×10^{-3}	0.29	4
Recomb. chambers	2	-8.0×10^{-4}	1.6	22
Bellows	1000	4.23×10^{-3}	2.5	34
Total		0.015	32.1 (25.7)	440 (330)

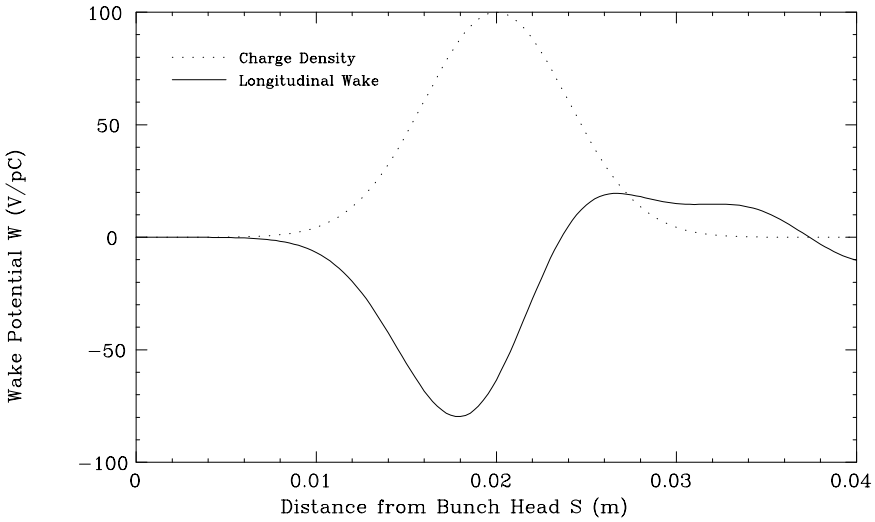

Figure 5.5: Total longitudinal wake potential for the KEKB LER.

5.2 Single-Bunch Collective Effects

In this section, we review our predictions of the singe-bunch collective effects, namely, the bunch lengthening and transverse mode-coupling instability. As mentioned earlier, these instabilities are expected to impose no fundamental limitation on the stored current, since the bunch current is relatively low compared to that of other large electron rings. However, the requirement of a short bunch ($\sigma_z = 4$ mm) demands that careful attention be paid to any possible causes for deviation from the nominal value. The transient ion problem and coupled-bunch instabilities due to photo-electrons will be discussed separately in sections 5.4 and 5.5, respectively.

5.2.1 Bunch Lengthening

There are two mechanisms to alter the bunch length from the nominal value. One is the potential-well distortion of the stationary bunch distribution due to the longitudinal wake potential. The deformed bunch distribution can be calculated by solving the Haissinski equation. The bunch can be either lengthened or shortened depending on the type of wake potential. Another mechanism is the microwave instability which has a clear threshold current for the onset of the instability.

Oide and Yokoya have developed a theory which includes both the potential-well distortion effect and the microwave instability [7]. A program is now available to compute the bunch length according to their theory. Figure 5.6 shows the calculated bunch length in the LER as a function of the number of particles in a bunch, N_p.

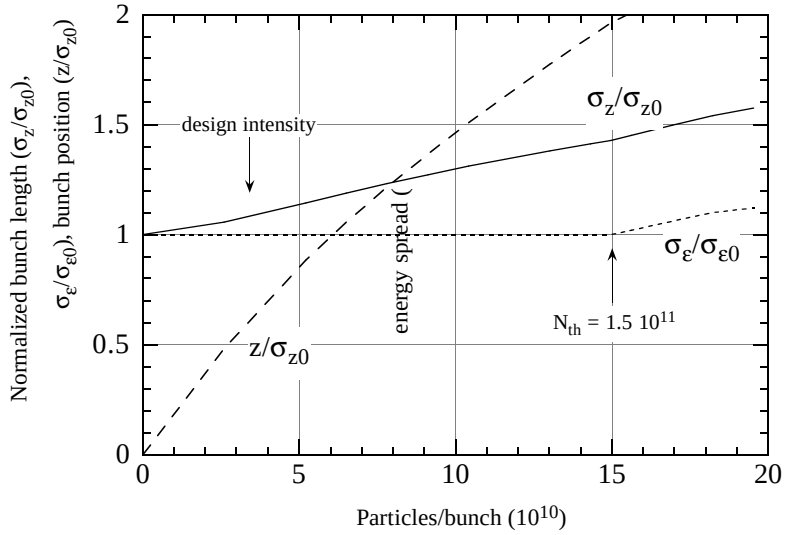

Figure 5.6: Bunch length and energy spread in the LER.

As can be seen, there is a constant bunch lengthening due to the potential-well distortion; and the microwave instability takes off at $N_p = 1.5 \times 10^{11}$, which is about four times larger than the proposed number of particles per bunch. At the design intensity, the bunch is lengthened by only 10%.

5.2.2 Transverse Mode-Coupling Instability

The transverse mode-coupling instability is known to be responsible for limiting the single-bunch current in large electron rings, such as PEP [8] and LEP. This instability takes place when two head-tail modes (m= 0 and m= -1 modes in most cases) share the same coherent frequencies. In the short bunch regime where the KEKB will be operated, the coherent frequency of the m= -1 mode keeps almost constant as a function of the bunch current, while that of the m= 0 mode keeps descending until it meets the m= -1 mode. Using the estimated transverse wake potential and the averaged beta function of 10 m, we found that the coherent tune shift of the m=0 dipole mode is only ~ -0.0002 at the design bunch current. This value is much smaller than the design value of the synchrotron tune (~ 0.017). Thus, the transverse mode-coupling instability will not impose a serious threat to the performance of KEKB.

5.3 Coupled-Bunch Instabilities

As mentioned earlier, the coupled-bunch instabilities due to high-Q structures, such as RF cavities and the resistive-wall beam pipes, are the main concerns in the KEKB rings because of the unusually large beam current. We have adopted the so-called damped-cavity-structure to sufficiently lower the Q-values of higher-order parasitic modes, typically less than 100. The calculation results of the longitudinal growth time due to the RF cavities will be given in detail in the RF section. Here, we focus on the transverse coupled-bunch instability due to the resistive-wall impedance and coupled-bunch instabilities (both transverse and longitudinal) that are excited by the crabbing mode of the crab cavity.

5.3.1 Transverse Resistive-Wall Instability

The growth rate of the instability in terms of the rigid particle model is given by

$$\tau_{RW}^{-1} = -\frac{\beta_\perp \omega_0 I_b}{4\pi E_b/e} \sum_{p=-\infty}^{\infty} \mathrm{Re}[Z_{RW}(\omega_{p,\mu,\nu_\beta})], \tag{5.20}$$

where

$$\omega_{p,\mu,\nu_\beta} = (pM + \mu + \nu_\beta)\omega_0. \tag{5.21}$$

Here, $\beta_\perp$ is the averaged beta function over the ring, $\mathrm{Re}[Z_{RW}]$ the real part of the resistive-wall impedance, I_b the beam current, E_b the beam energy, ν_β the betatron tune, μ the mode number of the coupled-bunch oscillation and M the number of bunches in the beam. In the above formula, it is assumed that the RF buckets are uniformly filled with equal numbers of particles (we ignore the effects of the gap in the bunch filling, which may be necessary to suppress ion trapping).

In Figures 5.7 and 5.8, the growth time of the most unstable mode in the LER and HER, respectively, are shown as a function of the betatron tune. In the current design of the LER (HER), the horizontal and vertical tunes are 45.52 (46.52) and 45.08 (46.08), respectively. The most unstable mode (5074 mode) in the LER has growth times of 5.9 and 8.1 msec at these tunes, respectively. On the other hand, the most unstable mode in the HER is the 5073 mode, which has growth times of 4.0 and 5.6 msec at the horizontal and vertical tunes, respectively. Conversely, plots of the growth time as a function of the coupled-bunch mode number at the tunes 45.52 and 46.52 for the LER and the HER are given in Figures 5.9 and 5.10, respectively.

One possible cure for this instability is a bunch-by-bunch feedback system. The growth rates obtained above are, however, close to the limit of the design capability of our feedback system. Fortunately, since the coherent frequencies of the unstable modes

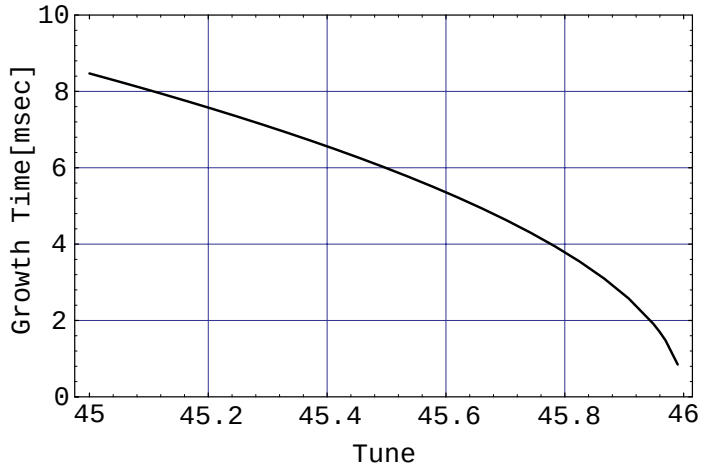

Figure 5.7: Growth time of the resistive-wall instability as a function of betatron tune in the LER.

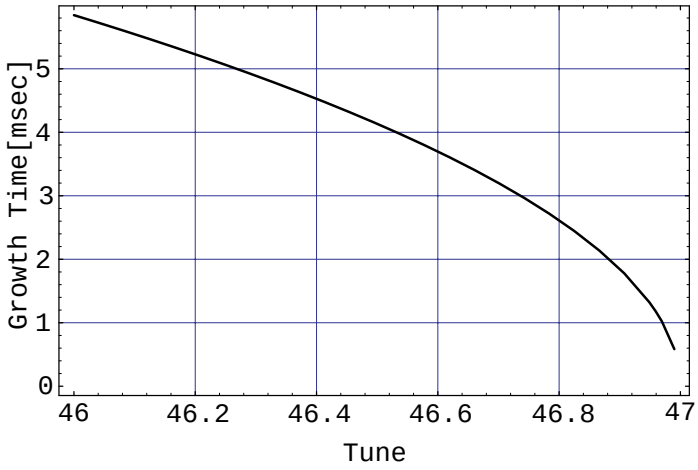

Figure 5.8: Growth time of the resistive-wall instability as a function of the betatron tune in the HER.

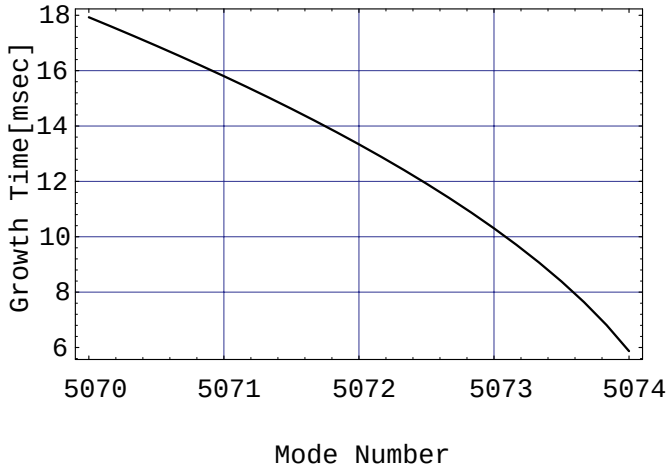

Figure 5.9: Growth time of the resistive-wall instability as a function of the mode number at the betatron tune of 45.52 in the LER.

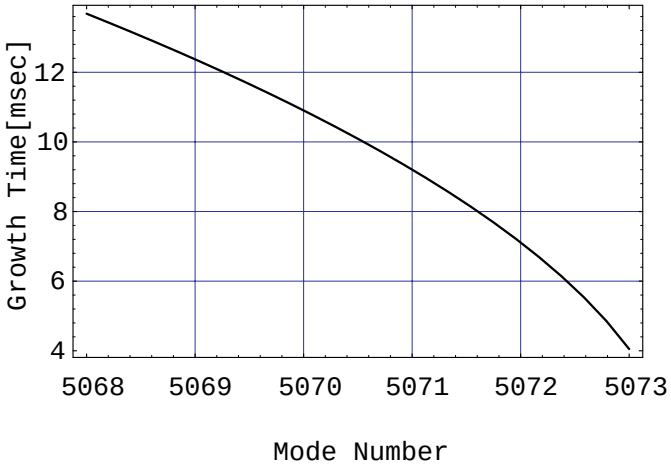

Figure 5.10: Growth time of the resistive-wall instability as a function of the mode number at the betatron tune of 46.52 in the HER.

stay in a narrow frequency range at low frequency, these modes may be stabilized by a narrow-band mode feedback system rather than a wide-band bunch-by-bunch feedback system. If the bunch-by-bunch feedback system can perform at a damping time of 10 msec, the mode feedback system must cover only one unstable mode for the LER and three modes for the HER, as seen from Figures 5.9 and 5.10. Then, a combination of two feedback systems is expected to provide a damping time of 1 msec for the fastest-growing modes.

5.3.2 Coupled-Bunch Instability by the Crabbing Mode

In this section we deal with only the instability due to the impedance of the crabbing mode. The instability due to the HOMs can be treated in a similar manner to those in accelerating cavities. The transverse coupling-impedance of a deflecting crabbing mode is expressed as

$$Z_\perp(\omega) = \frac{\omega_r}{\omega} \cdot \frac{\frac{R_\perp}{Q_0} Q_L}{1 + iQ_L(\frac{\omega}{\omega_r} - \frac{\omega_r}{\omega})}, \tag{5.22}$$

where ω_r is the resonant frequency of the crabbing mode, $R_\perp$ is the transverse shunt impedance, Q_0 is the unloaded Q-value and Q_L is the loaded Q-value. The most characteristic feature of the crabbing mode is that it operates at the same frequency as

Table 5.2: Main parameters of the crab cavity.

Beam energy	3.5 GeV
Beam current	2.6 A
Horizontal beta-function at the crab cavity	100 m
Horizontal betatron tune	45.52
Number of the crab cavities	2
Accelerating frequency	508.88 MHz
$R_\perp/Q_0$	277.4 Ω/m
Q_L	1×10^6

the accelerating mode unlike the HOMs. This feature renders this mode harmless by cancellation between the two betatron sidebands in both sides of the impedance peak, just like for the fundamental accelerating mode of a cavity. Unlike the accelerating mode, which must be detuned by a large amount of frequency to compensate for the heavy beam loading, we need not detune the crabbing mode. The growth rate of all coupled-bunch modes then almost vanishes as long as the resonant frequency of the crabbing mode is kept near the accelerating frequency.

The main parameters of the crab cavity, together with some machine parameters of LER, are summarized in Table 1.2.

The growth time of the most unstable mode (the 5074 mode for positive detuning, and the 5075 mode for negative detuning) in the LER is depicted in Fig. 5.11 as a function of the detuning frequency. In this figure, the radiation damping time (40 msec) with wiggler magnets is shown by the thick solid line. From this figure, it is clear that all modes are stable over a wide range of detuning from -6.5 kHz to 6.5 kHz. The growth time in the HER is even longer than in the LER. We can therefore conclude that the transverse coupled-bunch instability due to the crabbing mode will cause no serious problem as far as its frequency is well controlled.

Another problem may arise when the beam orbit has some offset at the cavity. In this case, longitudinal wake fields are excited which may cause a longitudinal coupled bunch instability. Even so, this type of instability can be stabilized by the fundamental mode of the accelerating cavities or by detuning the crab cavities to a lower frequency.

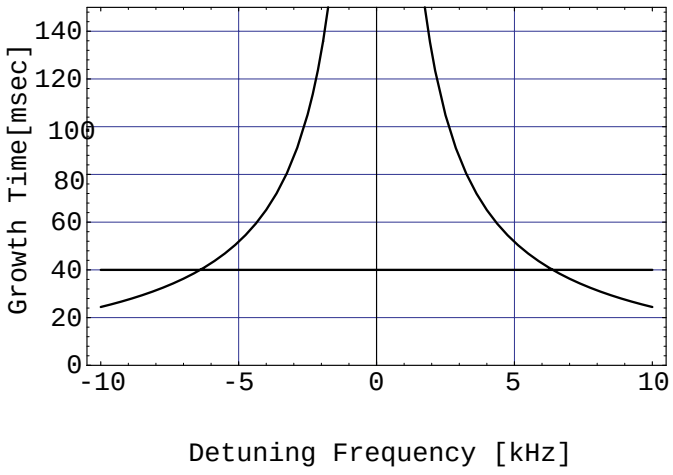

Figure 5.11: Growth time of the coupled bunch instability due to the crabbing mode in the LER versus the detuning frequency.

5.3.3 Summary of Collective Effects Sections

We have seen that neither bunch lengthening nor the transverse mode-coupling instability will impose a significant limitation on the stored bunch current. The luminosity performance of KEKB is rather affected by the couple-bunch instabilities due to the RF cavities (longitudinally) and the resistive-wall instability (transversely). Our carefully designed damped-cavity-structure helps to reduce the longitudinal growth to a manageable level. Even the most unstable mode has a growth time (60 msec) longer than the radiation damping time of 20 msec in the LER with wiggler magnets. Transversely, however, the growth time of the resistive-wall instability ($\sim$ 5 msec) is far shorter than the radiation damping time of 40 msec. The design of the fast feedback system that can deal with the remaining growth is one of the most challenging problems for KEKB.

5.4 Beam Blow-up due to Transient Ion Trapping in the Electron Ring

In any circular machines, the beam produces ions via ionization of residual gas molecules as well as through other processes. At an electron ring which stores many bunches, these positive ions are attracted towards the beam. After several turns the ions are concentrated near the beam orbit, where they can disturb the beam motion. This phenomenon, called ion trapping, has been studied for many years. One possible cure for this problem is a partial fill, i.e., to create a contiguous group of empty RF buckets

that are unoccupied by the beam, and to let the ions drift away during this gap.

It has been recently pointed out that a somewhat different process can also degrade the beam. This effect may be called transient ion trapping. With high intensity and low emittance beams, even if the ions eventually disappear in the bunch gap, they may cause a serious effect before disappearing through the following mechanism. While each bunch ionizes the residual gas, if a bunch is displaced from the design orbit, the ions left in space will also be displaced. Such ions execute off-centered oscillations in subsequent electron bunches, and act as an amplifier for electron oscillation. The purpose of this section is to present a theoretical study of this effect.

Since the vertical emittance is much smaller than the horizontal one, the effect is more serious in the vertical plane. We assume that n_b electron bunches are followed by a gap which is long enough to sweep out the ions. This bunch pattern of n_b bunches plus a gap may be repeated several times over the ring. The first bunch of each train travels in a fresh residual gas without ions.

This phenomenon is characterized by two important parameters, Θ and K. First, the phase advance of the ion oscillation between the arrival time interval of two adjacent electron bunches is

$$\Theta = \sqrt{\frac{2zNmr_eL}{AM_N\Sigma_y(\Sigma_x+\Sigma_y)}}.$$

Here,

- z,A the electrovalence and the mass number of the ion,
- L distance between bunches,
- N number of electrons per bunch,
- Σ_j $=(\sigma_{j,e}^2+\sigma_{j,i}^2)^{1/2}$ $(j=x,y)$, where $\sigma_{j,e}$ and $\sigma_{j,i}$ are the r.m.s. beam size of electrons and ions,
- m,M_N the mass of an electron and a nucleon,
- r_e classical electron radius.

The size of the ion cloud is equal to the electron beam size when it is created. It settles down to $\sim 1/\sqrt{2}$ of the electron size after a few oscillations due to non-linear smearing. In the case of the KEKB electron ring (HER), Θ for CO^+ ions, for example, is about 0.12 radian, which means that the CO^+ ions execute one cycle of oscillation during the passage of about 50 $(=2\pi/\Theta)$ electron bunches.

The ion cloud focuses the electron beam. The number of ions is proportional to the electron bunch index n (counted from the first bunch in each train). Therefore, the tune shift is proportional to n, and is given by

$$\Delta\nu_y = RKn, \qquad K=\frac{zn_ir_e\beta_y}{\gamma\Sigma_y(\Sigma_x+\Sigma_y)},$$

where

R the average radius of the ring,
β_y average beta function,
γ electron beam energy in units of rest mass,
n_i number of ions created by one electron bunch per unit length, given by $Nn_g\sigma_i$, n_g being the number density of the residual gas and σ_i the ionization cross section. In the case of CO^+, n_i will be about 100/m.

If the oscillation amplitudes of electrons and ions are small compared with $\sigma_{y,e}$, the buildup of the oscillation may be approximately described by linear theory. Let us denote the center-of-mass position of the n-th electron bunch after travelling a distance s by $y_n(s)$. Then, the mode which is unstable against ion perturbation is given by

$$y_n(s) \approx a_0 e^{i(\Theta n - ks)},$$

where k is the betatron wave number. The conjugate mode $e^{i(-\Theta n - ks)}$ is damped.

The amplitude blowup factor of the unstable mode is approximately given, in the linear regime, by

$$G \equiv \left|\frac{a_n(s)}{a_0}\right| \approx 1 + \frac{1}{\Gamma}\exp\left[\sqrt{\Gamma + (\alpha_0\Theta n)^2} - \alpha_0\Theta n\right] \qquad (\Gamma \gg 1),$$

where

$$\Gamma = K\Theta s n^2 = \sqrt{\frac{2m}{M_N}}\frac{\beta_y L^{1/2}}{\gamma}\frac{n_g\sigma_i}{\sqrt{A}}\left[\frac{r_e z N}{\Sigma_x\Sigma_y}\right]^{3/2} s n^2$$

for $\Gamma \gg 1$. The factor $\alpha_0 \approx 0.077$ approximately takes into account the non-linear smearing of the ion center-of-mass motion. (The center-of-mass of ions oscillates approximately as $\exp(-\alpha_0\theta)\cos\theta$.) The blowup is essentially described by the factor Γ. Since the ionization cross section σ_i is roughly proportional to Z (sum of the atomic numbers of the constituents of the molecule), the ion-species dependence of Γ is $\propto Zz^{3/2}/\sqrt{A}$. Therefore, heavier ions contribute more to the instability than lighter ones, if the partial pressure is the same.

The amplitude blowup factor G for the HER is plotted in Figure 5.12 as a function of the number of turns n_t for various values of the number of electron bunches n_b. The residual gas is assumed to be CO with a pressure of 10^{-9} Torr. The e-folding time of the amplitude is about 70 turns for n_b=500 ($\propto n_b^{-2}$), although the growth with respect to n_t is not exponential.

In practice, the ion phase advance Θ can have a spread for a number of reasons. This can lead to a damping effect. For example, since Θ depends on the electron beam size, it varies over the ring. In the periodic part of the arc sections of the HER, Θ modulates between 0.10 to 0.14 radian in the case of CO^+ ions, as shown in Figure 5.13.

hhh

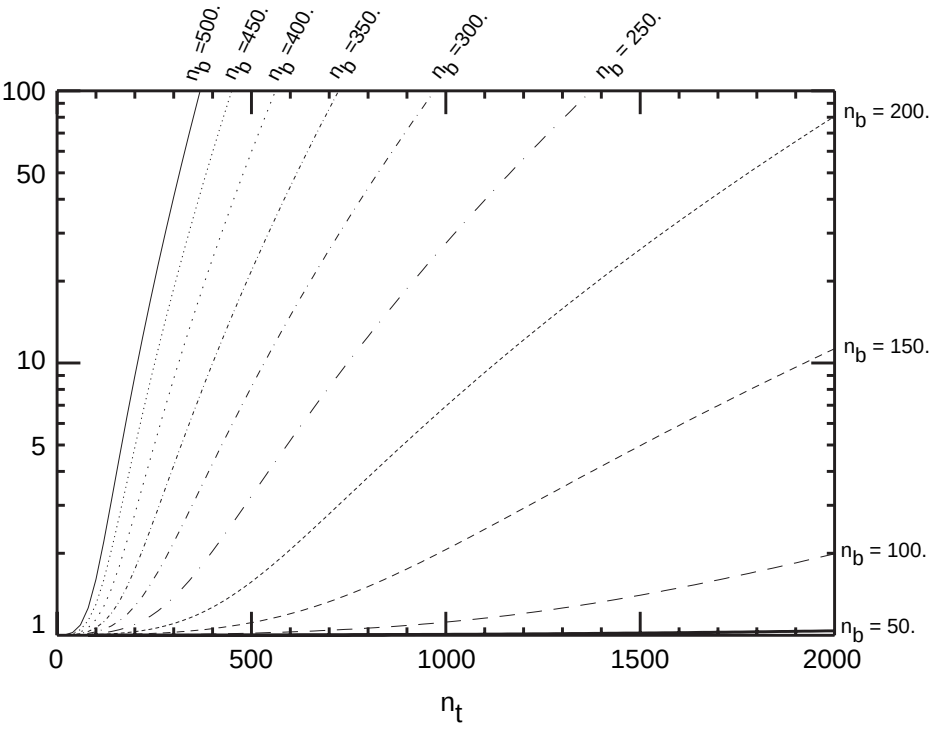

Figure 5.12: Amplitude blowup factor G for CO^+ of 10^{-9} Torr.

hhh

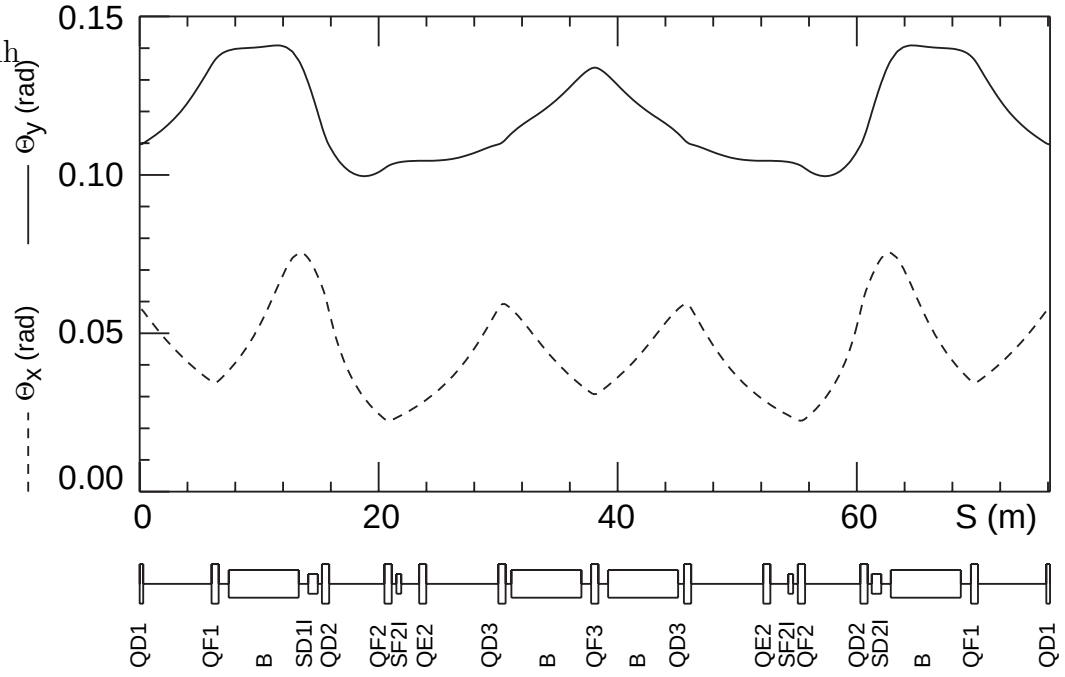

Figure 5.13: The Θ_x and Θ_y, phase advance of ion (CO^+) oscillations between the arrival of consecutive beam bunches in the HER arc.

Another reason for the spread in Θ comes from the existence of various ion species. However, since the dependence of Θ on A is weak ($\sim 1/\sqrt{A}$), the spread due to this is much smaller than the lattice effect. For example, a mixture of O_2, N_2, CO, CO_2, etc, cannot cause a more efficient spread than the lattice effect. It should be also noted that the contribution of H_2 is very small because of the small ionization cross section.

The nonlinear smearing expressed by the factor α_0 causes a similar effect. The value $\alpha_0 \approx 0.077$ has already been taken into account in Figure 5.12. It corresponds to a $\sim$30% full spread of Θ. Therefore, we cannot expect drastic damping due to the Θ spread.

Linear theory is valid only for small amplitude oscillations. It does not predict emittance growth, either. In order to take into account those effects that are ignored in linear theory, a computer simulation is being conducted. Some preliminary results are summarized here. The essential points in the simulation code are listed as follows:

1. The electron beam is represented by 10^5 macro-particles per bunch. The model ring consists only of periodic cells which are extracted in the HER arc.
2. Ions are also represented by macro-particles. Instead of a continuous distribution over the ring, they are placed at some selected points (ionization points) in the ring. It was confirmed that only a few ionization points in the ring are enough if the points are carefully selected so as to properly represent the spread of Θ. Eventually, only two points were selected for long-time calculations. The number of macro ions is at most 10^5 per ionization point. The longitudinal drift of ions is negligible.
3. The initial position of ions when they are created is that of the parent electron. The transverse velocity is generated according to the Maxwell distribution with a temperature of 300 K (this does not cause a sizable effect). Each electron bunch creates approximately 2×10^4 macro ions per point. When the number of macro ions exceeds 10^5 at one ionization point due to the passage of many bunches, some of them are randomly selected and thrown away. The subsequent ionization rate is accordingly reduced. (Although one could generate a small number of macro ions so that the final number does not exceed the limit, this is not statistically good, because the ions created by early electron bunches are more important.)
4. The interaction of an electron bunch and an ion cloud is calculated by solving the 2-dimensional (horizontal and vertical) Poison equation on a 2-D grid (64×64 to 64×256, equal space). The mesh size is typically 0.15 standard deviations in each plane. The grid for electrons and that for ions are not identical. However, because of the structure of the code, the aspect ratio (vertical to horizontal) has

to be the same. The interaction between ions is negligible.

5. The ions are assumed to disappear after interacting with n_b electron bunches before the electrons come in the next turn, so that the first electron bunch always travels in non-ionized residual gas.
6. Standard runs are performed with 512 electron bunches over 1000 turns.

The results of simulations up to now can be summarized as follows:

1. As long as the center-of-mass amplitude is small ($\lesssim$ 0.5 standard deviations), linear theory can describe the phenomena reasonably well.
2. The center-of-mass amplitude saturates at about $1\sigma_y$.
3. In order to study the effects of the bunch gaps, the electron bunch structures, like 256+[25]+256, 256+[50]+256, 128+[25]+128+[25]+128+[25]+128, etc (the number in [ ] is the number of missing bunches), have been simulated and compared with 512 continuous bunches. It turned out that the effect of up to 50 missing bunches does not considerably improve the situation.
4. The growth rate with 256 bunches (followed by long enough gap) is much smaller than that with 512 bunches as the linear theory predicts. However, the repetition of 256 bunches plus a gap of much more than 50 missing bunches will not be acceptable because of the luminosity reduction.
5. The emittance growth is about 30%.

Thus, in order to damp the growth with 512 successive bunches, a feedback system as fast as 50 to 100 turns (0.5 to 1 msec) is needed, if the gas pressure is 10^{-9} Torr. The fastest bunch mode will be about 50 bunches per cycle.

Remaining issues for future studies include:

1. It is desired to find out how many missing bunches are enough for terminating the chain of interaction. However, in order to try a longer bunch-gap, the simulation code has to be modified, because the ions after the gap extend to a large vertical dimension, whereas the newly created ions are concentrated on the axis. This ion distribution cannot be accurately expressed by an equally-spaced mesh.
2. It must be confirmed whether the emittance growth can be cured by the feedback system of the center-of-mass motion. (This is a question technically very hard to answer. The present calculation is done with a parallel processor with 64 cpu's. Interactions during tens of revolutions are simultaneously computed so that it is logically impossible to faithfully simulate a feedback system.)

5.5 Instabilities due to Beam-Photoelectron Interactions

Photoeletrons are produced by synchrotron radiation (SR) photons, when they hit the inner wall of the beam pipe. In the LER where the positrons are stored, those photoelectrons would migrate towards the beam path, where they can create a sizeable electric field. Although such individual electrons are not trapped around the beam, they form a flowing gas of electrons. Under certain conditions these photoelectrons can act as a media for transmitting perturbative forces from a particle bunch onto subsequent bunches. Thus, a coupled-bunch instability can emerge [9].

At the 2.5 GeV Photon Factory (PF) ring of KEK, when it is operated to store positrons, a coupled-bunch instability which may be consistent with this mechanism has been observed. At the PF with a stored current of 350 mA ($\sim 4\times10^9$ particles/bunch), the growth rate of the instability is much higher than the damping rate. The problem in the LER may be even more serious, since its stored current will be larger by a factor of 7.

This section presents a theoretical study of instabilities in the positron ring due to interactions between the beam and photelectrons, and discusses on a possible cure.

5.5.1 Synchrotron radiation and photoelectron

The number of photons emitted by a positron (or an electron) during one full revolution is given by[10]

$$N_\gamma = \frac{5\pi}{\sqrt{3}}\alpha\gamma \ , \tag{5.23}$$

where α and γ are the fine structure constant and the Lorentz factor, respectively. In the LER with $\gamma = 6850$, the number of photons emitted by a positron in one revolution is

$$N_\gamma = 453 \ . \tag{5.24}$$

We next estimate the production of photoelectrons by SR photons. We assume that the photoelectron production rate (quantum efficiency) is 0.02 for the copper chamber and that the energy of photoelectrons follows a Gaussian distribution with an r.m.s. value of 5 ± 15 eV[11]. Then the number of photoelectrons will be

$$N_e = 9.1/\text{particle} \ , \qquad N_{e,\text{bunch}} = N_e \times N = 3\times10^{11}/\text{bunch} \tag{5.25}$$

per revolution.

5.5.2 Coupled bunch instability caused by photoelectrons

Each photoelectron is unstable, and is lost within a short period in a presence of the positron beam due to the over-focusing effect. However, under a multi-bunch operation with uniformly filled bunches, a large number of photoelectrons are constantly supplied from the beam duct wall for every bunch passage. Consequently, the spatial distribution of photoelectrons becomes stationary. The positron bunches pass through this distribution of photoelectrons, which act as a medium of bunch-to-bunch interactions. A computer code has been developed to simulate this situation, and calculations have been carried out using the LER parameters. A full description of this method is given in [9]. A summary of the results of the calculations is presented in the following. The possible effects of magnetic fields are first ignored; cases with finite magnetic fields in the beam duct are presented later.

Figure 5.14 shows the stationary distribution of the photoelectrons. The wake force

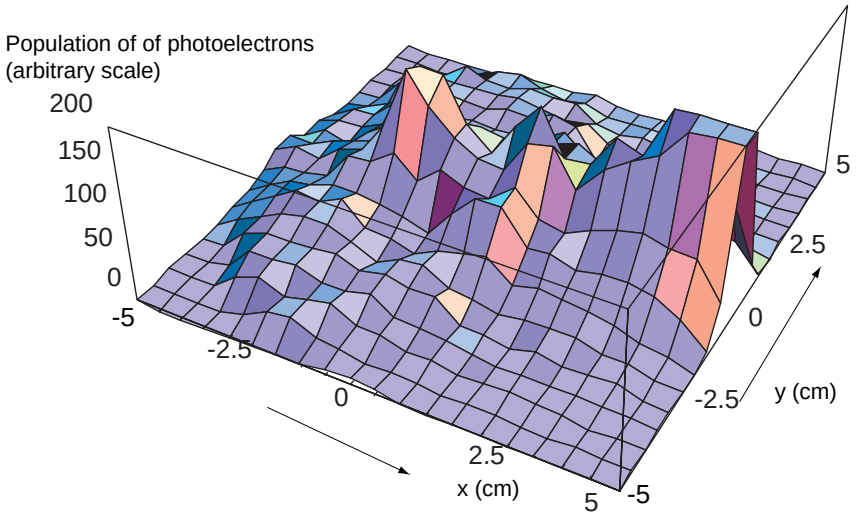

Figure 5.14: Distribution of photoelectrons in the x-y plane, where x and y refer to the horizontal and vertical coordinates (unit is cm) within the cross section of the vacuum pipe. The beam orbit is located at $(x, y) = (0, 0)$. The primary SR photons hit the inner surface of the vacuum pipe near (10, 0). Note that the LER vacuum pipe has a circular cross section an inner radius of 9.4 cm.

which causes the coupled bunch instability can be calculated by giving a perturbation to a bunch in the simulation, and by investigating the influence on the subsequent bunches. We treat the vertical instability first. Figure 5.15 shows the wake force. The wake forces are calculated in the cases of displacements of 0.5 mm and 1 mm. The linearity of the wake force can be seen. The growth rate of a coupled-bunch instability

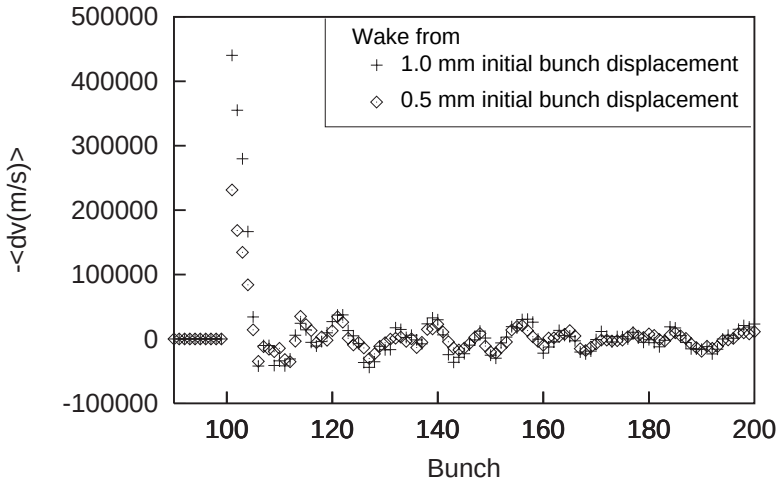

Figure 5.15: Vertical wake force. The strength of the wakes created by an initial bunch displacement of 0.5 mm (diamond and) and 1.0 mm (cross hair) are shown. It indicates that the wake strength is roughly proportional to the displacement of the initial bunch.

due to a wake force is generally given by

$$\Omega_m - \omega_\beta = \frac{1}{4\pi\gamma\nu_y}\frac{N_{e_\gamma}}{N_b}\sum_{n=1}^{n_0}\frac{d\bar{v}_y}{dy}\left(-\frac{ncT_{rev}}{h}\right)e^{2\pi in(m+\nu_y)/h}, \tag{5.26}$$

where the mode is defined by

$$y_n^{(m)}(t) = e^{2\pi imn/h}y_0^{(m)}(t) \tag{5.27}$$

and

$$y_j^{(m)}(t) = \tilde{y}_j^{(m)}e^{-i\Omega_m t}. \tag{5.28}$$

By using the wake force found in Figure 5.15 for dv in Equation 5.26, the growth rate of the instability can be estimated. The result is shown in Figure 5.16. The maximum growth rate is found to be about 2500 s^{-1}. This is much higher than the damping rate of the LER, which is 12.8 s^{-1}. Although the head-tail damping effect will reduce the instabilities, its damping rate ($\sim$ 200 s^{-1}) will not be sufficient to cure this instability.

The horizontal wake force is shown in Figure 5.17 for bunch displacements of 0.5 mm and 1 mm. The feature of the horizontal wake force is very different from that of the vertical wake force. The linearity of the wake is broken after the passage of a dozen or so bunches. The wake force remains non-zero even after a hundred bunches. Therefore, the conventional treatment to obtain the growth rate is not applicable. (If we use this wake force in Equation 5.26, a maximum growth rate of 1700 s^{-1} is obtained). To evaluate the horizontal growth rate correctly, tracking calculations of the beam motion passing through the electron distribution will be necessary.

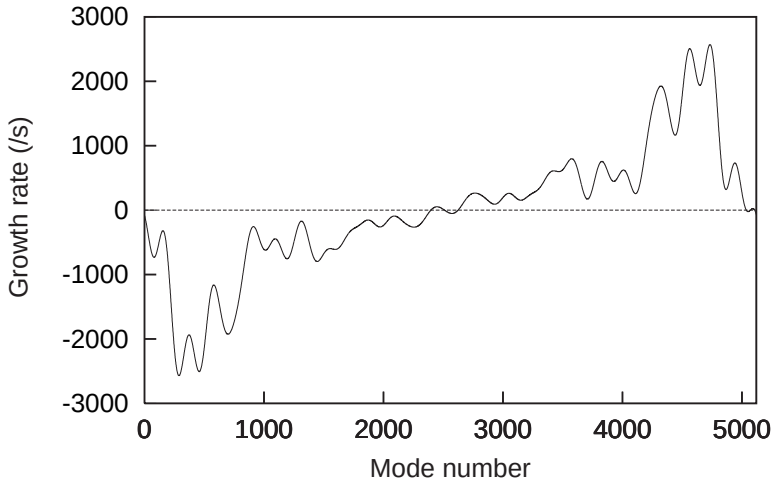

Figure 5.16: Growth rate of the vertical instability plotted against the mode number.

5.5.3 Possible cures

A possible cure for this instability is to apply magnetic fields, and to restrict the motion of photoelectrons (blocking magnetic field). For example, an electron with an energy of 10 eV has a Larmor radius of 1.1 cm in magnetic fields of 10 G. Thus the electrons will not propagate towards the beam. The wake force is expected to be smaller in this condition.

If the photoelectrons tend to reach the beam by drifting along a horizontal path, we can consider using a solenoid or a vertical dipole fields as the blocking magnetic field. Figure 5.18 shows the wake force when the solenoid field is applied in the vacuum duct with a strength of $B_z = 1$ G and 20 G. It is seen that with $B_z = 20$ G the wake force becomes small. In this condition the growth rate is estimated to be less than 200 s^{-1}.

Figure 5.19 shows the wake force when a vertical dipole field is applied in the vacuum duct. It is seen that the wake force becomes small for $B_y = 20$ G.

We next consider the case where a horizontal magnetic field is applied. Here, the electron motions are bounded on the horizontal plane. Thus, the photoelectrons produced by primary SR photons are freely allowed to reach the beam path area. Figure 5.20 shows that the wake field is stronger, as expected. The strength of the wake force shows that the wake force becomes 2.5 times larger due to the magnetic fields. By the way, we can find the cyclotron period, 18 ns, in the wake force.

Although the dominant source of photoelectrons may be concentrated on the area to be hit by primary SR photons, the effects of reflection and scattering of SR photons need to be taken into consideration. Therefore, even if the direction of the magnetic field is arranged to be vertical, electrons produced by the reflected photons may become

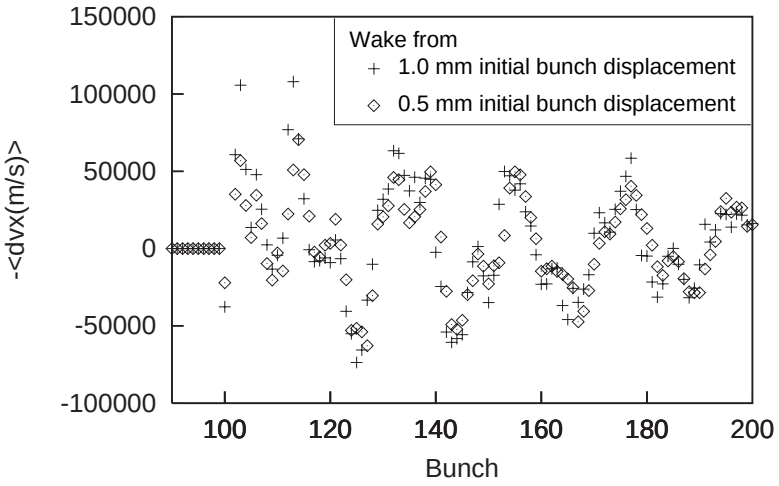

Figure 5.17: Horizontal wake force. The strength of the wakes created by an initial bunch displacement of 0.5 mm (diamond) and 1.0 mm (cross hair) are shown.

important. This has to be noted in applications to the real KEKB condition. Therefore, the use of the solenoid fields may be a better solution. By using solenoid coils of alternating field signs, the coupling effect on the beam is considered to be minimized.

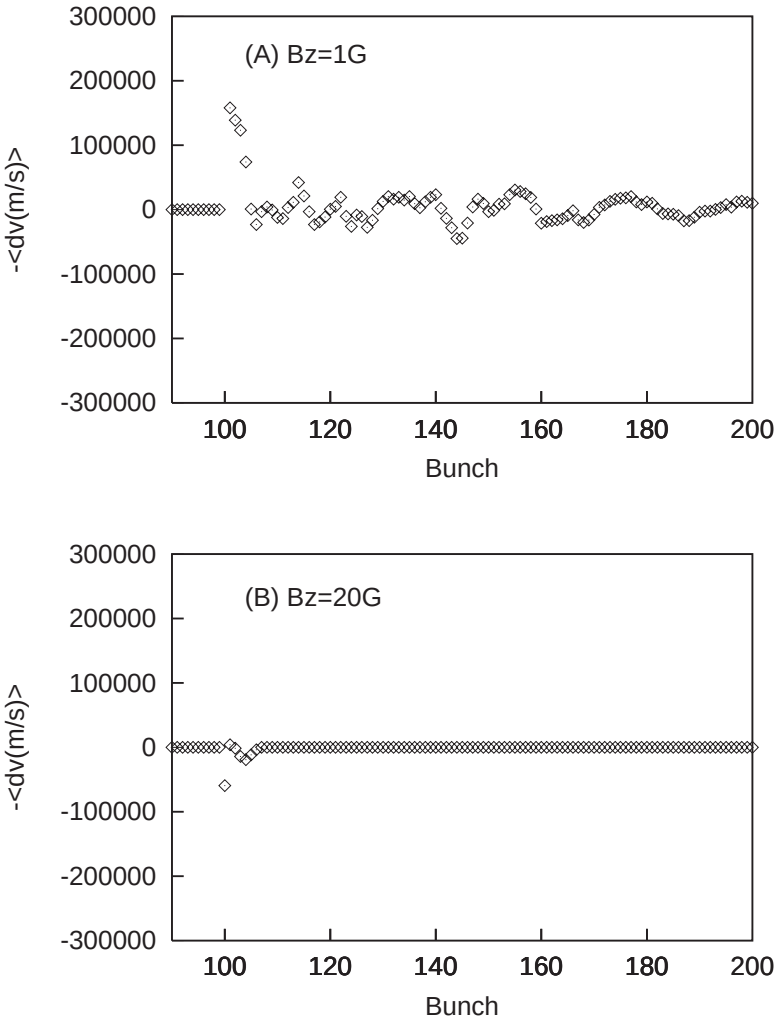

Figure 5.18: Wake force when applying solenoid fields.

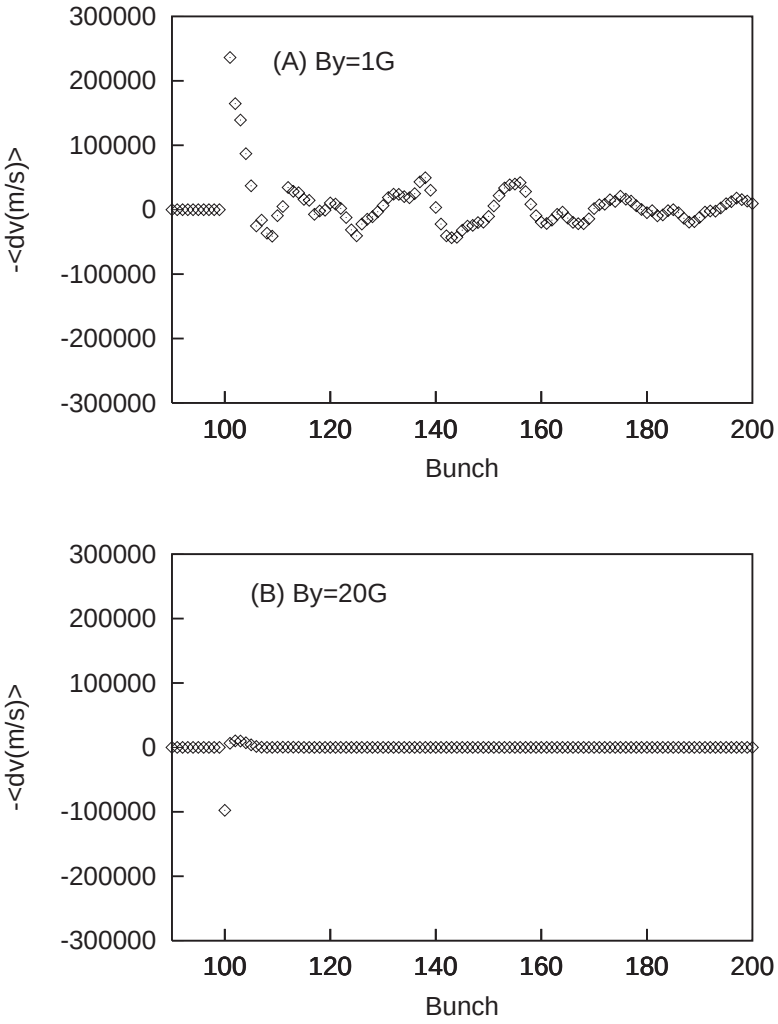

Figure 5.19: Wake force when applying vertical fields.

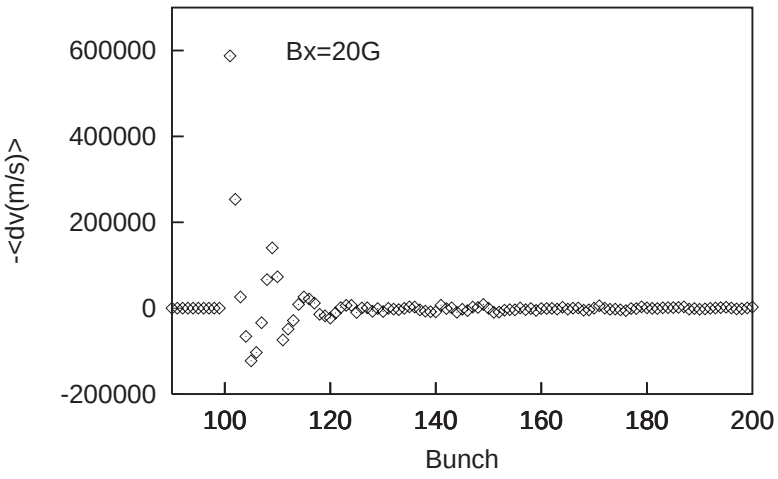

Figure 5.20: Wake force when applying horizontal fields.

5.5.4 Conclusions

The effects of interactions between the positron beam and photoelectrons have been evaluated for the LER. The growth rate is estimated to be 2500 s^{-1}. By applying solenoid or vertical magnetic fields of 20 G, the growth rate will be reduced by one order, which can be cured by the bunch-to-bunch feedback system.

Bibliography

[1] Y. H. Chin, *User's Guide for ABCI Version 8.8*, CERN SL/94-02 (AP) and LBL-35258 (1994).

[2] T. Akasaka, private communications.

[3] S. Kurennoy and Y. H. Chin, KEK Preprint 94-193 (1995). To be submitted to Part. Accelerators.

[4] R. L. Gluckstern, *Phys. Rev. A* **46**, 1106 (1992).

[5] S. S. Kurennoy, *Part. Accelerators* **39**, 1 (1992).

[6] G. V. Stupakov and S. S. Kurennoy, *Phys. Rev. E* **49**, 794 (1994).

[7] K. Oide and K. Yokoya, KEK Preprint 90-10 (1990).

[8] M. S. Zisman et. al., *Study of Collective Effects for the PEP Low-Emittance Optics*, LBL-25582 and SSRL ACD Note-59 (1988).

[9] K. Ohmi, KEK Preprint 94-198.

[10] M. Sands, *The Physics of Electron Storage Rings*, SLAC-121(1970).

[11] K. Kanazawa, private comunications.

Chapter 6

Lattice Design

This chapter discusses the lattice design of KEKB in detail. Specific requirements to consider are the following:

1. Realize the beam parameters listed in Table 2.2.
2. Ensure a sufficiently large dynamic aperture for a high injection efficiency and a long beam lifetime, particularly the Touschek lifetime in the LER.
3. Maintain a wide range of tunability for the beam parameters, especially for the horizontal emittance.
4. Allow a reasonable amount of tolerance for machine errors.

Because of the small β_y^* ($\sim$ 1 cm) at the interaction point (IP), a large amount of chromaticity is produced, and it has to be corrected without sacrificing the dynamic aperture. Discussions on the dynamic aperture and the sources that cause its reduction are given in section 6.1. The development of the ring lattice design is presented in section 6.2. Designs of the straight section beam optics are given in sections 6.3 and 6.4. Sections 6.5 and 6.6 examine the required magnet field qualities and tolerances.

6.1 Dynamic Aperture

For efficient beam injection at KEKB it is considered that the lattice design should allow a momentum aperture of at least $\pm 0.5\%$ and a transverse aperture of $> 1.2 \times 10^{-5}$ m. For maintaining a sufficiently long beam lifetime ($\sim$ 10 hours or better in the absence of machine errors), an even larger aperture is strongly favored.

A major cause for the reduction of the transverse dynamic aperture is the nonlinearity of sextupole magnets which are introduced to correct the chromaticity in the

ring. To solve this problem, it is considered best to use a pair of identical sextupole magnets that are connected with a $-I$ transformer in both the horizontal and vertical planes. This allows to cancel transverse nonlinearity of the sextupole magnets to the third order in the Hamiltonian[1]. Then, residual terms come to limit the dynamic aperture. In the case of KEKB, the vertical dynamic aperture is limited by: (1) the kinematic term of the drift space around the IP, and (2) the fringe field of the final quadrupole magnets at the edge, facing the IP[2].

A source of momentum aperture limitation is the modulation of linear betatron oscillations due to the synchrotron motion. If the beta functions at cavities have dependencies on the momentum, a change of the momentum by the cavity RF field produces a mismatch between the beam and the betatron phase space ellipse. This excites synchrotron-betatron resonances at $2\nu_{x,y} \pm m\nu_s = N$, and an exponential growth of transverse betatron amplitudes results. The momentum aperture is significantly degraded near these resonances. Resonances of smaller orders are more harmful. To avoid this problem a small synchrotron tune is required, such that those resonance conditions are not met[2]. The chromaticity in the x-y coupling terms is another source that limits the momentum aperture, since the compensation of the detector solenoid at the IP is not perfect, as described below.

As mentioned in the previous chapter, a small momentum compaction factor is needed to reduce the synchrotron tune, while keeping the bunch length and the momentum spread constant. When the linear momentum compaction is made small, the effects of higher-order momentum compaction becomes non-negligible. For example, the second order term produces an imbalance of the dynamic aperture for the positive and negative sides of the momentum deviation of a particle. This is due to eccentric motions of particles in the longitudinal phase space induced by the second-order momentum compaction.

Yet one more source of aperture limitation is the chromo-geometric aberration caused by a breakdown of the $-I$ transformer for off-momentum particles. This aberration becomes serious in the sextupole pairs for the local chromaticity correction scheme in the LER, which is discussed in Section 6.2.5. This problem arises, because the product of the sextupole strength and the vertical beta function at the sextupole magnets becomes much larger than in the arcs.

For a given lattice layout, the excitations of sextupole magnets are determined by evaluating the off-momentum optics directly, *i.e.* not by using perturbative methods. The solution of the sextupole excitations is calculated so as to simultaneously minimize the deviations of the betatron tune $\nu_{x,y}$ and Twiss parameters $\beta^{RF}_{x,y}$ and $\alpha^{RF}_{x,y}$ for a few points in the RF section. The momentum bandwidth considered is 1.5% for the HER

and $2 \sim 3\%$ for the LER. The number of fitting points of the momentum bandwidth is typically 20. All of the sextupole pairs are treated independently. (The results of the chromaticity correction are shown in Figures 6.5 and 6.6.) Optimization can be improved by matching for finite betatron amplitudes or by a nonlinear optimization of the dynamic aperture itself.

The dynamic aperture is estimated by tracking particles in six-dimensional phase space $(x, p_x, y, p_y, z, \delta)$ using SAD. Here, the variable z is defined as $z = -vt$, where t is the delay from the nominal particle. SAD is a fully symplectic tracking code, developed at KEK. It incorporates all known terms, such as linear and nonlinear fringe fields, thick lens multipole fields, kinematic terms, overlap of the solenoid field and other magnets, etc. In this study, the initial conditions are given as $p_{x0} = p_{y0} = z_0 = 0$ and $y_0 = ax_0$, where a is a constant. The dynamic aperture is expressed by the initial values of the action $2J_{x,y0}$ and the momentum deviation δ_0 of the particles which survived 1000 turns without damping due to synchrotron radiation. Although this period, which corresponds to 1000 turns, is only 1/8 of the transverse damping time of the LER, the results of 1000-turn tracking are almost equal to, or slightly smaller than, those of 8000-turn with radiation damping. Therefore, 1000-turn tracking is considered to be a sufficiently accurate estimation of the dynamic aperture.

The dynamic aperture is evaluated in two ways:

1. With the initial condition $y_0 = x_0/3$. This is to check the acceptance for horizontal beam injection.

2. With the initial condition $y_0 = x_0/\sqrt{50}$. This is for estimating the Touschek lifetime at collision with an emittance ratio of 2%. The Touschek lifetime is evaluated while assuming that the dynamic aperture in the J_x-J_z plane is given by $0 \leq (J_x/J_x^{\max}) + (J_z/J_z^{\max}) \leq 1$. See Figures 6.8 and 6.10 for illustrations of this approximation.

6.2 Development of Beam Optics Design

We have so far studied five types of optics design, as listed in Table 6.1. These optics have different combinations of cell structures and chromaticity correction schemes. All of the optics have been designed to give the required values of the horizontal emittance and the momentum spread. We have compared the performance of these optics in light of the following requirements:

1. To give a small synchrotron tune, and

2. To have a sufficiently large dynamic aperture for beam injection and for the Touschek lifetime.

The results are summarized in Table 6.1 and Figure 6.1. In the following subsections these designs are reviewed one by one. Since the second criterion above is especially challenging for the LER, we will discuss mainly issues concerning the LER.

	Injection	Touschek	ν_s
Interleaved $\pi/3$ FODO Cell	bad	bad	bad
Noninterleaved $\pi/2$ FODO Cell	good	fair	bad
Noninterleaved π Cell	excellent	fair	good
Noninterleaved 2.5π Cell	excellent	good	excellent
Noninterleaved 2.5π Cell +Local Chromaticity Correction	excellent	excellent	excellent

Table 6.1: Comparison of the performances of the cell structures and chromaticity correction schemes for the LER.

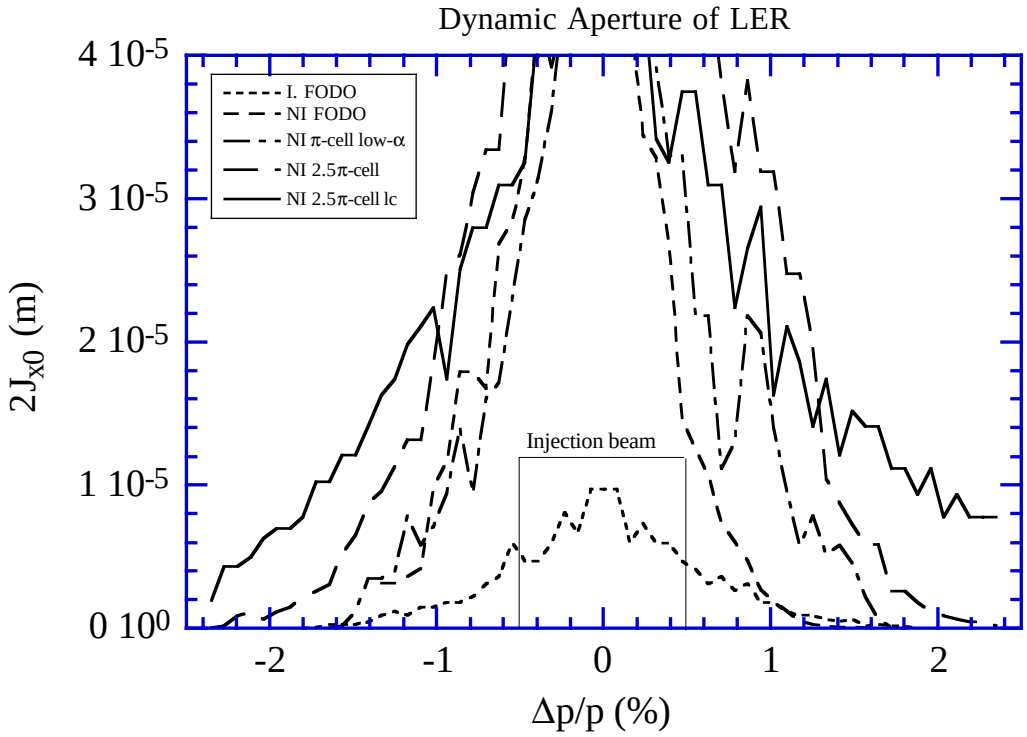

Figure 6.1: Dynamic aperture of the LER with five types of beam optics.

6.2.1 Interleaved $\pi/3$ FODO Cell

We have tried a conventional chromaticity correction scheme with interleaved sextupole magnets in $\pi/3$ FODO cells, where each quadrupole magnet is associated with a sextupole magnet. Sextupole magnets that are separated by the π phase difference are paired so as to cancel the lowest order of the transverse nonlinearity. We have tried chromaticity corrections with 6, 12, and 24 sextupole families. In all cases, the dynamic aperture remained too small, and did not satisfy the requirement. This interleaved sextupole scheme has been abandoned.

6.2.2 Noninterleaved $\pi/2$ FODO Cell

An arc lattice based on $\pi/2$ FODO cells with a chromaticity correction scheme with noninterleaved sextupole magnets has been considered. As the first step, the bend radius ρ is determined based on the requirement for the momentum spread. In electron storage rings with a constant bending radius and smooth focusing, the horizontal emittance ε_x and the momentum compaction factor α_p are given by

$$\varepsilon_x = 2\sigma_\delta^2 \langle H \rangle_{\text{bend}} \approx \frac{2R_A\sigma_\delta^2}{\nu_x^3}, \tag{6.1}$$

$$\alpha_p = \frac{2\pi}{C} \langle \eta_x \rangle_{\text{bend}} \approx \frac{2\pi R_A}{C\nu_x^2}. \tag{6.2}$$

Here, R_A is the average radius of the arc, ν_x the total horizontal tune of the arc, η_x the horizontal dispersion, and $H = \beta_x \left(\eta_x' + \alpha_x\eta_x/\beta_x\right)^2 + \eta_x^2/\beta_x$. The symbol $\langle f \rangle_{bend}$ represents the average of a quantity f in bend magnets.

According to Equations 6.1 and 6.2, once ρ is fixed, ε_x and α_p are uniquely determined by the total tune ν_x. Thus, if the arc is built with FODO cells to give $\varepsilon_x = 1.8 \times 10^{-8}$m, the momentum compaction factor becomes too big. This, in turn, means that $\nu_s \geq 0.06$, and produces serious difficulties in finding adequate operating points in the tune space. The anomalous emittance due to chromaticity can also become very large when ν_s is high [3]. In addition, the accelerating voltage becomes excessively high, if the short bunch length required in the design is to be achieved. Because of these difficulties, this scheme has been rejected.

6.2.3 Noninterleaved π Cell

To obtain small momentum compaction α_p, we must reduce $\langle \eta_x \rangle_{bend}$, while keeping $\langle H \rangle_{bend}$ constant. This can be done by combining two $\pi/2$ FODO cells, where four bend magnets are merged into two, as shown in Figure 6.2. In this scheme, in addition

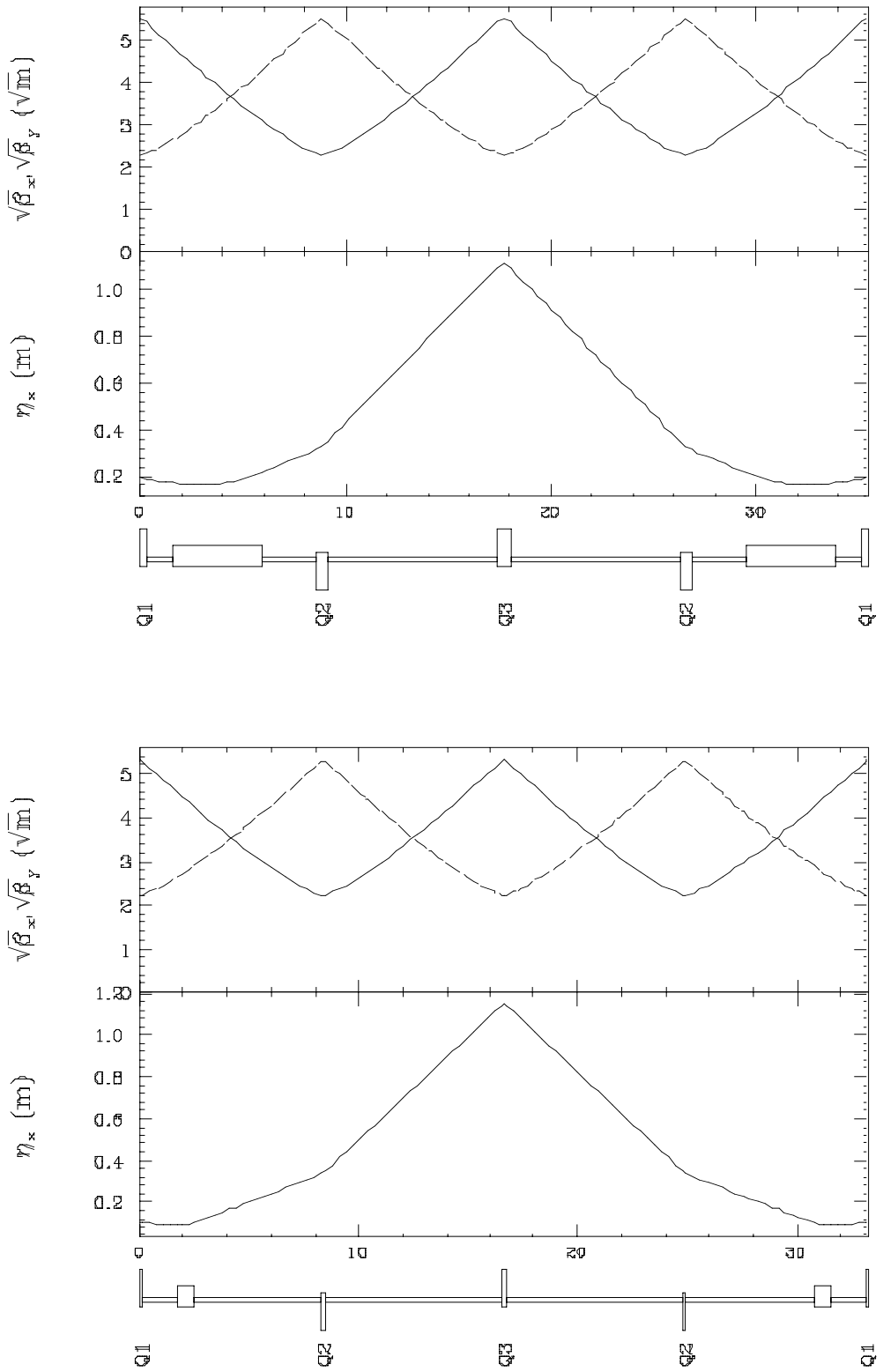

Figure 6.2: Structure of the π cell for the HER (above) and the LER (below).

to the total tune ν_x, the position of the bend magnets can also be taken as a free parameter for achieving the desired α_p and ε_x simultaneously. An acceptable solution was found for the LER. In the HER, since the bend magnets are longer than those in the LER, the variable range of α_p is narrower. The possible minimum α_p in the HER is somewhat larger than the required value.

From a chromaticity correction view point, the arc lattice built with π cells has a disadvantage in that the high peaks of η_x appear only in the phase steps of $N\pi$. This means that if we place sextupole pairs (SF's) for horizontal corrections only near the η_x peaks, corrections at the $(N + 1/2)\pi$ phases become difficult. Even if we add SF's at small η_x points, it is still less effective for $(N + 1/2)\pi$ phases than in the FODO case. As a result, the longitudinal dynamic aperture of the LER is unsatisfactory for the Touschek lifetime.

6.2.4 Noninterleaved 2.5π Cell

The 2.5π cell is created by combining five $\pi/2$ FODO cells and by merging ten bending magnets into four. In this cell structure, the bend magnets are arranged to form two dispersion bumps, so that we can keep small η_x at the dipole magnets, similar to the π cell case. By adjusting the positions of the bend magnets and η_x there, we can achieve the required emittance and momentum compaction factor at the same time for both rings. This flexibility of the 2.5π cell results in another merit for the HER: the existing bending magnets become re-usable in the HER arc, satisfying the requirements of the optics. Successive SF (SD) pairs in the 2.5π cell structure have a relative phase of $3\pi/2$. Thus, chromatic kicks at the $N\pi$ and $(N+1/2)\pi$ phases in both the horizontal and vertical planes can be corrected efficiently. The dynamic aperture of the 2.5π cell is significantly improved over previous schemes, and it satisfies all of the beam dynamics requirements. As shown in Figure 6.5, some higher-order chromaticity still remains, because the sextupole magnets are not sufficiently close to the main chromaticity sources in the interaction region. For this, further improvements can be achieved by a "localized chromaticity correction" in the interaction region, which is discussed in Section 6.2.5.

6.2.5 Noninterleaved 2.5π Cell with Local Chromaticity Correction

The local chromaticity correction refers to a scheme in which the large chromaticity produced by the final quadrupole magnets is corrected within the interaction region. Its advantage is that the creation of higher-order chromaticity can be avoided, by placing

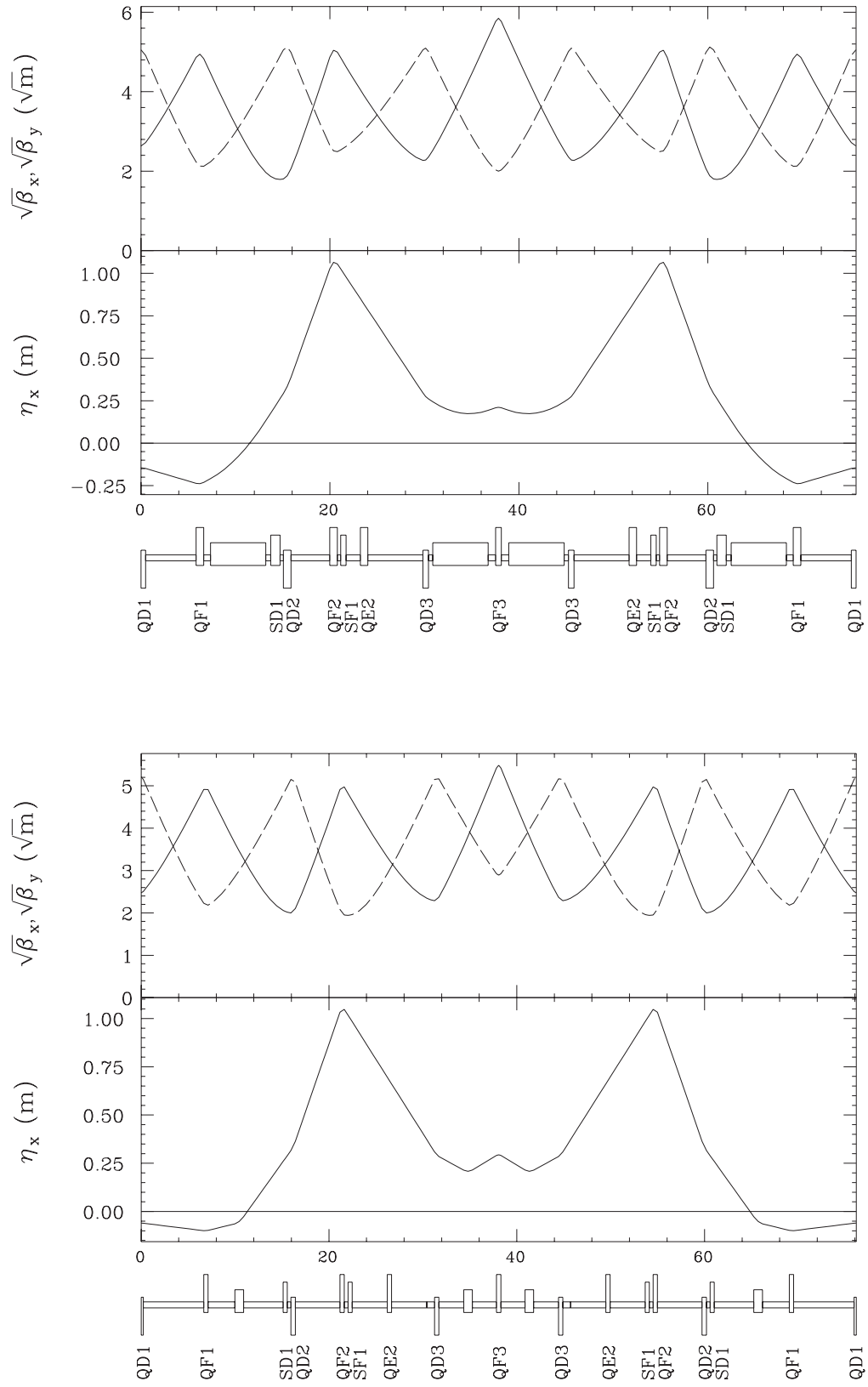

Figure 6.3: Structure of the 2.5π cell for the HER (above) and the LER (below).

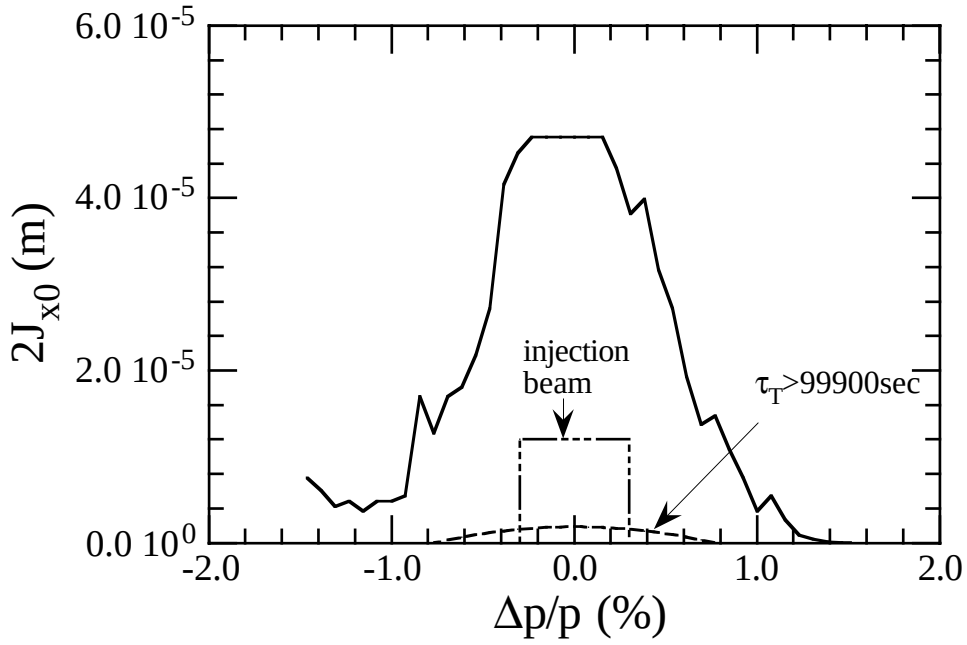

Figure 6.4: Dynamic aperture of the HER with the 2.5π cell.

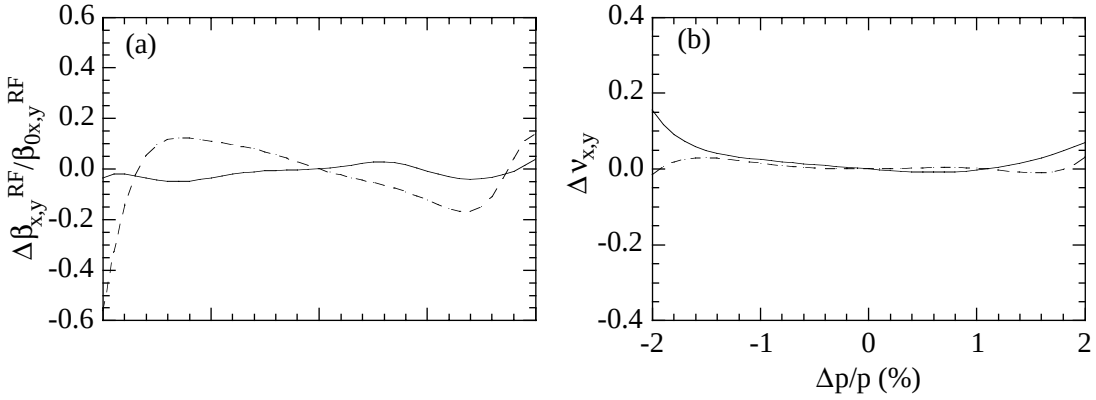

Figure 6.5: Chromaticity correction with the 2.5π cell for the LER.

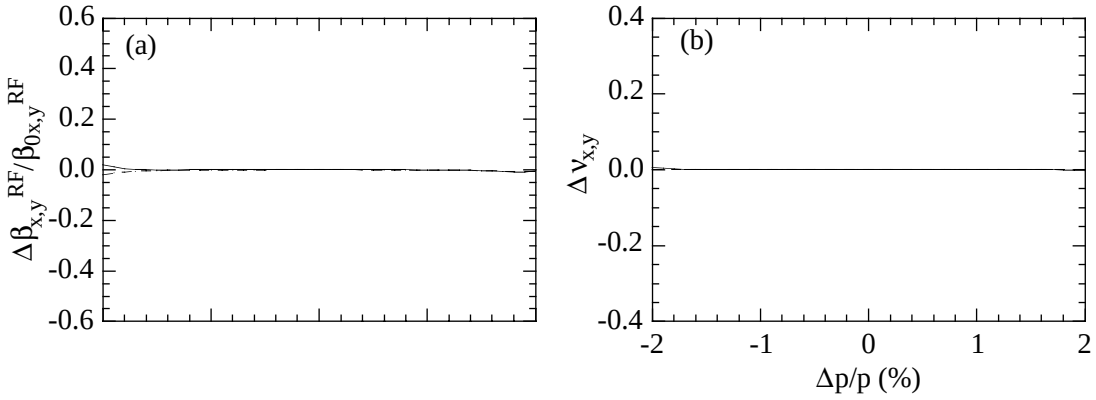

Figure 6.6: Chromaticity correction with the 2.5π cell and the local chromaticity correction for the LER.

sextupole magnets optically close to the final quadrupole magnets.

Pairs of vertical correction sextupole magnets are connected by the "pseudo $-I$" transformer, which is discussed in Section 6.2.6. Such sextupole pairs are placed in phase with the final quadrupole magnets near the IP. For those sextupole magnets, dispersive regions with large β_y/β_x ratios are created by adding bend magnets in the straight section. It is practically difficult to install two sextupole pairs for correcting both the horizontal and vertical planes in the IP straight section. Fortunately, the sources of the horizontal chromaticity are not so strongly localized as the vertical (*i.e.* a sizable amount of horizontal chromaticity comes from the arc and elsewhere, besides the final focusing section). Thus, we will place only one sextupole pair for the vertical correction in the straight section in each side of the IP. The last sextupole pairs (the pairs closest to the IP) at the end of the arc are used for the horizontal correction.

The design of the local chromaticity correction optics was done by minimizing the momentum dependence of optical parameters in a bandwidth of $2 \sim 3\%$. The optimum drift space length, and excitations of the quadrupole and sextupole magnets have been found. The local correction has significantly improved the chromaticity correction, as shown in Figure 6.6. Also, it has drastically improved the dynamic aperture in the region of large momentum deviations, resulting in a factor 1.5∼2 improvement of the Touschek lifetime over the optics without a local correction.

A local chromaticity correction scheme is considered for the LER to maximize the available dynamic aperture. Since the dynamic aperture requirement on the HER is less demanding, a local chromaticity correction will not be to implemented in HER.

6.2.6 Tunability of Beam Emittance and Momentum Compaction Factor with the Noninterleaved 2.5π Cell

It has been found that the 2.5π cell structure has a nice tunability feature, which allows us to adjust the beam emittance and momentum compaction. It is illustrated as follows. A noninterleaved sextupole pair in a 2.5π cell is connected with the transfer matrix,

$$\begin{pmatrix} -1 & 0 & 0 & 0 \\ m_{21} & -1 & 0 & 0 \\ 0 & 0 & -1 & 0 \\ 0 & 0 & m_{43} & -1 \end{pmatrix} . \tag{6.3}$$

Even if m_{21} and m_{43} are non-zero, nonlinear kicks by sextupole magnets are basically canceled within a pair. We have confirmed that this pseudo $-I$ transformer brings about a large dynamic aperture, comparable to a perfect $-I$. Then, by allowing $m_{21} \neq$

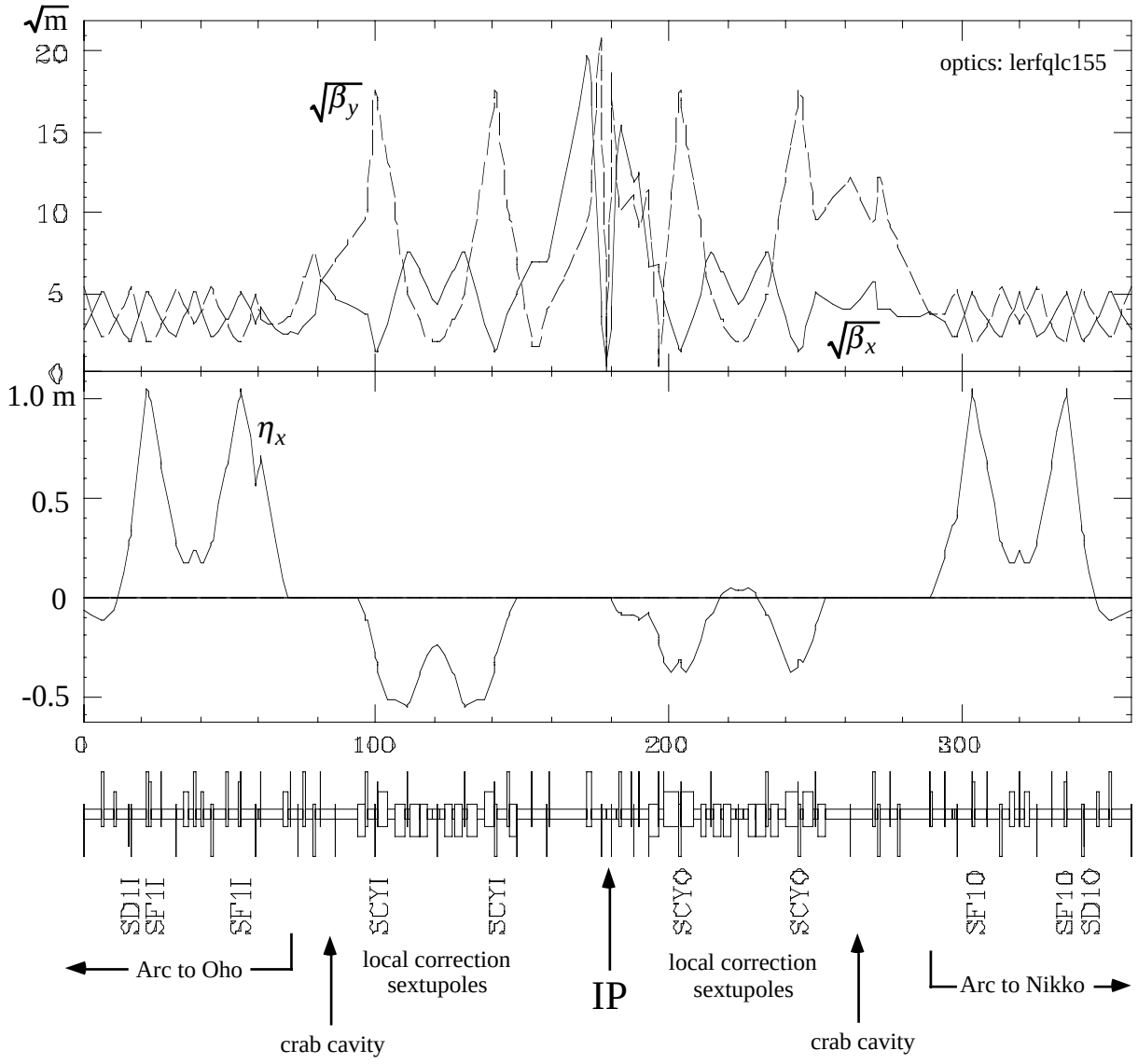

Figure 6.7: Optics of the local chromaticity correction for the LER. A pair of sextupole magnets for the vertical chromaticity correction is placed at each side of the IP.

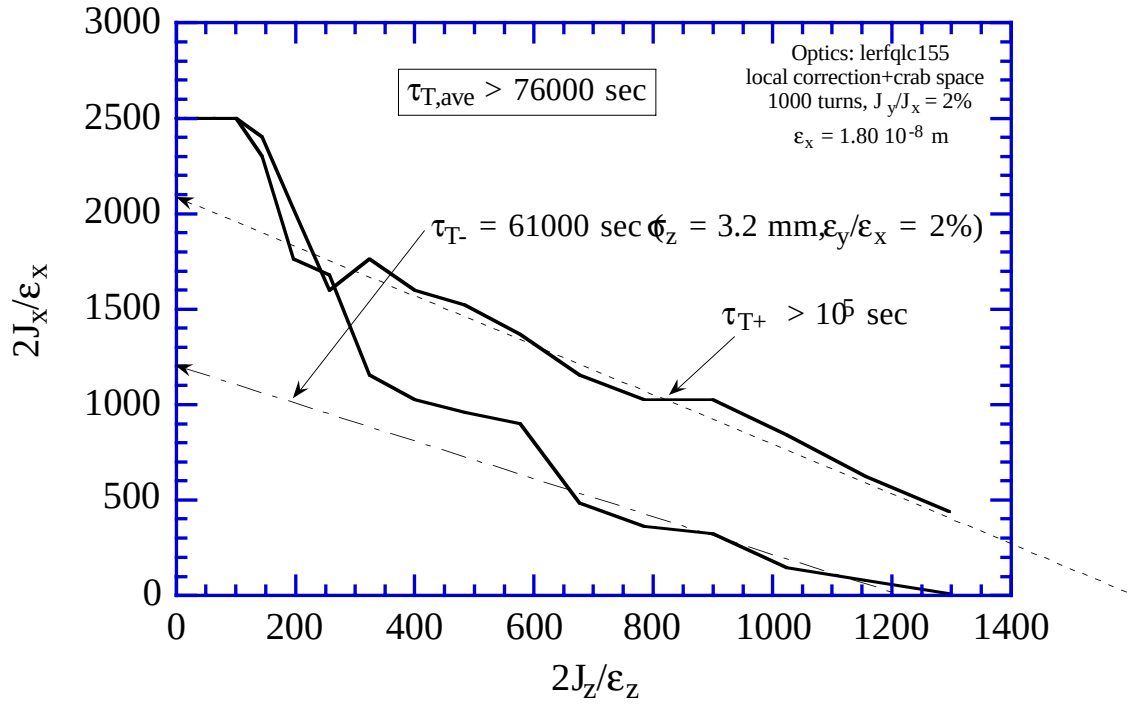

Figure 6.8: Dynamic aperture and Touschek lifetime of the LER with a local chromaticity correction.

0 and $m_{43} \neq 0$, two new free parameters become available for tuning. The "knobs" corresponding to these parameters may be the excitations of two families of quadrupole magnets (QF2 and QD2) outside the sextupole pairs. This allows us to tune α_p without breaking down the pseudo $-I$ transformation.

In the present design, the momentum compaction can be changed over the range of $-1 \times 10^{-4} \leq \alpha_p \leq 4 \times 10^{-4}$ by changing the strength of QF2's and QD2's by a few percent. During this time, ε_x is kept nearly constant. In practice, it is rather difficult to change ε_x over a wide range by only adjusting the two families of quadrupole magnets.

A cure to this restriction is to introduce a new family of quadrupole magnets QE2 inside the SF pair. By adjusting η_x at bend magnets, using five free parameters (QF2, QF3, QD2, QD3, and QE2), we can obtain the required tunability, $1.0 \times 10^{-8}\text{m} \leq \varepsilon_x \leq 3.6 \times 10^{-8}\text{m}$, while keeping α_p constant and maintaining the pseudo $-I$ condition between the SF's. In summary, a solution exists to tune ε_x and α_p independently by adding QE2's.

6.3 Optics Design of the Interaction Region

6.3.1 Compensation of the Detector Solenoid Field

One of the important issues in designing the optics around the IP is compensation of the x-y coupling effects generated by the detector solenoid field. Due to the finite crossing angle at the IP, the design beam orbits are not parallel to the detector solenoid axis. Thus, dispersion is also generated by the solenoid. Corrections have to be made for four coupling elements of the transfer matrix between the IP and the arc, as well as the dispersion near the IP.

A possible solution to this is to add four or more skew quadrupole magnets and several bend magnets at each side of the IP. This correction, however, is perfect only for on-momentum particles. The chromaticity of the x-y coupling remains uncorrected, and can significantly increase the "anomalous emittance" at

$$\begin{aligned} \nu_x \pm \nu_y \pm m\nu_s &= N \\ 2\nu_{x,y} \pm m\nu_s &= N \ . \end{aligned} \tag{6.4}$$

The use of skew quadrupole corrections reduces the dynamic aperture, as shown in Figure 6.10.

The best way to compensate for the x-y coupling effects of the detector solenoid is to use counter solenoids, so that the integrated field, $\int B_z ds$, becomes zero within the drift space around the IP. This compensation works perfectly for particles with any momentum. This is the solution that has been adopted in the design of KEKB.

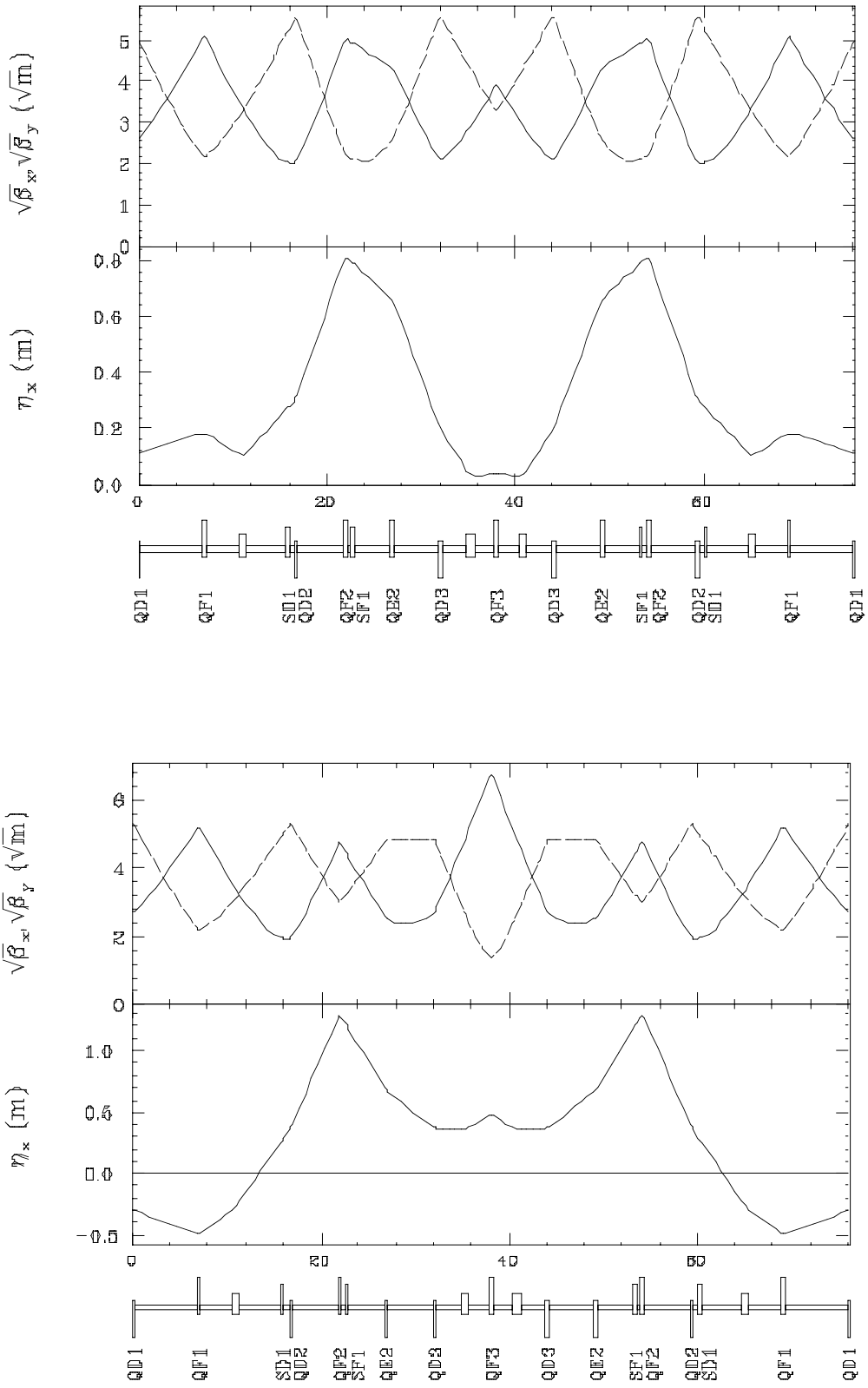

Figure 6.9: Examples of emittance control in the LER: $\epsilon_x = 1.0 \times 10^{-8}$m (above) and 3.6×10^{-8}m (below).

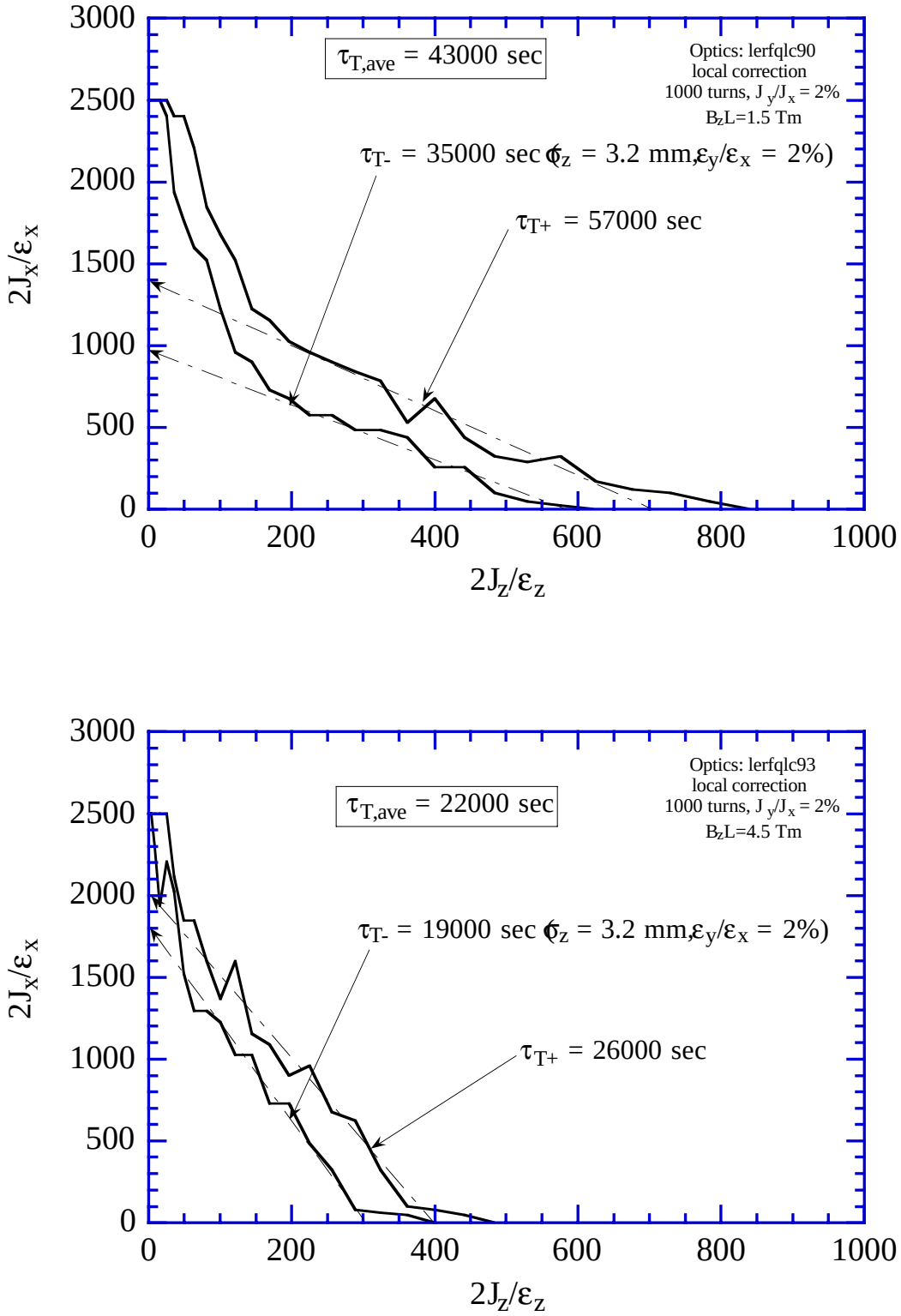

Figure 6.10: Dynamic aperture of the LER with an integrated solenoid field of 1.5 Tm (above) and 4.5 Tm (below).

6.3.2 Crab Cavities

An optional use of a crab crossing scheme is currently being studied. To minimize the required number of crab cavities, the transverse kicks given by the cavities should have a maximum effect on the bunch orientation at the IP. This means that the horizontal phase distance of the crab cavities from the IP should be $(N + 1/2)\pi$. From the lattice design view point, it is possible to reserve such a dispersion-free drift space in the straight section near the arc.

The dynamic aperture has also been checked with the crab cavities. It has been shown that the dynamic aperture is quite insensitive to the crab cavities, even with a large amount of errors in the amplitudes and phases of the crab-mode RF kicks.

6.4 Optics Design of Other Straight Sections

This area of the design is still in progress. The following issues will be discussed in a future version of the design report.

- Dispersion suppressors:
- Symmetry points of arcs:
- Optics with wigglers: As discussed in Chapter 2, the parameter sets for the HER and the LER are almost identical. However, if the radiation loss is assumed to come only from bend magnets in the arcs, the radiation damping time of the LER is longer than that of the HER by a factor of 2. To halve the LER damping time, without increasing the momentum spread, preparation is under way to install optional damping wigglers for a total length of 96 m in Oho and Nikko. These wigglers can be also used to control the LER beam emittance. We can obtain the required tunability of the horizontal emittance by the wigglers.
- Adjustment of the path length: Changes of the path length due to the wigglers can be adjusted by special sections called "chicanes". Each section is built with four bending magnets, which are placed in a way similar to that of a unit of wigglers. The LER has four 12 m-long chicanes, which provide a sufficient tunability of the path length. These chicanes can also be used to equalize the circumference of the LER to that of the HER. Figure 6.11 shows the optics design of the LER in the vicinity of the chicane structure. The chicane bend magnets are labelled BC1 and BC2 in Figure 6.11.
- Injection point:

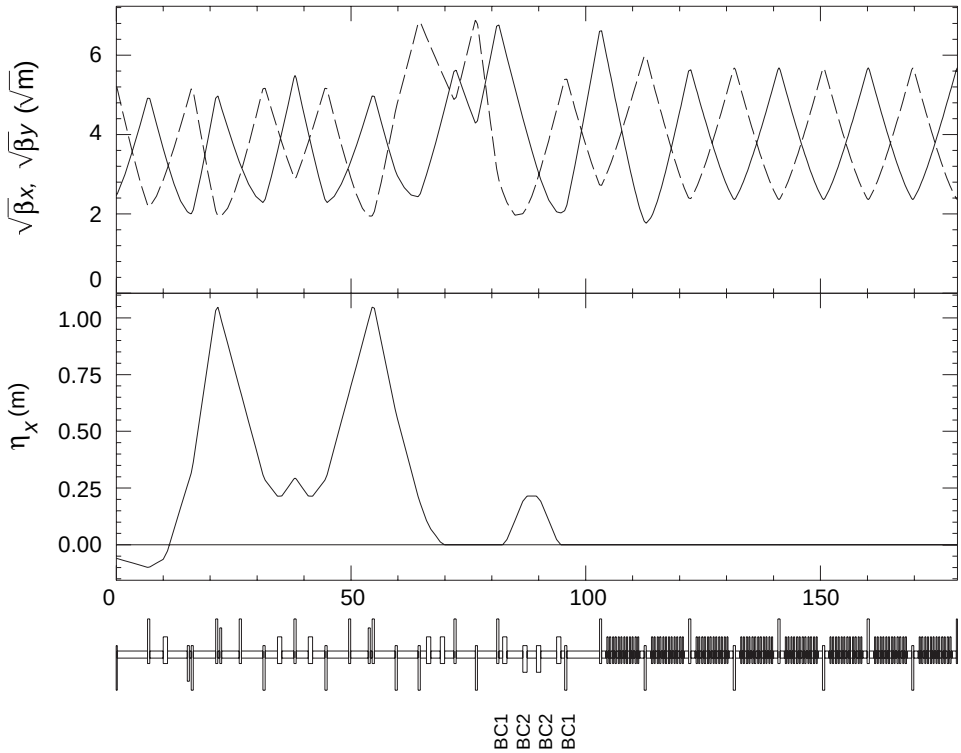

Figure 6.11: Optics design of the LER in the vicinity of the chicane structure for ring length adjustments. The chicane bend magnets are labelled as BC1 and BC2.

- Translation chicane:

6.5 Requirements on the Magnet Quality

The tolerances on the systematic multipole errors of the bend magnets and quadrupole magnets in the arcs have been estimated. The criteria is based on a 2% reduction of the dynamic aperture integrated in both the momentum and transverse phase spaces. The results are listed in Table 6.2. In the table K_n is defined as

$$K_n = \frac{1}{B\rho}\frac{\partial^n B_y}{\partial x^n}. \tag{6.5}$$

It is known that requirements similar to those listed in Table 6.2 have been met by existing magnets that are used for the TRISTAN main ring.

		$\Delta B/B$ at 50 mm radius
Dipole Magnets		
K_2/K_0	1.0m^{-2}	0.12%
K_4/K_0	17000m^{-4}	0.45%
Quadrupole Magnets		
K_5/K_1	22000m^{-4}	0.12%
K_9/K_1	$1.3 \times 10^{13}\text{m}^{-8}$	0.45%

Table 6.2: Tolerances of systematic multipole errors.

6.6 Effects of Machine Errors and Tuning Procedures

The performance of the noninterleaved scheme lattice may be sensitive to machine construction errors, which break down the cancellation of sextupole aberrations in the $-I$ transformation. This section considers the effects of the construction and setup errors in the ring lattice, and their tolerances for the acceptable operation of KEKB. The criteria used in this analysis are the emittance ratio, the dynamic aperture, and the miss-crossing at the IP. The errors considered include: the misalignment of magnets, BPM offset and field ripple.

Concerning magnet misalignment, we consider the combined effect of temperature-dependent drift, movement of the tunnel, vibration of the magnets and others. No attempts are being made to resolve individual errors, or to quote their tolerances separately. This is because there is no sufficient information available for fixing their relative contributions at this stage.

In this section the tolerances are *not* discussed in the form of the maximum allowable errors, which may be considered to be the common definition. Rather, we assume certain combinations of initial lattice errors, and simulate how the emittance ratio and dynamic aperture can be improved by applying a series of beam-based tuning procedures. This study has been performed by using a sophisticated beam simulation code SAD, which has been developed at KEK. In this study an analysis was made on what magnitude of combined errors are still acceptable, such that the target emittance ratio and the dynamic aperture, etc. can be achieved by realistic beam-based tuning. This approach clarifies the significance of each tuning process and its role. It also helps to create guidelines for the development of beam-based techniques of error analyses.

The errors used in the simulation are given in Table 6.3. The assumptions used in

Element	Δx(mm)	Δy(mm)	$\Delta\theta$(mrad)	Δk/k
Quadrupole Magnets	0.15	0.15	0.2	$1 \times 10^{-}3$
QC Quads[2)]	0.01	0.01	0.1	$1 \times 10^{-}4$
Sextupole Magnets	0.15	0.15	0.2	$2 \times 10^{-}3$
Bend Dipole Magnets		0.1	0.1	$2 \times 10^{-}3$
Steering Corrector Magnets		0.1	0.2	
BPMs[3)]	0.075	0.075		

[1)]The values are for one standard deviation (σ).

[2)] Two quads near IP(QCS and QC1).

[3)] Assume Beam-based measurement of BPM offset.

Table 6.3: Errors used in the simulation[1)]

the simulation are summarized as follows:

1. Only the LER has been considered. The situation at HER is expected to be similar, since its arc lattice structure is basically identical to that of the LER.

2. Errors of the quadrupole magnets close to the interaction point (QCS and QC1) are intentionally assumed to be very small compared to those in the arc section. This is done in order to magnify the effects of the errors in the arc section. We will consider the effects of QCS and QC1 separately in the near future.

3. Every sextupole magnet has a mover which can transversely move the magnet with a maximum stroke of ± 3 mm in both the horizontal and vertical directions.

4. The offset errors of the BPMs relative to the magnetic center of the quadrupole and sextupole magnets are assumed to be measurable with an accuracy of 75 μm. This is considered to be achievable, for example, by using the K-modulation method [4, 5].

5. The strength errors of the quadrupole magnets are assumed to be measurable with an accuracy of 0.1%. The measurement may be directly performed prior to installation, or by using beam orbit bumps across each magnet.

6. The errors are assumed to obey Gaussian distributions with a cut-off at 3 standard deviations (3σ). Their magnitudes are given in Table 6.3.

6.6.1 Emittance ratio and Dynamic aperture

Simulations with 20 different random seeds (events) have been conducted. Figure 6.12 shows the machine performance at various stages of beam tuning. The graphs show the emittance ratio plotted against β_y (m) at the interaction point, and the estimated dynamic aperture ($n_x \equiv \sqrt{2J_x/\epsilon_{x_0}}$ vs. dp/p). The operation point was set to be (ν_x,ν_y)=(46.52, 46.08), which is preferred from the viewpoint of beam-beam effects (see Chapter 3).

In the tracking calculation, the initial vertical amplitude was set to be one third that of the horizontal. In the plots for the emittance ratio, the black dots represent results from individual "events" that correspond to different random seeds for errors. The straight broken line indicates the design emittance ratio of 2%. In the dynamic aperture plots, the thick lines indicate the expected dynamic aperture in the error-free lattice, while the thin lines show the results from simulations with random lattice errors. The injected beam is expected to occupy the area indicated by the thick rectangle.

Plots (a1) and (a2) are for only orbit corrections, while (b1) and (b2) are for sextupole adjustments by movers, in addition to orbit corrections.

It can be seen that for the "orbit correction only" case, the emittance ratio is huge, and the dynamic aperture (DA) is degraded compared to the "error-free" case (thick line). Although the DA has sufficient space to accept the injected beam, it is desirable to have much more margins for safety, especially for large momenta, because it limits the Touschek lifetime.

In order to improve the emittance coupling, sextupole magnets are vertically moved, simulating movers, such that the orbit passes through their center within 75 μm. The emittance ratio is dramatically improved, as shown in (b1). The corresponding DA also shows a small improvement for the transverse direction.

The scatter of β_y^* in (a1) and (b1) is fairly large ($\sim \pm 25\%$). This is a reflection of strength errors of the quadrupole magnets that are included in the simulation. It has been found that DA is strongly correlated with β_y^*. Thus although those "events" with smaller β_y^* give a larger luminosity, they are also responsible in part for the deteriorated DA in (b2).

In the next simulation step optics matching was performed, assuming that the strength errors of the quadrupole magnets are known with an accuracy of 0.1%. This has the effect of making the expected β_y^* of each "event" closer to the design value. As shown in (c1), the spread of β_y^* is much reduced. However, as shown in (c2), DA becomes much worse for large momenta. This is because the strengths of the sextupole magnets are no longer optimum for the re-matched optics.

As the final step, by optimizing the sextupole magnets we could recover the DA

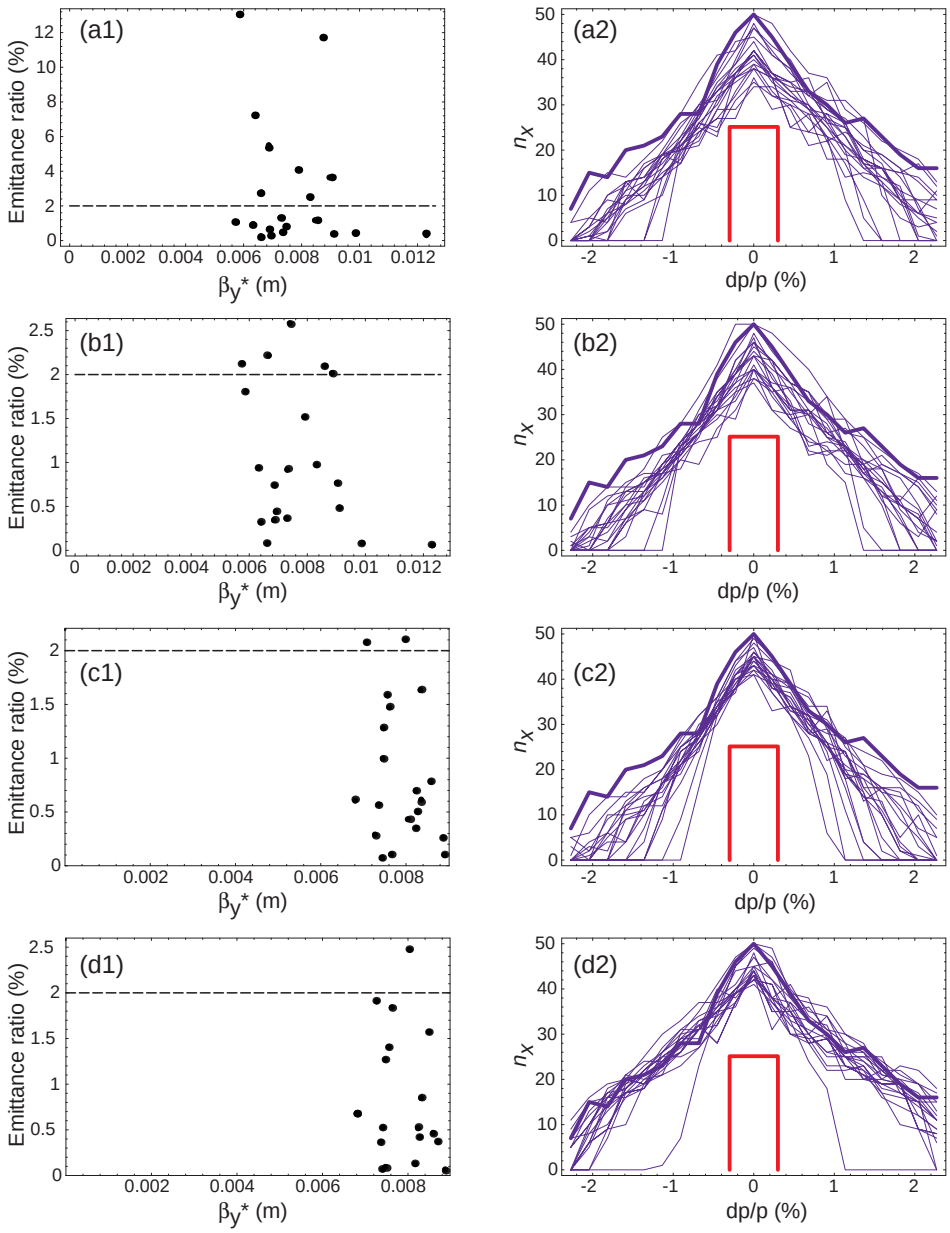

Figure 6.12: Simulated machine performance at various stages of beam tuning. The graphs show the emittance ratio plotted against β_y (m) at the interaction point, and the estimated dynamic aperture ($n_x \equiv (2J_x/\epsilon_{x_0})^{-1/2}$ vs. dp/p). Plots (a1) and (a2) are for only orbit corrections, while (b1) and (b2) are for sextupole adjustments by movers, in addition to the orbit corrections. Plots (c1) and (c2) show the case with optics re-matching. Plots (d1) and (d2) show the results with chromaticity correction for re-matched optics. For detailed descriptions see the text.

close to the ideal, as shown in (d1) and (d2). (There was one exception for which we could not find the optimum setting of the sextupole magnets).

It can be seen that tuning with sextupole mover is very effective to optimize the emittance coupling, because it is orthogonal to the DA: it does not affect the dynamic aperture.

6.6.2 Field Ripples

If the excitation strengths of the magnets change at frequencies for which the orbit feedback system cannot apply corrections effectively, then noticeable performance degradation may result. To evaluate this issue, the tolerances on the field jitter of the magnets have been calculated.

The criteria for calculating the jitter tolerances are that: (1) changes in the field do not induce either emittance growth or a deterioration of DA by more than 10%, and (2) shifts of the beam orbit at the IP do not exceed $0.1\sigma^*_{x,y}$.

The calculated tolerances of the field jitter are summarized in Table 6.4. The tolerances on the sextupole jitters are smaller than those for the quadrupole magnets. The QCS quadrupole magnets for the final focusing are assumed to be connected in series to a common power supply. The third column in the table gives the effect of jitter on the emittance or DA. The symbols Δx^* and Δy^* are the horizontal and vertical orbit deviations at the IP. The ratio $\Delta A/A_0$ is the relative change in the area of the dynamic aperture, *i.e.*, the sum of n_x for each dp/p point.

It should be noted that the tolerances quoted in the table are for the field, and that the numbers are not to be considered directly for the magnet power supply. To estimate the tolerances on the ripples of the magnet power-supplies, the effects of eddy currents in the vacuum chamber have to be taken into consideration. Generally, the power-supply ripple tolerances are much more relaxed than the values shown in Table 6.4. For example, the tolerances of the 50 Hz component of the power supply ripples are 10 times greater than those given in Table 6.4

6.7 Conclusions

Detailed studies on the lattice for the arc sections of KEKB have been performed. The present working design is based on a 2.5π cell structure. It offers an excellent dynamic aperture, and tunability of momentum compaction and beam emittance. The use of a local chromaticity correction scheme near the IP appears to be very promising. The requirements on the magnet field quality and errors of alignment and magnet excitations have been studied.

Element	relative jitter (σ)	what limits
Bend Dipole Magnets	1×10^{-5}	$\Delta x^* = 3.4\mu$m ($\sigma_x^* = 80\mu$m)
Quadrupole Magnets	1×10^{-4}	$\epsilon_y/\epsilon_{y_0} = 5 \pm 19\%$ $\Delta A/A_0 = -3 \pm 14\%$
QCS Quads	1×10^{-5}	$\epsilon_y/\epsilon_{y_0} = 10\%$ $\Delta A/A_0 = -10\%$
Sextupole Magnets		
Steering Corrector Magnets	1×10^{-5}	$\Delta y^* = 0.1\mu$m ($\sigma_y^* = 2\mu$m)

Table 6.4: Tolerances of field jitter. Symbols Δx^* and Δy^* denote the horizontal and vertical orbit deviations at the IP, while the $\Delta A/A_0$ is the relative change of the area of the dynamic aperture plot, *i.e.*, the sum of n_x for each dp/p point.

Bibliography

[1] K.L. Brown, IEEE Trans. Nucl. Sci. **NS-26**, 3490 (1979); K.L. Brown and R. Servranckx, in *Physics of High Energy Particle Accelerators*, Proc. the Third Annual U.S. Summer School in High Energy Particle Accelerators, AIP Conf. Proc. No. 127 (1983).

[2] K. Oide and H. Koiso, Phys. Rev. **E47**, 2010 (1993).

[3] K. Oide and H. Koiso, Phys. Rev. **E49**, 4474 (1994).

[4] R. Schmidt, *Misalignments from K-modulation*, Proceedings of The Third Workshop on LEP Performance, Chamonix, January, 1993, 139-145

[5] M. Kikuchi, K. Egawa, H. Fukuma and M. Tejima *Beam-Based Alignment of Sextupoles with Modulation Method*, to be published

Chapter 7

Interaction Region

7.1 Beam Line Layout

The design beam parameters of KEKB and their rationale have been discussed in Chapter 1. Some pertinent parameters are repeated in Table 7.1 for convenience.

A schematic layout of the beam line near the interaction point (IP) is shown in Figure 7.1. The figure shows the following magnets: S-R, QCS-R, QC1ER, S-L, QCS-L and QC1EL. The final vertical focusing of two beams is provided by a pair of superconducting quadrupole magnets, QCS-R and QCS-L. The superconducting solenoid magnets, S-R and S-L, are for compensating solenoid fields created by the detector facility. The QCS and S magnets on each side of the interaction point (IP) are contained in a common cryostat enclosure.

The vertical focusing field strength of QCS is tuned to the positron energy (3.5 GeV). Extra vertical focusing for the electron (8.0 GeV) is provided by a pair of normal conducting quadrupole magnets QC1E-L and QC1E-R. The beam separation and the geometry of QC1E magnets are designed such that only the electrons would see non-zero gradient fields when passing through them. To minimize the growth of chromaticity from this region, the QC1E magnets are placed close to the QCS magnets, in as much as the hardware design constraints allow.

The positrons enter the IP through QCS-R and leave the IP through QCS-L. The electrons proceed in the opposite direction. Since the two beams collide at the IP at a finite crossing angle of 2×11 mrad, inevitably one beam or the other must go off axis within the QCS. To minimize the flux of synchrotron radiation through the IP, the incoming positron beam orbit is set on the axis of QCS-R. Likewise, the incoming electron beam is set on the axis of QCS-L.

A sufficiently large beam separation is created at QC1E-L, so that a full quadrupole

	LER	HER	
Energy	3.5	8.0	GeV
Crossing angle	± 11		mrad
Luminosity	1×10^{34}		$\mathrm{cm}^{-2}\mathrm{s}^{-1}$
Tune shifts (ξ_x/ξ_y)	0.039/0.052		
Beta function (β_x^*/β_y^*)	0.33/0.01		m
Beam current	2.6	1.1	A
Bunch length	4		mm
Energy spread	7.1×10^{-4}	6.7×10^{-4}	
Bunch spacing	0.59		m
Particles/bunch	3.3×10^{10}	1.4×10^{10}	
Emittance ($\varepsilon_x/\varepsilon_y$)	$1.8 \times 10^{-8}/3.6 \times 10^{-10}$		m
Synchrotron tune	0.01∼0.02	0.01∼0.02	
Betatron tune (ν_x/ν_y)	45.52/45.08	47.52/43.08	

Table 7.1: Beam parameters related to the IR issues.

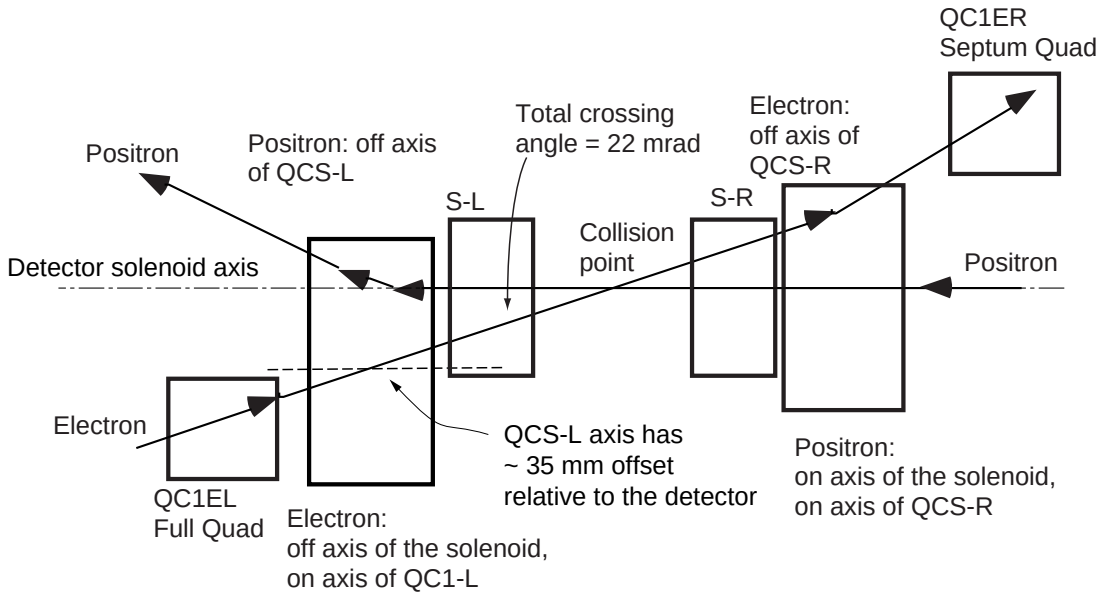

Figure 7.1: Schematic plan view layout of the magnets and the beam line near the interaction point. The superconducting solenoid S-R and the final focusing quad QCS-R are contained in a single cryostat. Similarly, S-L and QCS-L are contained in another cryostat.

Magnet	Detector solenoid	Electron	Positron
S-L	On axis		
QCS-L	Off axis	Incoming	Outgoing
	by -35 mm	on axis of QCS-L	off axis of QCS-L
S-R	On axis		
QCS-R	On axis	Outgoing	Incoming
		off axis of QCS-R	on axis of QCS-R

Table 7.2: Required transverse alignment of the QCS and S magnets relative to the detector solenoid and the beams.

magnet can be built for the incoming electrons to pass through its center. This is an important step to minimize the synchrotron radiation emitted by the electrons, which naturally propagates towards the IP. At the same time, magnetic perturbations to the outgoing positrons is minimized.

The orientation of the beam line relative to the detector solenoid field axis has been chosen, such that the incoming positron through QCS-R is on the axis of the detector solenoid. Because of the crossing angle, this means that the incoming electrons through QCS-L will be off-axis of the detector. This is the preferred arrangement based on considerations on the detector geometry. Since the QCS-R side is where the electrons (i.e. high energy beam) leave the IP, the detector facility would like to occupy a solid angle coverage closer to the beam line, compared to the QCS-L side. This means that a smaller space would be available for the QCS-R cryostat. If the QCS-L is aligned relative to the detector solenoid axis, the required aperture for QCS-R become larger, because the field axis of QCS-R cannot be in line with the detector solenoid axis. This leads to an increased exterior cryostat size for the QCS-R, which, in turn, would conflict with the detector solid angle coverage.

The compensation solenoid magnets S-R and S-L will have their field axis aligned to the detector solenoid. The relative transverse alignments of those superconducting magnets are summarized in Table 7.2.

The first horizontal focusing will be provided by the QC2 magnets, as shown in Figure 7.2. Like the QC1 magnets, iron-dominated normal conducting magnets will be used as QC2's. Their inner aperture shapes are designed so that either only an electron or positron beam will see the desired focusing field.

The locations of the QCS, QC1 and QC2 magnets and their field gradient values are summarized in Table 7.3. The distance z along the beam line from the IP is denoted

with positive values in the "right" direction, where the electron leaves the IP. The "left" direction, where the electron enters the IP, is denoted by negative values of z.

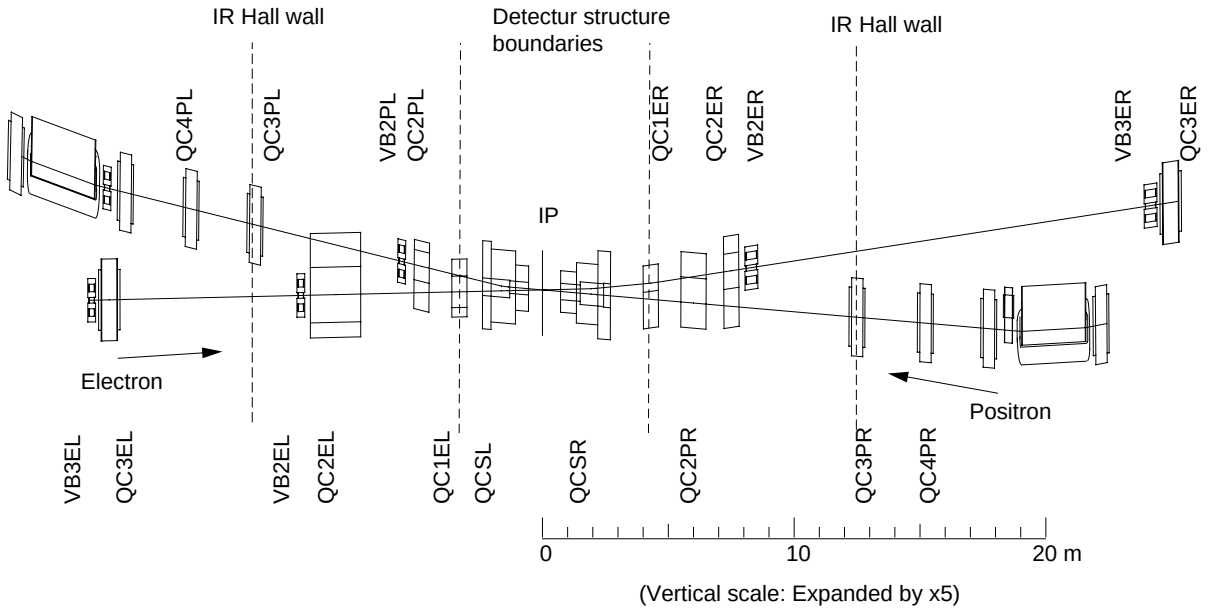

Figure 7.2: A schematic diagram of the beam line beyond QC1 magnets.

Magnet	Z_{min} (m)	$Z_{max}(m)$	Field gradient (T/m)	Purpose
QC2E-L	-8.0	-7.2	5.78	Horiz. focusing e^-
QC2P-L	-5.0	-4.4	6.42	Horiz. focusing e^+
QC1E-L	-3.6	-3.0	-14.6	Vert. focusing e^-
QCS-L	-1.85	-1.35	-16	Vert. focusing e^-e^+
QCS-R	1.685	2.185	-16	Vert. focusing e^-e^+
QC1E-R	4.0	4.6	-14.47	Vert. focusing e^-
QC2P-R	5.4	6.4	3.9	Horiz. focusing e^+
QC2E-R	7.2	7.8	9.7	Horiz. focusing e^-

Table 7.3: Positions relative to the IP and field gradients of the QCS, QC1 and QC2 magnets.

Several orbit correction dipole magnets will also be installed in the beam line. A few horizontal and vertical bend magnets are required to match the orbit to the rest of the straight section. As discussed in Chapter 2, local chromaticity corrections are

applied to the LER in the straight section that includes the IR. A schematic beam line layout of the IR, including a part of the chromaticity correction sections, is shown in Figure 7.3. Soft bend magnets will be used as the last dipole magnets for the incoming beam to see before reaching the IP. This is so that the critical energy of synchrotron radiation off these magnets will be sufficiently low, and that it would not cause harmful background to the detector facility.

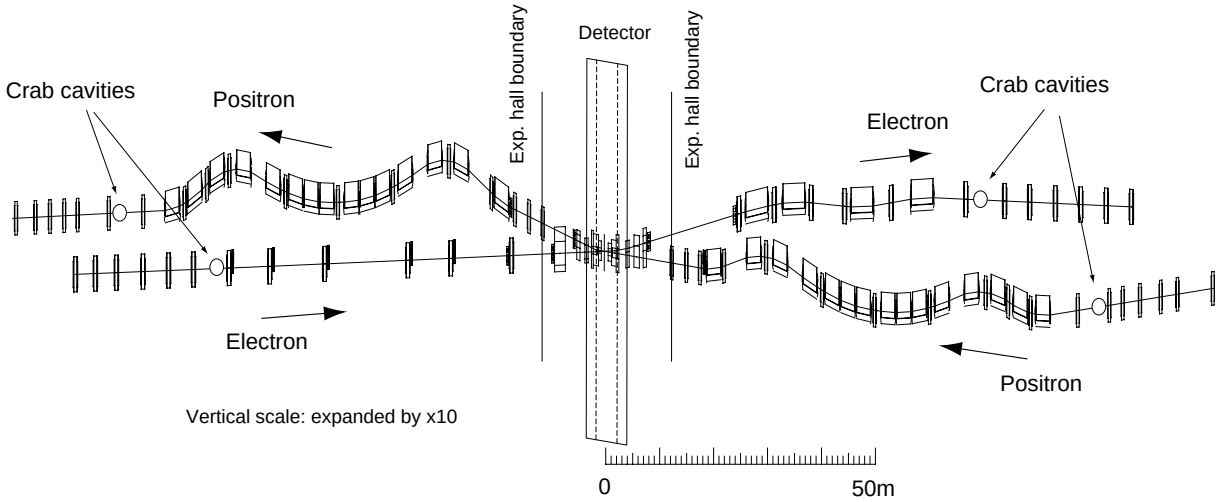

Figure 7.3: Schematic layout of the HER and LER beam lines in the straight section which includes the IR. Part of the LER local chromaticity corrections are shown.

Although the bulk of the x-y coupling effects due to the detector solenoid are cancelled by compensation solenoids S-L and S-R, the remaining coupling terms need to be corrected in the rest of the IR beam line. For this purpose, the support frames for QC1, QC2, QC3 and several other magnets allow us to introduce a variable amount of small rolls ($< 2^\circ$) for introducing skew components to the magnetic field. The roll angles will be remotely controlled using a magnet mover mechanism. Engineering development of these magnet support will begin soon.

7.2 Detector Boundary Conditions

7.2.1 Geometric Conditions

The detector facility for high energy physics experiments at KEKB has approximately an axially symmetric geometry around the beam line. Physics requirements call for a good solid angle coverage for detecting decay product particles from $e^+e^- \to B\overline{B}$ interactions. Figure 7.4 shows a schematic side view of the proposed detector facility.

Table 7.4 summarizes the solid angle coverage requested by proponents of the detector facility. In the table, the polar angle is measured from the forward extreme, i.e.

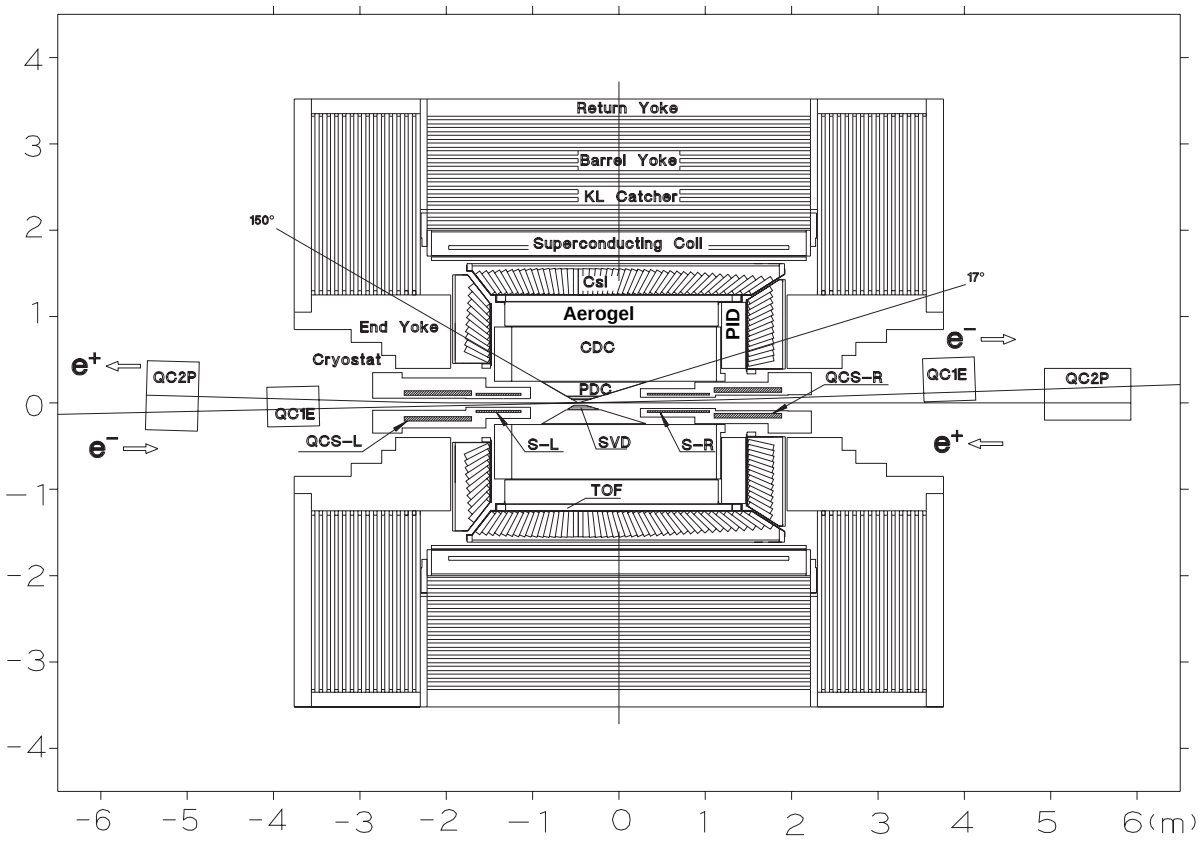

Figure 7.4: Schematic side view of the proposed detector facility, together with the accelerator cryostat for superconducting compensation solenoid and QCS magnets. A pair of normal conducting quadrupole magnets and QC1EL and QC1ER are also shown. Details of the detector configuration may vary in the final design.

Detector	Polar angle range
Barrel K_L catcher and μ detector	45° - 113°
Forward K_L catcher and μ detector	25° - 45°
Backward K_L catcher and μ detector	113° - 155°
Barrel Calorimeter	32.5° - 130°
Forward Calorimeter	11.5° - 32.5°
Backward Calorimeter	130° - 160°
Barrel TOF/TSC	32.5° - 130°
Barrel Particle ID device	32.5° - 130°
Forward Particle ID device	12.5° - 32.5°
Central Drift Chamber	17° - 150°
Silicon Vertex Detector	17° - 150°

Table 7.4: Polar angle coverage requested by the experimental detector facility.

the direction where the positrons enter the interaction point (IP).

The interaction point relative to the detector center is shifted towards the left by 470 mm. This is for increasing the solid angle coverage in the forward direction, while taking into account the Lorentz boost of the final state particles in the asymmetric collision.

The detector geometry that has a direct bearing on the accelerator design is that of the central drift chamber (CDC). In the latest design the CDC has an inner radius of 280 mm. Thus, the accelerator components must fit within a cone-shaped space with an opening angle of 17 degrees forward and 30 degrees backward, clipped by the CDC inner radius, minus the cable space for detector elements. The CDC occupies the Z space between -970 mm and $+1660$ mm, as measured from the IP.

Just at the IP, a high precision particle tracking device based on silicon micro strips will be installed. Its design calls for a small vacuum chamber around the IP with an inner radius of 20 mm for $-80 < Z < +80$ mm. The particle trajectories during the injection period and synchrotron radiation during the run must not be intercepted by this aperture.

7.2.2 Magnetic Conditions

The nominal solenoid field created by the detector magnet for charged particle tracking is 1.5 T. The field is extended in an effective volume length of $\sim \pm 2.5$ m. If the solenoid field of the detector is not cancelled in situ on the beam line, its coupling

effects must be corrected by using a set of skew quadrupole magnets, whose strength is approximately $K_{SQ} \approx 0.05$. However, corrections with skew quad magnets are exact only for on-energy particles. The remaining chromatic coupling term will result in an increased vertical emittance. Also, the use of skew quadrupole magnets will create extra chromaticity, which need to be compensated in chromaticity correction sections in the arcs and elsewhere. This tends to reduce the available dynamic aperture, and consequently, the expected beam lifetime. Furthermore, there is an indication from simulations on beam-beam effects, that the luminosity will tend to be reduced if the solenoid field compensation is not sufficient.

Beam dynamics calculations have been conducted to evaluate these effects. Cases with various sophistication of solenoid field compensation schemes have been examined. It has been found that if *the integral of the axial field B_z is cancelled to zero on the average*, the reduction of the dynamic aperture and its effects on the beam lifetime are negligible. In that condition, the accelerator performance is comparable to the case where the detector solenoid field is completely absent. The effects of fringe fields of the solenoid and quadrupole magnets are taken into account. As an example of incomplete field compensation, in the case with a left-over field of $\int B_z dz = 1.5$ T m, it has been found that up to a 30% reduction of the beam lifetime will result, because of the reduced dynamic aperture. Thus, the goal of field compensation for the accelerator within the detector volume should be to bring the *net value* $\int B_z dz$ to zero. The superconducting compensation solenoid magnets S-L and S-R will be implemented to achieve this.

Magnetic fields from S-L, S-R, QCS-L and QCS-R will leak into the detector volume, and distorts its solenoid tracking field. Their effects in physics analyses were a potential problem. Simulation work by the detector group has shown that the effects of the leak field due to S-L and S-R magnets are, in fact, manageable. Relatively straightforward tuning of the track analysis software can recover the full momentum resolution of charged particles. It has been also found that perturbations due to leak fields from QCS magnets are sufficiently isolated from the interaction point. In addition, the quadrupole field component quickly attenuates as a function of r, the radial distance from the beam line. Thus, the leak quad field is also manageable from the physics analysis view point. Therefore, no additional compensation magnets will be implemented to shield the detector volume from S and QCS accelerator magnets.

Since QCS-L is not in line with the detector axis, the field that is produced by QCS-L may couple with the detector iron in such a way as to create an axially non-symmetric field on the accelerator beam line. The magnitude of such multipole fields has been evaluated, and its effect on the beam dynamics examined. It has been found that their adverse effects are negligible. Consequently, no special measures will be

taken to shield QCS from the detector iron structure, either. However, it is felt that in any case it is desirable to introduce some correction devices for multiple pole field errors. A feasibility study of such devices is now being prepared.

Turning to outside the QCS region, the QC1E-L and QC1E-R magnets will be located near the outer edge of the detector structure. If the magnetic field from the detector solenoid is large there, the presence of QC1E iron can significantly distort the magnetic field near their entrance. Unless care is taken, this will lead to sizeable multipole field errors to be felt by the beams.

The magnitude of the detector leak field depends on the details of the relative geometry of the detector and the accelerator. There is a desire on the part of experimental physicists to increase the thickness of the end yoke for better muon detection coverage. This would tend to increase the leak field from the detector, unless care is taken to reduce the magnetic saturation within the detector structure. Or, both the accelerator and detector designers agree that increasing the inner aperture size of the detector end cap (currently set to be 1000 mm diameter) would relax the space problem for cabling, installation and maintenance. However, it would quickly increase the detector leak field.

In one version of the structure design, the detector leak field near QC1E could be reduced to $B_z < 20$ G and $B_r < 20$ G, which is considered to be acceptable from a beam dynamics viewpoint. Efforts are still on-going to optimize the structure configuration so that the detector coverage is maximized while the leak field is minimized. Preparations for high-precision 3-dimensional field calculations in this area are in progress. A possible use of weak compensation solenoid magnets or end-shimming is also being considered near QC1 magnets. However, the priority is on efforts to first reduce the strength of the detector leak field.

7.3 Beam Line Aperture Considerations

The aperture of the vacuum chambers in the QCS and S magnets have been determined, so that neither the beam during injection time nor the synchrotron radiation (SR) during the data acquisition time should directly hit the inner surface of the vacuum pipes.

The beam envelope considered in the injection system design is 1.2×10^{-5} m for x and 1.2×10^{-6} m for y. To include a safety margin, in the design of IR the beam envelope emittance of 2×10^{-5} m for x and 2×10^{-6} m for y is assumed. Parallel to these, the trajectories of SR photons from 10σ particles during the collision time have been calculated. The beam stay clear values have been determined from the maximum

of the injection time beam envelope and the run-time SR flux trajectory. This beam stay clear, plus 13 mm for the work space for the vacuum chambers is specified as the required inner aperture of the cryostats for QCS and S magnets.

The beam stay clear for QC1 and QC2 magnets has been determined by considering only the injection condition. The assumed beam envelope is 1.4×10^{-5} m for x and 2×10^{-6} m for y.

The vacuum chamber that connects the beam line between those magnets must fully contain the specified beam-stay clear. Since the β function values are rapidly changing in this area, the beam stay clear also varies along the beam line. The design of the vacuum chamber in the IR has to accommodate this situation. Also, attention must be paid to possible trapping of higher order mode (HOM) RF fields in this area. Although efforts are being made to reach an optimum solution, some amount of HOM trapping, and heating due to it, will be inevitable. To rectify this situation, the possibility of implementing some antenna structures to remove the HOM power from this section is being contemplated.

7.4 Superconducting Magnets for IR

7.4.1 Introduction

Four superconducting magnets will be used in the interaction region: solenoid field compensation magnets (S-L and S-R), and final focusing quadrupole magnets (QCS-L and QCS-R). Each pair of S + QCS magnets in the left and right side is contained in a single stainless steel vessel. It provides a sturdy structure which tightly holds the coil windings and prevents their motions during cooling down and excitation. The vessels (cryostat) are designed to withstand forces due to the magnetic field of the coils, themselves, and their interactions with the detector solenoid field. They have to be installed completely inside the detector facility. Figure 7.4 shows the layout of the interaction region with the superconducting magnets, surrounded by the detector elements. This section presents the engineering design work that has been done for the superconducting magnets.

7.4.2 Compensation solenoids

The two field compensation solenoids have magnetic fields opposite to the detector solenoid. Figures 7.5(A) and 7.5(B) show cross section views of the right and left solenoids in their horizontal cryostats. In both cases, the solenoid coil has an inner diameter of 190 mm, and a thickness of 15 mm. Between the inner helium vessel and

	S-R	S-L	
Central field	5.4	4.4	T
Coil current density	300	258	A/mm^2
Coil			
Inner diameter	190	190	mm
Outer diameter	220	220	mm
Length	650	470	mm
Max. field of the conductor	5.4	4.5	T
Stored energy	225	115	kJ
Magnetic pressure in radial direction	9.2	6.4	MN/m^2

Table 7.5: Main parameters for the solenoid magnets.

the coil, some space is allocated for accommodating a few kinds of correction coils. The main parameters of these solenoids are listed in Table 7.5. The final specifications of the conductor wire and the operating current will be decided in the near future, while tacking into account the magnetic coupling with the detector solenoid and the heat load to the cooling system.

A computer code OPERA-2D has been used to calculate the magnetic field from the combination of those solenoid magnets, the detector solenoid, and its field return yoke structure. Figure 7.6 shows the expected axial magnetic field B_z along the beam axis. With this configuration, the integral of B_z along the accelerator beam line is brought to zero.

The field distortions in the detector's tracking volume, which is caused by the leak field from these solenoids, have been evaluated. Figure 7.7 shows the contour lines of the field distortions relative to the nominal 1.5 T solenoid field. The number attached to each contour line indicates the field deviation expressed in the unit of percent. Except for the regions close to the compensation solenoids, the field deviation in the volume for charged particle tracking by the experimental facility is less than 5%. According to simulations studies carried out by the detector group, this is considered to be acceptable.

When the solenoid magnets are excited in the detector field, axial magnetic forces which act on the solenoid coils appear. The peak field values on the conductor will be shifted from the values in Table 7.5. These effects have also been evaluated using OPERA-2D. The estimated magnetic forces are listed in Table 7.6. The axial body force that acts on the S-L coil is 22 kN. Although it is somewhat large, it is well within

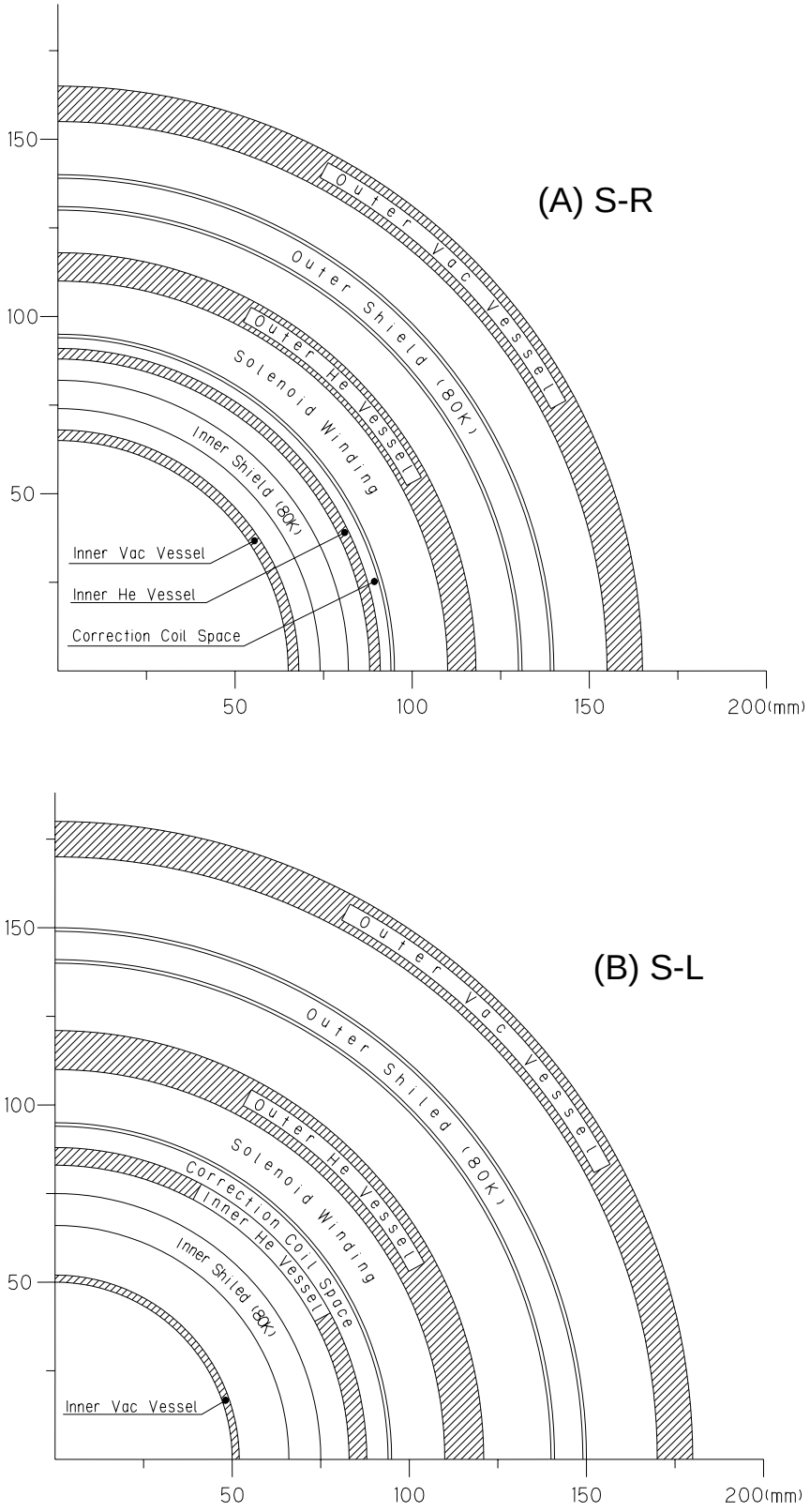

Figure 7.5: Cross section views of the S-R solenoid (A) and the S-L solenoid (B).

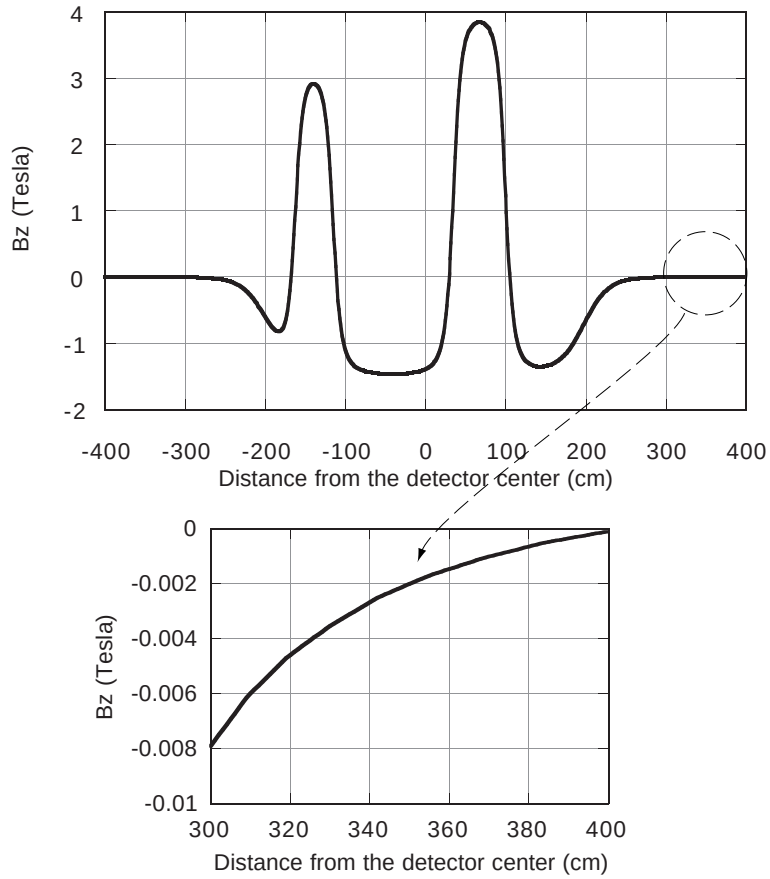

Figure 7.6: Distribution of the axial magnetic field B_z along the axis of the experimental facility.

	S-R	S-L	
Magnetic pressure			
in radial direction	3.1	1.4	MN/m^2
Body force			
in axial direction	2.8	22	kN

Table 7.6: Pressure and force on the solenoids placed in a 1.5 Tesla detector solenoid.

the acceptable level from engineering viewpoints. The maximum field strength on the conductors of both solenoids are decreased by 1.5 T, due to the opposite sign of the detector field.

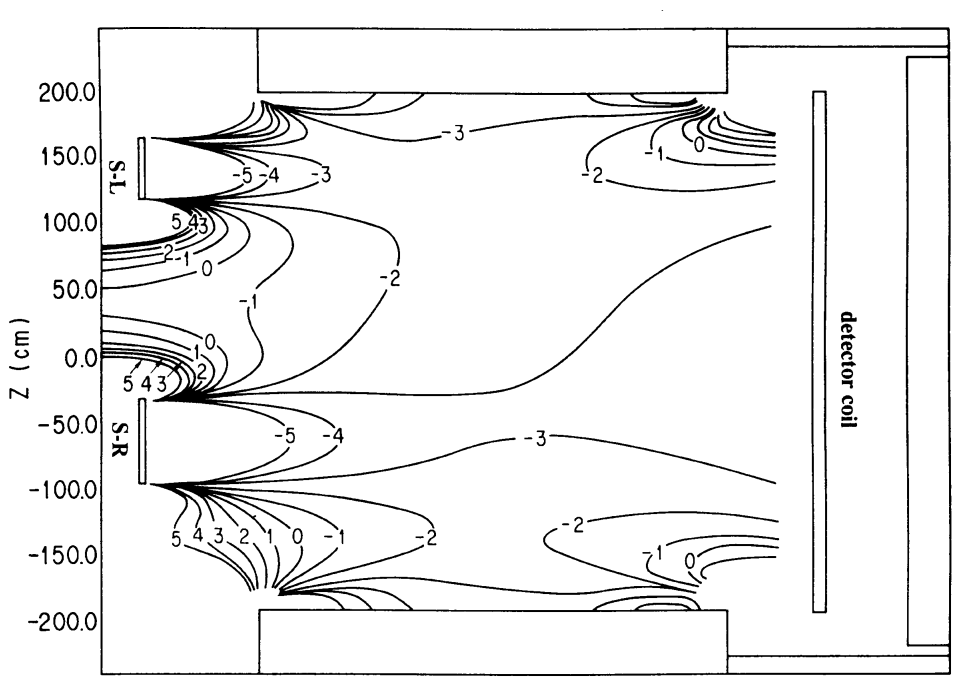

Figure 7.7: Contour lines of the field distortions relative to the nominal 1.5 T solenoid field. The number attached to each contour line indicates the field deviation expressed in the unit of percent.

Field gradient	18.8	T/m
Current	2224	A
Coil		
Inner diameter	260	mm
Outer diameter	295.4	mm
Overall length of the coil	780	mm (for QCS-L)
	710	mm (for QCS-R)
Collars		
Material	SUS316LN	
Radial thickness	27	mm
Integrated field uniformity (at $r = 40$ mm)		
B_6L/B_2L	$< 1 \times 10^{-4}$	
$B_{10}L/B_2L$	$< 1 \times 10^{-4}$	
Effective magnetic length	490	mm (for QCS-L)
	420	mm (for QCS-R)
Max. field on the conductor	3.1	T
Stored energy	157	kJ
Magnetic force per unit length in a coil octant		
F_x (horizontal)	125	kN/m
F_y (vertical)	-290	kN/m

Table 7.7: Parameters of the superconducting quadrupole magnet. The overall length of the coils does not include the coil end spacer and magnet end plates.

7.4.3 Quadrupole magnets

The final quadrupole magnets are iron-free, superconducting magnets. They provide a maximum field gradient of 18.8 T/m for an effective field length of 0.5 m in a usable aperture diameter of 80 mm. Extensive experience from the development, fabrication and operation of the TRISTAN superconducting mini-beta insertion magnets is reflected in the design work.

The basic design of QCS is similar to that of the TRISTAN magnets. It is based on a set of $\cos 2\theta$ winding layers clamped by stainless steel collars. The required warm bore aperture specifications of QCS-R and QCS-L are approximately the same. This allows us to use an identical coil structure for both sides, QCS-L and QCS-R. However, the dimensions of the cryostats will be different, as discussed in a previous section. The main parameters of the quadrupole magnet are listed in Table 7.7.

Cable dimensions		
width	8.35 ± 0.05	mm
thickness	0.925 ± 0.02	mm
Number of SC strands	16	
Number of Cu strands	16	
Cu / SC ratio of SC strand	2.0	
Strand diameter	0.510 ± 0.005	mm
Filament diameter	< 6	μm
RRR of stabilizing copper	180 ± 20	
Cable twist pitch	70 ± 5	mm
Critical current in cable (at 4.2 K)		
	more than 2900	A at 5T
	more than 4200	A at 3T

Table 7.8: Parameters of the superconducting cable.

Figure 7.8(A) shows a cross section of the QCS-R magnet in a horizontal cryostat. The inner diameter of the warm bore is 178 mm, and the outer diameter of the vacuum vessel is 480 mm. Starting with the innermost part, the main components of the magnet are: a warm bore, inner radiation shield, inner wall of the helium vessel, correction coils, main coil, stainless steel collar, outer wall of the helium vessel, outer radiation shield and vacuum vessel.

The main coil is made of two layers of superconducting windings. The $\cos 2\theta$ current distribution is approximated by using a copper wedge in the first layer. To keep the higher multipole fields within the tolerances, a computer code based on an analytical formula of field harmonics has been used to determine the two-dimensional cross section of the coil winding. The resultant shape has 115 turns in total, combining the first and second layers in each of the four quadrants. The operating current was chosen to be relatively small. This allows us to reduce the heat load on the cooling system.

The superconducting cable will be of the NbTi/Cu Rutherford type, which is commonly used in many accelerator magnets. Since the operating current is relatively low, it is planned to use a cable in which copper strands and NbTi/Cu strands are mixed for ease of the winding process. The main parameters of the cable are listed in Table 7.8.

Effects of various fabrication errors of the coils have been investigated. A basic eight-fold symmetry in the coil geometry is assumed. Table 7.9 summarizes the results of this study. The quoted numbers are for a 0.1 mm variation of the parameters listed.

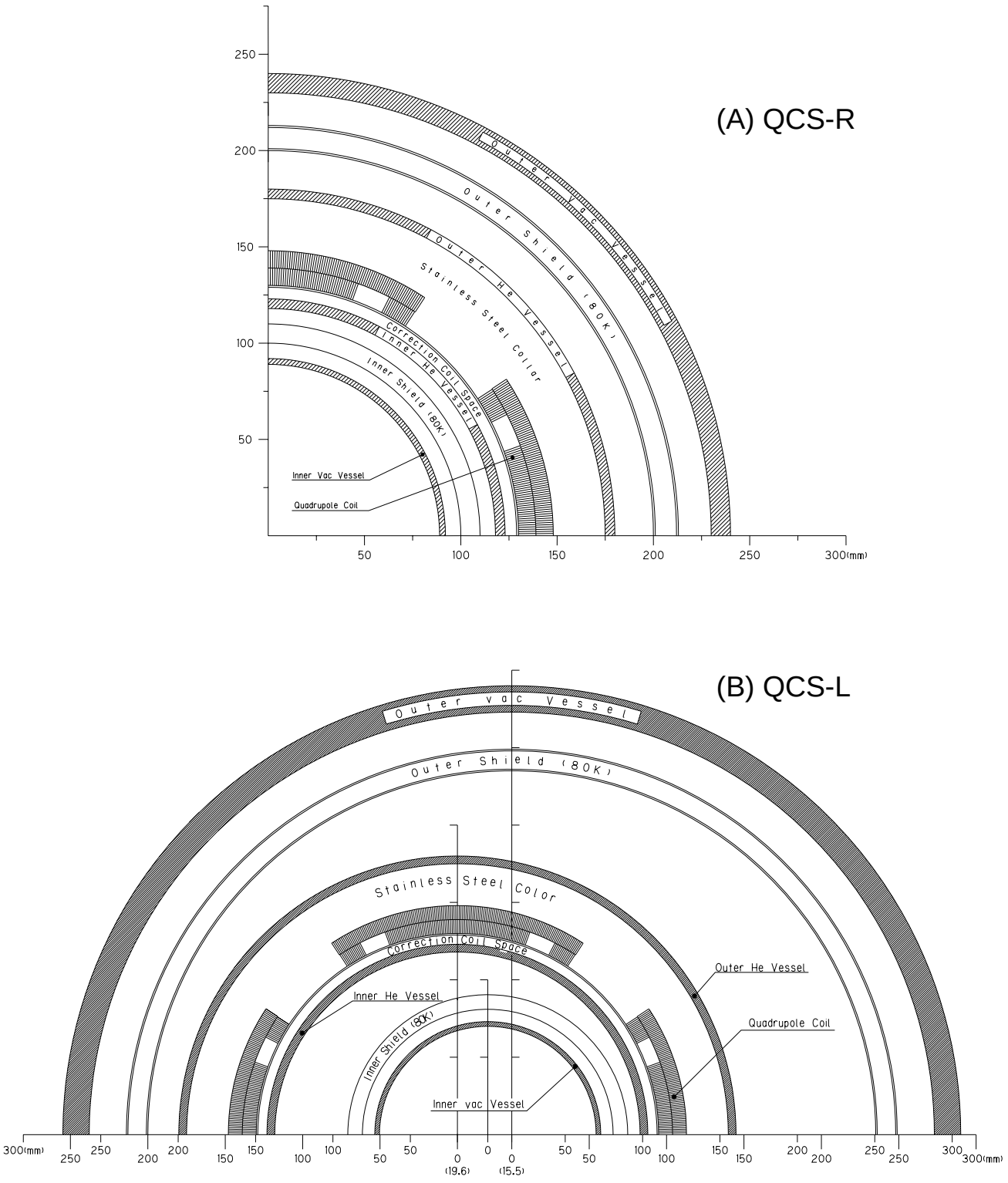

Figure 7.8: Cross section views of the QCS-R (A) and QCS-L (B) magnets.

Parameters changed	b_2 (mT/m)	b_6 10^{-4}	b_{10} 10^{-4}
Radius of inner coil	−11.0	−0.14	−0.00
Radius of outer coil	−32.6	−0.10	−0.00
Radius of inner No.1 coil	−9.41	−0.18	−0.00
Radius of inner No.2 coil	−4.73	−0.07	−0.00
Pole angle of inner coil	−4.96	−0.11	−0.00
Pole angle of outer coil	−19.0	−0.17	−0.00
Wedge of inner coil	−4.22	−0.20	−0.00

Table 7.9: The values show the effect of a 0.1 mm shift of the given parameter on the quadrupole field strength and higher harmonics at $r = 40$mm.

The harmonics are calculated at a reference radius of 40 mm.

Since the quadrupole magnets considered here are rather short compared to other typical accelerator superconducting magnets, the effects of the end parts are not negligible. Three-dimensional field calculations are in progress to investigate the field distribution, and to optimize the shape of the coil end.

Figure 7.8 shows a cross section of the QCS-L magnet in the horizontal cryostat. In this case, the quadrupole axis has to be shifted horizontally by 35.1 mm from the detector axis. Therefore, the cryostat has a rather complex structure, as shown in the figure. However, the engineering work for fabricating this magnet is considered to be quite possible. In this eccentric configuration, higher order multipole fields and the asymmetric electromagnetic forces can arise, due to the image current in the end yoke of the detector. An estimate of this effect has been made by treating the issue as a 2-dimensional problem. Beam dynamics calculations based on this estimate have found that the higher multipole fields are well within an acceptable level in terms of dynamic apertures. The strength of the attractive force between the end yoke and the quadrupole magnet is about 2.3 kN, which is within a manageable range.

7.4.4 Cryostat and cooling system

As mentioned earlier, two cryostats will be built and installed on each side of the interaction point. A preliminary design of these cryostats has been conducted, while taking into account the many practical constraints near the interaction point. They include: the desire for a small outer diameter, a narrow thermal insulation space, sufficient mechanical strength to sustain the forces acting on the magnets, a small heat load, and others. The longitudinal cross sections of these cryostats, including the

Cryostat	(including connection box)	35 W ×2	
Current leads			
	for QCS-R and QCS-L		11 ℓ/h
	for S-R and S-L		7 ℓ/h
	for six kinds of correction coils		9.5 ℓ/h
Transfer line	$\sim$ 35 m	56 W	
	(including 2 connection boxes)		
Subcooler		6.6 W	
	Total	97.6 W	+27.5 ℓ/h

Table 7.10: Estimated heat load and the required amount of liquid helium for the QCS cryogenic system.

coils, the radiation shield, and the helium vessel, are shown in Figures 7.9(A) and (B). Detailed designs of the support rods and piping are in progress. The heat load of a pair of cryostats is estimated to be less than 35 W.

The estimated head load of each cryogenic component is listed in Table 7.10. Allowing for a minimum safety margin of 2.1, the required capacity of the common refrigerator is 203 W + 27.5 ℓ/h. The cooling system that has been used for the Tristan mini-beta insertion quadrupole magnets since 1991 has a capacity of that level. It will, therefore, be recycled and reused. The basic components of the system (helium compressor, cold box, sub-cooler, and control computer) will be reused. Figure 7.10 shows a simplified flow diagram of this system. The system will use single phase liquid helium of 4.5 K and 0.16 MPa.

7.5 Special Quadrupole Magnets for IR

Near the interaction point, six iron-dominated quadrupole magnets of special type are required: QC2E-L, QC1E-L, QC1E-R and QC2E-R for HER, and QC2P-R and QC2P-L for LER. The specifications for these quadrupole magnets are listed in Tables 7.11 and 7.12.

The purpose of these magnets is to apply optimized focusing and defocusing fields on electrons and positrons, independent of each other. Figure 7.11 shows the areas occupied by beams of electrons and positrons and their center positions at the edges of QC1E-L and QC2P-R. The ellipses indicate the beam areas which correspond to the beam envelope during the injection time, plus the vacuum chamber thickness 5 mm.

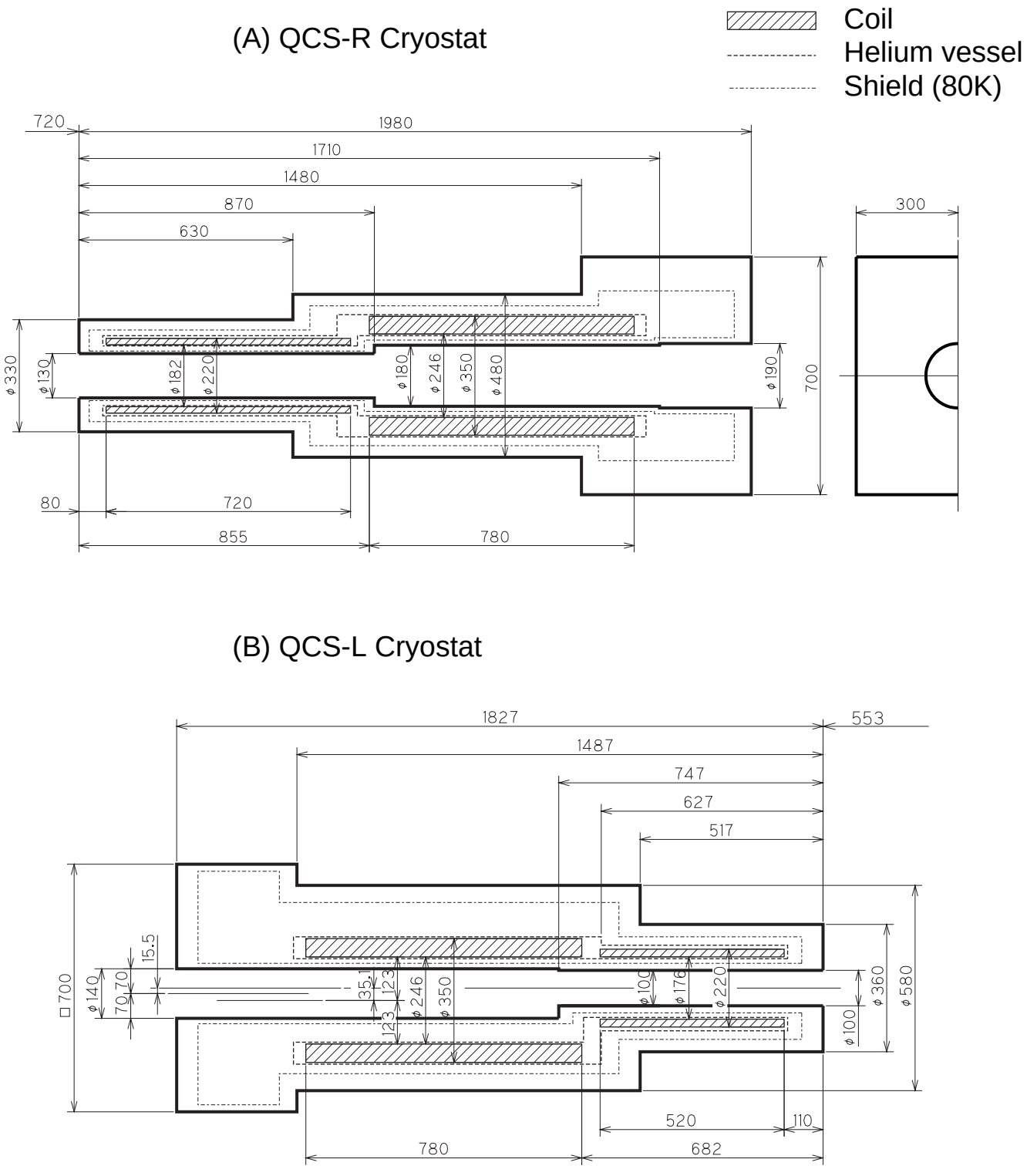

Figure 7.9: Longitudinal cross section views of the right-side cryostat (A) that contains S-R and QCS-R, and the left-side cryostat (B) that contains S-L and QCS-L. The dimensions are given in mm.

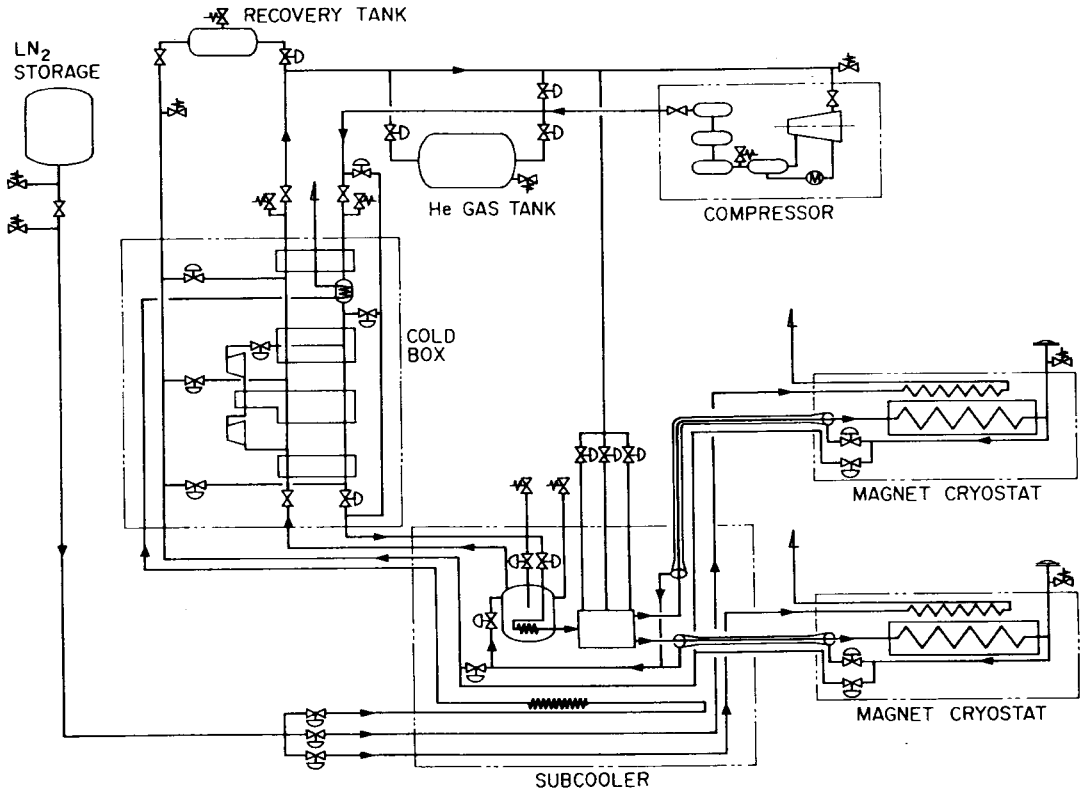

Figure 7.10: Simplified flow diagram of the helium cooling system.

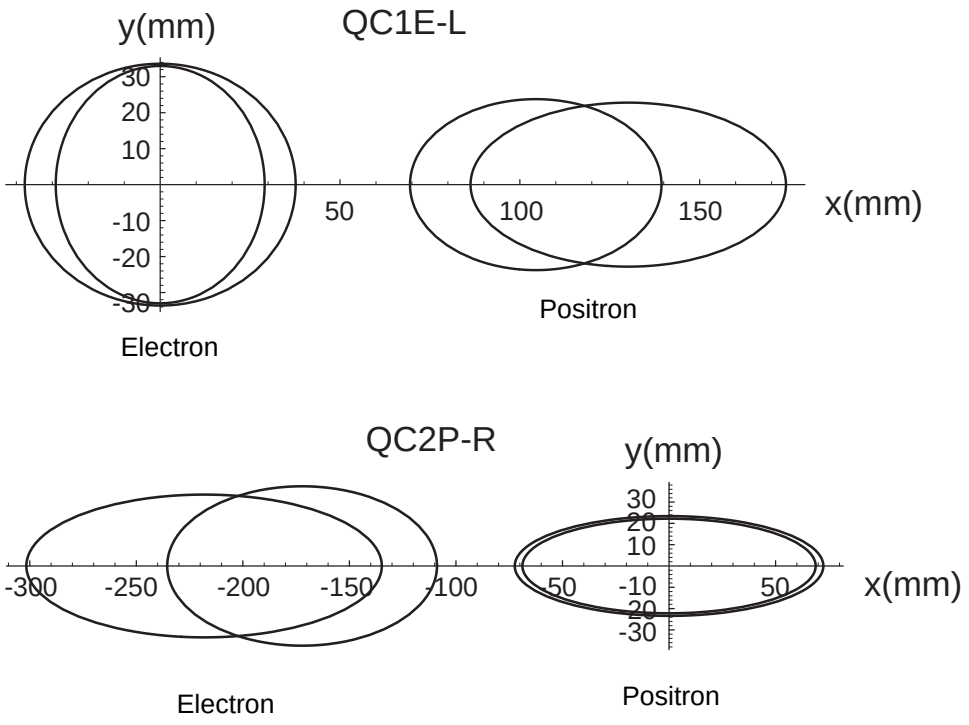

Figure 7.11: Beam positions and beam envelopes during the injection time at the edges of QC1E-L and QC2P-R.

		QC1E-L	QC2E-L	QC1E-R	QC2E-R
Entrance aperture(e^-)	horizontal(mm)	37.66	114.7	38.47	99.5
	vertical(mm)	33.62	18.5	39.85	30.4
Exit aperture(e^-)	horizontal(mm)	29.04	106.7	47.27	105.2
	vertical(mm)	32.99	20.4	40.43	29.8
Entrance aperture(e^+)	horizontal(mm)	43.85	50.9	48.1	61.5
	vertical(mm)	22.8	33.9	24.5	29.2
Exit aperture(e^+)	horizontal(mm)	34.96	53.1	56.95	66.2
	vertical(mm)	23.77	30.8	23.51	26.7
Beam separation	entrance(mm)	130.14	339.0	112.2	254.8
Beam separation	exit(mm)	100.42	302.0	132.2	283.0
Max. field gradient	(T/m)	15.4	6.1	12.6	10.2
Pole length	(m)	0.6	1.0	0.6	0.6

Table 7.11: Specification of the IR quads for HER.

		QC2P-L	QC2P-R
Entrance aperture(e^-)	horizontal(mm)	52.99	63.3
	vertical(mm)	30.69	37.4
Exit aperture(e^-)	horizontal(mm)	64.51	83.4
	vertical(mm)	28.48	33.5
Entrance aperture(e^+)	horizontal(mm)	55.7	68.8
	vertical(mm)	21.52	22.2
Exit Aperture(e^+)	horizontal(mm)	59.37	72.4
	vertical(mm)	22.19	23.4
Beam separation	entrance(mm)	170.0	172.2
Beam separation	exit(mm)	200.0	218.2
Max. field gradient	(T/m)	7.3	4.1
Pole length	(m)	0.6	1.0

Table 7.12: Specifications of the IR quads for LER.

The beam emittance envelope of $\varepsilon_x = 1.4 \times 10^{-5}$m and $\varepsilon_y = 1.4 \times 10^{-6}$m is assumed for the beam during the injection time. The beam line has been designed to create a sufficient beam separation within those magnets, so that magnets with realistic engineering design can be built. Five of these magnets will be built as full quadrupole magnets. They have to have non-standard shapes in which a field free space is embedded for the beam of the other ring. Due to the limited beam separation, one of them, QC1E-R, will have to be a half quadrupole magnet.

Although a large region with good field quality must be created, in the region for the other beam ("spectator beam") the field strength must be minimized. This has to be achieved while the beam separation is only marginal. For example, the free space thickness for QC1E-L and QC2P-R is merely $30 \sim 40$ mm. Consequently, the thickness of the conductor in between must be minimized. The conductor shape resembles that of a septum magnet. Therefore, QC1E-L and QC2P-R will have very high current density in the conductors. The field distribution in those magnets have been calculated using the computer code Poisson. The cross section shapes of QC2E-L, QC2P-R, QC1E-L and QC1E-R have been determined, as shown in Figure 7.12.

The magnet that has the highest current density in the coil is QC1E-L; the overall current density of its "septum conductor" is about 56 A/mm^2. Although not trivial, it is considered to be possible to cool the conductor by minimizing the length of the cooling circuit. It is considered relatively easy to build QC2E-R and QC2P-L, because

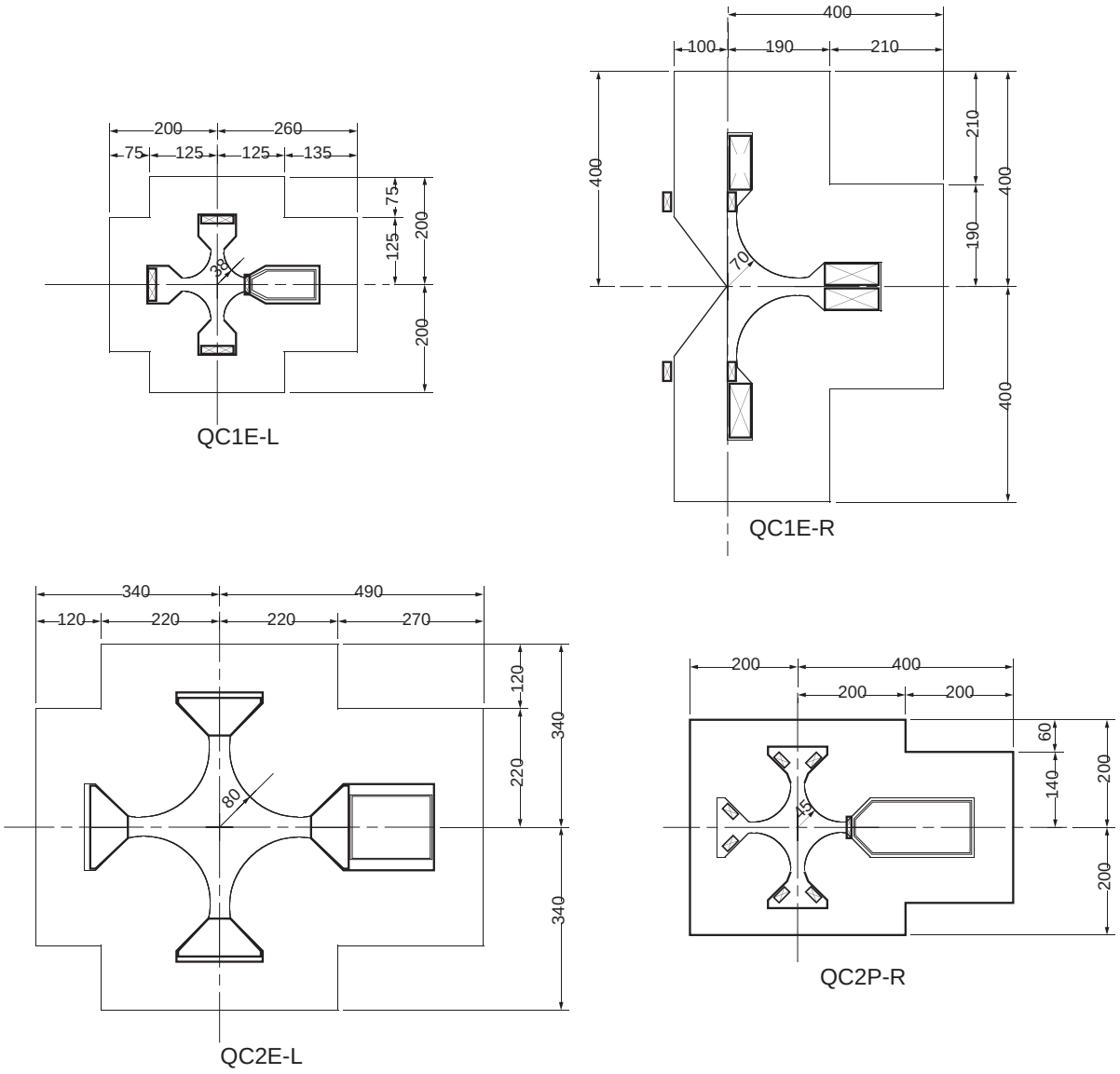

Figure 7.12: Cross section shapes of some of the special IR quadrupole magnets.

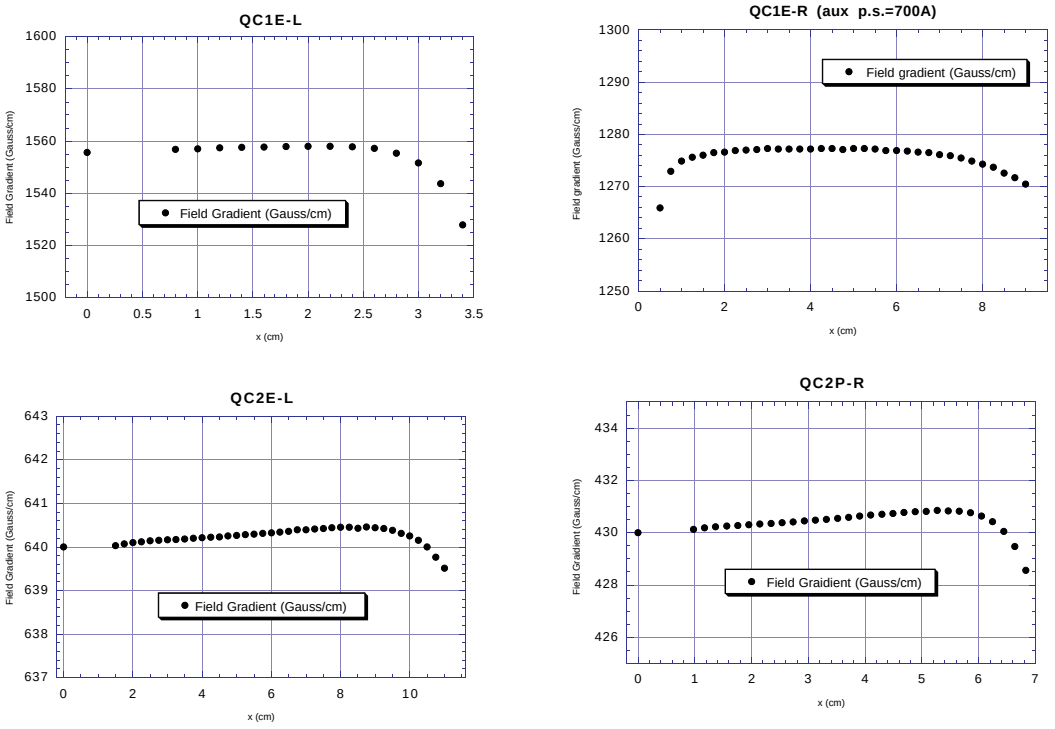

Figure 7.13: Calculated distributions of the field gradient of the IP quads.

the free space between two beam areas is much larger. Since the field distribution near the pole edge is also affected by the position of the conductor, it is important to mechanically firmly fix the "septum conductor" against its thermal expansion and magnetic forces.

As for the half quad (QC1E-R), the field distribution near the iron septum is determined by a delicate relation between the magnetic resistance of the flux circuits. To make corrections for possible errors, trim coils will be attached to the iron septum.

The calculated field gradient distributions of QC2E-L, QC2P-R, QC1E-L and QC1E-R are shown in Figure 7.13. If a further reduction of the field gradient near the aperture boundary is proved necessary, this can be done, to some extent, by adding end-shims. Because of the lack of 90-degree rotation symmetry, this magnet geometry is prone to produce sextupole and octapole fields due to errors. If these multipole components are found to be larger than the tolerance, a magnet geometry with a 90-degree rotation symmetry may have to be implemented. Investigations of these possibilities will be made in the near future, before freezing the final design of these magnets. The parameters of four of six IR special quads are listed in Table 7.13.

	QC1E-L	QC1E-R	QC2E-L	QC2P-R
Aperture radius(mm)	38	70	80	45
Pole length(m)	0.6	0.6	1.0	1.0
Max. field gradient(T/m)	15.6	12.7	6.4	4.3
Current(AT)	9000	27000	16500	3500
Current density of the septum conductor(A/mm^2)	56	6.8	4.6	22
Field in the area for counter-circulating beam (with magnetic shield)(Gauss)	$0 \sim -1$	$0 \sim -2$	$2 \sim -0.6$	$0 \sim -1$

Table 7.13: Parameters of QC1E-L, QC1E-R, QC2E-L and QC2P-R.

7.6 Installation and Magnet Support for IR

The magnets which will be placed in the Tsukuba experimental hall (IR hall) are superconducting magnets in the QCS solenoids, QC1E, QC2E and QC2P magnets. The support structure of the QCS cryostat is illustrated in Figure 7.14. The QCS cryostats are supported from a movable stage. This movable stage serves as a common support base for other accelerator magnets (QC1 and QC2 for both the LER and HER) located in the IR hall.

The movable stage can move along the beam line by approximately 4 m. The QCS magnets can be pulled out and pushed in with this motion. The alignment position and angle of the QCS cryostats can be adjusted by a mechanism installed on the support base. The relative positions between the cryostat and the endcap calorimeters are monitored by four units of a position measurement device called "holo-gauge." These gauges have been tested to be operational in a high magnetic field up to 1 T with radiation dose up to 10 krad.

In order to prevent vibration of the QCS head during an earthquake, movement of the cryostat body is limited by four support bars which are stretched radially from the support rails of the endcap calorimeter. When the QCS cryostat or the endcap calorimeter needs to be moved, the support bars are mechanically moved, and its connection to the cryostat is loosened. This allows the cryostats to slip off the support bars. When the cryostat is to be stationed in the operational location, the cryostat body is latched to the support bars.

To align the left and right QCS magnets, hair cross targets are installed on the

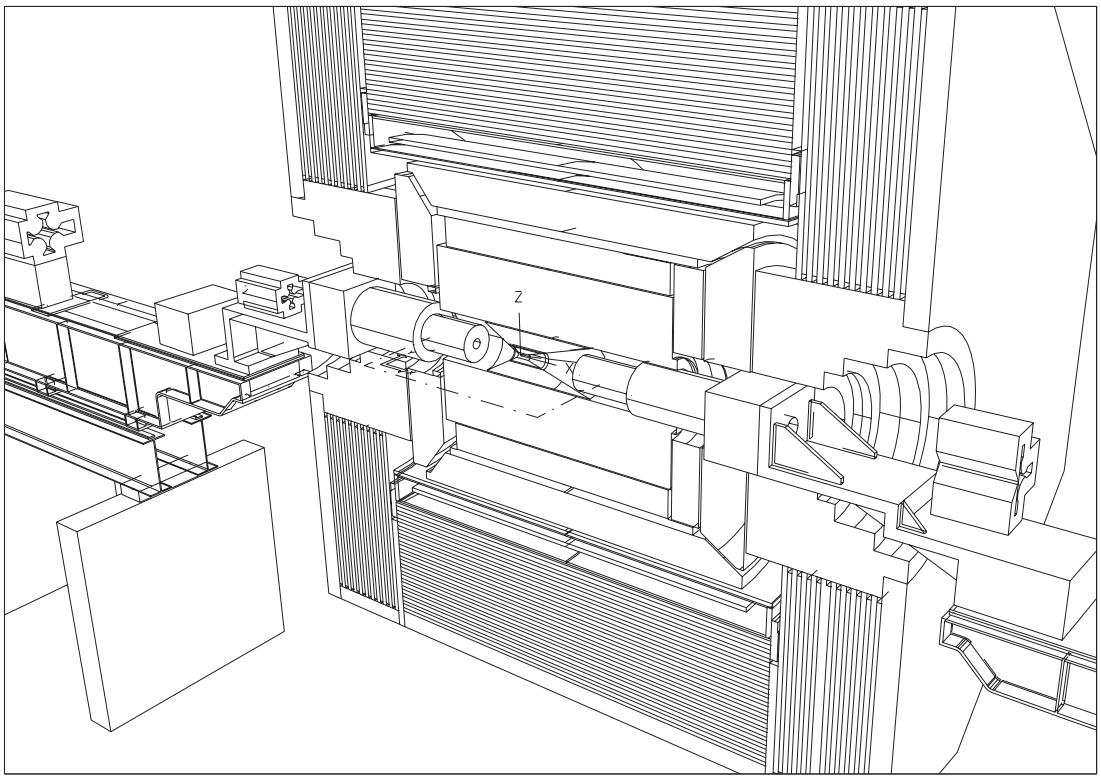

Figure 7.14: The QCS cryostats and other IR special magnets placed near the IP. A cut-away view of the detector facility is also shown.

surface of each QCS cryostat. The targets are grouped in two pairs, each of which determine the horizontal and vertical position of the cryostats. On each endplate of the central drift chamber, two quartz windows with a radius of ~ 7 mm will be installed. They will allow the surveyors to look through the left and the right pair of targets. This way, the pair of QCS magnets can be aligned within 0.1 mm. Then, the position of the QCS pair can be used as a reference to connect the beam lines on both sides of the detector.

The cryogenic transfer tubes, which deliver the superconducting power cables and liquid coolant from the outside connection boxes to the cryostat, will have an outer diameter of 26 cm. Its routing in the neighborhood of the crowded beamline near the IP has been studied. A workable solution has been found. Details concerning installation procedures for the entire beam line near the IP, including the cryostats, vacuum components and transfer tubes, are being worked out.

Magnets beyond QC2s will reside in the straight section tunnels next to the IR hall. Figure 7.15 shows a schematic plan view of the beam line near the IR hall.

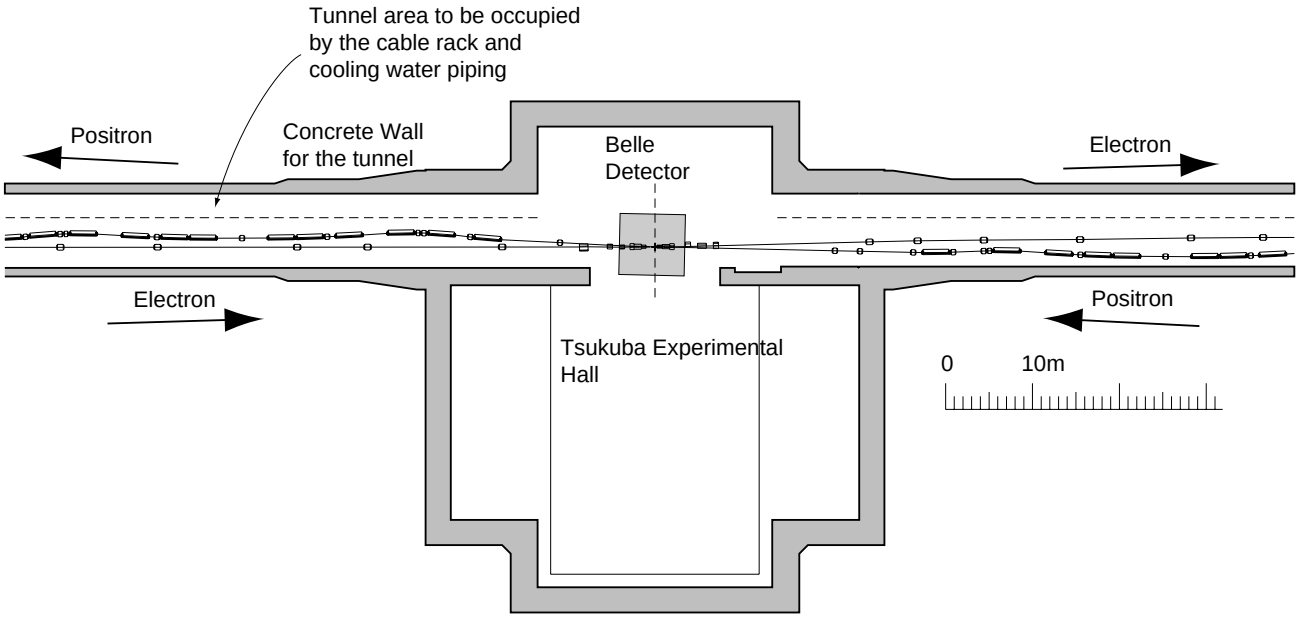

Figure 7.15: Schematic plan view of the beam line near the IR hall. The LER and HER beams collide at the interaction point within the detector facility, called "Belle." The concrete walls for the tunnels are included. The beam line components are not allowed to extend into the tunnel area that will be occupied by the cable rack and cooling water piping. The allowed boundary is indicated by broken lines.

7.7 Beam Background

7.7.1 General

Since a finite crossing angle scheme is adopted, and separation bend magnets will no longer be used, the conditions to consider the background issues have become much more relaxed than the past case which is described was the detector reference design in 1994 [1] [2]. Still, much detailed simulation work is required before freezing the final design of the masking system. This section briefly outlines the strategies used for handling synchrotron radiation (SR) and the particle background near the IP.

A high precision charged particle tracking device with silicon micro-strips will be installed, surrounding the IP. The requirement on the momentum resolution of the tracking system calls for using a cylindrical beam pipe with an inner diameter of 40 mm for $-80 < z < +80$ mm. This beam pipe will be made of a double-wall beryllium structure for efficient cooling with a minimum amount of material. At the edge of this beryllium central vacuum pipe, Mask-A will be implemented so that the Be pipe is shielded from back-scattered photons. The arrangement of the beryllium pipe and Mask-A are illustrated in Figure 7.16. Mask-A and vacuum chambers outside will be made of copper.

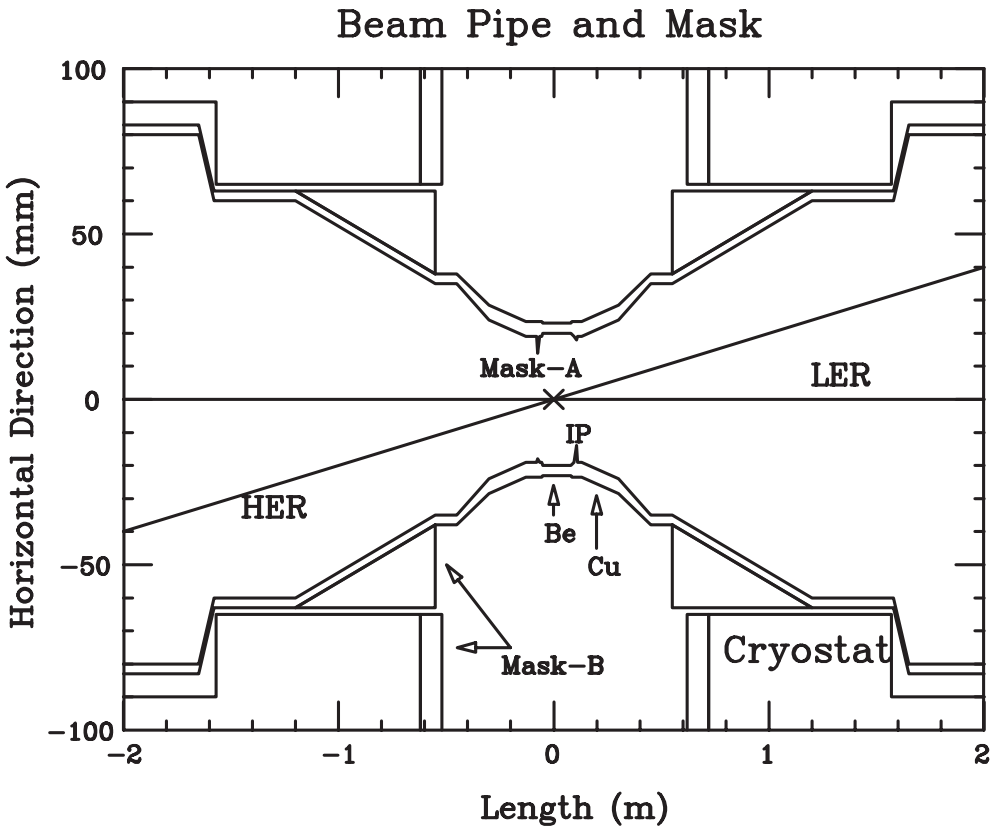

Figure 7.16: Arrangement of the central beam pipe at the IP and horizontal masks

7.7.2 Synchrotron radiation

The SR from bunch particles going through QCS and QC1 are required not to directly hit the Be pipe and Mask-A. The geometry of the magnet layout in the IR and their excitations have been chosen so that this requirement is satisfied. Calculations have shown that if the fractional particle population beyond $10\sigma_x$ and $30\sigma_y$ is kept below 10^{-5}, the SR background should have no significant harmful effects for data acquisition and analysis. Simulations of bunch tail development indicate that this condition will be met.

Some of the photons from upstream magnets QC2 and QC3 can hit Mask-A. Since those photons will have a critical energy below 2 keV, they can be easily absorbed by heavy metal. The masks and the inner surface of vacuum chambers will be gold-plated for this purpose. Photons from far upstream magnets away from the IP should be intercepted by movable masks installed just upstream of QC3. The design of these movable masks will soon be started.

7.7.3 Particle background

The particle background is, again, expected to be less severe than in the case of the past reference design. In the presence of separation bend magnets, the low-momentum charged particles could be easily swept into the detector. This is no longer the case with the finite-angle crossing scheme. However, the particle background can be potentially more serious than the SR background.

Calculations by the computer code Decay Turtle have been done. It has been found that the rate of spent particles from the two beams to directly hit the beam pipe between the two cryostats is 130 kHz, when the vacuum pressure is 10^{-9} torr. (This rate is a factor of three smaller than that for the past reference design.)

According to the simulation, the vacuum pressure outside QC2 is more important than that inside the detector, where the pumping speed is limited by the beam pipe aperture. The best efforts will be made to implement efficient pumping systems near QC2 magnets. The design goal for the vacuum level in the region outside QC2 is 10^{-10} torr.

Mask-B (shown in Figure 7.16) will be installed outside of the beam pipe to reduce the particle background. Movable masks should be installed in the arcs and the non-IR straight sections to clip the beam tails. They will help reduce the radiation level at the detector facility during the injection time. Detailed design work of these mask systems will start soon.

Bibliography

[1] The BELLE Collaboration, KEK Report 94-2, 1995. p. 58.

[2] BELLE Collaboration, Technical Design Report, KEK Report 95-1, 1995.

Chapter 8

RF System

In this chapter we describe the RF hardware components for KEKB. RF stations will be located in three straight sections, called Oho, Fuji, and Nikko (see, Figure 8.1). It has been recommended from simulations regarding the ring dynamic aperture that the RF cavities for the LER should be located at the Fuji straight section which is opposite to the Tsukuba interaction region. The RF stations for the HER will be located in the Oho and Nikko straight sections.

A block diagram of each RF unit for the ARES cavities is shown in Figure 8.2. A 508 MHz 1MW CW klystron will feed the power to two ARES normal-conducting cavities or one superconducting cavity. Best efforts will be made to use the existing infrastructures and facilities in the TRISTAN accelerator to minimize the construction cost. In particular, the existing klystrons, together with the power supply systems and the cooling systems for the klystrons, wave guide components, magic tees and circulators will be re-used in KEKB. In addition, a 6kW large refrigerator system, which has been operated for the superconducting cavities in TRISTAN, can be re-used.

Extensive R&D work is in progress on both the ARES and the superconducting cavity. Coupled-bunch instabilities arising from the accelerating mode and the higher order modes are expected to be sufficiently suppressed, as discussed in chapter 4.

In the following, detailed descriptions of the ARES and the superconducting cavity are given in section 8.1 and section 8.2, respectively. Section 8.3 treats the issues related to the RF low level system, including the effect of a bunch gap and the R&D work of an RF cavity feedback system. Section 8.4 discusses a crab cavity for the crab crossing, which will be implemented as a fall-back solution to the problems encountered with the finite angle crossing scheme.

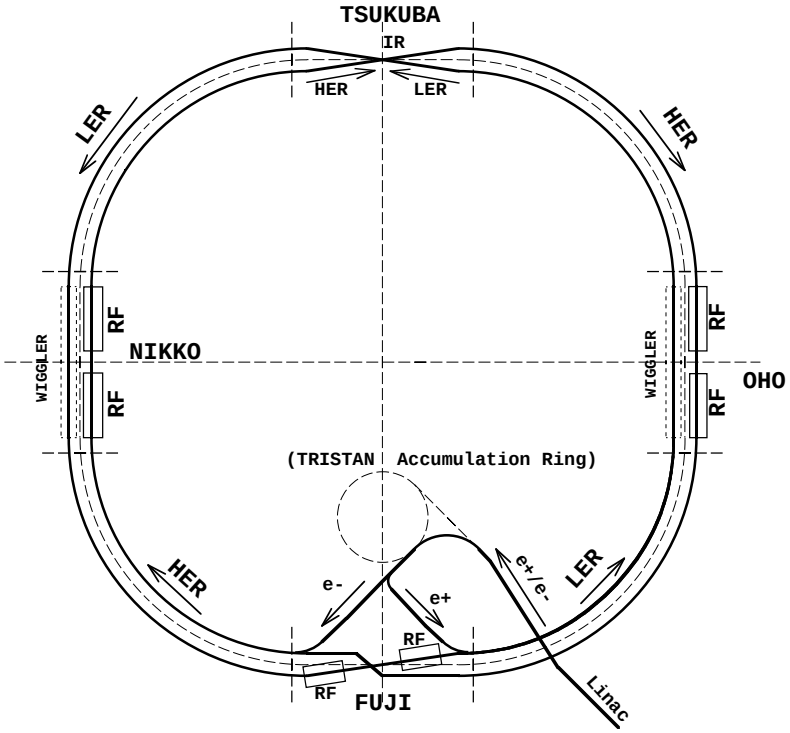

Figure 8.1: Schematic plan view layout of KEKB.

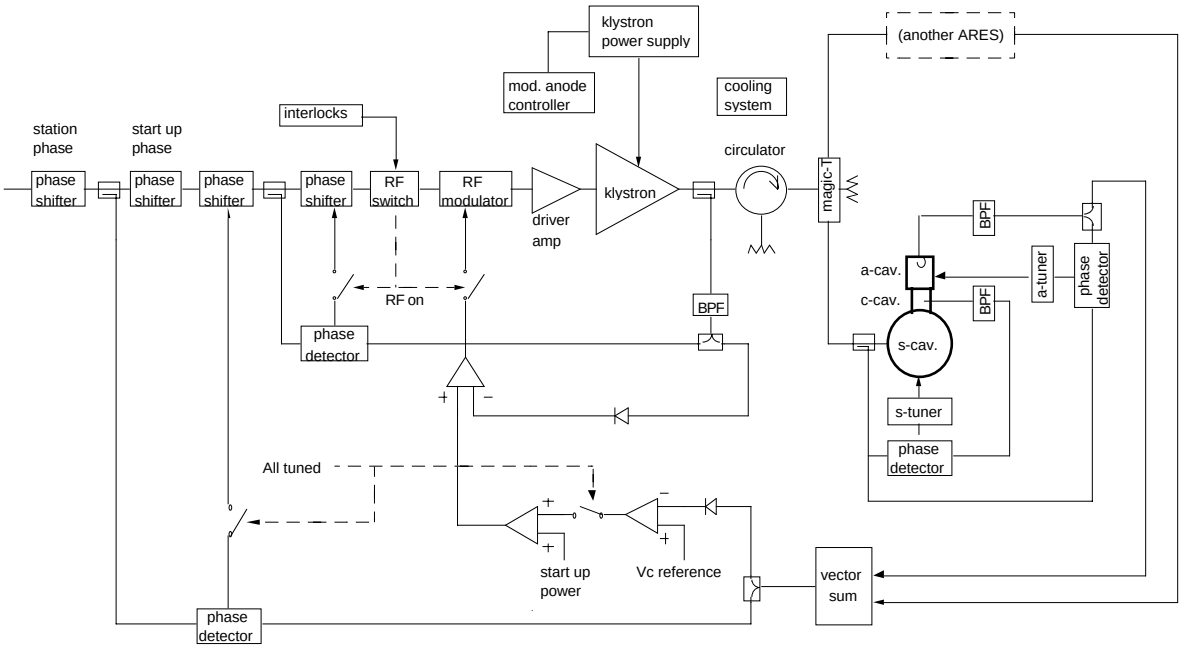

Figure 8.2: Block diagram of one RF unit with the ARES cavities.

8.1 Normal Conducting Cavity

8.1.1 ARES scheme

The accelerator resonantly coupled with an energy storage (ARES) [1] is expected to break through the difficulties concerning the coupled-bunch instabilities arising from the accelerating mode. As shown in Figure 8.3, it has an energy storage cavity coupled with an accelerating cavity via a coupling cavity. As discussed in chapter 4, owing to a large stored energy in the storage cavity, the detuning frequency is reduced and the instability is sufficiently suppressed.

The reason why the coupling cavity is implemented is explained in the following. The original scheme of employing an energy storage cavity was proposed by T. Shintake [2], where no coupling cavity is used. However, this scheme has a couple of problems. The first one is an instability arising from a parasitic mode which exists near the accelerating mode. When the accelerating cavity is coupled with the energy storage cavity, the accelerating mode splits into two eigenmodes. One is called the 0

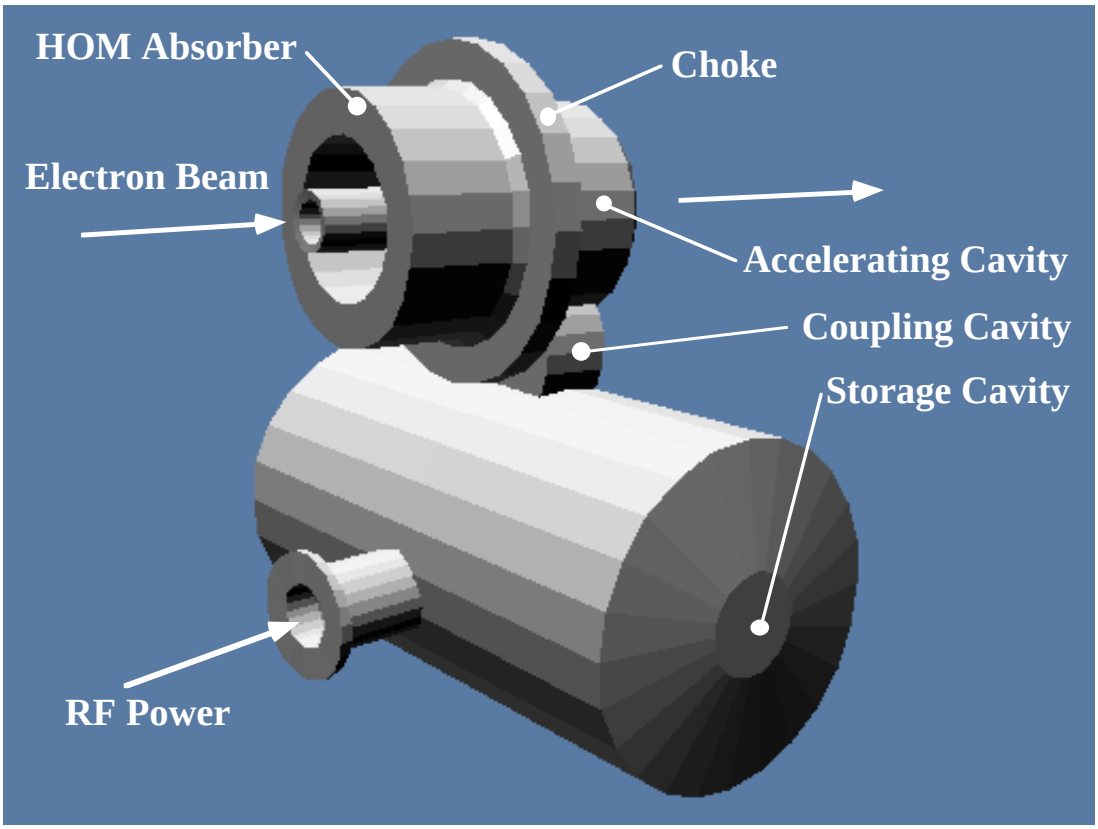

Figure 8.3: Schematic view of ARES.

mode, and the other the π mode, according to the phase difference between the two cavities. For example, the 0 mode becomes the parasitic mode when the π mode is employed for beam acceleration. The coupling impedance of the parasitic mode has the same order of magnitude as that of the accelerating mode. Therefore, the growth rate of the instability will be as large as that due to the accelerating mode of a conventional single-cell cavity. The second problem is that the field amplitude and phase of the π mode is unstable against heavy beam loading.

By employing a coupling cavity in the ARES, these difficulties in using an energy storage cavity can be successfully solved. Since the ARES has three resonators, the accelerating mode splits into three eigenmodes: the 0 mode, the $\pi/2$ mode, and the π mode. The ARES scheme has the following advantages over the former coupled-cavity system where an accelerating cavity is directly coupled with a storage cavity. First, the operating mode of the ARES is the $\pi/2$ mode, which has excellent field stability against the heavy beam loading. Second, the ratio of the stored energy in the storage cavity relative to that in the accelerating cavity can be adjusted by changing the relative strength of the coupling factor between the storage and coupling cavities vs. that between the accelerating and coupling cavities. Third, the $\pi/2$ mode has almost no field excitation in the coupling cavity. Therefore, the two parasitic modes (the 0 and π modes) can be selectively damped by installing a coupler in the coupling cavity, while the $\pi/2$ mode is not affected. Finally, the 0 and π modes are located nearly symmetrically with respect to the $\pi/2$ mode. Therefore, the contributions of the impedance of the damped parasitic modes to the instability are expected to be counter-balanced to some extent.

The basic design of the ARES was carried out on the basis of a three-dimensional analysis of the RF properties [3] by using the computer code MAFIA.

Storage Cavity

As the storage cavity, we chose a cylindrical cavity operating in the TE015 mode, which is the same mode employed in the SLED [4]. For an RF frequency of 509 MHz, the dimensions of the storage cavity are about 1100 mm in diameter and about 2000 mm in axial length. Assuming the standard value of copper conductivity, the Q value of the TE015 mode is estimated to be 2.6×10^5, which is sufficiently high to store a large amount of the field energy with a low wall power dissipation.

Since the storage cavity has many parasitic modes in the vicinity of the TE015 mode, the perturbation of opening a slot to the coupling cavity easily mixes parasitic modes into the TE015 mode. Mixing with a low-Q mode would deteriorate the high Q value of the operating mode. Therefore, careful fine tuning of the cavity dimensions

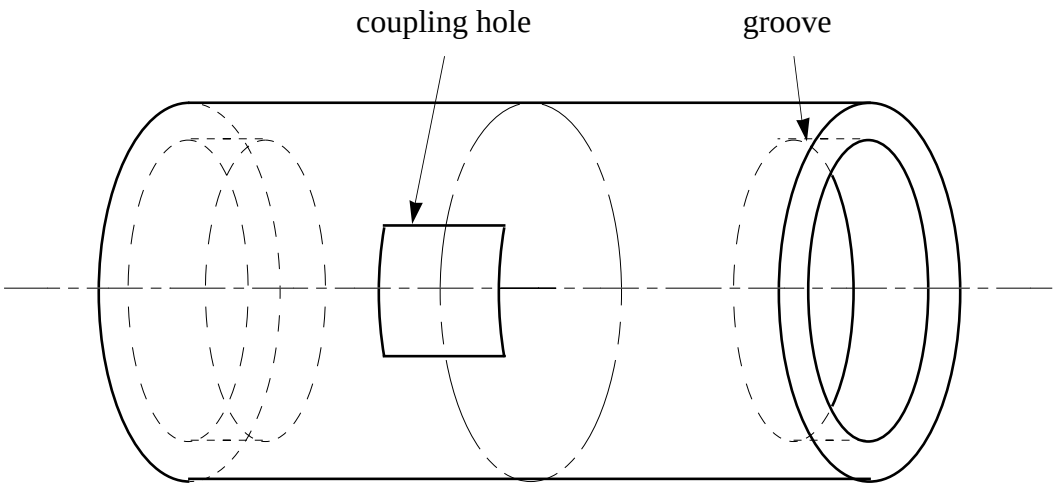

Figure 8.4: Schematic view of the storage cavity.

is required to prevent parasitic mode mixing.

Figure 8.4 shows a schematic drawing of the storage cavity with a coupling slot arranged to keep the mirror symmetry with respect to the mid-plane between the two end plates. The circumferences of both end plates are grooved in order to remove the degeneracy of the TE015 and TM115 modes. This method was first applied in the SLED cavities [4]. A groove depth of 80 mm gives a sufficient mode separation of 16 MHz.

According to a precise study [3] concerning the perturbative effect of the coupling slot, the TE015 mode should be kept away from the TEmnp(p=odd) and TMmnp($m >$ 0, p=odd) modes to minimize the parasitic mode mixing. Figure 8.5 shows a mode diagram of a cylindrical cavity without grooves at the end plates. The ratio of the radius to the axial length was carefully chosen to obtain the best location of the TE015 mode among the harmful parasitic modes. The frequency shift of each harmful parasitic mode due to the grooves must also be taken into account. For example, the frequency of the TM213 mode, which is close to the TE015 mode in the mode diagram, is actually lowered by 10 MHz due to the grooves.

Basic RF Design of the ARES

In the RF design of the ARES, we started with the most simple case, where a cylindrical accelerating cavity is coupled with the storage cavity via a cylindrical coupling cavity. Figure 8.6 shows a schematic view of the structure. The ratio of the axial length of the coupling cavity to that of the accelerating cavity was chosen to be just half.

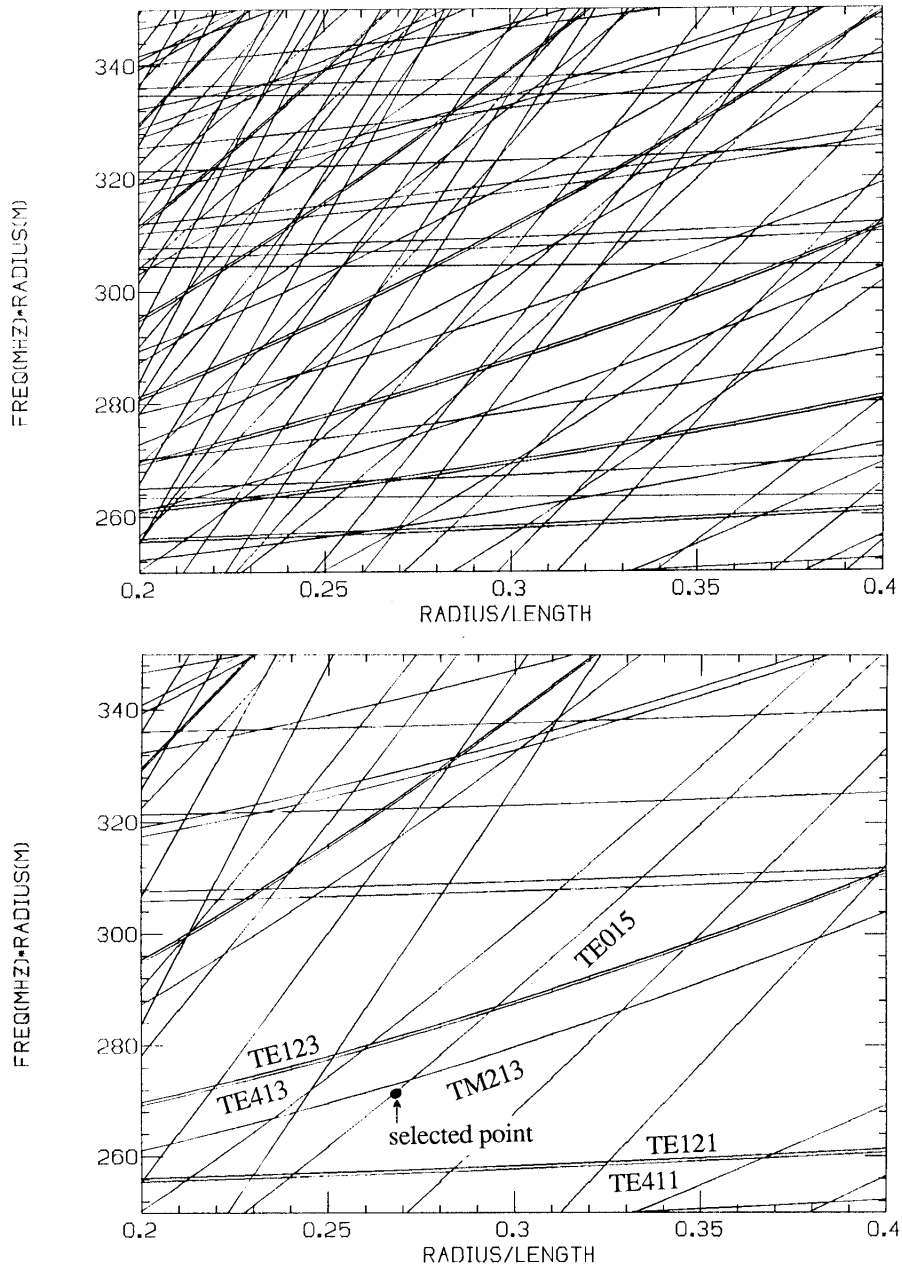

Figure 8.5: Mode diagram in a pillbox cavity. (upper) all TE and TM modes, and (lower) TEmnp (p=odd) and TMmnp ($m > 0$, p=odd) modes.

Iterative optimization of the structure is performed [3] using MAFIA until the following requirements are satisfied:

1. Each cavity should be tuned to the same frequency of 508 MHz under the $\pi/2$-mode boundary condition. This assures that almost no field is excited in the coupling cavity for the operating mode.

2. The stored energy in the storage cavity should be larger than that in the accelerating cavity by factor 10. This reduces the detuning frequency under beam loading by an order of magnitude.

3. The 0 and π modes should be nearly symmetrically located with respect to the $\pi/2$ mode. This assures counter-balancing the contributions of the 0- and π-mode impedance to the coupled-bunch instability.

Each cavity frequency was tuned by changing its radius. The ratio of stored energies was adjusted by changing the ratio of the coupling factor k_s between the storage and coupling cavities to k_a between the accelerating and coupling cavities.

The optimized dimensions of the ARES are listed in Table 8.1. The RF properties of the operating mode are listed in Table 8.2, together with those of the parasitic modes. Figure 8.7 shows the electromagnetic fields of the $\pi/2$ mode. As can be seen from the field pattern, the mixing of parasitic modes into the TE015 mode is successfully suppressed, and almost no field is excited in the coupling cavity. Most of the field energy is stored in the storage cavity in the form of the low-loss TE015 mode. The R/Q value of the total ARES system is reduced by an order of magnitude compared to that of a conventional single-cell copper cavity. This means that the required detuning frequency is also reduced by the same magnitude. On the other hand, the Q value of the system is increased by factor 5, compared to a copper cavity. Therefore, the shunt impedance of the ARES is kept at a reasonable level. According to the operating RF parameters discussed in chapter 4, the growth time of the instability due to the accelerating mode is longer than 30 ms (LER) and than 100 ms (HER), which is sufficiently long compared with the radiation damping time.

Figure 8.8 shows the field patterns of the parasitic modes in the vicinity of the operating mode, including the 0 mode at 501.7 MHz and the π mode at 512.8 MHz. Since the coupling cavity is excited for all parasitic modes, these can be damped by extracting the field energy through a coupler attached to the coupling cavity. The growth time of the instability due to the damped parasitic modes has been calculated [3] using the R/Q values in Table 8.2. Figure 8.9 shows the fastest growth time as a function of the loaded Q value. If the loaded Q values of the parasitic modes are

Table 8.1: Dimensions of the optimized shape.

cavities	accelerating	coupling	storage
radius (mm)	224.0	213.5	535.2
length (mm)	260.0	130.0	1989.4
coupling holes			
location	between a- and c-		between s- and c-
length (mm)	130.0		200.0
width (mm)	180.0		130.0
distance (mm)	0.0		0.0

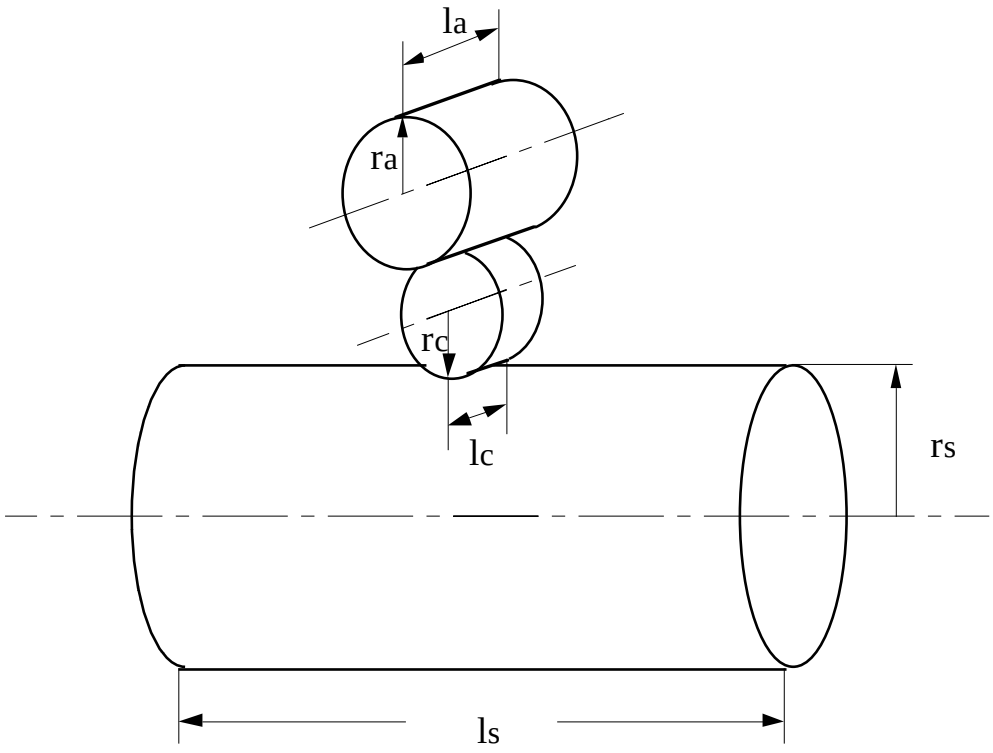

Figure 8.6: Schematic view of the three-cavity system.

Table 8.2: Properties of the optimized design.

operating mode (TE015, $\pi/2$)				
	frequency	(MHz)	508	
	$Q_{\rm total}$		1.8×10^5	
	$R/Q_{\rm total}$	(Ω)	13.9	
	ka		5.6 %	
	ks		1.0 %	
parasitic modes				
TEmnp (p=odd), TMmnp (m>0, p=odd)				
	frequency (MHz)	mode in s-cav.	$R/Q_{\rm total}$ (Ω)	
	474.0	TE411	0.12	
	479.5	TE121	0.04	
	491.2	TM115	0.02	
	499.1	TM213	0.75	
	501.7	TE413/TM213	105.	(0 mode)
	512.8	TE413	71.8	(π mode)
	518.3	TE315	1.04	
	521.0	TE413	16.4	
TEmnp (p=even), TMmnp (p=even)				
	472.3	TM212		
	473.4	TE116		
	475.0	TE314		
	492.0	TE412		
	497.2	TE122		
	516.4	TE216/TM214		
	537.3	TE216/TM214		
	537.7	TM116		
TM0np				
	484.3	TM016		
	501.0	TM022		
	522.4	TM023		

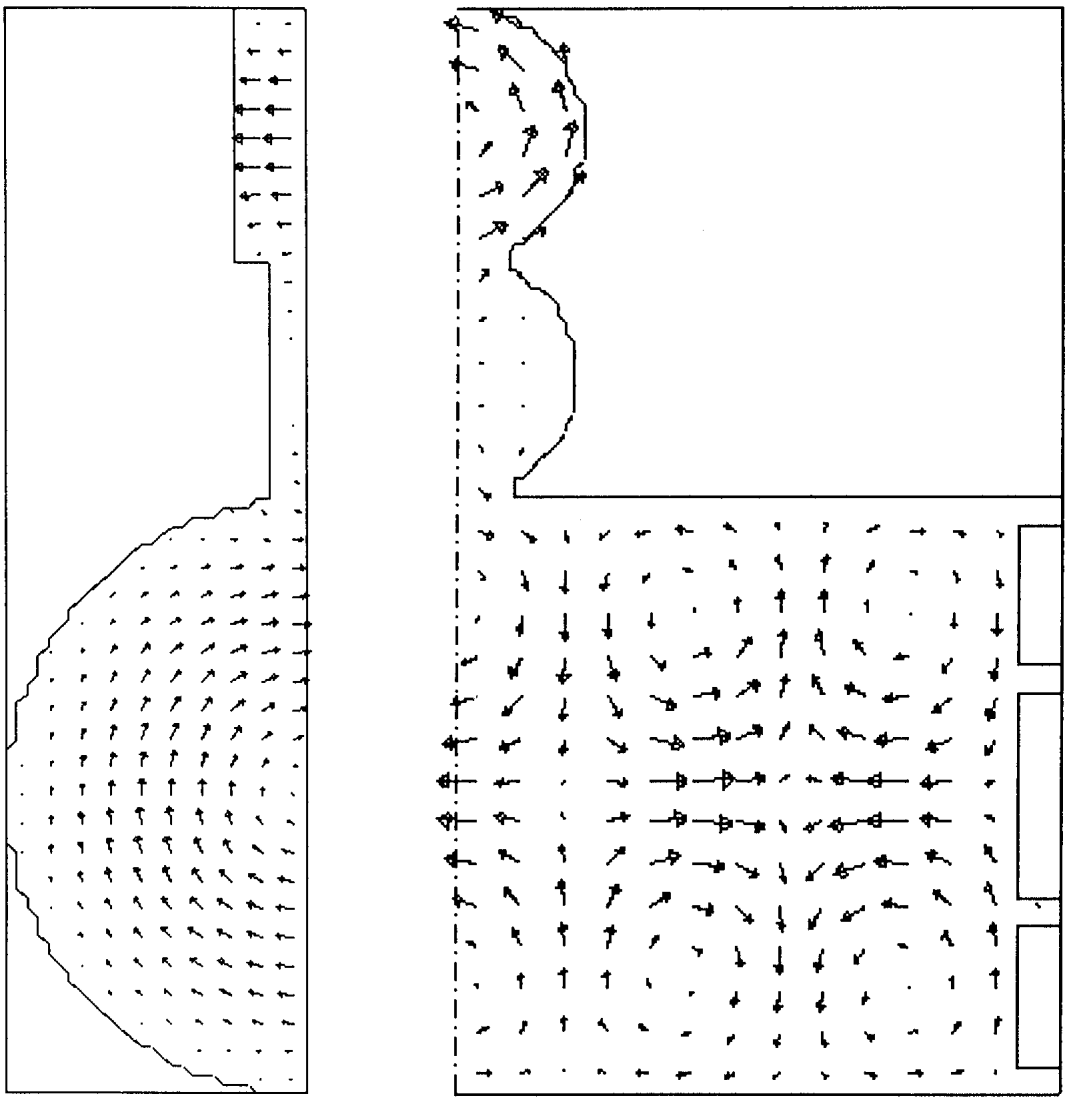

Figure 8.7: Field pattern of the $\pi/2$ mode calculated with the MAFIA code. The electric field (left) and the magnetic field (right) patterns are shown.

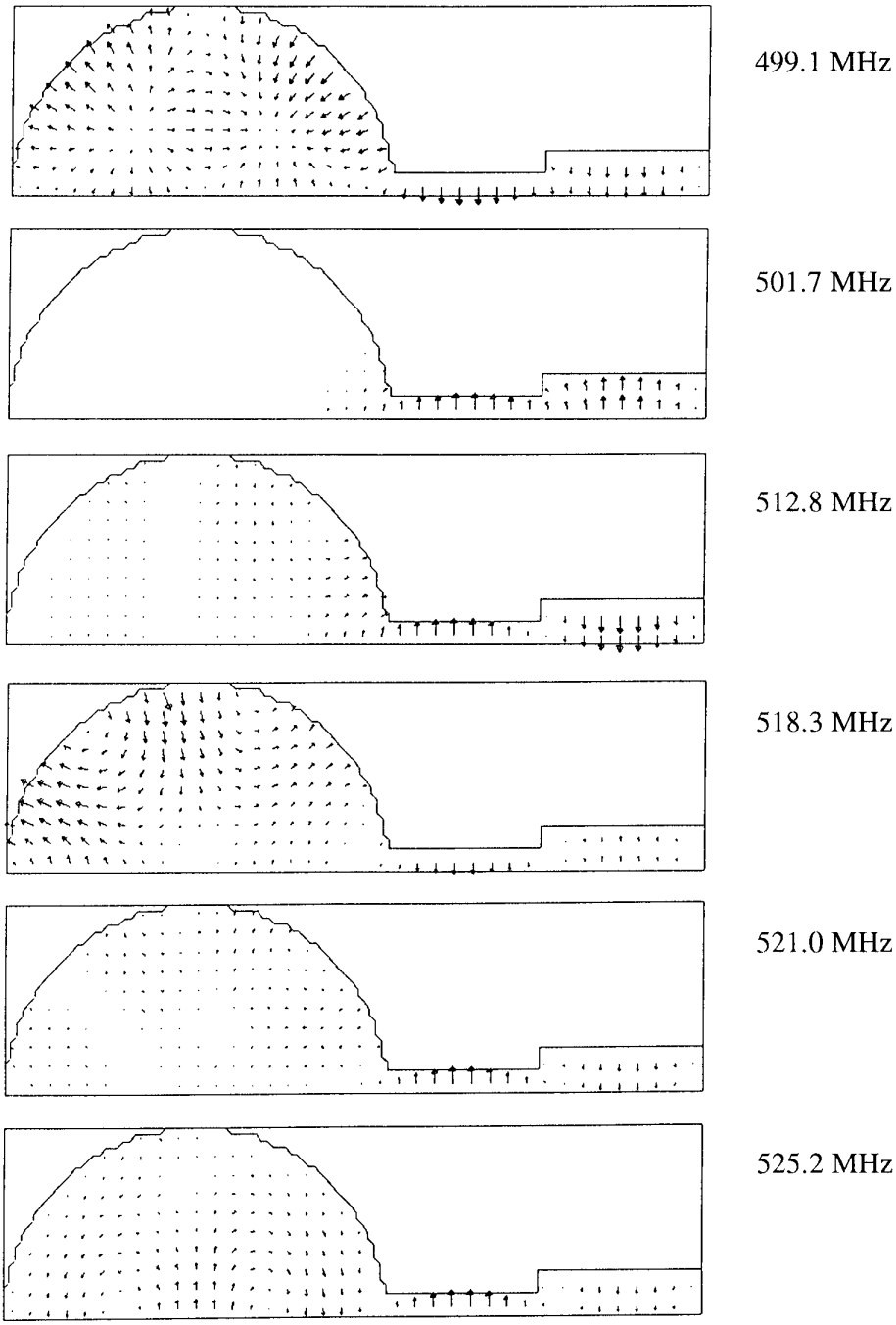

Figure 8.8: Field patterns of the parasitic modes, with frequencies close to the operating mode.

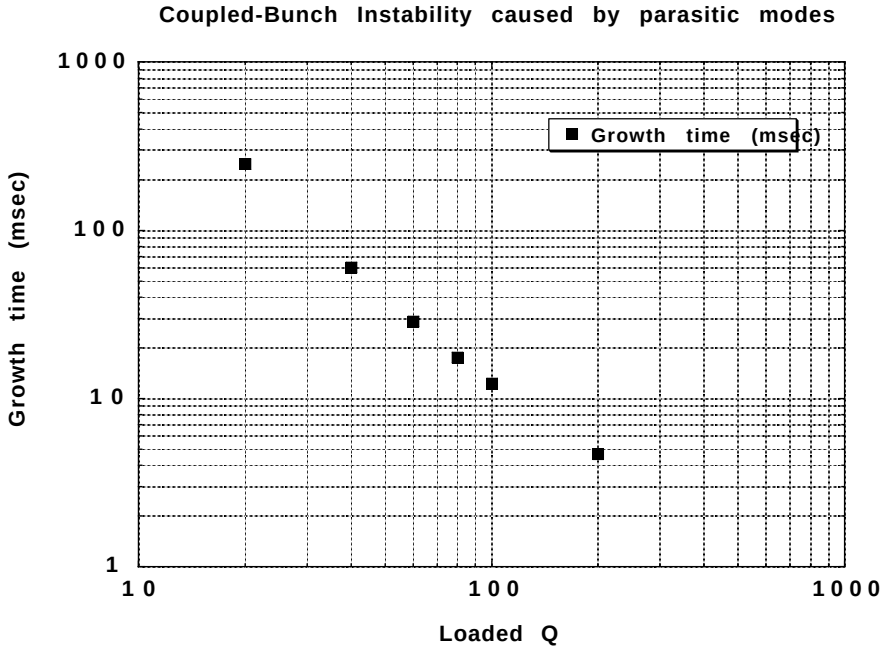

Figure 8.9: Fastest growth time of the coupled bunch instability caused by the parasitic modes plotted against the damped Q value.

reduced below 100, the instability growth time becomes longer than 10 ms, where the beam instability can be controlled by a feedback system.

Results of Cold Model Test

Two aluminum 1/5 scale cold models have been fabricated to confirm the design described above. They are equipped with two tuners for each of the accelerating, coupling and storage cavities. The resonant frequencies of the three cavities are adjusted by these tuners to coincide with each other. There is no damping structure on the coupling cavity of the first model. The measured Q value of the $\pi/2$ mode is 3.3×10^4, which corresponds to 1.40×10^5 for a full scale copper cavity. The effect of the surface finish on the Q value has been estimated by measuring the Q value of a pillbox cavity of the same material, same surface finish and same inner shape as the accelerating cavity of the cold model ("reference pillbox"). Taking this effect into account, the measured Q value of the $\pi/2$ mode is 0.85 times that calculated by MAFIA. The shift of the resonant frequency of the $\pi/2$ mode was measured by placing a small metallic

Table 8.3: Measured parameters of the 0 and π modes.

	f [MHz]	Q	R/Q [Ω]
0 mode	503.4	110	103
π mode	514.9	150	72

bead in the accelerating cavity to simulate the effect of detuning. The ratio of this frequency shift to the shift obtained by the same measurement for the reference pillbox was 0.069. This agrees well with the expected value 0.065. This means that R/Q of the accelerating mode is reduced by a factor of about 1/14, clearly showing that detuning of the ARES $\pi/2$ mode is greatly reduced.

The second cold model has two coaxial lines at the center of the end plates of the coupling cavity. The coupling cavity can be damped by connecting loads to these coaxial lines. The cavity surface around the inner conductor of a coaxial line protrudes into the cavity like a nose cone for concentrating the electric field and to stabilize the mode. The transmission between a beam port and an end plate of the storage cavity is shown in Figure 8.10: (a) the coupling cavity is not damped and (b) is damped. The measured Q, R/Q and frequency are listed in Table 8.3. Using the parameters in Table 8.3, the growth time of the longitudinal coupled bunch instability was calculated to be 17 ms for 20 ARESs in LER. We have also calculated the response of the growth

(a) (b)

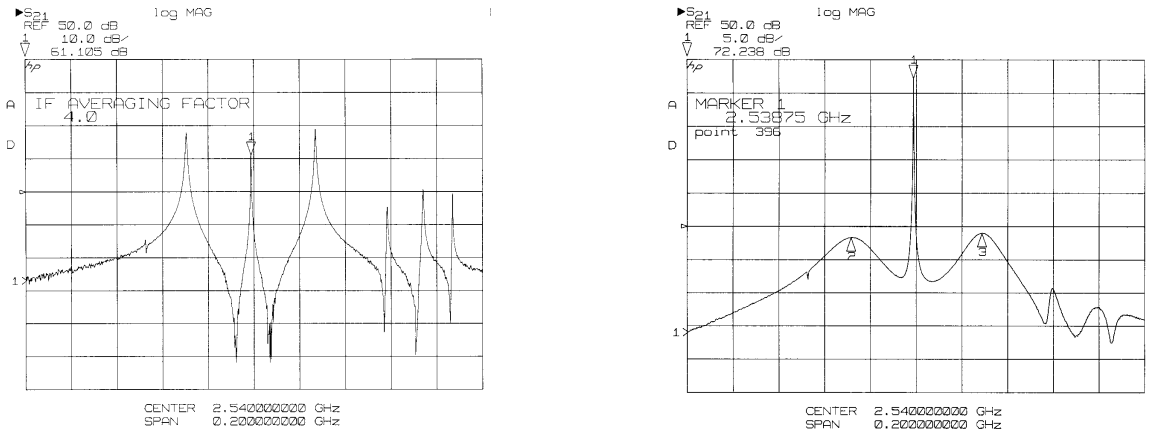

Figure 8.10: Transmission between beam ports: (a) coupling cavity is not damped and (b) is damped.

time to the skewness of the passband, which is defined as

$$\frac{|(f_\pi - f_{\frac{\pi}{2}}) - (f_{\frac{\pi}{2}} - f_0)|}{|f_\pi - f_0|}.$$

It has been found that the growth time decreases from 35 ms to 10 ms as the skewness increases from 0 to $\sim 10\%$.

Mechanical Design

The accelerating and coupling cavities are made of oxygen-free copper (OFC) to handle large power dissipation on the cavity wall. The water-cooling channels are milled out at the outer surface of the cavity. They are covered by copper plates by means of electron beam welding. Their configuration is carefully designed so that cooling water does not leak into the cavity if there should be an imperfection of brazing or welding at any connecting part. In the case of the storage cavity, the experience of the KEK APS cavities is fully utilized, since the wall loss density is not very high. Steel is used for the structural material, because it is of higher strength and is less expensive than copper. Copper is electroplated on its inner surface. The side cylinder is separated to form three parts at the nodes of the axial component of the magnetic field farthest from the center. This allows us to electroplate the structure in a moderately-sized vessel. Two end plates and three side cylinders are welded together. Welding deformation offers good electrical contact.

The accelerating and coupling cavities are joined by brazing. The coupling cavity is then bolted to the storage cavity. The two parts of ARES are transported from factory and installed at their position in the tunnel separately, where they are eventually bolted together. These procedures would be difficult if ARES is not detachable.

8.1.2 HOM-Damped Cavity

The HOM-damped accelerating cavity of the ARES is shown in Figure 8.11. The cavity has a HOM-damping coaxial waveguide which is equipped with a notch filter. Monopole and dipole HOM's excited in the cavity are coupled with the TEM and TE11 waves of the coaxial waveguide, respectively. On the other hand, the notch filter blocks the TEM wave coupled with the accelerating mode, while passing other waves of HOM's. RF waves passing through the filter are absorbed by microwave absorbers inserted from the waveguide end. This damping scheme was originally proposed independently for a crab cavity for B-factories [5] and for a damped structure for linear colliders (a radial line is used instead of the coaxial wave guide) [6]. As the absorbers, sixteen bullet-shape sintered SiC will be used.

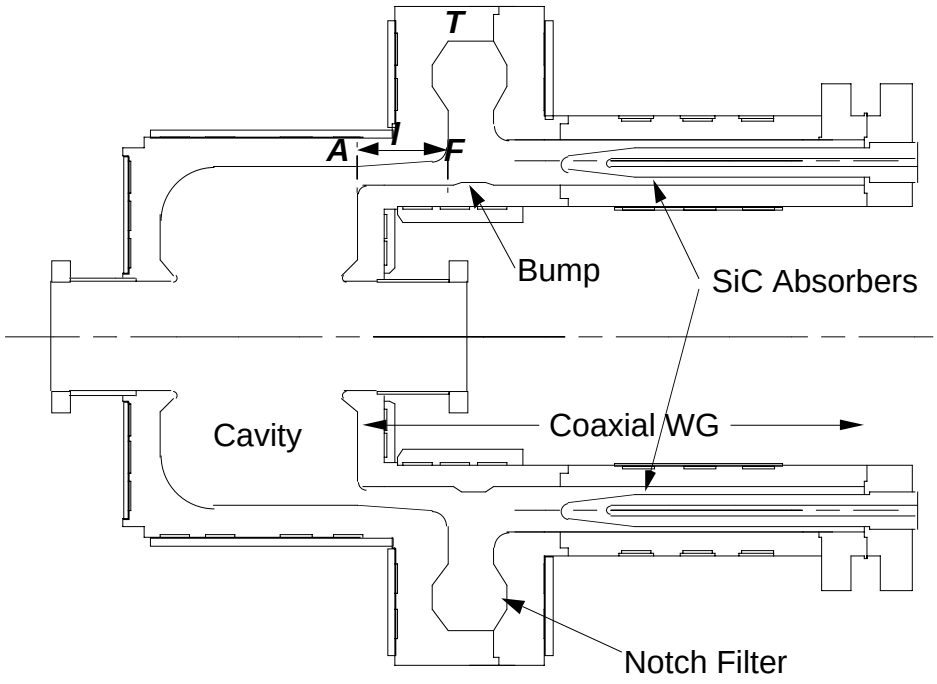

Figure 8.11: Schematic drawing of the KEKB HOM-damped cavity.

The cavity that is loaded with a coaxial waveguide is axially symmetric. This design has the following advantages:

- No concentration of wall currents of the accelerating mode assures good performance under high power operation.
- The main cavity parts can be precisely machined by using a turning lathe.
- Precise electromagnetic and thermal-structural analyses are possible by using only two-dimensional codes.

The first prototype to verify the performance in high power operation is under construction. A verification for high-current beam handling at the TRISTAN accumulation ring is scheduled in 1996.

Design

The gap dimensions of the notch filter and the coaxial waveguide have been carefully determined so as to avoid multipactoring discharges at the accelerating frequency. The S parameters of the notch filter have been calculated using the computer code HFSS (High Frequency Structure Simulator) [7]. Figure 8.12 shows the frequency responses

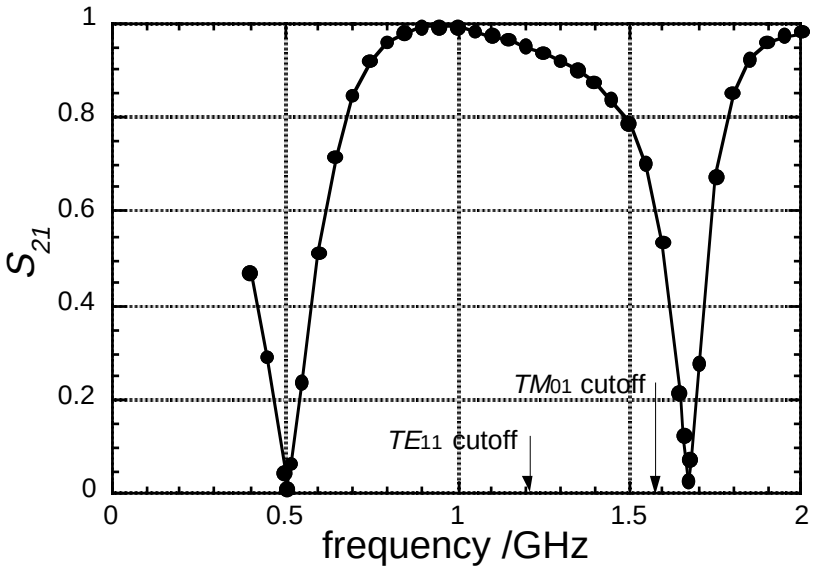

Figure 8.12: Frequency response of S_{21} of the notch filter.

of S_{21} (transmission) for TEM waves. The first stop frequency for TEM waves can be precisely tuned to the accelerating frequency 508.9 MHz by lathe-machining of the bump at the bottom of the filter structure. The TEM second stop frequency is raised to 1.67 GHz from 1.39 GHz by deforming the outer volume of the filter. The first and second stop frequencies for TE11 waves are 0.53 GHz and 1.68 GHz, respectively. Near the TEM and TE11 second stop frequencies, some HOM's may be trapped within the cavity. To avoid this problem, the beam bore diameter was increased to 145 mm. This lowers the TM01 and TE11 cutoff frequencies as indicated by the arrows in Figure 8.12.

RF Properties of the Accelerating Mode

The filter position along the waveguide affects the HOM-damping properties as well as the shunt impedance of the accelerating mode.

First, we examine the RF properties of the accelerating mode. Let us define the filter position along the waveguide by l, which is the distance between surfaces A and F, as shown in Figure 8.11. Let us also represent the stored energy and power dissipation in the cavity (the left side of surface A) by U_a and P_a, and those in the notch filter by U_f and P_f. Figure 8.13 shows the ratio P_f/P_a as a function of l, together with the response of the shunt impedance. They have been calculated using the program SUPERFISH. The notch filter functions as a quarter-wavelength resonator at the accelerating frequency. When the total electrical length from the waveguide aper-

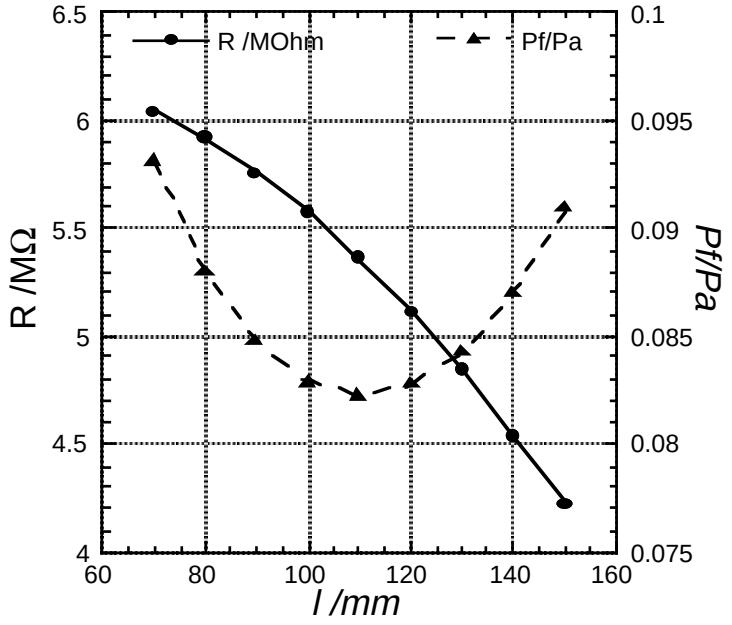

Figure 8.13: Ratio P_f/P_a and the shunt impedance are plotted as a function of l.

Table 8.4: RF parameters of the accelerating mode.

$f = 508.6\,\mathrm{MHz}$	$V_c = 0.6\,\mathrm{MV}$	$P_c = 70\,\mathrm{KW}^{(*)}$
$R/Q = 150\Omega$	$Q = 3.3 \times 10^{4(*)}$	$R = 5.0\,\mathrm{M}\Omega$

(*) a degradation of $\sim 5\%$ due to copper surface imperfections is taken into account.

ture (surface A) to the top end of the filter (surface T) is close to a half wavelength ($l = 110\,\mathrm{mm}$ in Figure 8.13), the electrically-short boundary at surface T is mapped onto surface A, and the ratio $U_f/U_a(also, P_f/P_a)$ becomes minimum. However, this is not a necessary condition in designing the choke mode cavity. For optimizing the efficiency of beam acceleration, a shorter coaxial waveguide between A and F is desirable. Figure 8.13 shows that the shunt impedance increases as l becomes smaller. The waveguide length l was determined to be 120 mm. This gives better HOM damping properties at little sacrifice of the shunt impedance of the accelerating mode. Table 8.4 is a set of cavity parameters for the case when $l = 120\,\mathrm{mm}$.

HOM Damping Properties

The distance l also changes the HOM damping properties of the choke mode cavity

Table 8.5: Ring parameters used in to calculate the growth time of the coupled bunch instability in Figure 8.14(b).

Parameters		
Beam Energy	3.5	GeV
Beam Current	2.6	A
RF Frequency	508.9	MHz
Number of Bunches	5120	
Momentum Compaction	1.5×10^{-4}	
Synchrotron Frequency	1.7	kHz
Number of Cavities	20	

(a) (b)

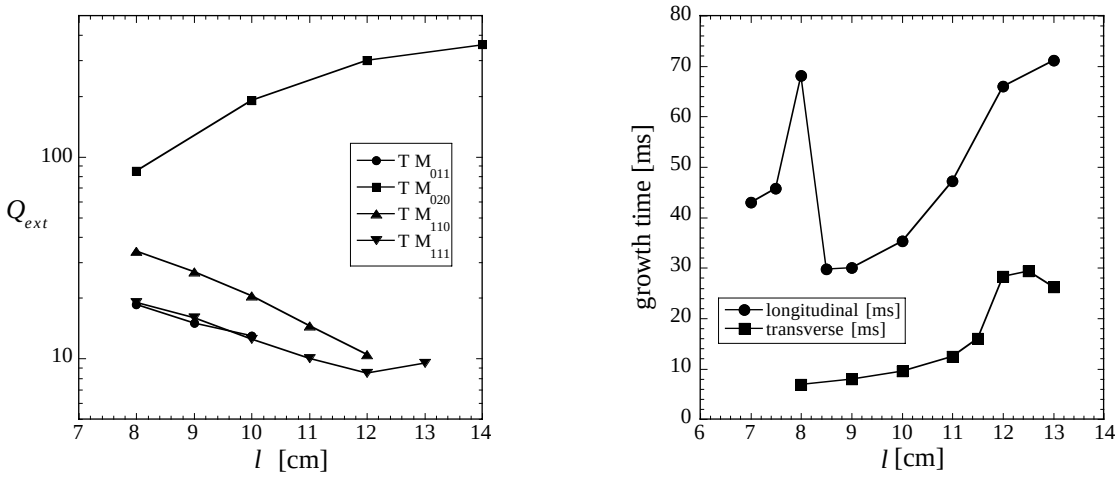

Figure 8.14: (a) Q_{ext} and (b) growth time of the coupled bunch instability as a function of the length between the cavity and notch filter l.

through Q_{ext}. Figure 8.14(a) shows the values of Q_{ext} as a function of l. The time domain method with MAFIA [8] was used in the calculation. For TM011 and TM110 modes, the time domain method was not applicable for larger l because of unwanted excitation of nearby modes in the calculation. The value of l around 12 cm provides a small Q_{ext} for the modes other than TM020. The TM020 mode needs not be damped like the TM011 mode, since R/Q of the TM020 mode is much smaller than that of the TM011 mode.

We also calculated the growth time of a coupled bunch instability as a function of l

Table 8.6: HOM impedance of the accelerating cavity of the ARES.

monopole			
f(MHz)	$R/Q(\Omega)$	Q_L	$(R/Q) \times Q_L$ (Ω)
76.2	17.4	71.5	1243
190	4.5	24.5	109
662.6	2.8	25.4	72.2
731.7	11.0	35.7	394
821.8	7.9	22.7	180
925.2	3.8	16.6	62.4
1331.9	3.2	28.7	90.7
1389.5	3.1	27.8	86.4
dipole			
f(MHz)	R/Q (Ω/m)	Q_L	$(R/Q) \times Q_L$ $(k\Omega/m)$
275.4	50.7	63.4	3.21
670.0	16.6	37.1	0.62
766.2	167	50.9	8.51
826.7	113	30.4	3.43
905.8	109	20.5	2.23
986.8	210	23.2	4.85
1067.5	68.1	10.4	0.70

by using the formulae of Sacherer [9]. The modes which are trapped in the notch filter or coaxial line have to be taken into account. The eigenmodes were calculated with the MAFIA 2D eigenmode solver. As an approximation, the absorbers were modelled by an axially symmetric structure. The permittivity was assumed to be 7, which is about half the measured value of some sample blocks of SiC [10]. This is to compensate for the packing factor of the bullet-shaped SiC. The Q value and shunt impedance have been calculated in the MAFIA postprocessor assuming that $\tan\delta$ of the absorber was 0.3. Then, the calculated frequencies, impedance and Q values were substituted in the formulae of Sacherer with the ring parameters shown in Table 8.5. The results are plotted in Figure 8.14(b). It shows that $l = 12 \sim 13\,\mathrm{cm}$ is a good choice for l. This is consistent with the time domain Q_{ext} calculation. The growth time will be then $\sim 70\,\mathrm{ms}$ for the longitudinal instability and $\sim 30\,\mathrm{ms}$ for the transverse. The R/Q and Q values with this design are summarized in Table 8.6. However, we must be careful

about this value, because the Q calculation in the MAFIA postprocessor is based on the eigenmode that assumes no loss in the absorber.

Mechanical Design

The cavity parts, whose inner surfaces must withstand the heat due to wall currents of the accelerating mode, are made of oxygen-free copper (OFC). The coaxial waveguide parts are made of stainless steel to reinforce the entire cavity structure. Vacuum furnace brazing and electron-beam welding techniques are employed to assemble the parts. For the prototype cavity at 70-kW wall dissipation, thermal and thermal-stress analyses have been carried out using the finite element analysis program ANSYS. Figure 8.15 shows the temperature contour over the model based on the thermal analysis. The boundary conditions are as follows: on the surfaces of the cooling-water channels, the temperature is fixed at 30 °C. The outside surfaces of the cavity are thermally insulated to the air.

In Figure 8.15, there are two points with the maximum temperature rise: one is at the tip of the right nosecone; the other around the corner of the waveguide aperture. A maximum temperature rise less than 30 °C is acceptable. Therefore, the prototype cavity will be capable of stable continuous operation at the design value of the wall dissipation.

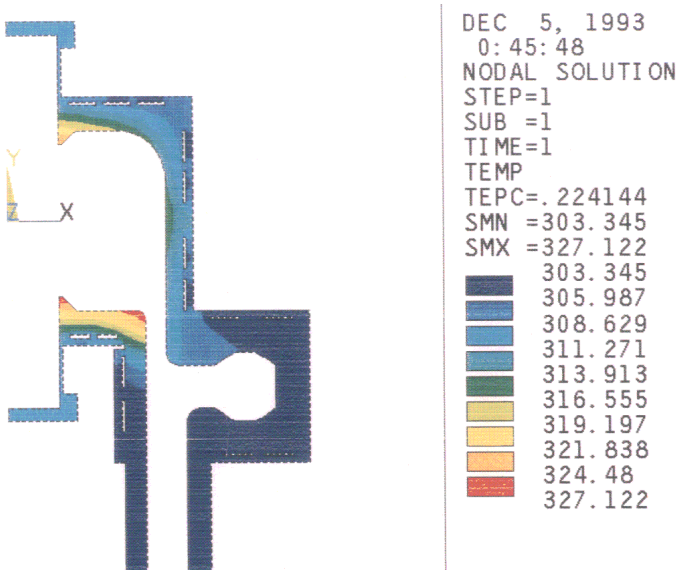

Figure 8.15: Temperature contour over the model resulting from the thermal analysis.

8.1.3 HOM Absorber

For HOM absorption, sixteen bullet-shape sintered SiC (silicon carbide) ceramics are inserted from the end of the coaxial waveguide, as shown in Figure 8.11. The absorber is 40 mm in diameter and 400 mm in total effective length, including a 100 mm nose-cone section. Each SiC absorber is directly cooled by cooling water through a water channel that is bored inside. The HOM power to be handled will be on an order of $\sim 10\,\mathrm{kW}$ per cavity, leading to ~ 1 kW per absorber. Figure 8.16 shows the frequency responses of the dielectric constant ϵ' and the loss tangent $\tan\delta$, which have been measured using a dielectric probe kit (HP85070B). The reasons for choosing SiC ceramics are as follows:

- SiC is a fine and dense ceramic material which has high mechanical strength, a low outgassing rate, and is chemically inert.
- SiC has a relatively high thermal conductivity of $\sim 120\,\mathrm{W/mK}$ at room temperature, which is about one half that of aluminum (230 W/mK).

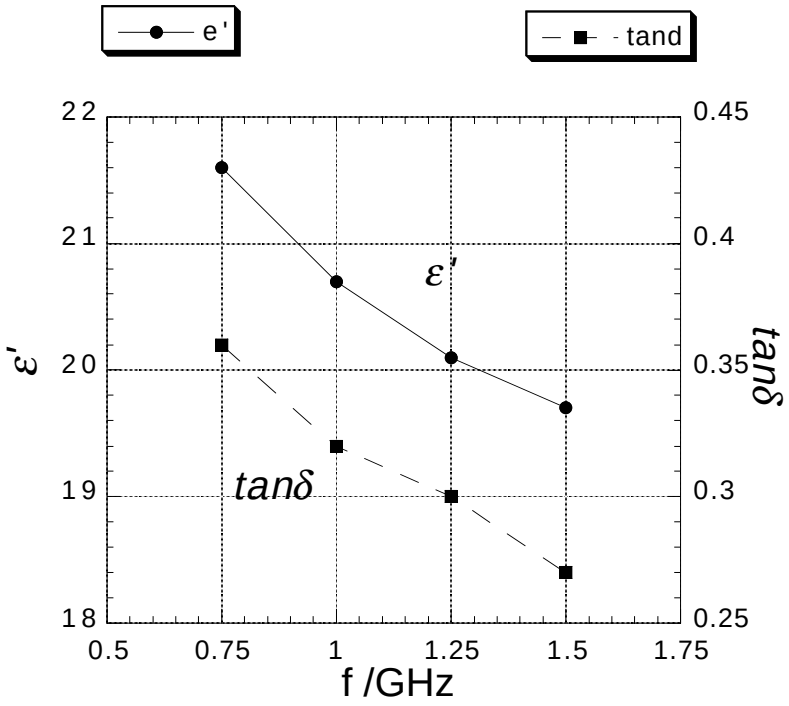

Figure 8.16: Dielectric constant and loss tangent of the SiC ceramics are plotted as a function of the frequency.

- At the 2.5-GeV electron linac of KEK, nearly two hundred SiC absorbers (diameter = 24 mm, length = 300 mm) have been used for the S-band waveguide loads without any trouble for about ten years. A prototype of the S-band SiC absorber has been tested up to a peak power of 10 MW with a pulse width of 3.5 μsec at 50Hz, corresponding to an average power of 1.75 kW [11].

Among these reasons, the third one encouraged us most to use SiC ceramics. A prototype of the SiC absorber for the KEKB cavity was fabricated to verify its performance in a vacuum environment. Figure 8.17 shows the layout of the high power test. The prototype absorber was inserted from the end of an L-band rectangular waveguide (WR650), where the standing-wave ratio VSWR was measured to be ~ 1.1. A metal O-ring was used for the vacuum seal between the SiC ceramics and the SUS flange. The vacuum pressure was about $10^{-9} \sim 10^{-8}$ Torr. The high power test was carried out using a pulsed klystron ($f = 1296$ MHz) up to a peak power of 105 kW with a pulse width 538 μsec at 50 Hz, which corresponds to a average power of $\sim$2.8 kW. The prototype SiC absorber functioned normally without any vacuum, thermal, or discharge problems. The outgass rate of the SiC ceramics was also measured using a cylindrical sample (diameter = 50 mm, height = 50 mm). After baking for 24 hours at 150°C, the outgass rate at room temperature was 3×10^{-12} Torr$\cdot l$/s$\cdot$cm^2.

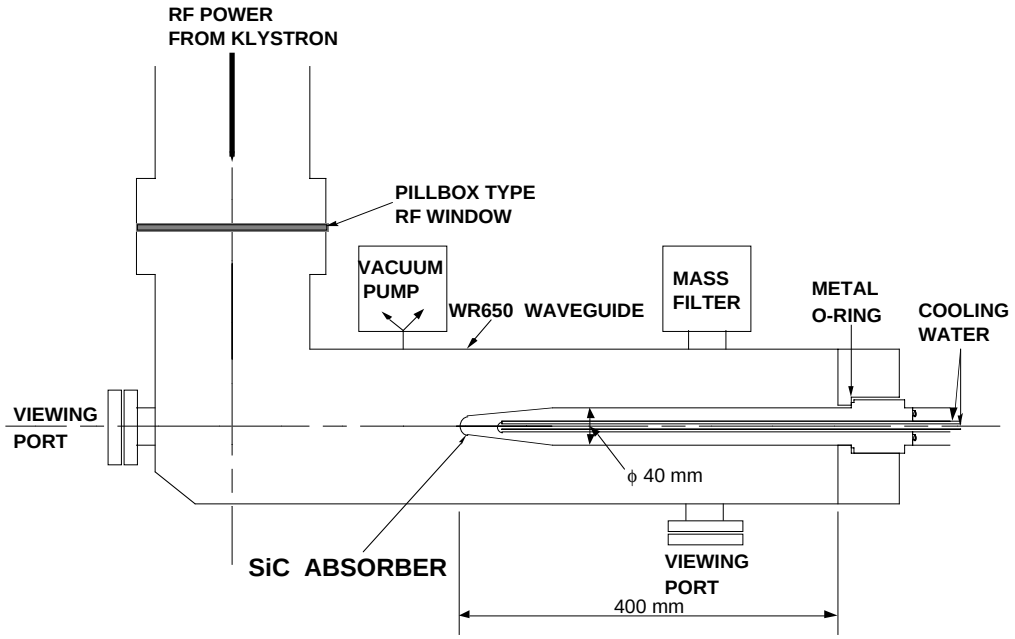

Figure 8.17: Layout of the high power test.

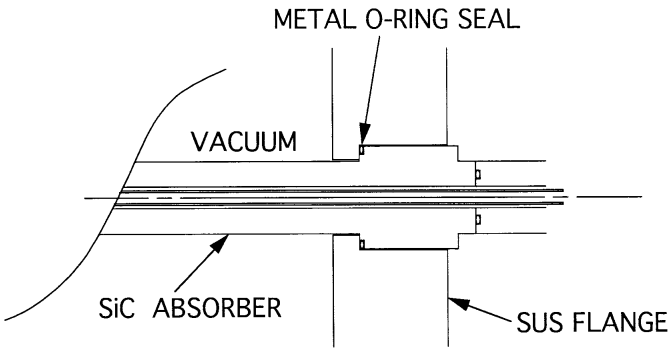

Figure 8.18: Prototype of the SiC absorber using a metal O-ring for vacuum sealing.

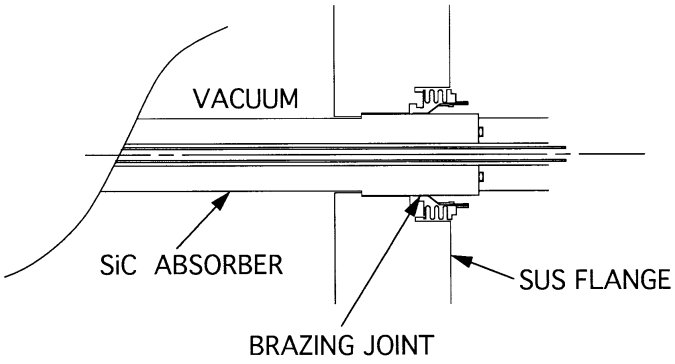

Figure 8.19: Next prototype of the SiC absorber using a brazing joint. The SiC ceramics is directly brazed to the copper sleeve.

For the second prototype cavity, we are planning to braze a thin copper sleeve to an SiC ceramic absorber for vacuum tightness. Figures 8.18 and 8.19 show an SiC absorber structure that uses a metal O-ring seal and another that uses a brazing joint, respectively. For both structures, a series of heat-cycle tests will be carried out, which simulates the baking processes, in order to study the reliability of the vacuum tightness during long term operation.

8.1.4 Input Coupler

Requirements

The most important parameters for the coupler are the transmitted RF power and its frequency. At the present stage the cavity for KEKB requires $\sim$ 400 kW (CW) RF power at 508.9 MHz. In order to maintain stable operation at $\sim$ 400 kW, the coupler is required to be able to transmit the RF power that is much larger than $\sim$ 400 kW. We have thus set the target value of the transmitted RF power to be $\sim$ 800 kW (CW) that is twice the required power.

The requirements for the mechanical structures are as follows:

1. The RF power is fed from a klystron through the WR1500 rectangular waveguide.
2. The coupler couples with the cavity by a loop (magnetic) coupling.
3. The size of the coupler port of the cavity is designed for the WX77D coaxial waveguide.
4. The ceramic window must be shielded from the beam and the cavity surface. This is to reduce direct irradiation by the x-rays and charged particles produced by collisions between the beam, field-emitted electrons, sputtered ions and residual gases and to avoid the adsorption of Cu evaporated from the cavity wall.
5. The coupler matches the APS cavity in TRISTAN, because the coupler of the APS will be used for the first beam test of the cavity.

The coupler has several transitions. Every transition is designed so that the its VSWR is less than 1.05 and that of the coupler assembled with the transitions is less than 1.1 at 509 MHz.

Design Status

The design of the input coupler is based on the structure of the output coupler of the UHF klystron for TRISTAN. The first design for the RF structure was completed by using the computer simulation code HFSS. The mechanical design is in progress. The RF properties of the coupler will be measured by a low-power model so as to confirm the simulated results. A high-power test for the coupler is planned for the summer os 1995 with an RF power up to 800 kW (CW).

Choice of Window Structure

Many problems with the coupler are related to multipactoring on the window. Several experiments and analyses of the ceramic window in couplers suggest the following [12, 13]: the uniformity of the electric field distribution around the window is very important for preventing the local heating of the ceramic induced by multipactor; the multipactor induced by an electric field that is perpendicular to the window causes the damage on the surface, while the multipactor induced by the parallel field causes no serious problem.

Two types of ceramic windows are in use for the coupler at KEK. One is a cylindrical-type ceramic window that has been used in the APS cavity. It was tested at up to 300 kW (CW) RF-power [14]. The other is a disk-type ceramic window that has been adopted for the UHF (508 MHz) klystron. It transmits 1.2 MW (CW) RF-power [12]. Since our target value for the transmitted RF-power is 1MW (CW), we chose the disk-type ceramic as the window for the coupler.

The disk-type ceramic window is contained in a coaxial waveguide. The waveguide near the window has an impedance matching section, because the permittivity of ceramic is about nine.

One of the typical matching sections is a choke-type structure. The output coupler of the klystron and the input coupler of the superconducting cavity (SCC) of the TRISTAN have the choke structure. (Recently a high-power test of the SCC coupler was successfully performed up to an RF power of 800 kW (CW) [15].)

An over- and under-cutting (OUC) is another structure for the matching section. This structure is in use for the couplers of the high-power models of the RFQ [16] linac and DTL [17, 18] for the Japanese Hadron Project (JHP). For the RFQ the coupler transmits an RF pulse that is 300 kW peak, with 300 μsec duration at 50 Hz. The transmitted RF pulse for the DTL coupler is 150 kW peak, with 600 μsec duration at 50 Hz.

Two types of couplers with choke or OUC structures will be made for the high-power test.

Design

The coupler consists of three transition sections:

1. The door-knob transition between the WX152D coaxial wave guide and the WR1500 rectangular wave guide;

2. The disk-type ceramic window in the WX152D waveguide;

3. The transformer between the coaxial wave guide of the WX77D and that of the WX152D.

The door-knob transition with a capacitive iris has a wider band width. A schematic view of the transition is shown in Figure 8.20. The calculated VSWR is shown in Figure 8.21.

The choke and OUC structures of the window are shown in Figures 8.22 and 8.23. Both figures include the transition from the WX152D coaxial waveguide to the WX77D coaxial waveguide. The waveguide has bumps for window shields. The VSWRs of the transitions with the window are plotted in Figure 8.24. Figure 8.25 shows the radial dependence of the electric field strength at a location 1 mm away from the window surface. The value of the ordinate is normalized to the field strength on the surface of the inner cylinder of the WX152D coaxial waveguide. This plot shows: (1) that the uniformity of the field strength of the OUC structure is better than that of the choke-type structure; (2) that the electric field strength of the choke-type structure is about 70% of the OUC structure near the inner triple junction of the window. Figures 8.26 and 8.27 show the electric field lines when the maximum electric field is at the center of the ceramic. These show that the direction of the electric field is almost parallel to the window for the OUC structure, while for the choke structure the lines concentrate in the tip of the choke.

The window is $5/8\lambda$ away from the detuned short plane (DSP). The DSP of the coupler is located about 55 mm inside the cavity wall.

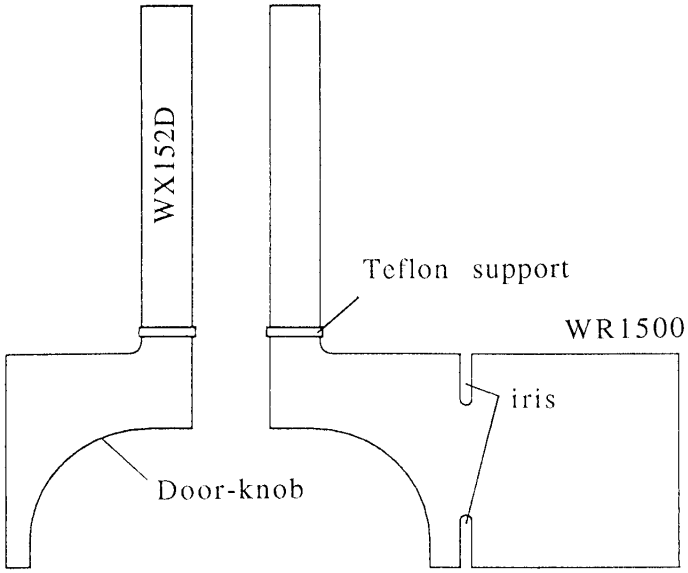

Figure 8.20: Schematic view of the door-knob transition.

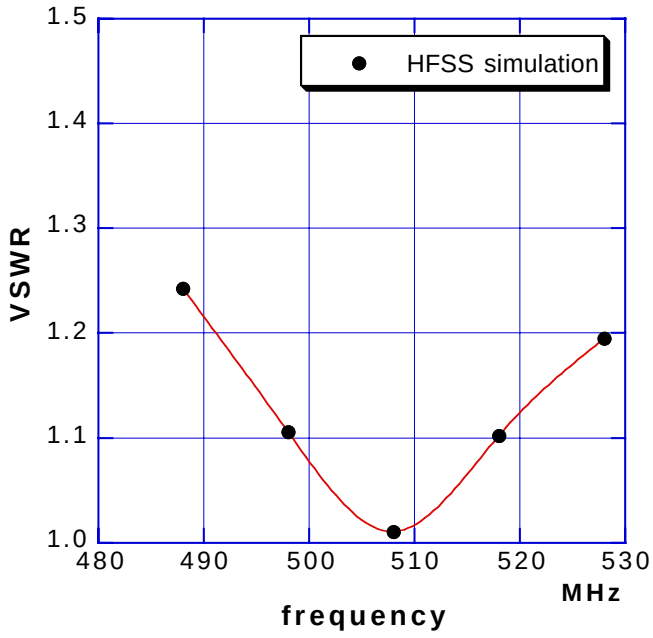

Figure 8.21: Calculated VSWR of the door-knob transition.

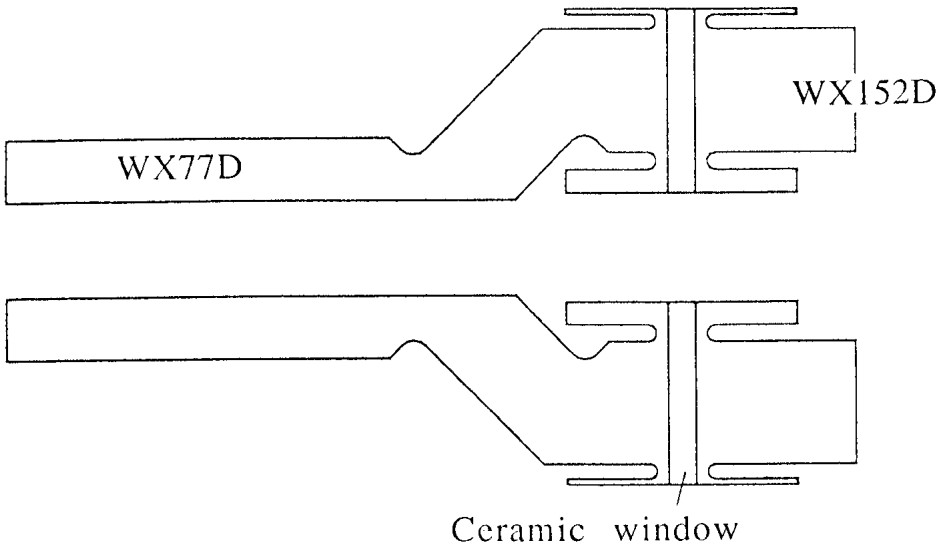

Figure 8.22: Choke structure of the ceramic window with the transition between the coaxial waveguides.

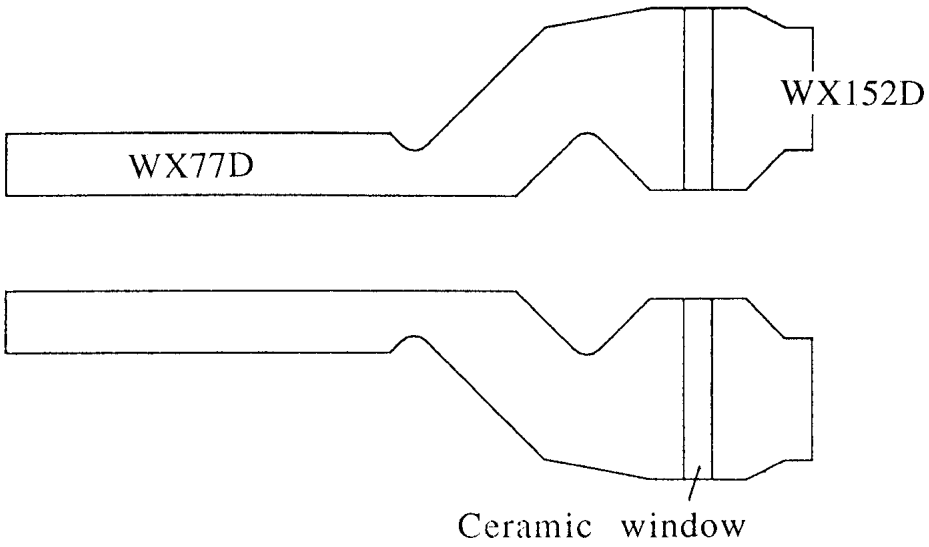

Figure 8.23: Over- and under-cut (OUC) structure of the ceramic window with the transition between the coaxial waveguides.

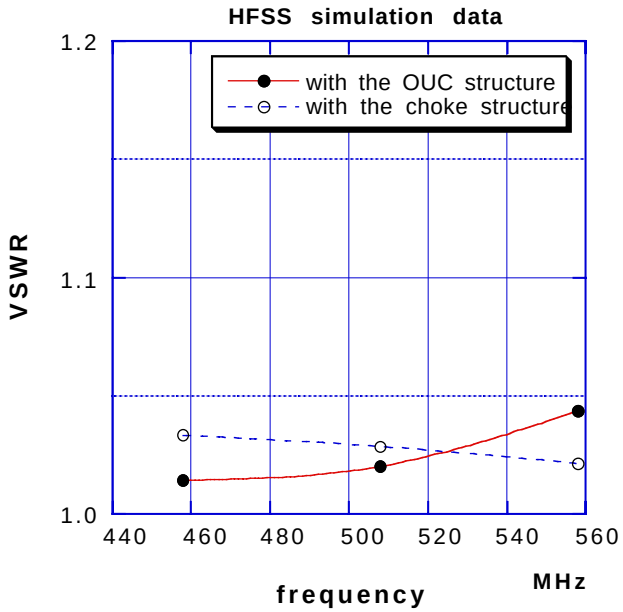

Figure 8.24: Calculated VSWR of the choke and OUC structures with the transition between the coaxial waveguides.

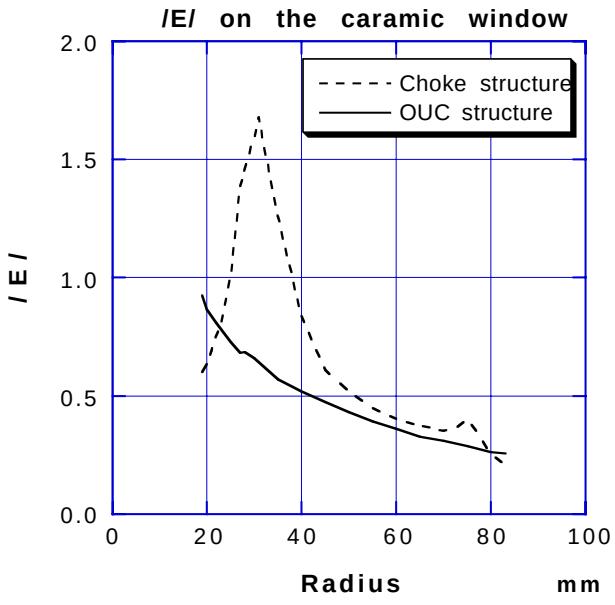

Figure 8.25: Asolute strength of the electric field. (Simulation) The abscissa is the radial direction of the window. See the text for the unit of the ordinate. The solid line is the OUC structure data and the dotted one is the data of the choke structure.

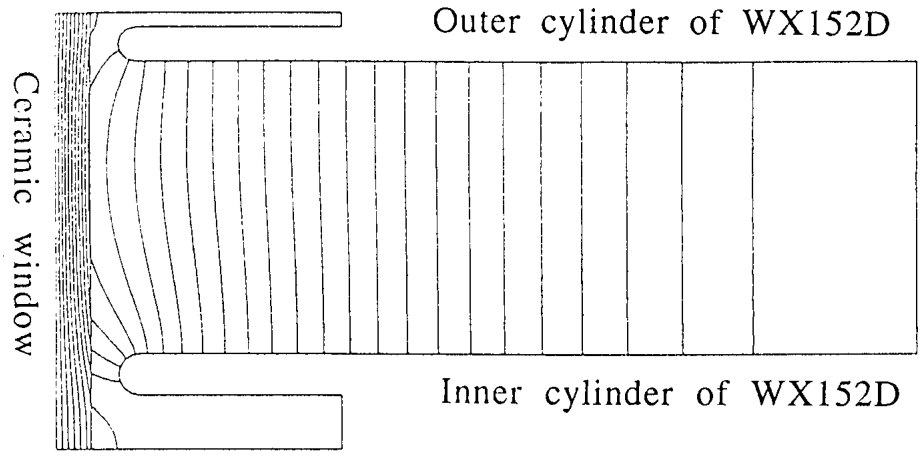

Figure 8.26: Line of the electric force for the choke structure. (Simulation)

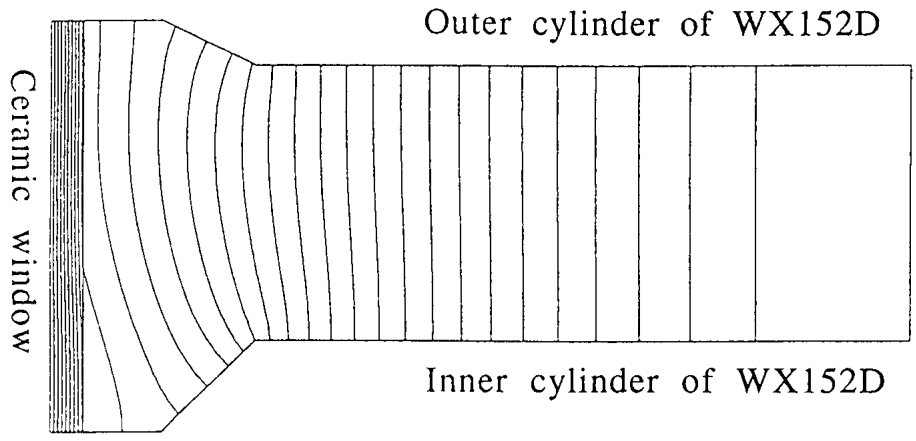

Figure 8.27: Line of the electric force for the OUC structure. (Simulation)

8.1.5 Summary

The ARES structure, where an accelerating cavity is resonantly coupled with a low-loss energy storage cavity, is expected to be a breakthrough for high-current, low-emittance beam accelerators such as KEKB. The results of 1/5-scale ARES model cavities are very encouraging. The fabrication of a full-scale storage cavity model, operating in the TE013 mode, is under way.

In parallel with the development of the ARES structure, the first prototype of the accelerating cavity, which will be employed as a part of the ARES scheme, is currently being fabricated in order to verify its performance in high power operation. The cavity has a coaxial waveguide with a notch filter to block the TEM wave of the accelerating frequency while passing other waves of HOM's to the load.

As the HOM load, sixteen bullet-shape sintered SiC absorbers will be used. SiC is a fine and dense material with high mechanical strength and relatively high thermal conductivity. It has been experimentally shown that a single SiC absorber can handle an average RF power of 2 kW, and that the outgass rate is as low as those of such metals as copper and stainless steel.

The RF window is another key issue. Two types of coaxial RF windows that can transmit CW RF power of 500 kW have been designed. Cold models of both types are currently being fabricated, and a series of high-power tests are scheduled for the summer of 1995.

8.2 Superconducting Cavity

8.2.1 Introduction

At KEK the superconducting (SC) RF system for the TRISTAN Main Ring has been successfully operated since 1988. On the basis of extensive experience in its construction and operation, the application of SC cavities to KEKB have been studied.

An advantage of the SC system is that a relatively small number of cavities can provide the required RF voltage without greatly increasing the impedance of the system for higher order modes (HOMs). This is because of the high accelerating field in the SC cavities. Due to recent technologies the field gradient of SC cavities can exceed 5 MV/m in large-scale applications. It is higher than typical normal conducting cavities by a factor of $3 \sim 5$. In addition, because of the high values of the unloaded Q, the SC cavities do not require a very high R/Q. Consequently, a HOM damping system with SC cavities will be less complicated than normal-conducting cavity systems.

Another advantage of the SC cavity system is that it is fairly immune against the coupled-bunch instability arising from the accelerating mode. As discussed in chapter 4, a consistent set of operating parameters was obtained for the HER, while the growth time is still fast in the LER. In addition, a large refrigerator that has been used for the TRISTAN SC cavities in the Nikko straight section can be re-used in KEKB. From these points, in the HER the SC cavity is considered to be a good candidate for the accelerating cavities.

8.2.2 R&D Status

A preliminary design of the cavity cell structure has been completed. An aluminum model and two niobium test cavities have been built. The HOM characteristics of the aluminum test cavity have been measured using ferrite absorbers that are attached to the beam pipe. Sufficient HOM damping has been observed. In vertical cold tests of the Nb cavities, a gap voltage of 3 MV has been achieved. A bench test of TRISTAN-style input couplers has shown that they can transmit a traveling wave RF power of 850 kW. A prototype module including these components (Figure 8.28) is currently being prepared for a beam test at the TRISTAN Accumulation Ring. The test is scheduled for 1996. The goal is to store a total current of 0.5 A.

Cavity Shape

A single-cell cavity design has been chosen, so as to reduce the number of HOMs as well as to minimize the coupler power. The concept of HOM damping is based on the

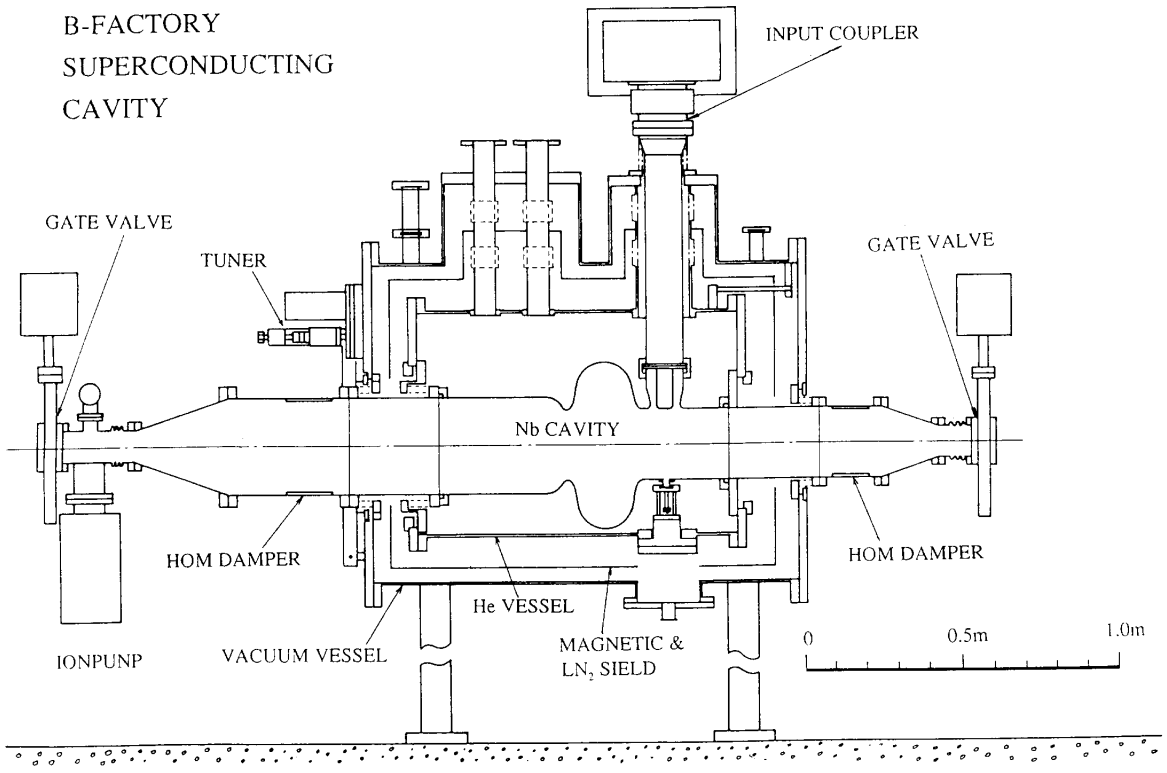

Figure 8.28: A cryomodule for a SC damped cavity for beam testing at the TRISTAN Accumulation Ring.

single-mode cavity idea, proposed by T.Weiland in 1983 [19]. All HOMs of a cavity are extracted out through large beam holes towards the beam pipes. They are damped by ferrite absorbers attached on the inner surface of the beam pipes. This scheme is favored for the SC cavities. Even if the large beam holes reduce the R/Q somewhat, the high impedance of the accelerating mode can be maintained, because of the high Q value of the SC cavities.

The spherical cell shape of the cavity with large beam holes was optimized by using computer codes, URMEL and SUPERFISH [20]. The diameter of the hole (220mm) was chosen to maintain the desired coupling of the lowest monopole modes of TM011 and TM020. Furthermore, a large cylindrical beam pipe (LBP) of 300 mm diameter is connected on one side to obtain a sufficient coupling of the lowest dipole modes, TE111 and TM110. This cylindrical geometry allows easy fabrication and surface treatment in contrast to a grooved beam pipe [21]. The external Q of each HOM was estimated using the tuning curve method by J. Slater [22]. The cavity parameters of the accelerating mode are summarized in Table 8.7. The design of the cavity shape is

Table 8.7: Cavity parameters of the accelerating mode (by SUPERFISH).

frequency	508	MHz
gap length	243	mm
dia. of iris	220	mm
dia. of LBP	300	mm
R/Q	93	Ohm/cavity
loss factor	0.074	V/pC
$E_{surfacepeak}/E_{acc}$	1.84	
$H_{surfacepeak}/E_{acc}$	40.3	Gauss/(MV/m)

R is defined by V^2/P.

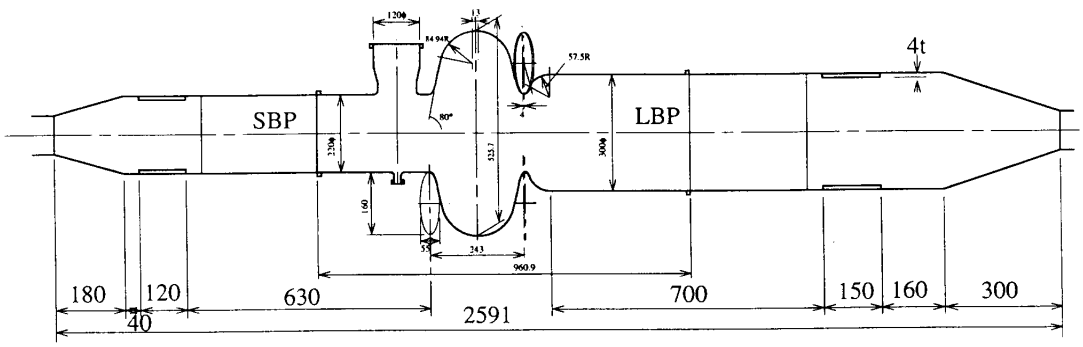

Figure 8.29: Optimized cell shape and ferrite absorbers.

shown in Figure 8.29.

HOM Damping

IB-004 ferrite has been chosen as the HOM absorber, because of its superior RF properties around 1 GHz. The damping characteristics of the absorbers strongly depend on geometrical parameters: the distance from a cell, the length and the thickness of ferrite, and the taper angle between absorbers and a beam duct. These parameters are optimized by using the computer code SEAFISH, which can calculate the Q value of monopole modes for the cavity, including the effects of resistive materials.

An aluminum model cavity was built to confirm the damping characteristics. The experimental results using full size ferrite absorbers have demonstrated the validity of

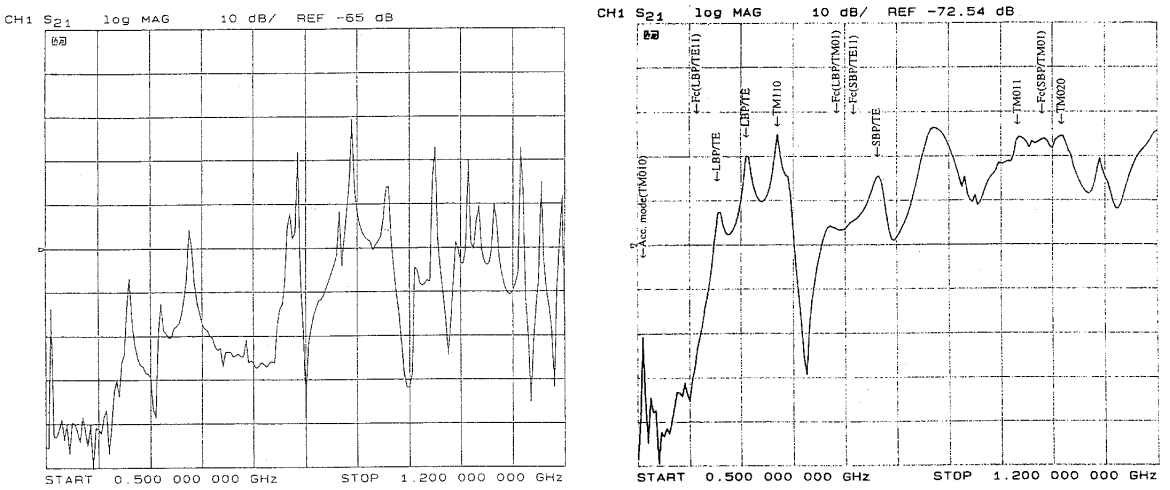

Figure 8.30: HOMs of an Al model cavity with and without ferrite absorbers. The horizontal axis shows the frequency from 0.5 to 1.2 GHz.

the calculations. It has been shown that both the monopole and dipole modes have Q values close to 100. The HOM spectra in an aluminum model cavity with and without absorbers are shown in Figure 8.30. The measured frequency and the Q value of HOMs are listed in Table 8.8 together with the power generated by a beam of 1.1A in the HER.

Because of the short bunch length (4 mm) specified in the design of KEKB, the HOM impedance for frequencies up to 20GHz should be considered. A study using the ABCI code shows that the loss factor of the cell alone is relatively low, 0.3 V/pC. However, the total loss factor for the system has been calculated to be 2.3 V/pC per cavity. This is caused mainly by the pair of tapers that connect the cavity to beam ducts whose diameter is 100 mm. In the case of a duct with 150 mm, the loss factor is reduced to 1.5 V/pC as shown in Figure 8.31.

In this case powers of 3.5 kW and 20 kW will be absorbed by a pair of ferrite absorbers in the HER and the LER, respectively. An optimization study of the taper shape, which reduces the absorber load, is in progress.

Cavity Performance

Two Nb cavities have been fabricated and tested at 4.2 K̇ in a vertical cryostat. These cavities have identical cell shapes. One of them will be dedicated to studies of the mechanical strength of the cavity after a series of cold tests.

The cavities are made of pure Nb sheet of 2.5mm thickness. After welding was completed, the cavities were treated in the same procedure as that for TRISTAN SC

Table 8.8: Measured frequency and the Q value of HOMs together with the power generated by a beam of 1.1A in the HER.

monopole

frequency	mode	R/Q	Q	power
(measured)		(URMEL)	(measured)	
MHz		Ohm		$Watts$
783	LBP-TM01	0.12	132	-
834	LBP-TM01	0.34	72	-
1018	TM011	6.6	106	900
1027	TM020	6.4	95	201
1065	SBP-TM01	1.6	76	4
1076	LBP-TM01	3.2	65	6
1134	LBP-TM01	1.7	54	1

dipole

frequency	mode	R/Q'	Q
(measured)		(URMEL)	(measured)
MHz		Ohm/m	
609	LBP-TE11	1.9	92
648	LBP-TE11	40.19	120
688	LBP-TE11	170.4	145
705	TM110	227.3	94
825	SBP-TE11	6.16	60
888	SBP-TE11	3.52	97

$R/Q' = (R/Q)_r/kr^2, \quad (\ r = 5cm\ )$

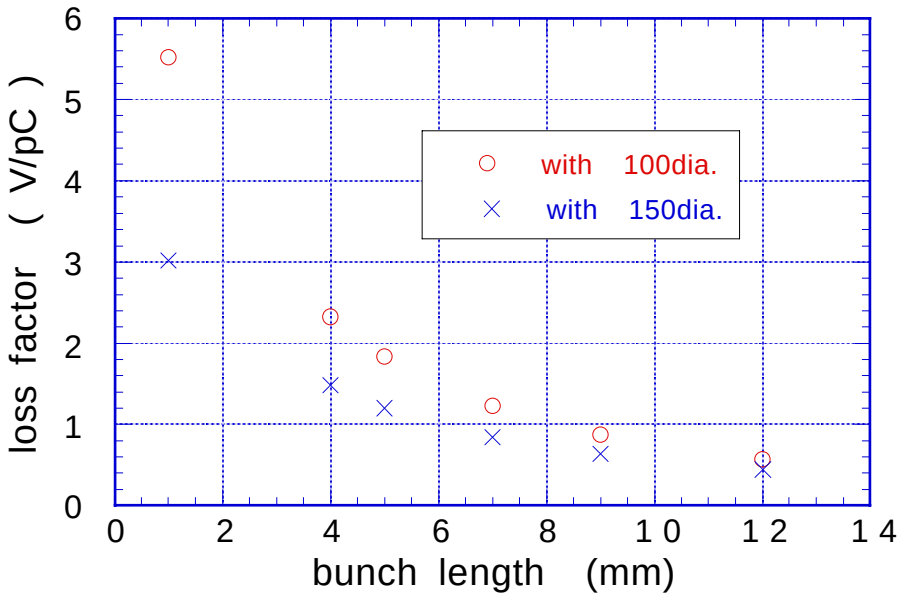

Figure 8.31: Loss factor of a cavity with a beam duct of 100mm/150mm in diameter (calculated by ABCI).

cavities: electropolishing (EP) of 90μm, annealing (700°C) and the final EP of 15μm followed by thorough rinsing with pure and ultra pure water. The results of cold tests are shown in Figure 8.32. A similar performance of Q and the accelerating field ($E_{\rm acc}$) could be obtained for both cavities, where maximum $E_{\rm acc}$ of 12.4 MV/m and 14.4 MV/m were obtained.

The field gradient is limited by electron emission, which is observed by a temperature and X-ray mapping system based on carbon resistors and PIN diodes (Figure 8.33). It has been observed that electron emission is increased for gradients exceeding 7 MV/m, if the cavity surface is exposed to air. To reduce the electron emission and to improve the stability of the RF-processed surface, ozonized ultra pure water rinsing is under study [23].

HOM Absorber

The priority of our efforts concerning ferrite absorbers has been to establish the fabrication procedure. Three bonding methods have been investigated to fix IB-004 ferrite onto the surfaces of copper beam pipes: ultrasonic soldering, vacuum brazing and HIP (Hot Isostatic Press) method. Among these methods, HIP has proven to be the most promising. There, the powder of IB-004 is packed in an iron vessel together with a

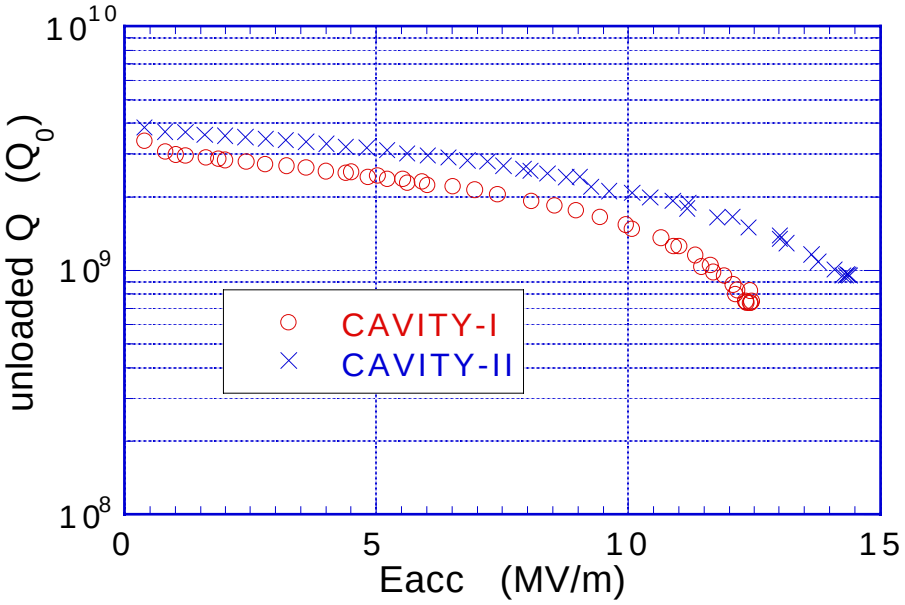

Figure 8.32: Q vs E_{acc} at vertical cold tests of the superconducting Nb cavities.

copper cylinder. After pumping the vessel to a vacuum, it is heated to 900°C in a furnace under a pressure of 1000 bar. In this vacuum environment the ferrite is sintered in a cylindrical form which is firmly attached to the inner surface of the copper [24].

To study its RF power capacity, small scale models of a HIP'ed ferrite cylinder have been fabricated. They are 15 cm long and 10 cm in diameter. A traveling RF power of 5 kW at 2.45 GHz has been applied. An RF absorption of 3.4 kW, which corresponds to 25 W/cm^2 at the front edge, caused the temperature to rise to 200°C. No cracking has occurred. The effective area of the power absorption was determined by the temperature distribution, and the average power density on the ferrite was calculated to be 14W/cm^2. An RF power test of full size models is currently being prepared.

Figure 8.34 shows a ferrite absorber for the LBP side. The out-gas rate of a full size model has been measured to be 2×10^{-7} Torrl/sec at room temperature, after baking at $150 \sim 250$°C. Pre-baking of the ferrite powder is under examination to reduce the outgas rate. The measurement of a loss factor of a ferrite wall has been conducted using the synthetic pulse method. Analytic calculations and preliminary experiments using full size models predict the loss factor of 0.3 V/pC per absorber for a bunch length of 4 mm. It will cause an additional loss of 1.4 kW for the HER and 8 kW for the LER.

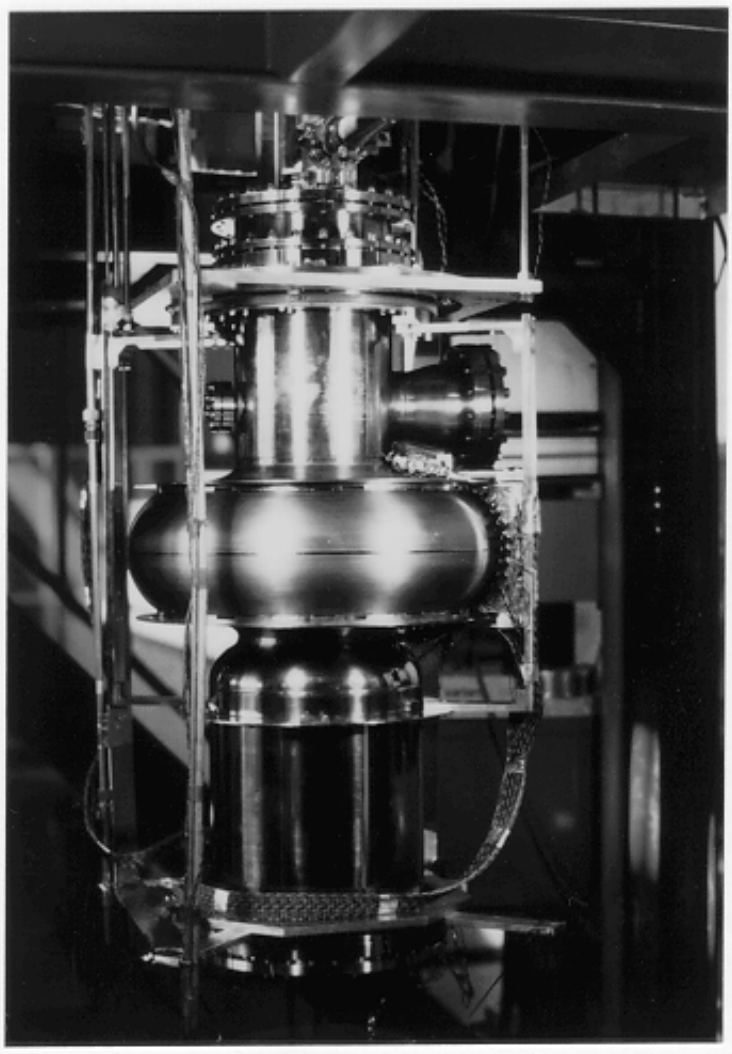

Figure 8.33: A niobium cavity module with a mapping system using 25 carbon resisters and 19 PIN photo diodes.

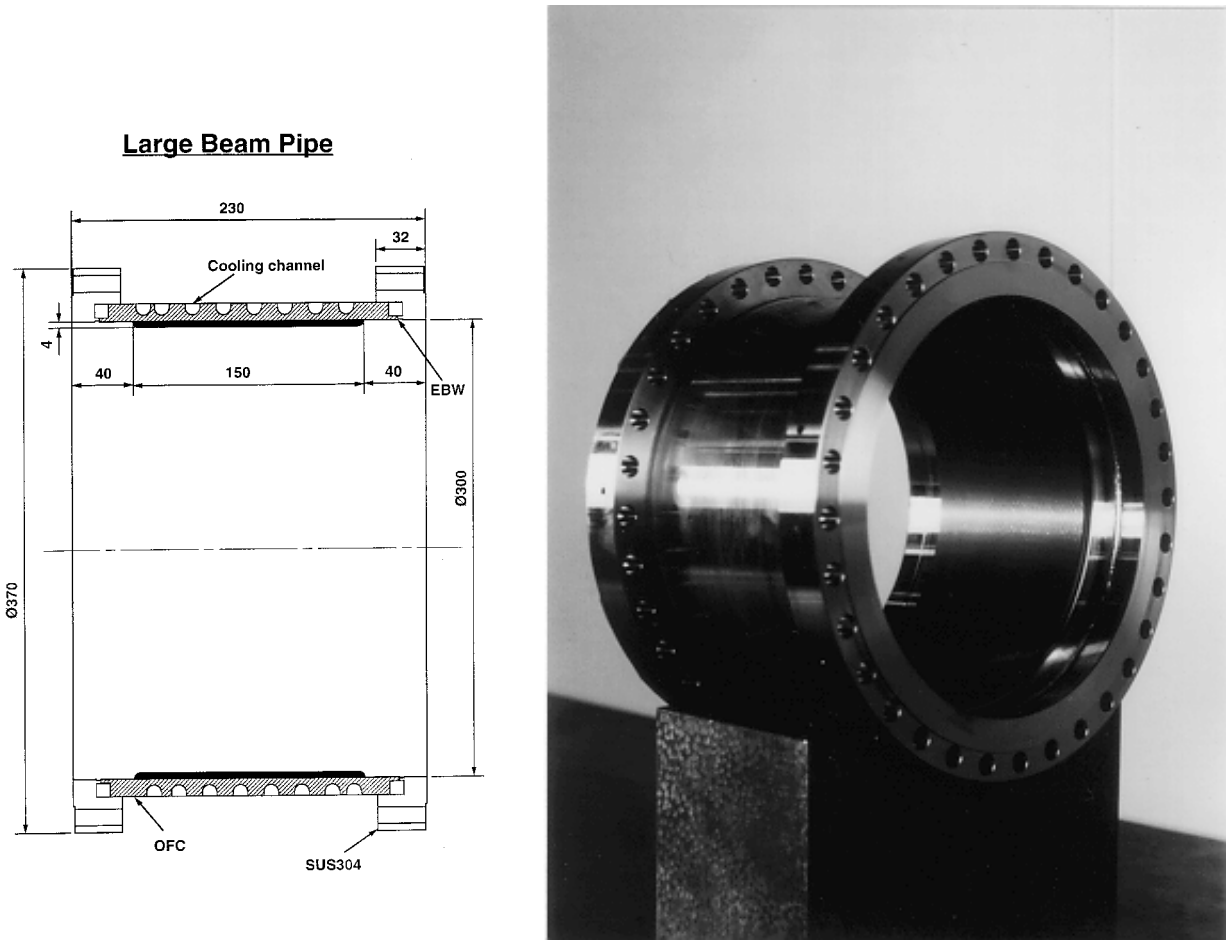

Figure 8.34: A Full size model of the ferrite absorber. The powder of IB-004 ferrite was sintered and bonded to a Cu pipe by HIPping.

Input Coupler

A coaxial antenna coupler will be used as an input coupler, which is the same type as what has been used for the TRISTAN SC cavities. A schematic drawing is shown in Figure 8.35. The ceramic window of the coupler is a 152D coaxial. The same ceramic window has been used as the output window of 1 MW klystrons for TRISTAN.

After 9 hours of RF processing, a CW-traveling RF power of 800 kW could be successfully supplied to two pairs of couplers in a test bench for more than 30 min (Figure 8.36). Most of the processing time was spent to overcome the multipactoring levels of 50 kW and 160 kW. Less processing was needed at higher power levels. A peak power of 850 kW, that was limited by the Klystron output power, could be supplied to a pair of couplers for 5 minutes, and no cracking occurred on the ceramics. A power

test with reflecting RF will be made after completing these traveling wave tests.

An analysis of cooling or heating has just started. The heating of the inner copper conductor is estimated to be 360 W for an RF power of 500 kW. The temperature rise is kept to within 10 degrees by cooling water. On the other hand, the loss of the outer conductor, which is made of copper plated stainless steel, is 160 W/m on the room temperature side and 30 W/m on the 4.2K side. This power will introduce a heat loss of about 50 W to liquid He. Optimization of He gas cooling for the outer conductor has to be done.

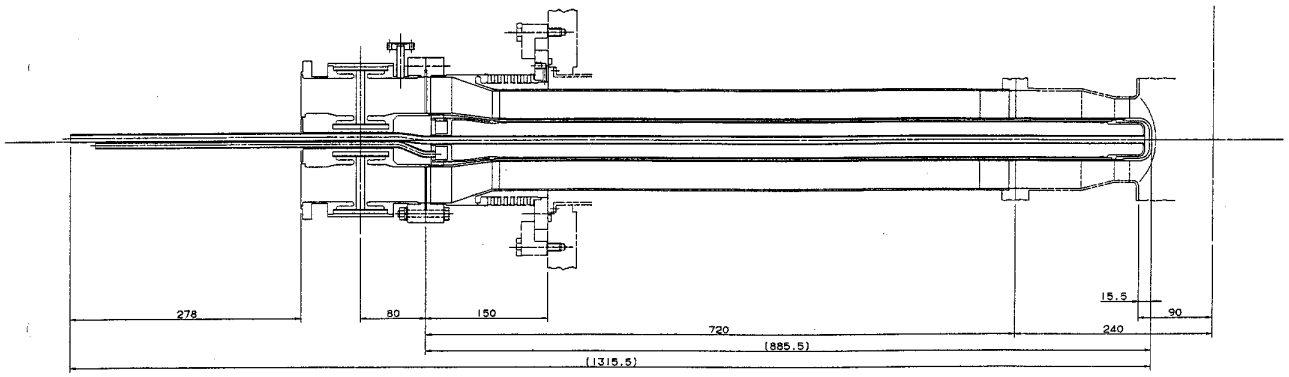

Figure 8.35: Coaxial input coupler for SC cavities.

8.2.3 Summary

The development of main components for an SC damped cavity for KEKB is in progress. A spherical single-cell cavity with large beam pipes has demonstrated satisfactory damping of HOMs using IB-004 ferrite absorbers fixed onto the beam pipes. The gap voltage of 3 MV has been obtained with Nb cavities in vertical cold tests. Tests of reduced model absorbers have been successfully conducted with RF powers of 25 W/cm^2 in peak and 14 W/cm^2 in average. No cracking of the absorbers has been observed. Coaxial input couplers that are the same as those for the TRISTAN cavities could transfer the traveling wave of 850 kW at a test bed.

The RF parameters of the HER can be realized with the recent superconducting RF technology, where $10 \sim 12$ single cell cavities will be used to maintain a beam of 1.1 A. The field gradient of each cavity is $4 \sim 6.5$ MV/m, and $400 \sim 500$ kW couplers with the $Q_{\rm ext}$ of 5×10^4 will be required. Induced HOMs of 6 kW should be absorbed by a

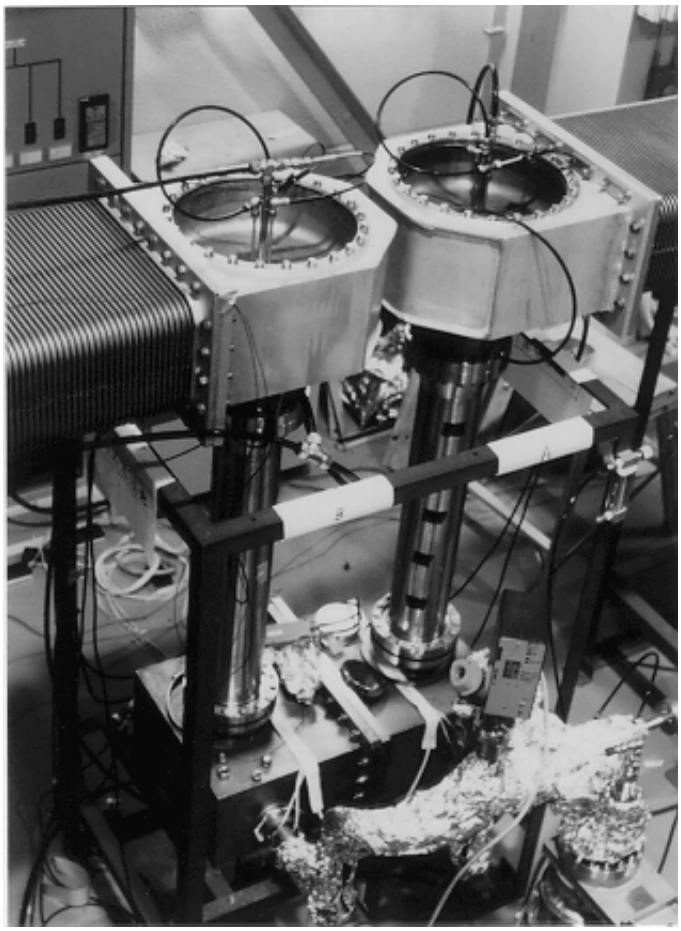

Figure 8.36: High power test bed for input couplers; a travelling RF power of 850kW was supplied to a pair of couplers.

pair of ferrite absorbers. This corresponds to an absorber power density of 3 W/cm^2. The main components, such as Nb cavities, HOM absorbers and input couplers, have been extensively tested. The experimental results demonstrate the feasibility of SC cavities for the HER. On the other hand, the application to the LER will involve many difficulties caused by the heavy beam loading under a low RF voltage. High power couplers with a low external Q and the absorption of a HOM power of 34 kW will be required.

A prototype module which includes these components and a frequency tuner is under construction for a beam test of 0.5 A in the TRISTAN Accumulation Ring. The test is scheduled for 1996.

8.3 Low Level RF Issues

8.3.1 Phase and Tuner Control

The low level RF system consists of RF signal generators, a reference line system which distributes the RF signal to all RF stations, and a low level RF control system for each RF unit. The low level system for each RF unit has feedback loops to control the cavity field, the klystron output and the cavity tuners. Phase detection is conducted at an intermediate frequency of 1 MHz.

The cavity phase should be controlled with an accuracy of less than 1 degree. This requirement is considerably tighter than that at ordinary storage rings due to the following reasons. In a double ring collider with a small β^* at the colliding point, a phase error of one ring relative to the other gives rise to a displacement of the colliding point from the minimum β^*. This results in a luminosity reduction. Another reason is that a phase error in one cavity causes extra input power and reflection power to that cavity due to the heavy beam loading. For example, if the phase of one superconducting cavity is different from the others by 1 degree, an extra power of 30$\sim$40 kW is fed to that cavity in order to keep the cavity voltage constant.

We will improve the accuracy of the existing RF reference system and phase control modules that have been used for TRISTAN. In addition, we will use a computer-aided real-time phase correction scheme, where the input power, reflection power, and cavity voltage of every cavity are monitored, and the phase error of each cavity is then calculated and corrected. This correction scheme takes advantage of the high beam-induced voltage.

In order to reduce fast ripples of the klystron power supply and phase changes of the klystron, which is on the order of ten degrees, we need a control loop for the klystron output which acts as an inner loop within the cavity voltage loop.

As seen in Figure 8.2, the ARES requires two tuner control loops: one is for the accelerating cavity; the other for the storage cavity. The accelerating cavity tuner is controlled according to its phase with respect to the input phase, which is the usual method used to compensate for the reactive component of beam loading. The storage cavity tuner is controlled not by its own phase, but by the phase of the coupling cavity; otherwise, the phase tolerance would be extremely severe.

8.3.2 Bunch gap transient

Ion-trapping is one of the problems which arises from a high electron beam current. In storage rings, some part of residual gas molecules is ionized due to collisions with

stored beams. The ions can be trapped around the beam orbit by the potential well of the electron beam. The trapped ions can: (1) shorten the beam lifetime due to the collisions, (2) give rise to a two-beam instability, and (3) affect the betatron tune.

In order to cure the ion trapping problem, several methods have been proposed. Among them, introducing a bunch gap is the most attractive solution for KEKB. In this scheme, beams are partially filled in the ring with one or more gaps, instead of being filled uniformly. The ions escape from the beam orbit to the duct wall when they encounter the bunch gap. Other methods are less attractive. For example, a method using clearing electrodes increases the ring impedance, or gives rise to local heat problems. Thus, a 5$\sim$10% bunch gap will be introduced in HER.

The bunch gap, however, modulates the accelerating field and the synchronous phase of each bunch, resulting in unequally-spaced bunches. A bunch phase modulation of $\pm$ 2.4 degrees corresponds to a longitudinal displacement of $\pm$ 1 σ_z (=4 mm) in KEKB. Furthermore, since a finite crossing angle of 2 $\times$11 mrad will be adopted, this modulation gives rise to a transverse displacement of 77 μm at the collision point, which is close to 1/3 of σ_x^*. Both effects reduce the luminosity.

The bunch phase modulation has been calculated for the cases of the ARES and SCC [25]. The results are summarized in Table 8.9. Because of the large stored energy, the phase modulation is much smaller than that of conventional normal-conducting damped cavities, which would give a modulation of typically 20$\sim$30 degrees at KEKB. The displacement of the collision point can be further reduced by introducing a corresponding gap in the positron ring (LER), which makes a similar gap transient response in LER to that in HER. Figure 8.37 shows the relative bunch phase with and without the compensation gap. By controlling the bunch charge at the compensation gap in a range from 50 to 60% of that of other bunches, the bunch phase modulation is kept below 0.5 degrees (=$0.2\sigma_z$), which is acceptable.

Table 8.9: Bunch phase modulation due to a bunch gap.

Cavity in HER	Gap length (%)	Bunch phase modulation (degree)	
		with compensation gap?	
		No	Yes
ARES	10	2.7	~ 0.3
	5	1.3	~ 0.1
SCC	10	4.9	~ 0.5
	5	2.4	~ 0.3

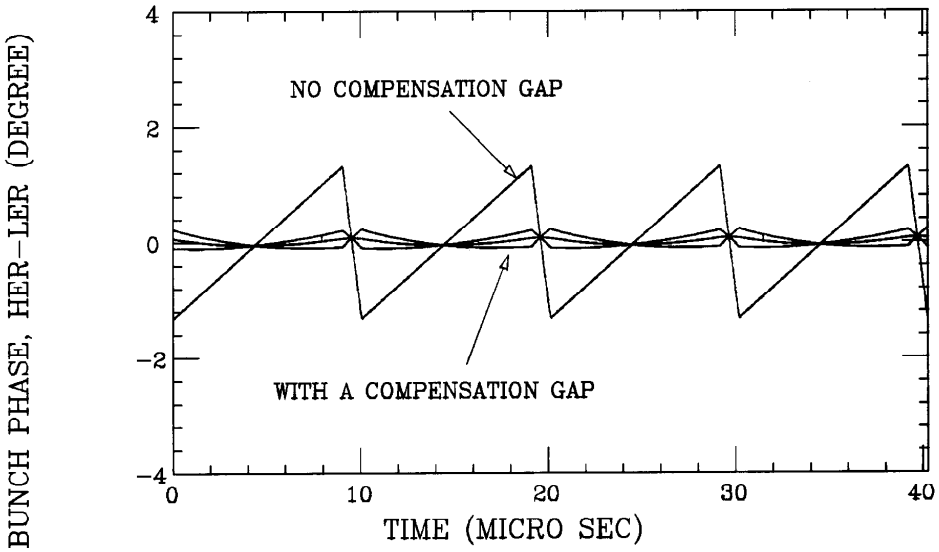

Figure 8.37: Bunch phase modulation due to a bunch gap and the effect of a compensation gap. The ARES cavities were assumed. The relative gap length is set to be 10%. The bunch current in the compensation gap is set 50, 55, and 60% of that of other bunches.

8.3.3 RF Cavity Feedback

Background

By using the ARES or the SCC the two particular beam-loading effects can be reduced: namely, the excitation of longitudinal coupled-bunch instabilities by the detuned accelerating mode, and the presence of bunch-phase modulation due to gaps in the bunch-train. Along with the development of those cavities, we are developing an RF cavity feedback system. The purpose of the feedback development is to reduce the beam-loading effects to the extent that the HOM-damped accelerating cavity of the ARES itself, without the energy storage cavity, can be used as the KEKB accelerating structure. It is obvious that, in the case where the ARES or the SCC are employed, the feedback can be used as an auxiliary means to reduce the beam-loading effects.

Here, we discuss the RF cavity feedback to be used for damping the instabilities that will arise, if the beam is accelerated solely by the HOM-damped accelerating cavities of the ARES. Figure 8.38 shows the calculated growth rates of the longitudinal coupled-bunch instabilities due to the accelerating mode of the cavities in the LER (Figure 8.38-a) and in the HER (Figure 8.38-b). The parameters used in the calculations are listed in Table 8.10. For simplicity, we refer to the mode $m = M - n$ as the mode $m = -n$. Here, M is the number of bunches, and m ranges from 0 to $M - 1$. The expected damping rate by the longitudinal bunch-by-bunch feedback system is also shown in the figure, together with the longitudinal radiation damping rate. As shown in Figure 8.38, the growth rates in the LER are higher than those in the HER, mainly due to its higher

Table 8.10: Parameters used in the instability calculations

		LER	HER	
Type of cavity		accelerating cavity of ARES		
Total cavity voltage	V_c	8.6	15.7	MV
Number of cells	N_c	20	32	
Cavity voltage/cell	V_c/cell	0.43	0.49	MV/cell
Shunt impedance/cell	R_s	5.3		MΩ
Unloaded Q	Q_0	35000		
R/Q		147		Ω
Maximum frequency detuning	Δf	−232	−82	kHz
Synchrotron frequency	f_s	1.7	1.6	kHz
Energy loss/turn	U_0	0.87	4.8	MV

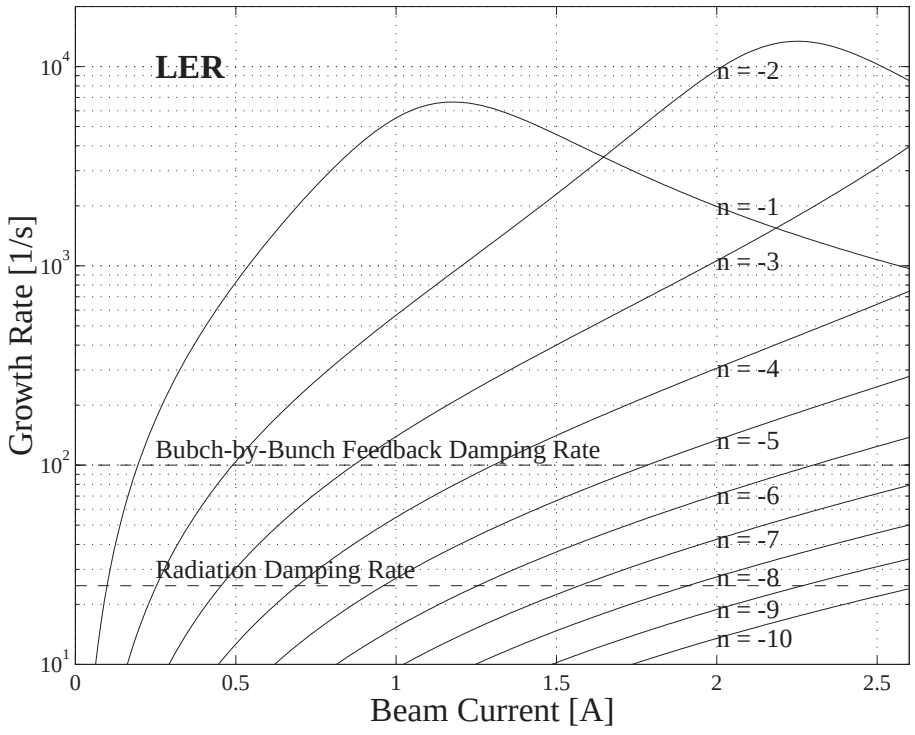

(a)

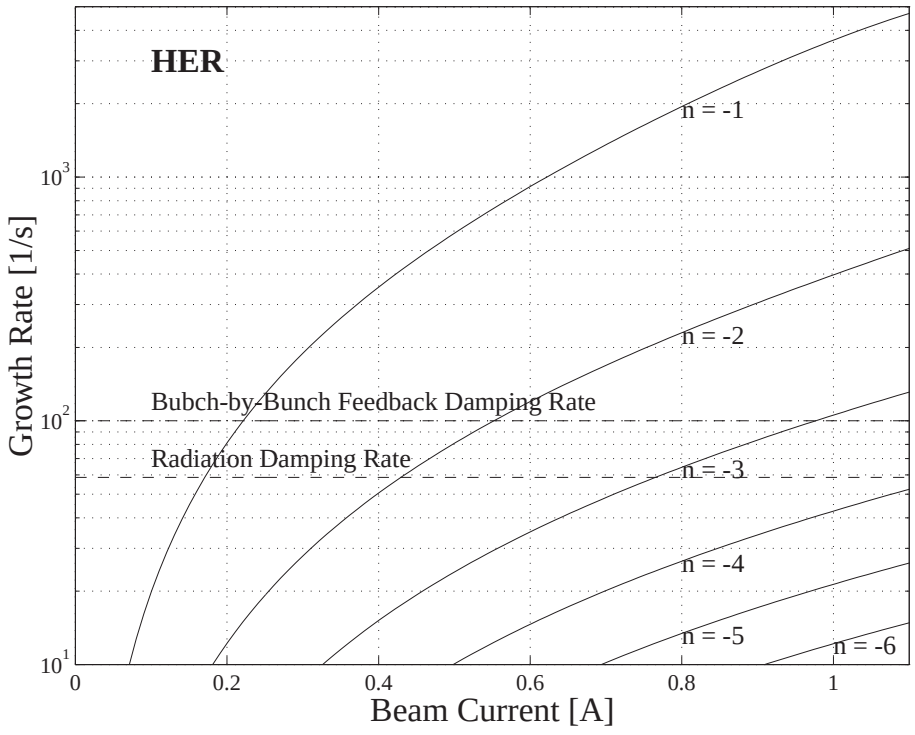

(b)

Figure 8.38: Calculated growth rates of longitudinal coupled-bunch instabilities caused by the accelerating mode of the cavities in the LER(a) and in the HER (b). The type of cavity used in the calculations is the accelerating cavity of the ARES, that is, the HOM-damped normal conducting cavity not equipped with the storage cavity.

beam current. The RF cavity feedback must reduce the growth rates, at least, down to a level which can be damped by the bunch-by-bunch feedback system. This means that the damping rate by the cavity feedback must be higher than 35 dB in the LER and higher than 23 dB in the HER. The number of modes to be damped are six ($m = -1$ to -6) in the LER and three ($m = -1$ to -3) in the HER. Since the revolution frequency of the bunches is about 100 kHz, the frequency range to be covered by the cavity feedback is more than 600 kHz in the LER and more than 300 kHz in the HER.

Principle of the System

In an RF cavity feedback, a part of the cavity voltage is picked up, filtered and vectorially added to the RF drive with an appropriate amplitude and phase so as to reduce the beam-induced cavity voltage. In this way, the magnitude of the effective cavity impedance seen by the beam is reduced. In the case of KEKB, however, an unavoidable large group delay in the feedback loop limits the bandwidth of the system to less than 100 kHz. Cables and waveguides cause a constant group delay of about 1 μs, while the klystron causes a frequency-dependent group delay of about 0.6 μs at maximum. To circumvent this problem, we are developing a feedback system with a large loop-gain only in the vicinity of the frequencies $nf_{\rm rev} + f_{\rm s}$. They are the upper synchrotron sidebands of the revolution harmonics, and are responsible for driving the coupled-bunch oscillations. This feedback is realized by using a comb-filter comprising of an array of resonators. Each resonator is tuned to a particular frequency of $nf_{\rm rev} + f_{\rm s}$, and its phase is shifted properly to compensate for the phase differences among the sideband frequencies. The comb-filter can also compensate for the frequency-dependent amplitude response of the feedback loop by adjusting the attenuation of the resonators. The array of resonators is, from here on, referred to as the parallel comb-filter. A block diagram of the RF cavity feedback system is shown in Figure 8.39.

R&D Status

We have carried out a preliminary experiment of the parallel comb-filter feedback through the RF cavity. Figure 8.40 shows the experimental setup, which includes a parallel comb-filter, a 2-cell damped cavity of the Palmer type and a klystron. Since the cavity used was a cold model, only a small portion of the klystron output power was extracted with a 55dB directional coupler, to be fed into the cavity. The parallel comb-filter consists of five individual LC resonators arranged at 100 kHz intervals, and each resonator has a 2 kHz 3dB-bandwidth. A network analyzer was used to measure the amplitude and phase of the cavity voltage over the frequency range from 508 MHz

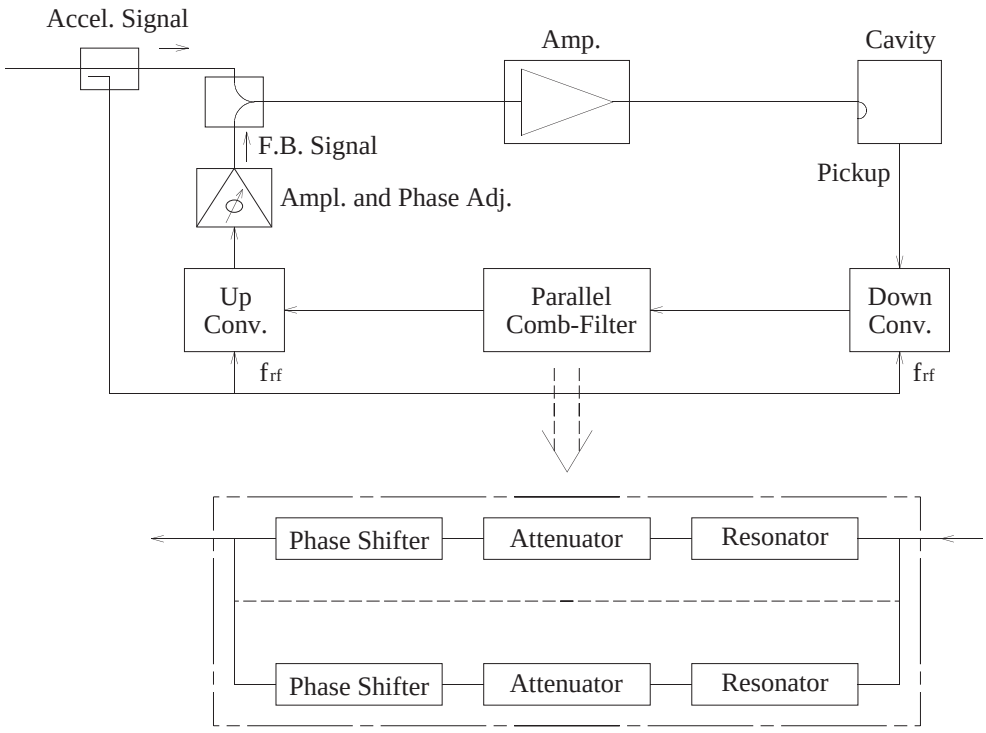

Figure 8.39: Block diagram of the RF cavity feedback system using a parallel comb-filter.

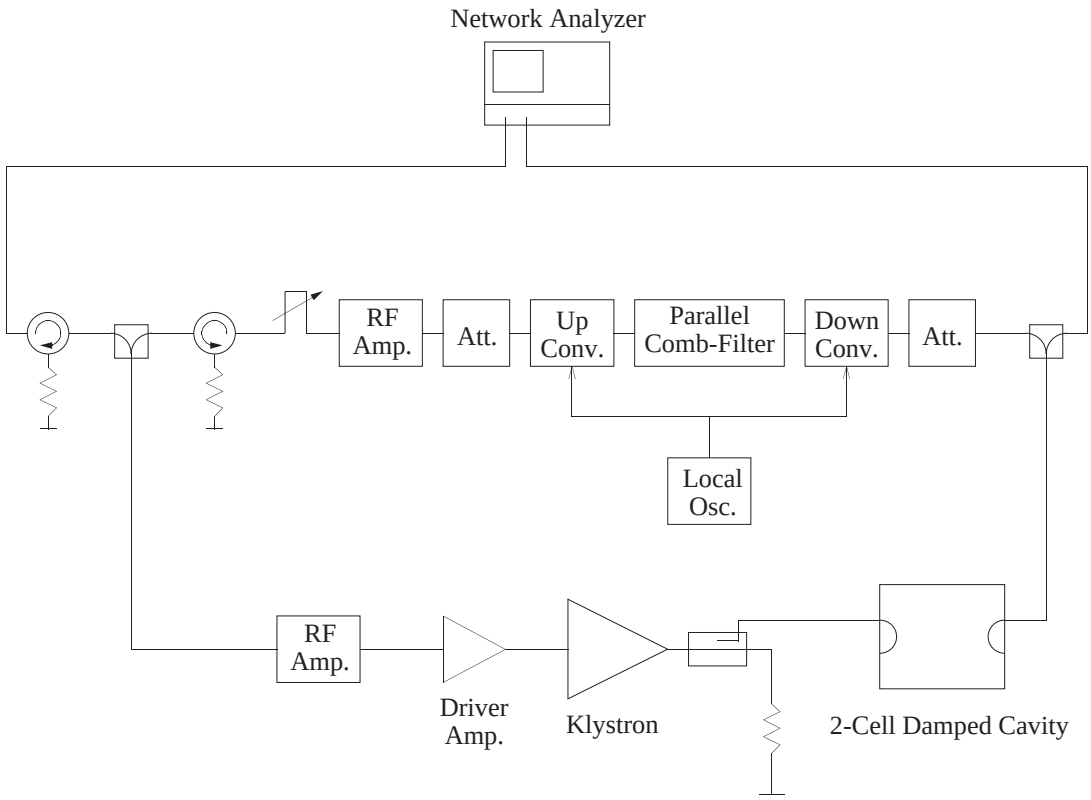

Figure 8.40: Block diagram of the experimental RF cavity feedback loop, which includes a parallel comb-filter, a low-power damped cavity and a klystron.

to 509 MHz. The bandwidth and the center frequency of the cavity were 236 kHz and 508.5 MHz, respectively.

The results of the measurement are shown in Figure 8.41; the top figure shows the magnitude and the real part of the effective cavity impedance, with or without feedback, as a function of the normalized frequency $(f - f_{\mathrm{rf}})/f_{\mathrm{rev}}$, and the bottom figure shows the phase of the cavity. With the feedback, the real part of the impedance was reduced by 17 dB to 25 dB, at five sideband frequencies. The measured values are in good agreement with estimations obtained by using the measured parameters of loop the components. The maximum gain of the feedback loop is limited by the top-to-bottom amplitude ratio of the filter, because the loop gain must be less than 0 dB at the bottom where the filter becomes 180° out of phase. The increase in the impedance between the revolution harmonics in Figure 8.41 is the result of a positive feedback due to an improper phase relationship in this region. An estimate shows that to reduce the real part of the cavity impedance by more than 35 dB, the 3dB-bandwidth of the resonator needs to be smaller than 1 kHz.

A new comb-filter with ten parallel resonators is currently being built. The center frequency of the resonator can be adjusted continuously and the bandwidth in a step-

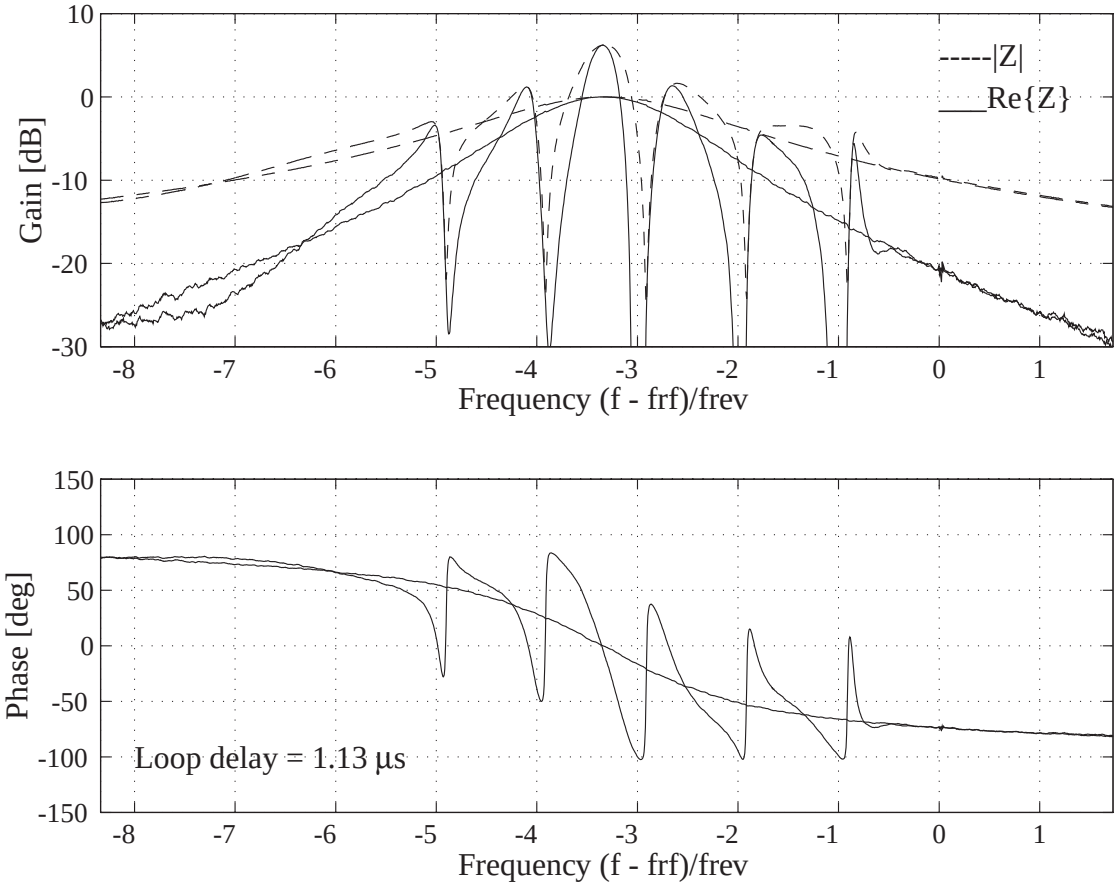

Figure 8.41: The results of the RF cavity feedback experiment. The top figure shows the magnitude and real part of the effective cavity impedance, with or without feedback, as a function of the normalized frequency $(f - f_{\rm rf})/f_{\rm rev}$; the bottom figure shows the phase of the cavity.

wise manner. The new comb-filter will be tested soon. The main purpose of the test is to improve the loop gain by more than 10dB. The RF cavity feedback system will be tested using a beam of the TRISTAN Main Ring (scheduled in May 1995).

8.4 Crab Cavity

8.4.1 Introduction

A large number of buckets in each ring (the HER and LER) must be filled with beams to obtain the design luminosity of 10^{34} /cm^{2}sec. Consequently KEKB has to operate with a short bunch spacing of minimum 60 cm. It is necessary, therefore, to separate both beams quickly near the interaction point (IP) to avoid parasitic collisions. It is also necessary to minimize synchrotron radiation generated near the IP, particularly just upstream of the crossing point. In order to meet these requirements, the interaction region (IR) design of KEKB is based on beam crossing with a finite angle of ± 11 mrad.

One consequence of employing a finite crossing angle is a luminosity reduction due to geometrical effects. Another important effect of a finite crossing angle is the possibility to excite synchrotron-betatron resonances. The crab crossing scheme [26], [27] is considered to solve these problems. Figure 8.42 shows the crab crossing scheme, where bunches are tilted by a time-dependent transverse kick in an RF deflector (crab cavity) located before the IP in each ring. After the bunches collide head-on, this bunch tilt is kicked back to the original orientation in another deflector after the IP.

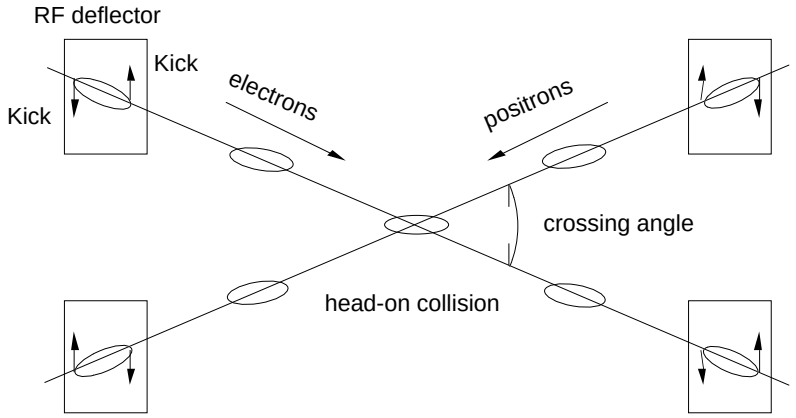

Figure 8.42: crab crossing scheme.

The R&D work on the crab cavity was carried out in 1991 and 1992 in collaboration with Cornell university, where superconducting crab cavities operating in the TM110 mode were designed for CESR-B at Cornell. In order to damp the parasitic modes, a new damping scheme that employs a coaxial beam pipe and a notch filter was proposed [5]. The damping scheme was verified by measurements of model cavities made of copper and aluminum. The high field performance was tested with a one-third scale niobium cavity in liquid helium. A cold measurement showed that the design values of

the necessary kick voltage and Q-value were achieved.

At KEK we started an R&D effort for the crab cavity aimed at making full-scale niobium cavities for KEKB in three years. We decided to adopt the same design of the crab cavity as that designed for CESR-B, although a slight modification is needed, since the frequency of KEKB is 508.9 MHz, which is slightly higher than that of CESR-B (500 MHz). In this section we describe the design and measurement results of the crab cavity that has been developed under the KEK-Cornell collaboration [5], [28]. At the end of this section our R&D plan for the crab cavity at KEK is presented.

8.4.2 Design Concept

Deflecting Mode

The required transverse deflecting voltage ($V_\perp$) is determined by the desired crossing angle at the IP and the operating frequency of the crab cavity:

$$V_\perp = \frac{cE \tan\theta_x}{\omega_{RF}\sqrt{\beta_x^* \beta_{crab}}}, \tag{8.1}$$

where β_x^*, β_{crab}, E, θ_x and ω_{RF} are the beta-function at the IP, the beta-function at the crab cavity, the beam energy, the half crossing angle and the RF frequency of the crab cavity, respectively. Table 8.11 summarizes the basic parameters for the crab cavities in the LER and the HER of KEKB. The required deflecting voltage is 1.4 MV in each ring.

One possible method to realize the crab crossing scheme is to use RF cavities operating in a transverse deflecting mode. The best choice for this would be the TM110 mode, which has a high transverse shunt impedance. Since superconducting

Table 8.11: Parameters for the Crab Cavity in KEKB.

Ring	LER	HER	
Beam energy	3.5	8.0	GeV
RF frequency	508.887		MHz
Crossing angle	±11		mrad
β_x^*	0.33	0.33	m
β_{crab}	20	100	m
Required kick	1.41	1.44	MV

cavities can be operated in a high field gradient, a single-cell superconducting cavity would be sufficient to provide the necessary transverse kick voltage.

Damping Scheme for Parasitic Modes

Coupled-bunch instabilities caused by the crab cavities must be sufficiently suppressed, as well as those caused by the accelerating cavities of KEKB. The Q-values of dangerous parasitic modes should be sufficiently lowered, typically to the order of 100. In the case of superconducting accelerating cavities, the accelerating mode is the lowest frequency mode, and all parasitic modes have higher frequencies. As a damping scheme for higher order modes, the superconducting accelerating cavity for KEKB employs large-diameter beam pipes, through which the field energy of those modes can be extracted and absorbed by microwave absorbers attached to the beam pipe.

In the case of a crab cavity, however, since the operating mode (TM110) used for the crabbing is not the lowest frequency mode, there are some modes with lower, or about the same, frequencies. Four unwanted parasitic modes remain trapped in the cavity region with high Q-values, even if a beam pipe with a large diameter is attached. Those are the TM010 monopole mode, two polarizations of the TE111 dipole mode and an unwanted polarization of the TM110 mode. In order to overcome this problem, a coaxial beam pipe and a notch filter are employed in the crab cavity. A schematic view of this damping scheme is shown in Figure 8.43. With this scheme, not only the higher order parasitic modes, but also the lower frequency parasitic modes, can be damped, as will be discussed in the following.

In a coaxial transmission line, although there is no cut-off frequency for TEM mode waves, there is a cut-off frequency for the dipole modes. By attaching a coaxial beam

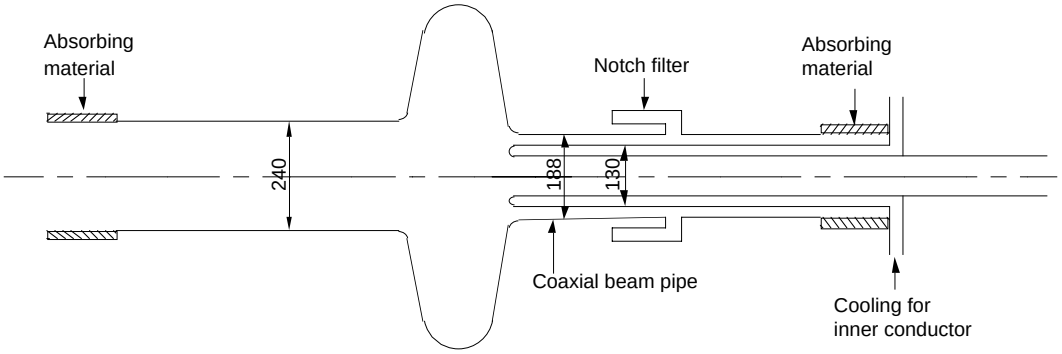

Figure 8.43: A schematic view of the crab cavity.

pipe to the crab cavity, every monopole resonant mode in the cavity can couple to the coaxial beam pipe as a TEM mode wave, and then propagate. In addition, every dipole resonant mode in the cavity can couple to the coaxial beam pipe as a dipole mode wave; it will propagate if its frequency is higher than the cut-off value. By designing a cell shape such that f(TM110)$<$ f(cut off)$<$ f(TE111), all monopole and dipole modes, except the TM110 mode, in the cavity can be extracted out of the cavity via the coaxial beam pipe.

However, one unwanted polarization of the TM110 mode is still trapped in the cavity. Since this mode has a high transverse shunt impedance, it must be cured. Two possible measures for cure have been considered:

- Use of a slightly polarized cell, and tuning this mode at a safe frequency. If we control the frequency of this mode at a damping side of transverse coupled-bunch instability, we can avoid the instability driven by this mode. For this method we designed a round cell shape cavity using cylindrical symmetric calculations. A slight polarization will be introduced to separate the unwanted polarization mode from the operating mode.

- Extremely polarized cell ("Squashed" crab cavity). By making the cross section of the cavity cell an ellipse or race-track shape with a large eccentricity, we can increase the frequency of the unwanted TM110 mode to be above the cut-off of the dipole mode wave in the coaxial beam pipe. An analytical calculation of a rectangular cavity has shown that when the ratio of the longer to shorter dimension in the cross section is 2:1, the unwanted TM110 mode goes up to 700 MHz, while the operating mode is kept at 500 MHz. We designed such an extremely polarized cell cavity.

In the following we describe both designs of the round cell and the squashed cell.

8.4.3 Design Optimization

Coaxial beam pipe

Since we will operate the crabbing mode TM110, at 509 MHz, the cut-off frequency of the dipole mode in the coaxial beam pipe should be higher than that frequency. In order to have a sufficient attenuation for the crabbing mode, it is desirable to make the cut-off frequency high enough. On the other hand, the cut-off frequency should be lower than the lowest parasitic dipole mode (TE111 in this case). The dimensions of the coaxial beam pipe were chosen so that: (1) it has a cut-off frequency of 600 MHz, which gives an attenuation of 60 dB/m for the crabbing mode, and (2) it has a sufficient

thickness of the inner conductor to allow a cooling system in it. We have chosen the radius of the inner surface of the outer pipe to be 94 mm and the outer and inner radii of the inner conductor to be 65 mm and 45 mm, respectively.

Round cell design

Computer studies involving a cylindrical symmetry have been carried out in order to optimize the cell shape. The variables in the optimization were the cell length, the iris radius, the equator radius and the slope of the wall. Several points taken into account in designing the cell shape were:

- The frequencies of all dipole parasitic modes should be higher than the cut-off frequency of the dipole mode in the coaxial beam pipe.
- The ratio of the kick voltage to the surface peak field should be high.
- The R/Q values of the parasitic modes (especially for the most dangerous TM010 mode) should be low.
- The external Q for parasitic modes having high R/Q should be low (typically less than on the order of 100).

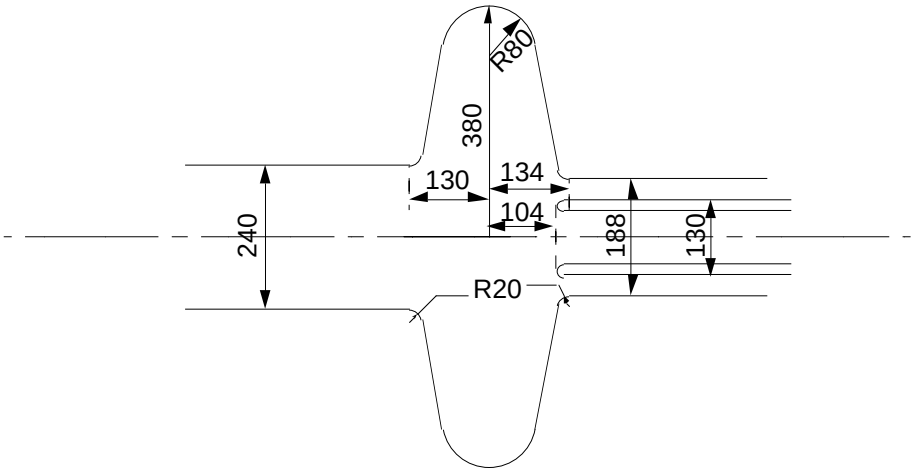

Figure 8.44: Cell shape of the round crab cavity.

The kick voltage, surface field, frequency and the R/Q value were calculated by using URMEL. The external Q-values were calculated with URMEL by changing the short position of the beam pipe by using Slater's formula [22]. The external Q-values for monopole modes were also calculated using SEAFISH by assuming a ferrite absorber

Table 8.12: RF properties of the round cell crab cavity.

Crabbing Mode (TM110)					
Frequency	500	(MHz)			
$R*/Q$	51.2	Ω/cell			
Kick voltage	(MV)	2.0	at E_{sp}=21.7 MV/m, H_{sp}=750 Oe		
Loss factor	(V/pC)	0.58			
Parasitic modes					
mode	frequency (MHz)	R/Q (Ω/cell)	Q_{ext} coax	Q_{ext} hollow	Q_{loaded} total
(Monopole modes)					
TM010	342	135	108	-	108
TM020	731	26	40	-	40
TM011	914	21	38	-	38
TM030	1107	1	141	165	76
TM021	$\sim$1200	4	$<$100	$<$100	$<$100
(Dipole modes)					
TE111	720	6	18	-	18
TM120	898	6	160	37	30
TE112	1048	1	$\sim$1000	186	$\sim$161
TE121	$\sim$1100			$<$100	$<$100

$R/Q = (V(r_0)^2/\omega U)/(kr_0)^{2m}$, where m=0 (monopole) and m=1 (dipole).
E_{sp} and H_{sp} is the surface peak electric and magnetic field, respectively.

attached to the beam pipe. The loss factor was calculated using TBCI. Figure 8.44 and Table 8.12 show the cell shape and RF properties of the final design. The Q-values of dangerous (high R/Q) monopole and dipole parasitic modes are damped to less than 100 with the coaxial beam pipe.

Squashed cell design

The design of the extremely polarized cell (squashed cell) was carried out by using MAFIA. In addition to the considerations taken in the round cell design, the frequency of the unwanted polarization of the TM110 mode was increased up to 700 MHz so that it propagates in the coaxial beam pipe. Figure 8.45 and Table 8.13 show the cell shape and RF properties of the final design. The Q-values of dangerous (high R/Q) monopole and dipole parasitic modes are damped to less than 100 with the coaxial beam pipe, similarly as for the round cell case.

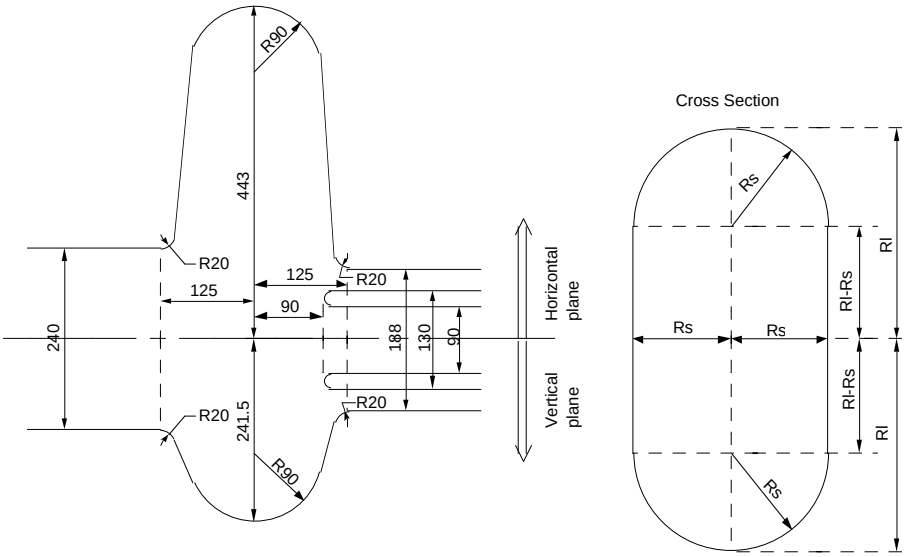

Figure 8.45: Cell shape of the squashed crab cavity. In the left side figure, the upper part shows the cross section in the horizontal plane, while the lower part shows that in the vertical plane.

Notch filter

Since the crabbing mode is a dipole mode and its frequency is below the cut-off of the coaxial beam pipe, the crabbing mode attenuates in the coaxial beam pipe. With our design, the crabbing mode is sufficiently attenuated and the power dissipation

Table 8.13: RF properties of the squashed cavity.

Crabbing mode							
Frequency	(MHz)	501.7					
$R*/Q$	(Ω/cell)	47.2					
Kick voltage	(MV)	2.0	at Esp=24.6 MV/m				
Parasitic modes							
MAFIA calculation						Model measurement	
mode	Frequency	R/Q	Q_{ext}	Q_{ext}	Q_{loaded}	Frequency	Q_{loaded}
*x-y-z	(MHz)	(Ω/cell)	coax	hollow	total	(MHz)	w/ferrite
[Monopole-like parasitic modes]							
TM1-1-0	413.3	99.8	96	-	96	415.0	123
TM3-1-0	670.6	17.3	76	-	76	672.6	50
TM1-1-1	946.6	9.9	118	-	118	938.6	$\sim$130
TM5-1-0	967.2	0.08	358	1273	279	966.2	$\sim$130
TM1-3-0	992.3	$\sim$2.2		379	$<$379	1000.1	$\sim$130
[Dipole-like parasitic modes]							
TE1-0-1	650.6	10.0	149	-	149	641.2	66
TE0-1-1	677.6	5.9	46	-	46	666.4	50
TM1-2-0†	686.5	23.0	37	-	37	686.5	22
TM4-1-0	792.9	8.1	97	99	49	789.4	70
TM3-2-0	870.0	1.1	161	56	42	891.0	60
TE3-0-1	964.1	1.2	144	63	44	936.1	$<$60
TM2-1-1	1024.9	1.2	29000	1414	1350		$<$350
TM2-3-0	1044.1	0.13	74000	578	574		$<$350
TE1-2-1	1095.7	0.28	$>$1000	82	82		

**Each mode number is identified by a rectangular coordinate system instead of a cylindrical coordinate system.

† – This mode is the unwanted polarization of the crabbing mode.

$R/Q = (V(r_0)^2/\omega U)/(kr_0)^{2m}$, where m=0 (monopole) and m=1 (dipole).

E_{sp} and H_{sp} is the surface peak electric and magnetic field, respectively.

For the convenience of comparison, the numbers quoted as the "model measurement frequency" are the actual frequency divided by three. This is because the module used in the test is a one-third scale test model.

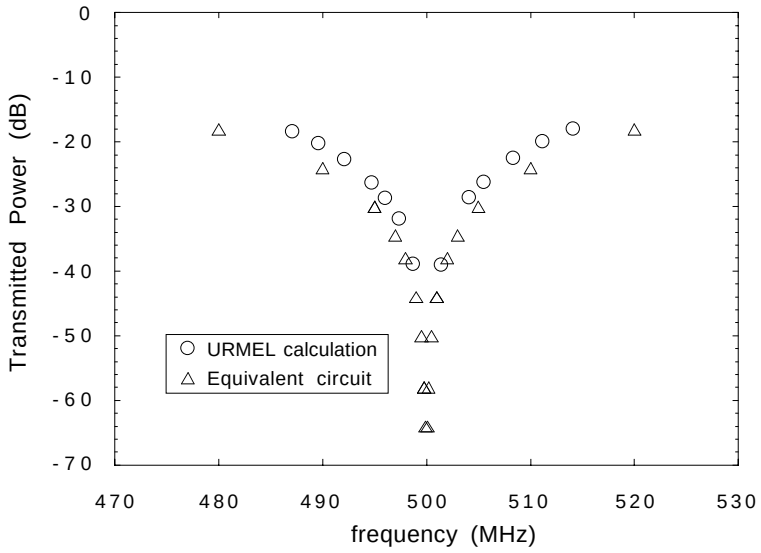

Figure 8.46: Frequency characteristics of the notch filter.

caused by this mode in the ferrite absorber at the end of the coaxial beam pipe is less than 1 kW. In a real cavity, however, some asymmetry due to machining errors or a misalignment of the coaxial beam pipe can transfer a part of the field energy of the crabbing mode into a TEM mode wave in the coaxial beam pipe. This TEM wave propagates down the coaxial beam pipe without attenuation, resulting in an increase of the dissipation power at the ferrite absorber. In order to avoid this, we have attached a notch filter which rejects the TEM-coupled crabbing mode back to the cavity.

Figure 8.46 shows the transmission property of the notch filter calculated using URMEL, together with the results of an analytical calculation of an equivalent circuit. If the resonant frequency of the filter is tuned within ± 0.5 MHz, a rejection rate higher than 50 dB is obtained. Even if the external Q for the crabbing mode might be reduced to 10^5 for a machining error or misalignment, this rejection of 50 dB assures an external Q of 10^{10}, which is sufficiently high.

The resonant frequency of the filter can be tuned by changing the filter iris. According to SUPERFISH calculations, the rate of the frequency shift is 1.8$\sim$3.6 MHz/mm.

In addition to the stopband at 500 MHz, the notch filter has a higher order TEM stopband at 1.45 GHz. Since there are several parasitic modes near this frequency, the hollow beam pipe opposite to the coaxial beam pipe has been opened wide enough so that the monopole modes above 1.3 GHz and the dipole modes above 1 GHz escape from the hollow beam pipe.

8.4.4 Model Measurements

In order to examine new ideas concerning the parasitic mode damping, we have built a one-third scale (L-band) round copper cavity and a one-third scale squashed aluminum cavity, with a coaxial beam pipe and ferrite absorbers. In addition, a high field performance test was made in liquid helium with a one-third scale round cell niobium cavity equipped with a coaxial beam pipe and a notch filter made of niobium.

Coaxial Beam Pipe Measurement

First, we measured the effect of the coaxial beam pipe on the damping property of the TM010 monopole mode, and on the Q-value of the crabbing mode. Figure 8.47 shows the loaded Q-value of the TM010 mode as a function of the penetration length of the inner conductor of the coaxial beam pipe into the cavity cell. The Q-value is damped below 100 with moderate penetration. The result agrees with a SEAFISH calculation within a factor of two.

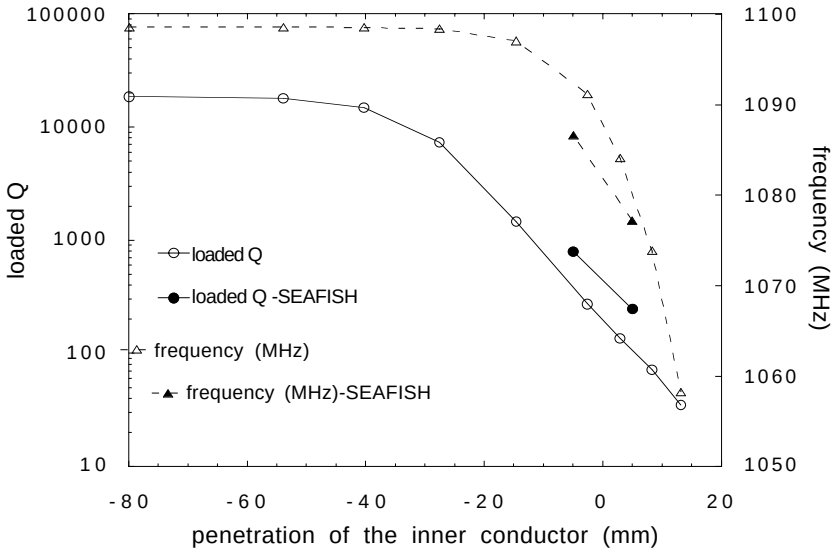

Figure 8.47: Damping of the TM010 mode in the crab cavity with a coaxial beam pipe.

Figure 8.48 shows how a misalignment of the inner conductor relative to the outer conductor affects the crabbing mode. When the inner conductor is aligned within 1 mm, the loaded Q-value with and without the coaxial beam pipe are nearly the same. Since the intrinsic Q of this copper cavity is 23000, this means that the external Q of the coaxial beam pipe, when thus-aligned, is at least on the order of 10^5. As mentioned earlier, the notch filter assures an additional 50 dB reduction, which makes

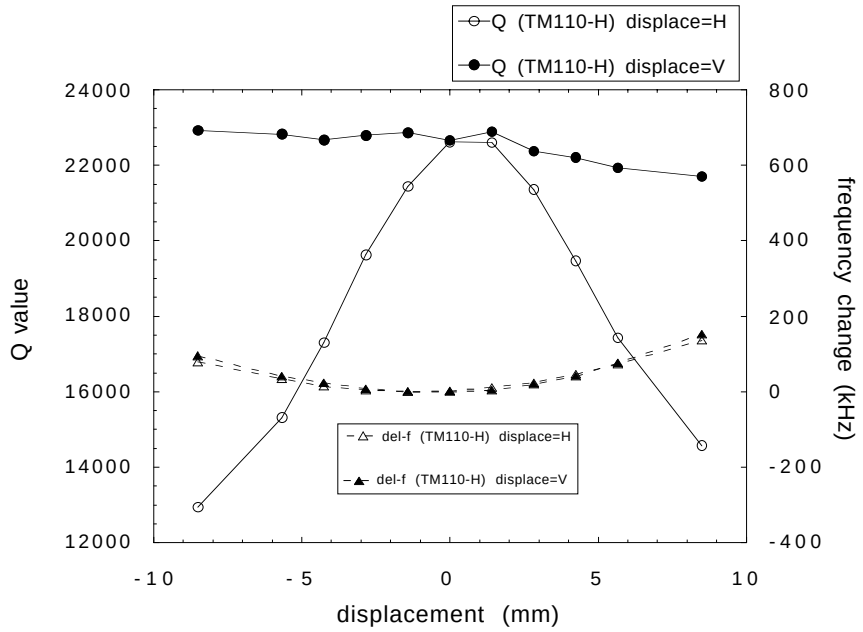

Figure 8.48: Effect of misalignment of the coaxial beam pipe on the crabbing mode.

the external Q-value above 10^{10}. Different sensitivities of the Q-values with respect to the horizontal and vertical displacements are considered to be due to the fact that the electric field at the tip of the coaxial beam pipe is polarized horizontally. Since this is a result of the one-third scale model, the alignment tolerance for the full-scale cavity is expected to be about 3 mm, which can be easily achieved.

Squashed Cavity Model Measurement

The resonant frequency and the damping properties have been measured with the one-third scale squashed crab cavity. Figure 8.49 shows the frequency spectrum with and without the coaxial beam pipe and ferrite absorbers. The measured frequency of each mode and the Q-values with the ferrite absorbers are listed in Table 8.13 together with the results of MAFIA calculations. As expected from the MAFIA calculation, all the dangerous monopole and dipole modes are damped to less than on the order of 100, including the unwanted polarization of the crabbing mode. A high Q-value is maintained for the crabbing mode. The external Q-value of the crabbing mode via the coaxial beam pipe was estimated from the measured loaded Q-value with and without the coaxial beam pipe. It has been estimated to be at least on the order of 10^5, which is the same result as in the case of a round-cell cavity.

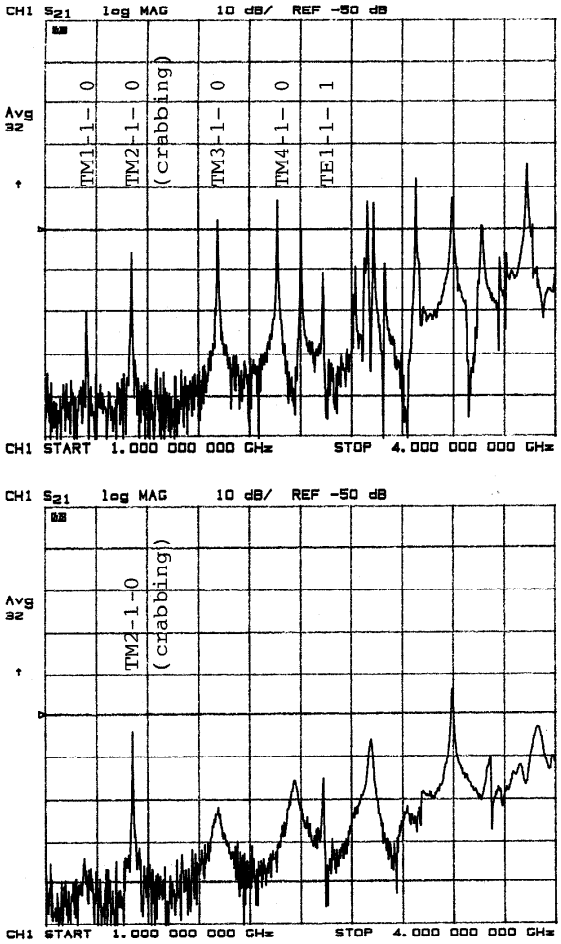

Figure 8.49: Frequency spectrum of a squashed crab cavity: (upper) without a coaxial beam pipe and (lower) with a coaxial beam pipe and a ferrite absorber.

High Field Performance

The kick voltage required for crabbing is 1.4 MV which corresponds to a surface peak field of 15 MV/m. According to the present technology of superconducting accelerating cavities at around 500 MHz, a surface peak field of 20 MV/m can be easily achieved, which corresponds to an accelerating gradient of about 10 MV/m . For the crab cavity, it is still crucial to confirm high field performances, because it has several new features, such as the coaxial beam pipe and the notch filter on the beam pipe, which might cause some limitation to the field due to multipactoring or other causes.

Figure 8.50 shows the one-third scale niobium cavity mounted on a test stand. Measurements of the TM110 mode at 1.5 GHz were made when the system was cooled down to 1.5 K in liquid helium. At a surface peak field of 1 MV/m a multipactoring was encountered, which is considered to have occurred at the coaxial beam pipe. The multipactoring was processed away after an hour of RF processing. Figure 8.51 shows the Q-value versus the surface peak field. The maximum surface peak field was 25 MV/m, where we experienced field emission. The kick voltage required for KEKB has been achieved with a sufficiently high Q-value. Thus, the feasibility of the crab cavity has been realistically demonstrated.

Figure 8.50: One-third scale Niobium round-cell crab cavity mounted on a test stand.

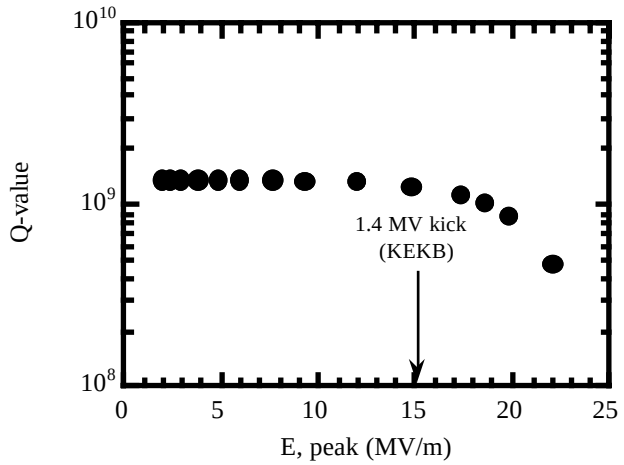

Figure 8.51: Surface peak field vs Q-value measured in liquid helium.

8.4.5 R&D Schedule

In the R&D program of the crab cavity at KEK, we are planning to fabricate full-scale superconducting cavities in three years. For the base line design of the crab cavity, we have adopted a squashed cell shape cavity scheme, which was designed and extensively studied at Cornell for CESR-B under the KEK-Cornell collaboration. The R&D work on the crab cavities at KEK will take advantage of the fabrication and measurement techniques of niobium superconducting cavities that have been established through constructing the TRISTAN SCRF system.

Figure 8.52 shows the R&D schedule of the crab cavity for KEKB. At the first stage of the R&D program, a test stand with a vertical cryostat and an RF measurement system for a one-third scale model will be completed by the end of JFY1994. The one-third scale round cell shape Nb cavity that has been designed, fabricated and tested at Cornell for CESR-B will be tested again at KEK. Three one-third scale squashed cell shape model cavities will be designed and built to establish the fabrication technique for a non-axially symmetric structure by the end of FY1995. At the final stage of the R&D, two full-scale squashed cell shape prototype cavities, equipped with coaxial beam pipe and notch filter, will be designed and fabricated. After an RF test in a vertical cryostat, one of these cavities will be installed in a horizontal cryostat. The prototype cavity in a horizontal cryostat will be cooled down by a helium refrigerator, and a high power RF test will be conducted to confirm the performances that are required for KEKB.

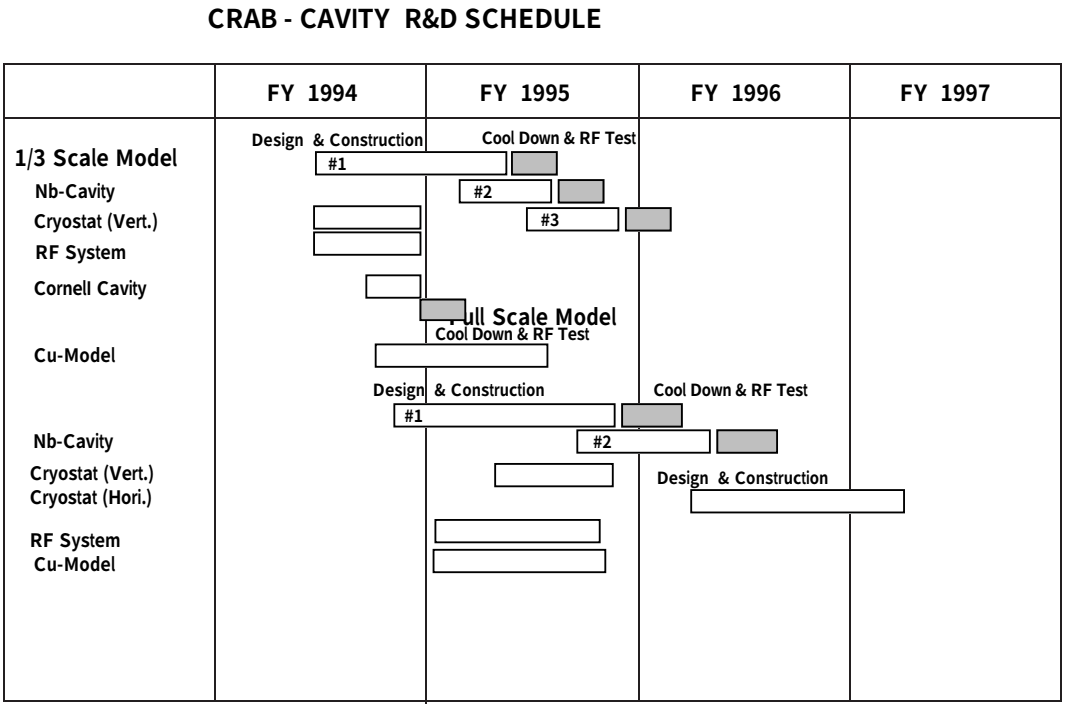

Figure 8.52: R&D schedule of the crab cavity at KEK.

Bibliography

[1] Y. Yamazaki and T. Kageyama, *Particle Accelerators* **44** 107 (1994).

[2] T. Shintake, *Particle Accelerators* **44** 131 (1994).

[3] K. Akai and Y. Yamazaki, *Particle Accelerators* **46** 197 (1994).

[4] Z. D. Farkas *et al.*, *Proc. 9th Int. Conf. on High Energy Accel.* , SLAC 576 (1974).

[5] K. Akai, J. Kirchgessner, D. Moffat, H. Padamsee, J. Sears, T. Stowe and M. Tigner, *Proc. B Factories* **SLAC-400** 181 Apr. 6-10 SLAC (1992), and *Proc. 15th Int. Conf. on High Energy Accel.* 757 (1992).

[6] T. Shintake, *Jpn. J. Appl. Phys.*, **31** L1567 (1992).

[7] HP Part No. 85180A., HP Corp.

[8] N. Akasaka, T. Kageyama and Y. Yamazaki, *Proc. 4th European Part. Accel. Conf.* , 2137 (1994).

[9] F. J. Sacherer, *IEEE Trans. Nucl. Sci.* **NS-20** 825 (1973).

[10] T. Kageyama, N. Akasaka, Y. Takeuchi and Y. Yamazaki, *Proc. 4th European Part. Accel. Conf.* , 2098 (1994).

[11] H. Matsumoto *et al.*, *Proc. 9th Linear Accelerator Meeting in Japan*, Kyoto, pp. 124-126 (1984).

[12] S. Isagawa, *et al.*, *Proc. IEEE Part. Accel. Conf.* , Washington, D.C., 1934 (1987).

[13] S. Yamaguti, *et al.*, *IEEE Trans. Nucl. Sci.* , **39, No. 2**, 278 (1992).

[14] M. Akemoto, KEK preprint 91-45 (1991).

[15] S. Mitsunobu, private communication.

[16] A. Ueno, *et al.*, KEK preprint 94-117 (1994).

[17] F. Naito, *et al.*, KEK preprint 90-99 (1990).

[18] F. Naito, *et al.*, KEK preprint 94-115 (1994).

[19] T. Weiland, DESY report 83-073, (1983).

[20] T. Takahashi *et al.*, *Proc. 9th Symposium on Accelerator Science and Technology*, KEK, 327 (1993).

[21] T. Kageyama, *Proc. 15th Linear Accelerator Meeting in Japan*, (1990).

[22] J. C. Slater, *Microwave Electronics*, Van Nostrand (1950).

[23] K. Asano *et al.*, submitted to the 1995 Part. Accel. Conf.

[24] T. Tajima *et al.*, *Proc. 6th Workshop on RF Superconductivity*, CEBAF, 962 (1993).

[25] K. Akai and E. Ezura, *Proc. 4th European Part. Accel. Conf.* , 1141 (1994).

[26] R. B. Palmer, SLAC-PUB 4707 (1988).

[27] K. Oide and K. Yokoya, *Phy. Rev.* **A40** 315 (1989).

[28] K. Akai, J. Kirchgessner, D. Moffat, H. Padamsee, J. Sears and M. Tigner, *Proc. IEEE Part. Accel. Conf.* (1993).

Chapter 9

Magnet System

This chapter discusses the parameters and the design of the magnets to use at KEKB. Plans on the magnet power supply systems, magnet installation procedure and alignment strategies are also presented. Special magnets required near the beam collision point are discussed in a separate chapter on the Interaction Region.

9.1 Magnets in the Arc and Straight Sections

Tables 9.1 and 9.2 tabulates the magnets that are required for KEKB. The tolerances on the multipole field errors for the dipole and quadrupole magnets have been determined from studies on the expected dynamic aperture and emittance coupling. Table 9.3 summarizes the required field qualities. It has been found that these requirements are well met by existing magnets in the TRISTAN Main Ring (hereafter abbreviated as "TR"). Table 9.4 shows the field quality achieved by TR magnets for reference.

From considerations on the cost and schedule, a decision has been made to make maximum use of magnets from the existing TR. However, it is still necessary to fabricate new magnets to fill the requirements for KEKB. When new magnets are built, they will be all made of lamination (the TR magnets to be re-used are also all lamination-type). Steering correction magnets will be also built with lamination, since very fine and rapid beam control is required at KEKB. The core material will be 0.5 mm-thick silicon steel, with inorganic insulation layers on both sides. The specifications for the lamination include: induction $B^{50} > 1.6$ T and coercive force $H_c^{1.5} < 70$ A/m with $\Delta B^{50}/B^{50} < \pm 1$ % and $\Delta H_c^{1.5}/H_c^{1.5} < \pm 5$ %.

Compared to the TR magnets, the LER magnets generally will have a wider gap, larger bore and shorter length. The HER magnets have similar dimensions as TR.

Designation	Half gap or bore radius (mm)	Lamination length (m)	B (T), B' (T/m), or B'' (T/m^2)	Number of magnets	Usage	Comments
Dipole magnets						
B_{arc}	57	0.76	0.848	108	normal bend	new
	57	0.76	0.848	8	half bend	new
	57	0.76	0.08	2	crossing	new
	57	0.76	0.848	16	chicane	new
B_{lc}	57	2.5	0.42	30	local correction	new
B_v	57	1.5	0.2	4	vertical bend	new
B_t	57	0.3	0.65	3	near IR	new
Quadrupole magnets						
Q_{arc}	55	0.4	10.3	436	arc, straight	new
Q_{rf}	80	0.5	6.6	16	RF section	new
Sextupole magnets						
SxF	56	0.39	350	52	focus	recycle
SxD.1	56	0.39	350	44	defocus	recycle
SxD.2	56	0.54	350	8	defocus	recycle

Table 9.1: LER Magnet types.

Designation	Half gap or bore radius (mm)	Lamination length (m)	B (T), B' (T/m), or B'' (T/m^2)	Number of magnets	Usage	Comments
Dipole magnets						
B_{arc}	35	5.804	0.3	112	normal bend	recycle
	35	5.804		2	crossing	recycle
Quadrupole magnets						
Q_{arc}	50	0.6	10.9	144	arc, straight	new
Q_{rf}	80	1.0	6.6	32	RF section	new
QA	50	0.762	8.5	184	arc, straight	recycle
QB	50	0.95	8.5	92	arc, straight	recycle
Sextupole magnets						
SxF	56	0.54	350	52	focus	recycle
SxD	56	0.80	350	52	defocus	new

Table 9.2: HER Magnet types.

	Tolerance at 50 mm radius
Dipole magnets	$B_3/B_1 < 0.12$ %
	$B_5/B_1 < 0.45$ %
Quadrupole magnets	$B_6/B_2 < 0.12$ %
	$B_{10}/B_2 < 0.14$ %

Table 9.3: Tolerances of systematic multipole errors

Dipole		
Field uniformity within the aperture ($\pm$60 mm)	$< \pm 2 \times 10^{-4}$	
Integral dipole strength error $\Delta L_B/L_B$	$\sigma = 4.1 \times 10^{-4}$	for $B = 0.97$ kG
	4.0×10^{-4}	4.2
	4.8×10^{-4}	5.2
	0.028	remanent
Gap error $\Delta g/g$	$\sigma = 2.8 \times 10^{-4}$	
Core length error $\Delta L/L$	$\sigma = 0.8 \times 10^{-4}$	
Quadrupole (QA)		
High multipoles at aperture / Quadrupole field	$< 2 \times 10^{-4}$	with end shim
Integral quadrupole strength error $\Delta L_q/L_q$	$\sigma = 4.2 \times 10^{-4}$	for $g = 4.7$ T/m
	7.9×10^{-4}	18.2
	9.6×10^{-4}	21.
	0.046	remanent
Bore error $\Delta r/r$	$\sigma = 1.2 \times 10^{-4}$	
Core length error $\Delta L/L$	$\sigma = 1.7 \times 10^{-4}$	
Quadrupole (QB)		
High multipoles	almost the same as QA	
Integral quadrupole strength error $\Delta L_q/L_q$	$\sigma = 4.0 \times 10^{-4}$	for $g = 4.7 \sim 21.7$ T/m
Insertion Quadrupole Magnets		
Integral quadrupole strength error $\Delta L_q/L_q$	$\sigma = 5.0 \times 10^{-4}$	for $g = 3.5 \sim 16$ T/m
Sextupole Magnets		
High multipoles at aperture / Sextupole field	18 poles $< 3 \times 10^{-3}$	
	others $< 1 \times 10^{-3}$	
Integral sextupole strength error $\Delta L_s/L_s$	$\sigma = 2.1 \times 10^{-3}$	for SXF at 350 T/m^2
	2.3×10^{-3}	for SXD

Table 9.4: Performance of the TRISTAN magnets for reference.

Shorter magnets are known to have inferior field qualities, because of increased end-field effects. In addition, the accuracy of 2-dimensional calculations will be less reliable for shorter magnets. However, we believe that the field qualities similar to the TR magnets would be possible with a careful design and fabrication process control.

The physical designs have been made for the main dipole and quadrupole magnets, the sextupole and vertical steering magnets used for the LER and HER. The 2-dimensional magnetic field code POISSON and the 3-dimensional code OPERA-3d have been used for field calculations. The full engineering design of the KEKB magnet system will be completed as soon as the final beam optics design is finalized.

9.1.1 LER

Table 9.1 summarizes the magnets that are required for the LER. Four types of dipole bend magnets are needed in the LER: B_{arc}, B_{lc}, B_v and B_t. The LER also requires two types of quadrupole magnets (Q_{arc} and Q_{rf}), and two types of sextupole magnets (SxF_{TR} and SxD_{TR}). All of them except the sextupole magnets will be newly fabricated. The LER sextupole magnets will be recycled from the TR.

Dipole Magnets

The LER requires 171 dipole magnets in total. They include 134 B_{arc}, from which 108 B_{arc} will be used for normal bends, 8 for half bends, 2 for beam crossing (the LER-HER cross-over) and 16 for the chicane structure. From the special dipole magnets, 30 B_{lc} will be used for local chromaticity correction, 4 B_v for vertical bends and 3 B_t for special use near the IR section located near the Tsukuba experimental hall.

The mechanical and electric parameters of B_{arc} are listed in Table 9.5. The lamination core length in the table does not include the side plates and electrodes. Thus the physical magnet sizes will be larger. A cross section view of the preliminary design of a LER dipole magnet (B_{arc}) is shown in Figure 9.1. The final designs of the special dipole magnets have not been fixed yet. We will proceed with physical designs of these magnets as soon as their final parameters are finalized.

Quadrupole Magnets

There are 452 quadrupoles in the LER. The 436 Q_{arc} will be used for the arc and the straight sections, except for the beam line that includes RF cavities. For the RF sections, 16 Q_{rf} which have larger aperture will be used. The mechanical and electric parameters of Q_{arc} and Q_{rf} are listed in Tables 9.6 and 9.7. Figure 9.2 shows a cross section view of the preliminary design of a LER quadrupole magnet (Q_{arc}).

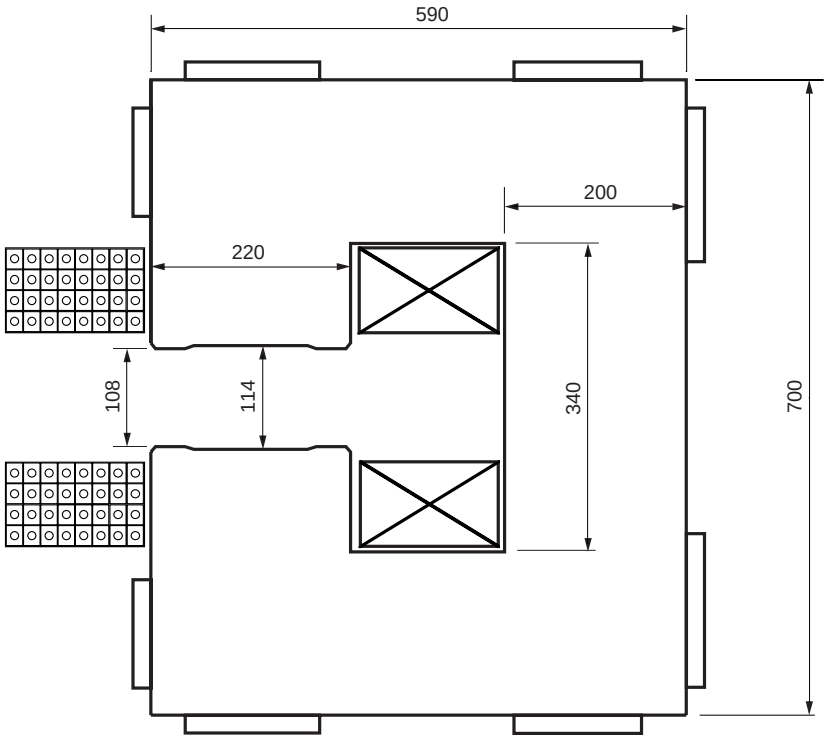

Figure 9.1: A cross section view of the preliminary design of a LER dipole magnet (B_{arc}).

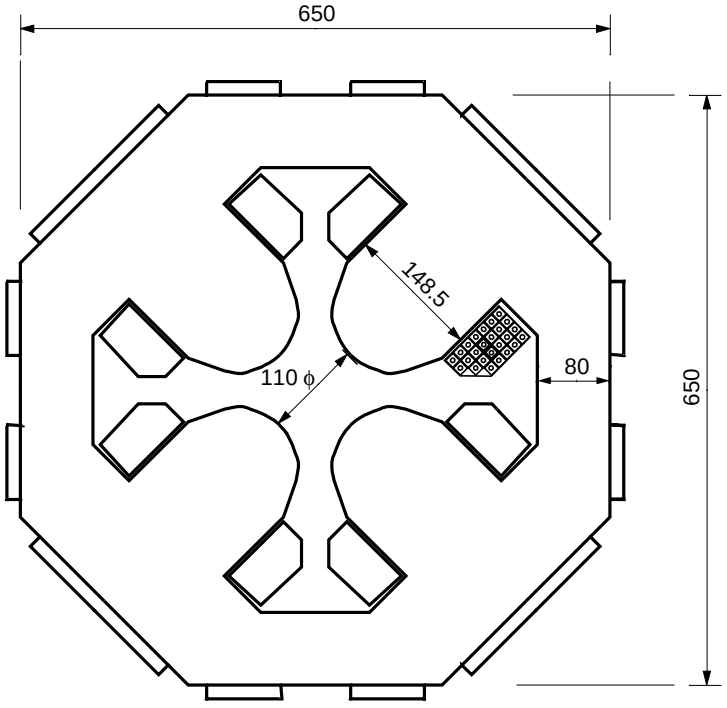

Figure 9.2: A cross section view of the preliminary design of a LER quadrupole magnet (Q_{arc}).

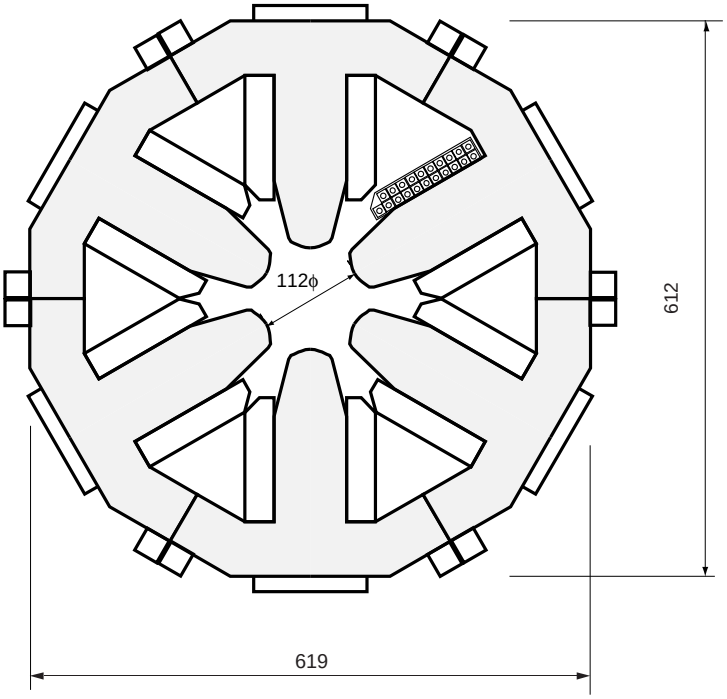

Figure 9.3: A cross section view of the preliminary design of a LER sextupole magnet.

Sextupole Magnets

The mechanical and electric parameters of the sextupoles are listed in Table 9.9. The LER will require 104 sextupoles, which consist of 56 SxF's and 48 SxD's. The present plan is to re-use the TR sextupoles, SxF_{TR} and SxD_{TR}. For each of SxF_{TR} and SxD_{TR} from TRISTAN, 96 units out of 120 are expected to be negligibly radio-active and thus adequate for re-use. The 96 SxF_{TR}'s will be recycled to provide all of the 56 SxF's and 40 SxD's. The remaining 8 SxD's will come from SxD_{TR}'s.

Radiation damages on the TR magnets will be closely inspected in the summer of 1995. Exactly which part (iron core and the coils) of the TR magnets should be reused will be decided based on the results of this inspection.

Figure 9.3 shows a cross section view of the preliminary design of a LER sextupole magnet. The HER sextupole magnets will have a similar cross section shape.

Steering Correction Magnets

The parameters of the vertical steering magnets are given in Table 9.10. The LER will require 450 vertical steering magnets, which will be located adjacent to each quadrupoles. The maximum kick angle of 1 mrad is assumed for the vertical steering magnets. Almost same number of horizontal steering magnets would be necessary

in the future.

Wiggler Magnets

The wiggler magnets will be used for the LER to control the radiation damping time. The field strength of the wiggler is the same as the arc dipole magnets. The total length of wigglers will be 96 m. This is close to the total length of the arc dipoles. Detailed design of the wiggler magnet is being worked out.

9.1.2 HER

Table 9.2 summarizes the magnets that are required for the HER. There will be one type of bending magnet called B_{arc}, 4 types of quadrupoles Q_{arc}, Q_{rf}, QA and QB, and 2 types of sextupoles SxF and SxD. The Q_{arc}, Q_{rf} and SxD will be newly fabricated, while the others will be recycled from TR. Details of the recycle plan will be determined after the inspections on the TR magnets planned in the summer of 1995.

Dipole Magnets

The HER needs 114 B_{arc}'s, in which 112 B_{arc} will be used for the arc and 2 for beam crossing. The TR bending magnets will be recycled for these dipole magnets. The mechanical and electric parameters of B_{arc} are listed in Table 9.5.

Quadrupole Magnets

The HER requires 452 quadrupole magnets in total. The 144 Q_{arc} and 32 Q_{rf} will be newly fabricated. The 184 QA and 92 QB will be recycled from TR for the arc and straight sections except the beam line that includes the RF cavities. The Q_{rf}'s, which have 80 mm bore radius, will be used for the RF sections. The mechanical and electric parameters of these quadrupole magnets are listed in Tables 9.6, 9.7 and 9.8.

Sextupole Magnets

There will be 104 sextupoles in HER; 52 SxF's and 52 SxD's. At present, the SxF's will use the SxD_{TR}'s recycled from TR, while 52 SxD's with 0.8 m length will be newly fabricated. The mechanical and electric parameters of the sextupoles are listed in Table 9.9.

Dipole : $\mathbf{B}_{arc}$	**LER**	**HER**
Number of Magnets	134	114
Half gap	57 mm	35 mm
Minimum half gap	54 mm	33.15 mm
Lamination core length	0.76 m	5.804 m
Total length	< 1.27 m	< 6.18 m
Full width (without electrodes)	~ 0.8 m	~ 0.62 m
Required field strength	0.76 T	0.258 T
Current $\times$ turns/pole	1250 A $\times$ 32	840 A $\times$ 10
$B_{0,max}$	0.848 T	0.3 T
Resistance	10.0 mΩ	14.0*, 10.1^{tr} mΩ
Inductance	$11 \sim 12$ mH	12.3 mH
Voltage	12.5 V	11.76*, 8.48^{tr} V
Power	15.6 kW	9.9*, 7.1^{tr} kW
Correction coil/pole	10 A $\times$ 40	10 A $\times$ 10
Weight (core + coil)	$\sim$ 3000 kg (2400 kg + 540 kg)	$\sim$ 9600 kg

Table 9.5: Parameters of the dipole magnets for the LER and HER. The tag '*' indicates the value for new coils. The tag 'tr' is for the coils recycled from the TRISTAN Main Ring.

Steering Correction Magnets

The HER will require 450 vertical steering correction magnets. A vertical correction magnet will be installed adjacent to each individual quadrupole magnet. The requirement on the kick angle is maximum 1 mrad. Approximately the same number of horizontal steering correction magnets will be necessary in the future. The parameters of the steering correction magnets are listed in Table 9.10.

9.1.3 Magnetic Field Measurement

Newly fabricated and recycled magnets will be exercised on a test bench, and their field qualities and magnetic axes will be measured. Since the magnetic field strength is very sensitive to the temperature of the magnet and the cooling water, close attentions will be paid to measure and control such temperature during the test.

Quadrupole : $\mathbf{Q}_{arc}$	**LER**	**HER**
Number of Magnets	436	144
Bore radius	55 mm	50 mm
Lamination core length	0.4 m	0.6 m
Total length	< 0.63 m	< 0.83 m
Half width (without electrodes)	~ 0.35 m	~ 0.35 m
Required field strength	8.5 T/m	11 T/m
Current $\times$ turns/pole	500 A $\times$ 25	500 A $\times$ 22
$B'_{0,max}$	10.3 T/m	10.9 T/m
Resistivity	25.1 mΩ	32.2 mΩ
Inductance	~ 22 mH	~ 30 mH
Voltage	12.6 V	16.1 V
Power	6.28 kW	8.04 kW
Correction coil/pole	10 A $\times$ 12	10 A $\times$ 12
Weight (core + coil)	~ 1230 kg (1100 kg + 130 kg)	~ 1750 kg (1550 kg + 160 kg)

Table 9.6: Parameters of the arc quadrupole magnets for the LER and HER.

Quadrupole : $\mathbf{Q}_{rf}$	**LER**	**HER**
Number of Magnets	16	32
Bore radius	80 mm	80 mm
Lamination core length	0.5 m	1.0 m
Total length	< 0.75 m	< 1.25 m
Half width (without electrodes)	~ 0.40 m	~ 0.40 m
Required field strength	5.1 T/m	6.0 T/m
Current $\times$ turns/pole	500 A $\times$ 34	500 A $\times$ 34
$B'_{0,max}$	6.6 T/m	6.6 T/m
Resistivity	52 mΩ	86 mΩ
Inductance	~ 27 mH	~ 49 mH
Voltage	26 V	43 V
Power	12.9 kW	21.5 kW
Correction coil/pole	10 A $\times$ 17	10 A $\times$ 17
Weight (core + coil)	~ 1700 kg (1480 kg + 200 kg)	~ 3150 kg (2820 kg + 300 kg)

Table 9.7: Parameters of the quadrupole magnets in the RF sections for the LER and HER.

Quadrupole : QA, QB	**HER: QA** (recycled from TR)	**HER: QB** (recycled from TR)
Number of Magnets	184	92
Bore radius	50 mm	50 mm
Lamination core length	0.762 m	0.95 m
Total length	< 1.0 m	< 1.2 m
Half width (without electrodes)	0.42 m	0.42 m
Required field strength	T/m	T/m
Current $\times$ turns/pole	500 A $\times$ 17	500 A $\times$ 17
$B'_{0,max}$	8.5 T/m	8.5 T/m
Resistivity	13.0 mΩ	15.2 mΩ
Inductance	15.5 mH	19 mH
Voltage	6.5 V	7.6 V
Power	3.25 kW	3.8 kW
Correction coil/pole	10 A $\times$ 10	10 A $\times$ 10
Weight (core + coil)	$\sim$ 4500 kg	$\sim$ 5600 kg

Table 9.8: Parameters of the QA and QB quadrupole magnets for the HER. Calculations have been made with an assumption that these magnets are recycled from the TRISTAN main ring.

Sextupole	**LER**	**HER**
	Sx: 0.39 m long (recycled from SXF_{TR})	**SxF: 0.54 m long** (recycled from SXD_{TR})
Number of Magnets	96	52
Bore radius	56 mm	56 mm
Lamination core length	0.39 m	0.54 m
Total length	< 0.51 m	< 0.66 m
Half width (without electrodes)	~ 0.36 m	~ 0.36 m
Required field strength	350 T/m^2	350 T/m^2
Current $\times$ turns/pole	425 A $\times$ 21	425 A $\times$ 21
$B''_{0,max}$ measured	350 T/m^2	350 T/m^2
Resistivity	32.8 mΩ	40.9 mΩ
Inductance	15.5 mH	19 mH
Voltage	13.9 V	17.4 V
Power	5.9 kW	7.4 kW
Correction coil/pole		
Weight (core + coil)	830 kg $(720 + 110)$	1100 kg $(960 + 140)$
	Sx: 0.54 m long (recycled from SXD_{TR})	**SxD: 0.8 m long** (new)
Number of Magnets	8	52
Bore radius	56 mm	56 mm
Lamination core length	0.54 m	0.8 m
Total length	< 0.66 m	< 0.92 m
Half width (without electrodes)	~ 0.36 m	~ 0.36 m
Required field strength	350 T/m^2	350 T/m^2
Current $\times$ turns/pole	425 A $\times$ 21	425 A $\times$ 21
$B''_{0,max}$ measured	350 T/m^2	350 T/m^2
Resistivity	40.9 mΩ	56.6 mΩ
Inductance	19 mH	28 mH
Voltage	17.4 V	24.1 V
Power	7.4 kW	10.2 kW
Correction coil/pole		
Weight (core + coil)	1100 kg $(960 + 140)$	1590 kg $(1390 + 200)$

Table 9.9: Parameters of the sextupole magnets for the LER and HER.

	LER	HER
Steering: STV		
Number of Magnets	450	450
Bore radius	80 mm	80 mm
Lamination core length	0.2 m	0.2 m
Total length	< 0.3 m	< 0.35 m
Required kick angle	1 mrad	1 mrad
Current $\times$ turns/pole	5 A $\times$ 760	5 A $\times$ 1700
Steering: STH		
Number of Magnets	450	450
Bore radius	80 mm	80 mm
Lamination core length	0.2 m	0.2 m
Total length	< 0.3 m	< 0.35 m
Required kick angle	1 mrad	1 mrad
Current $\times$ turns/pole	5 A $\times$ 760	5 A $\times$ 1700

Table 9.10: Parameters of the steering correction magnets for the LER and HER.

Dipole Magnets

A long flip coil and a small flip coil will be used for measurements of dipole magnets. The integral dipole field is obtained by measuring the voltage induced on the long flip coil which rotates in the magnetic field. The small flip coil is used for field mapping. This small flip coil system is mounted on 3-axes mover, and it measures the magnetic field in the fiducial volume point by point.

The absolute values of the integral and the center field strength will be also measured by using some devices. These measurement systems will be developed soon.

Quadrupole and Sextupole Magnets

The magnetic field of quadrupole and sextupole magnets of KEKB will be measured by harmonic coil (rotating coil) systems. Each harmonic coil system consists of one long coil and three short coils located at the center and both ends. The long coil measures the integral field strength directly and its quality. The center field is measured by the middle short coil. The two short coils at both ends are used to assess the end effects and to locate the magnetic axis to the measuring system.

Before conducting field measurements, the magnet should be pre-aligned to the measuring bench. A laser beam is used as the reference axis. A 3-axes magnet mover

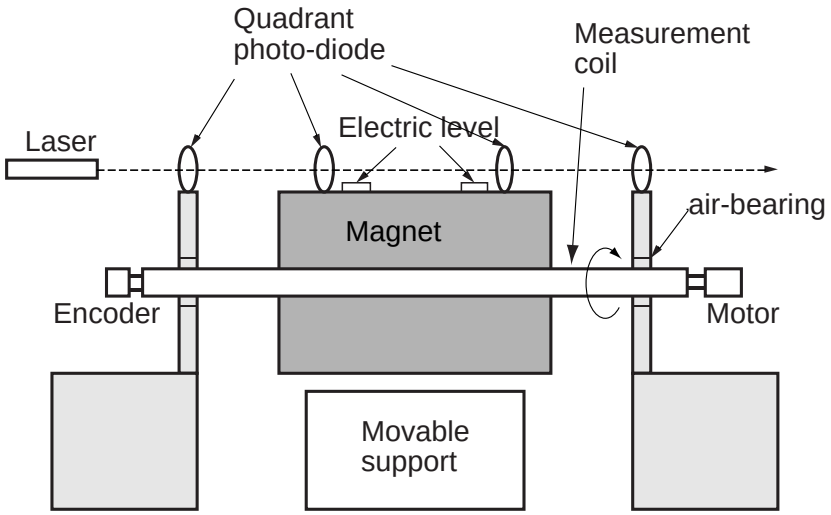

Figure 9.4: A schematic view of the magnetic field measurement system using a rotating coil.

is used to control the magnet position, which is monitored by electric level gauges. The laser beam is also used for checking the positions of surveying targets on each magnet relative to the magnetic axis. Figure 9.4 shows the principle of field measurements with a rotating coil.

The small flip coil for the dipole field mapping can be also used for field mapping of the quadrupoles and sextupoles. These harmonic coil systems, some devices for the absolute value measurements and the 3-axes magnet movers should be developed soon.

9.1.4 Near-Future Plans

Conceptual designs have been done on the main dipole, quadrupole, sextupole and vertical steering magnets for both the LER and HER. As soon as the beam optics design is finalized, we will proceed with complete engineering designs of all the magnets. Various cost saving measures will be taken, in as much as requirements on the accelerator performance allows. Optimization of the magnet parameters will be made to make maximum use of the existing power supplies, which will be recycled from TRISTAN.

Since KEKB accelerator must handle high intensity beams with small bunch sizes, the magnet system needs a very precise control. Temperature measurements of the magnets, cooling water and tunnel air are planned to analyze variations of beam parameters. Magnetic flux monitors may be also useful.

9.2 Magnet Power Supplies and Cabling

9.2.1 Magnet Power Supply

The magnet power supply units required at KEKB are listed in Table 9.11. The total number of large power supplies for the dipole, quadrupole and sextupole magnets is 382. From the existing TRISTAN facility about 80 units will be recycled for operating the dipole and quadrupole magnets at KEKB. Thus the remaining 300 units, which include most of the sextupole magnet power supplies, need to be newly installed.

The output voltage and the current from the power supplies have been determined by considering the impedance of power feeding cables with adequate margins for the output voltage. The designs of the power supply units assume that a substantial fraction of dipole, quadrupole and sextupole magnets will be recycled from TRISTAN, as stated earlier. It should be noted that the specifications for the HER magnet power supplies are subject to change, if the coils are rewound for those TRISTAN magnets.

The maximum output current of the majority of large power supplies is set to be 500 A for two reasons: (1) the cost of power feeding cables, which are very long, can be reduced by using relatively thin cables, and (2) the room that is available on the cable ladders in the tunnel is limited, such that not much thick cables can be used. With this system design choice, both the DC output voltage and the current of large power supplies are smaller than the case with TRISTAN.

For the power supplies that are recycled from TRISTAN, the DCCT (DC Current Transformer) heads will be replaced by new units, which have an optimized range for current measurements at KEKB. If it is found necessary for improved power factor and better regulation, three-phase AC transformers will be applied to the input of some of the power supplies.

Table 9.12 shows a list of stability requirements and limits on the ripple content for magnet power supplies at KEKB.

The requirements on the steering correction magnets at KEKB are much more stringent than the case with TRISTAN. Adequate power supplies for the steering correction magnets will be newly developed and will be fabricated.

9.2.2 Installation

Along the TRISTAN tunnel there exist 8 power supply stations: 4 big and 4 small. Most of the TRISTAN magnet power supplies that are housed in the 4 big supply stations will be re-used for KEKB with some improvements, as discussed earlier.

Ring	Magnet type	Voltage (V)	Current (A)	Number of units	Total
LER	Dipole	1400	1250	1	
		120	1250	2	
		70	1250	2	
		30	1250	2	
			1250	15	
	Wiggler		1250	8	
					30
	Quadrupole	700	500	4	
		600	500	1	
		400	500	2	
		90	500	5	
		60	500	21	
		40	500	26	
		30	500	59	
				2	120
	Sextupole	40	425	52	
			425	2	54
	Steering			886	886
HER	Dipole	1400	840	1	
		40	840	4	
		20	840	3	
			840	9	17
	Quadrupole	900	500	1	
		500	500	3	
		400	500	4	
		300	500	3	
		100	500	10	
		60	500	12	
		30	500	46	
		20	500	29	
			500	1	109
	Sextupole	60	425	24	
		40	425	28	52
	Steering			886	886

Table 9.11: The list of magnet power supplies required at KEKB.

Magnet type	Stability	Ripple content
Dipole	1×10^{-4} / 8 h	5×10^{-5}
Quadrupole	1×10^{-4} / 8 h	1×10^{-5}
Sextupole	5×10^{-4} / 1 h	5×10^{-4}
Steering correction	5×10^{-4} / 8 h	5×10^{-5}

Table 9.12: Stability requirements and limits on the ripple content for magnet power supplies at KEKB

The four small power supply stations will house the power supplies as follows: 12 units for quadrupole, 26 for sextupole and 443 for steering correction magnets.

In addition, a part of Oho, Fuji, and Nikko experimental halls, and the Tsukuba RF power station will be used for remaining dipole, wiggler and quadrupole magnet power supplies. A multi-stage structure will be built in each of these halls to make maximum use of available areas.

9.2.3 Cooling Water

The large power supplies in the existing 4 big power supply stations are all cooled by pure water. The consumption of pure water has been about 750 ℓ/min for each power station in the TRISTAN MR operation. The requirement will be reduced to roughly a half for KEKB.

In a new power supply station in the Oho experimental hall, 14 large power supplies (a few hundred KW each) need to be installed. Those power supplies will be water-cooled, considering the limited air conditioning capacity of the station.

All other power supplies that are newly built will be air-cooled for improved handling in the maintenance work.

9.2.4 Electric Power

The maximum total electric power of the magnet power supplies is 19 MW. Considering the power factor, the capacity of the input power line will somewhat exceed 20 MVA. However, during actual accelerator operation the total electric power is estimated to be less than 15 MW. Overall, it is not considered necessary to increase the power of the input power line.

9.2.5 Wiring of DC Power Feed Cables

Approximately 500 km of 2-core cables in total is required for the steering correction magnets in the entire KEKB. The total length of the cables for quadrupole magnets will be roughly 100 km. Thus the cabling cost can be quite large. As discussed earlier, the maximum DC current of most of large power supplies is kept below 500 A to alleviate this situation. Still the weight of cable bundles can exceed 300 kg/m in the most crowded areas.

9.2.6 Power Supply Controls

All power supplies will be controlled by distributed VME computers. Since KEKB has a large number of steering correction magnets, the cost of their control interface is a non-trivial problem. To address this issue, a specialized interface will be developed, where control set points are serially sent to the power supply units.

9.2.7 R & D for Magnet Power Supplies

Two prototype power supply units will be built in JFY 1995. One is a relatively low-power magnet power supply with a power of 20 kW. A switch-mode power supply will be developed for reducing the physical size of the unit, while increasing the power factor. The other is a power supply for steering correction magnets. The techniques required for satisfying the tight tolerance and stability specifications will be studied.

9.2.8 Schedule

The bulk of magnet power supply units will be built in 1997 and 1998. The wiring of the DC power cables and the installation of the control system will be carried out before installing the power supply units. The work is coordinated with the rest of the accelerator construction schedule.

9.3 Installation and alignment

About 300 primary network reference points will be installed on the floor inside the ring tunnel. The interval of the reference points is roughly 10 m. The work will be done by using a laser tracker system. The overall precision for those primary network points is expected to be about 2 mm.

After all the old TRISTAN accelerator elements are brought out of the tunnel and the floor is cleared, reference points will be marked on the floor by referring to those primary network points.

Two points will be marked for each dipole magnet in arc sections, one at the position of the upstream edge and another at the downstream edge. By connecting those points the lines will be created on which other individual magnets should be installed. The positions to install all these magnets can be easily obtained by measuring the distance along those connection lines. In straight sections, reference points will be marked on the floor every 10 m in distance.

Magnets for the straight sections can be brought in from both experimental halls and from carry-in entrances in the arc sections. The magnets for the arc sections are brought into the tunnel from carry-in entrances by using magnet carriers.

Magnets are aligned by using a laser tracker and reflector targets. According to the vendor catalog, the precision for the position measurement is 1 ppm for the distance and 10 ppm for the angle. The precision of the angle measurement is improved to 5 ppm by averaging the data taken at the same position. The data can be collected at the rate of 500 Hz. The relative precision of alignment in the distance of 50 m is expected to be about 0.1 mm.

In the straight sections, magnets are also aligned by using the laser tracker. The location along the beam line is measured by a mekometer, a polarization modulated laser interferometer. With this technique, the expected precision for the distance is 0.2 mm in the distance of 200 m.

9.3.1 Layout for arc and straight sections

Both the LER and HER rings consist of four arc sections and four straight sections. Each arc quadrant consists of 7 regular cells, each of which includes 5 dipole magnets B_{arc}.

Portions of the plan view of the arc sections are shown in Figure 9.5. In the part (A) the LER is placed outside and the HER, and in the part (B) the LER is outside the HER.

The two rings of the LER and HER cross each other in the north (Tsukuba) and the south (Fuji) straight sections. The electron and the positron beams collide in the Tsukuba experimental hall and cross each other in the Fuji region.

The RF cavities for the low energy ring are located in the Fuji region, and those for the high energy ring in the Nikko and the Oho region. Wiggler magnets are placed in the Nikko and the Oho region to adjust the beam dumping times. A schematic layout view of the Nikko straight section is shown in Figure 9.6

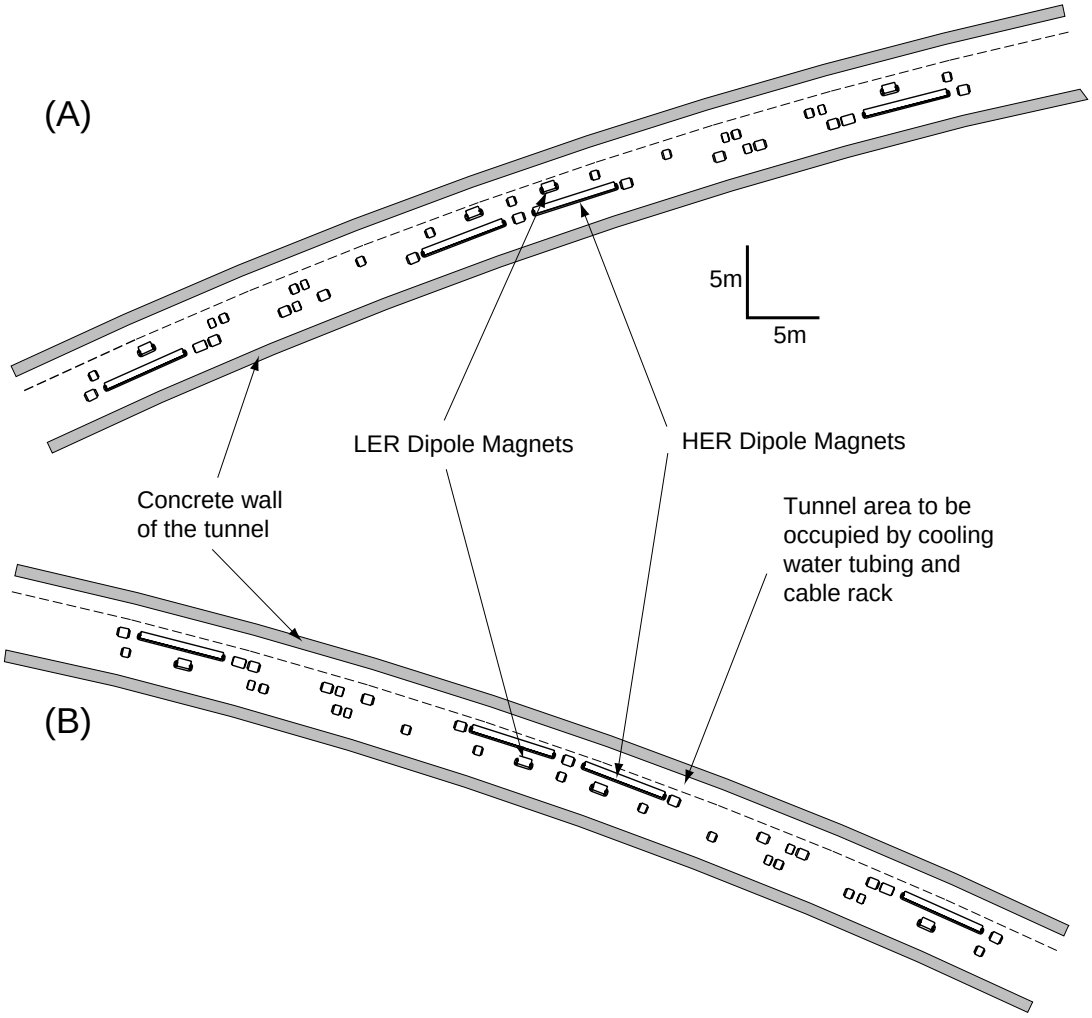

Figure 9.5: The magnet layout diagram in arc sections. The dipole, quadrupole and sextupole magnets for the LER and HER are shown. The outline of the tunnel walls is also indicated. The part (A) shows a portion where the LER is built outside the HER. The part (B) is for a portion where the LER is outside HER.

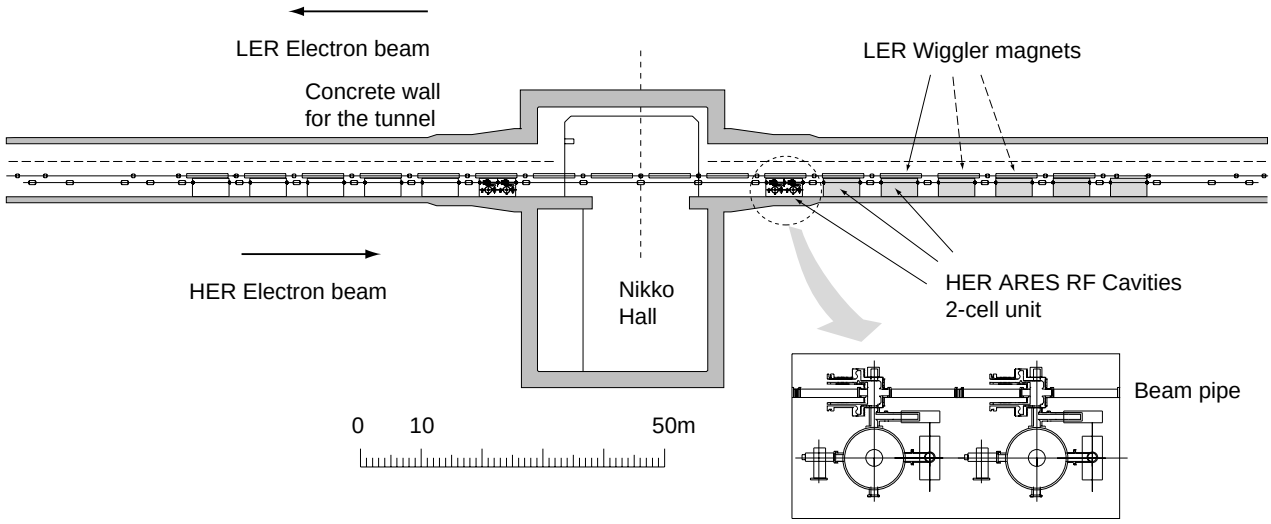

Figure 9.6: Layout of the Nikko straight section which includes RF acceleration cavities for the HER and wiggler magnets for the LER.

Chapter 10

Vacuum System

10.1 LER Vacuum System

This section discusses the vacuum system design for the LER regular arc sections, which occupy 2200 m out of the 3000 m circumference. The remaining parts of the LER are four 200 m long straight sections. One straight section is dedicated to beam collision and the interaction region for physics experiments. The others are reserved for beam injection, RF cavities and wiggler magnets.

10.1.1 LER System Considerations

Copper has been chosen as the vacuum duct material for its ability to withstand a high peak heat load, and to shield radiation from the beam. The beam duct has a circular cross section with an outer diameter of 106 mm. The wall thickness is 6 mm, which is sufficient for radiation shielding, while being appropriate for fabrication. The expected radiation dose outside vacuum duct is well bellow 1×10^8 rad/year. The grade of copper is ASM C10100 (oxygen-free electronic copper) for vacuum surface, and C10200 (oxygen-free copper) elsewhere. Vacuum flanges are made of stainless steel AISI304. The magnetic permeability of stainless steel must be less than 1.2 so as not to magnetically disturb the beam.

The LER stores a positron beam having an energy of 3.5 GeV at a maximum current of 2.6 A. The bending radius of a dipole magnet is 16.31 m. The total power of synchrotron radiation will be 2117.1 kW, and its critical energy 5.84 keV. As an option, there is a plan to add wiggler magnets to the LER, so that its radiation damping time will equal that of the HER. When this is done, the total radiation power will be increased to 3817.2 kW (i.e. the same as HER).

The cooling capacity of the refrigerators for the TRISTAN vacuum chamber has

been 4464 kW. This capacity must be increased to $3817.2 \times 2 = 7634.4$ kW. A total water flow rate of 1600 ℓ/min is available for each quadrant of two rings, whose combined length is 1500 m. To ensure a 15 ℓ/min flow of water which is required based on thermal calculations, one loop of peripheral circulation must cover about 10 m of the vacuum duct.

With a bending angle of 3.214° per dipole magnet, the linear heat load on the chamber wall is estimated to be between 27.6 W m^{-1} and 14.8 kW m^{-1}. Due to this horizontally localized heat, the temperature of the beam duct rises locally to 120° C. Consequently, a high local strain of -0.15% appears along the z direction. Applying a 0.15% strain over 10^8 cycles does not cause cracking on a half or quarter tempered OFC [1]. However, localized heating will lead to an annealing of the material, which can reduce the local mechanical strength. Annealed OFC can still withstand 10^4 cycles of a 0.5% deformation at 150° C [2]. However, it is preferred to keep the local temperature below 140° C at KEKB.

The gas desorption induced by synchrotron radiation, and its implications to the expected vacuum pressure, have been analyzed. The desorption rate is proportional to the number of incident photons. The linear photon density (N) averaged over the entire LER arc (2200 m) is 3.3×10^{18} photons s^{-1}m^{-1} for the LER. While the desorption coefficient η (molecules per photon) is dependent on the surface finish, roughly it is decreased with the accumulated photon dose. An average pressure P (Torr) is given by

$$P = K^{-1}\eta N/Sd = 0.1\eta/Sd, \tag{10.1}$$

where K is a unit conversion coefficient ($= 3.3 \times 10^{19}$ molecules Torr$^{-1}\ell^{-1}$) and Sd is the distributed pumping speed in units of ℓ s^{-1}m^{-1}.

The pressure-level goal to achieve at KEKB in the presence of the beam is 1×10^{-9} Torr. Our vacuum system has been designed such that this is achieved when η reaches 10^{-6}. At storage rings an assumption is often made that $\eta = 10^{-5}$. However, this requires an enormous pumping speed, which will be impractical at KEKB. An η value of 10^{-6} is considered to be realistic after a reasonable running time and the resultant beam dose ($\sim$ 1000 Ah) at KEKB. The required pumping speed under this condition is 100 ℓs^{-1}m^{-1}.

Small bunch sizes and the high current of KEKB place additional requirements on the vacuum system design. The size of any steps of the vacuum duct (i.e. discontinuity of the inner surface shape) may not exceed 0.5 mm. Pumping slots must be backed up by a grid, so that the penetration of wake fields, which causes a heat-up of the pumping elements, is reduced. Bellows and flange connections should be protected from direct synchrotron radiation hits. This will be accomplished by using suitably shaped masks

in the vacuum duct. However, the height of a mask must be lower than 5 mm. In this regard, a large bend angle in the LER creates a challenging condition for the bellows immediately downstream of the dipole magnets.

10.1.2 LER Vacuum System Components

Our design does not adopt an ante-chamber scheme. In the LER the synchrotron radiation is simply distributed on the duct wall. In this configuration it is preferred to distribute pumping slots along the beam duct.

An issue here is how to cope with possible beam-induced radiation onto the vacuum pumps. Unfortunately no reliable estimation is available concerning the magnitude of the radiation that propagates through pumping slots. Consequently, the vacuum system design must be prepared for an unexpectedly high power penetration. This will be done by making it possible to install a second grid between the slots and pumping elements.

All of the pumping elements are, therefore, attached to the vacuum duct via a flange connection to a pumping port. With the relatively large vacuum conductance of the beam duct (98 ℓs^{-1}), it has been shown that a distributed pumping speed of 100 $\ell s^{-1} m^{-1}$ should be possible by installing pumps having a capacity of 100 ℓs^{-1} every 1 m. In practice, because of the presence of magnets, such a uniform distribution of the vacuum pumps cannot always be realized. This causes about a 20% reduction of the distributed pumping speed. Figure 10.1 shows the basic arrangement of the vacuum duct in a regular cell. A calculation of the distributed pumping speed for a part of the regular cell is shown in Figure 10.2.

In the current design three types of beam ducts will be fabricated for the LER. The first is the "B chamber" which is used with dipole bend magnets. It has a cooling channel and a mask, as well as pumping ports. The second is the "Q chamber" which is used for quadrupole magnets. It includes a beam position monitor and a mask, but no pumping port. The cooling channels are welded on both sides. The third is a straight "S chamber" which has a cooling channel, a mask and pumping ports. Examples of those chambers are shown in Figures 10.3, 10.4 and 10.5.

A typical cross section of a LER vacuum duct is shown in Figure 10.6. Two water channels are electron-beam welded to the outside of the S chamber in a symmetric way. One of the beam-based alignment techniques of magnets planned at KEKB will utilize an active modulation of the excitation of the quadrupole and sextupole magnets. The symmetric arrangement of water channels causes a eddy current to be induced with a good left-right symmetry. This symmetry helps analyze the data without having to make corrections for asymmetric systematic effects.

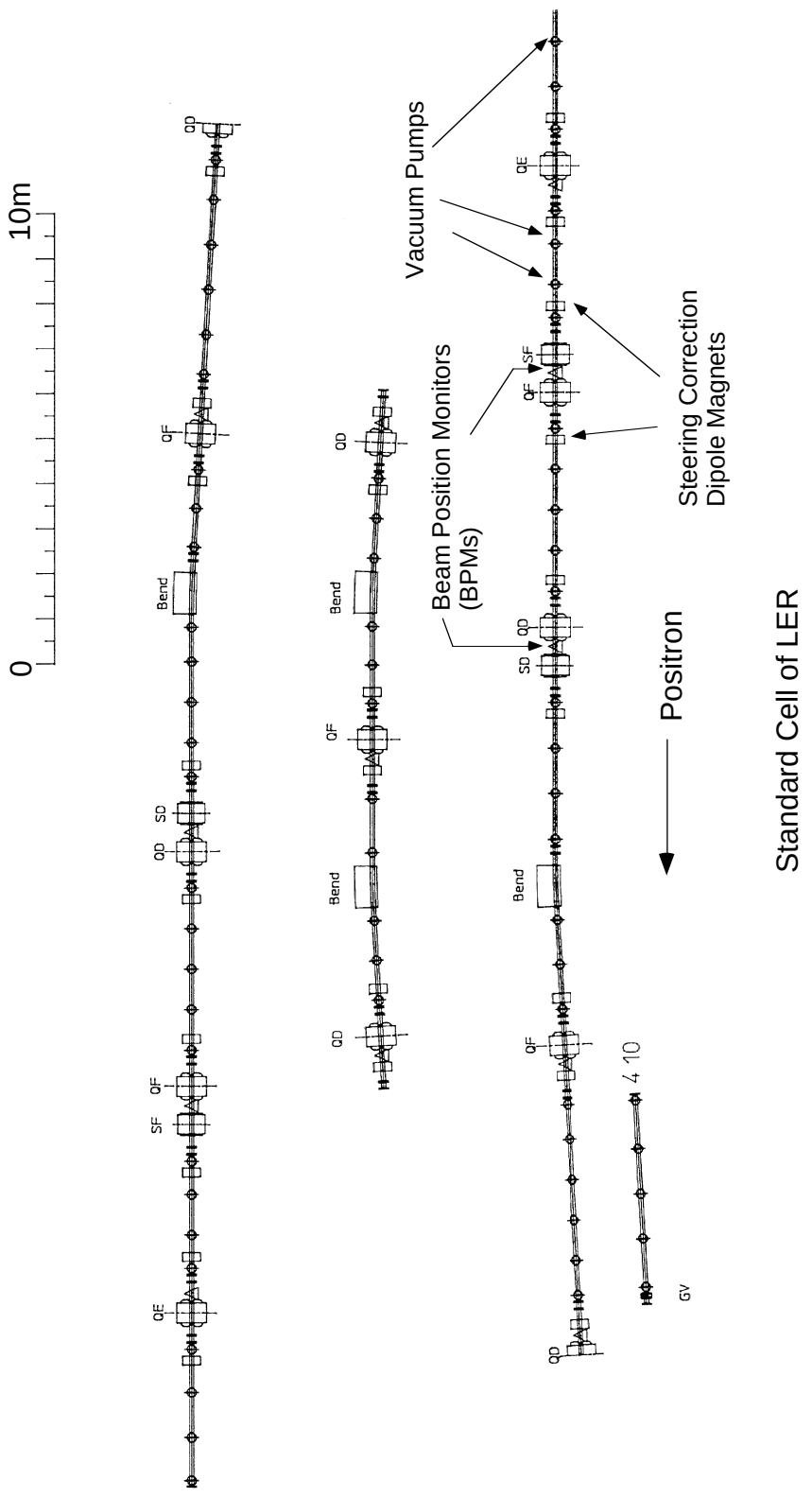

Figure 10.1: Basic layout of the vacuum duct in a LER regular cell.

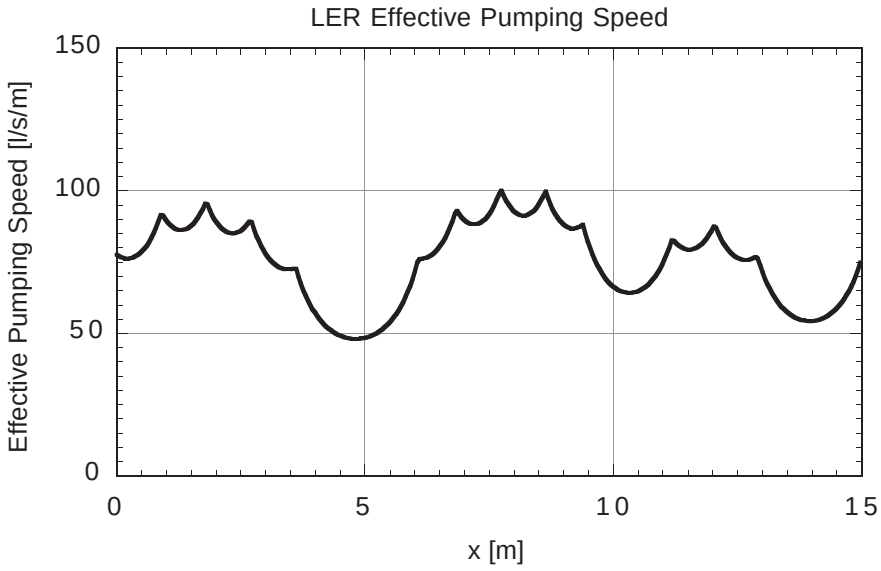

Figure 10.2: Expected pressure profile along the beam direction in the LER.

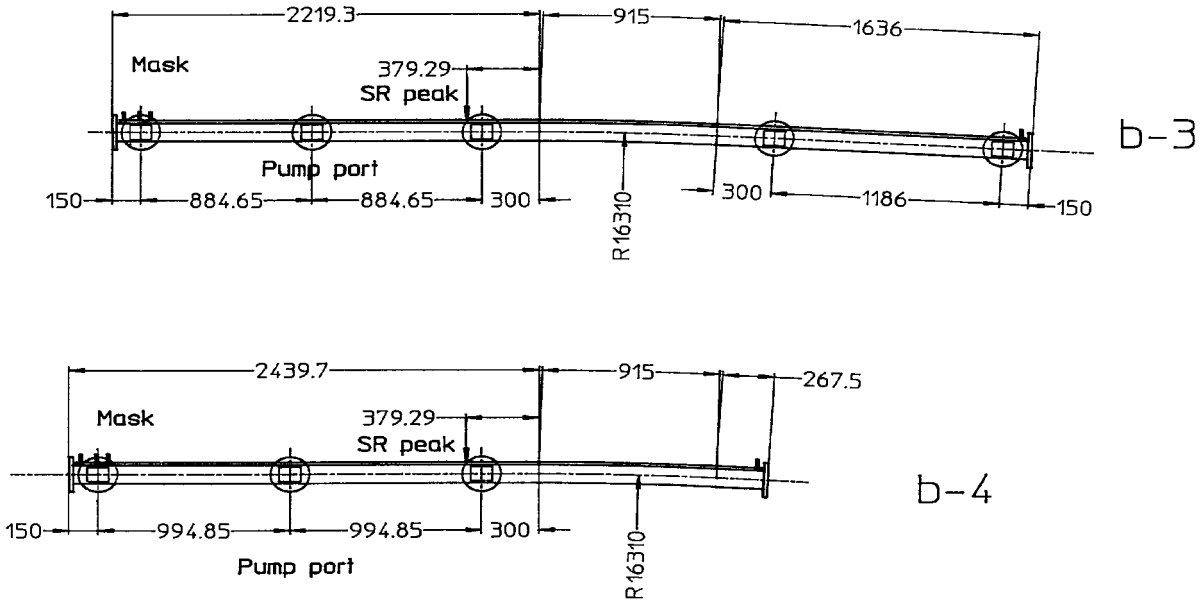

Figure 10.3: An example of the "B chamber" for the LER.

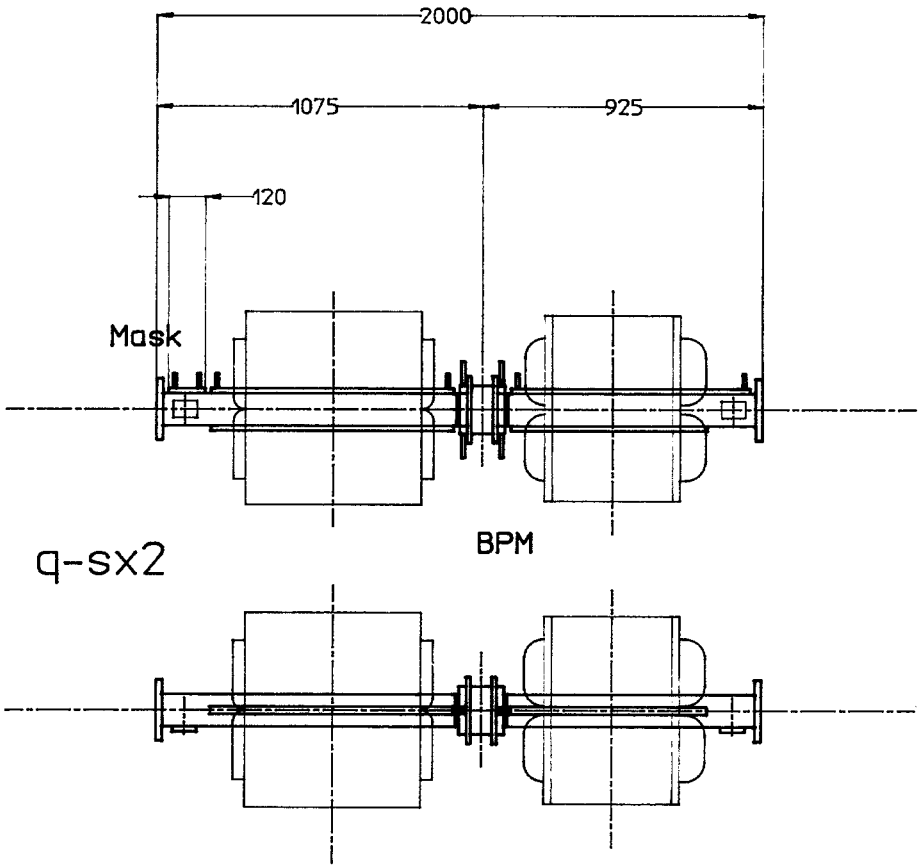

Figure 10.4: An example of the "Q chamber" for the LER.

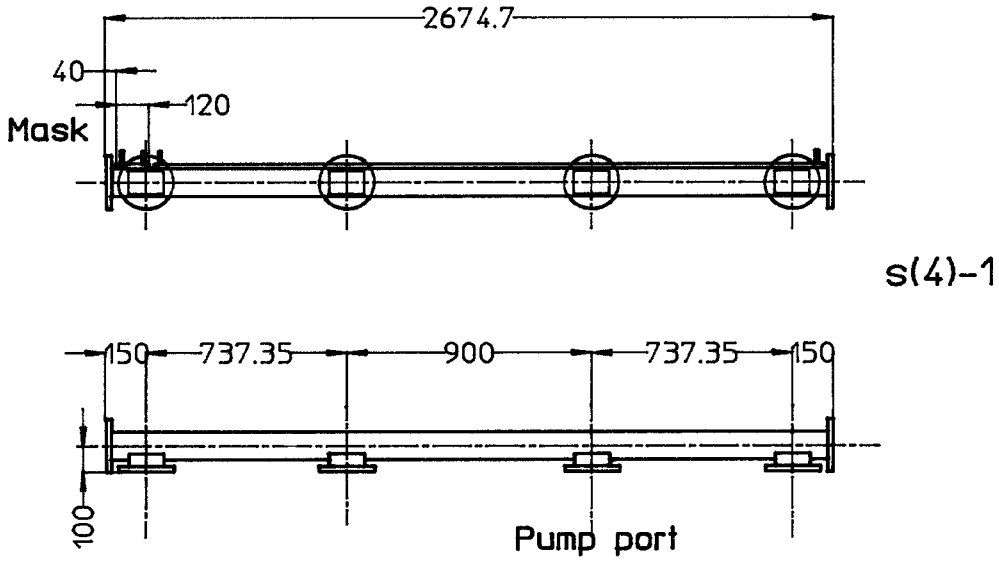

Figure 10.5: An example of the "S chamber" for the LER.

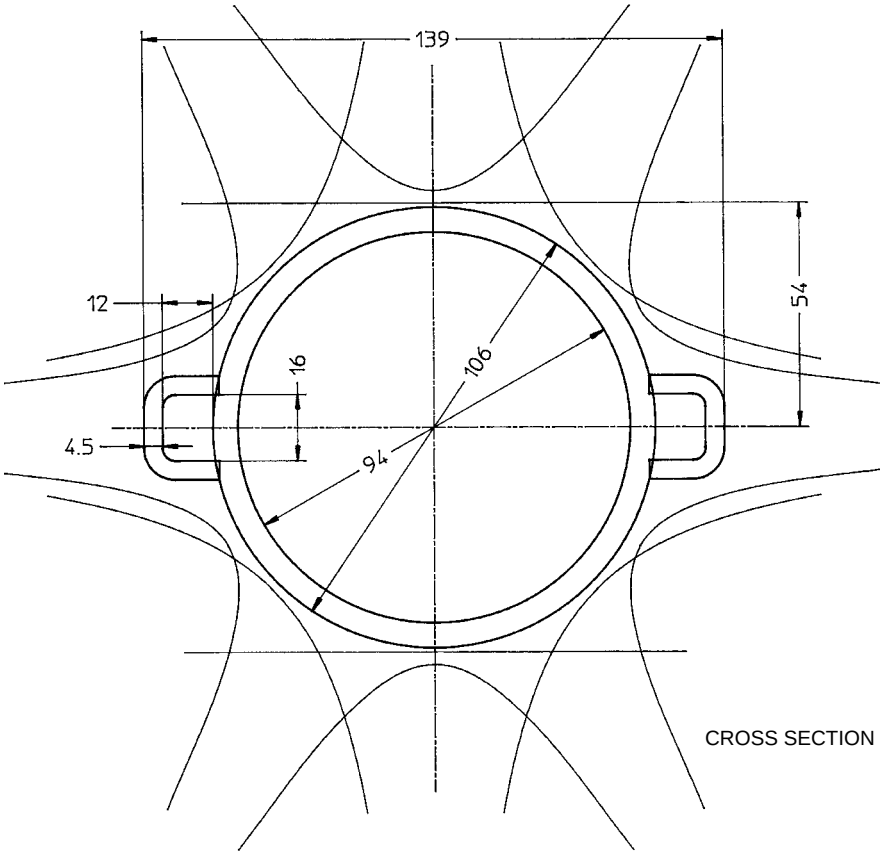

Figure 10.6: Cross section of an arc vacuum chamber for the LER. Two cooling water channels are symmetrically arranged. Outlines of the pole faces of quadrupole and sextupole magnets are also shown.

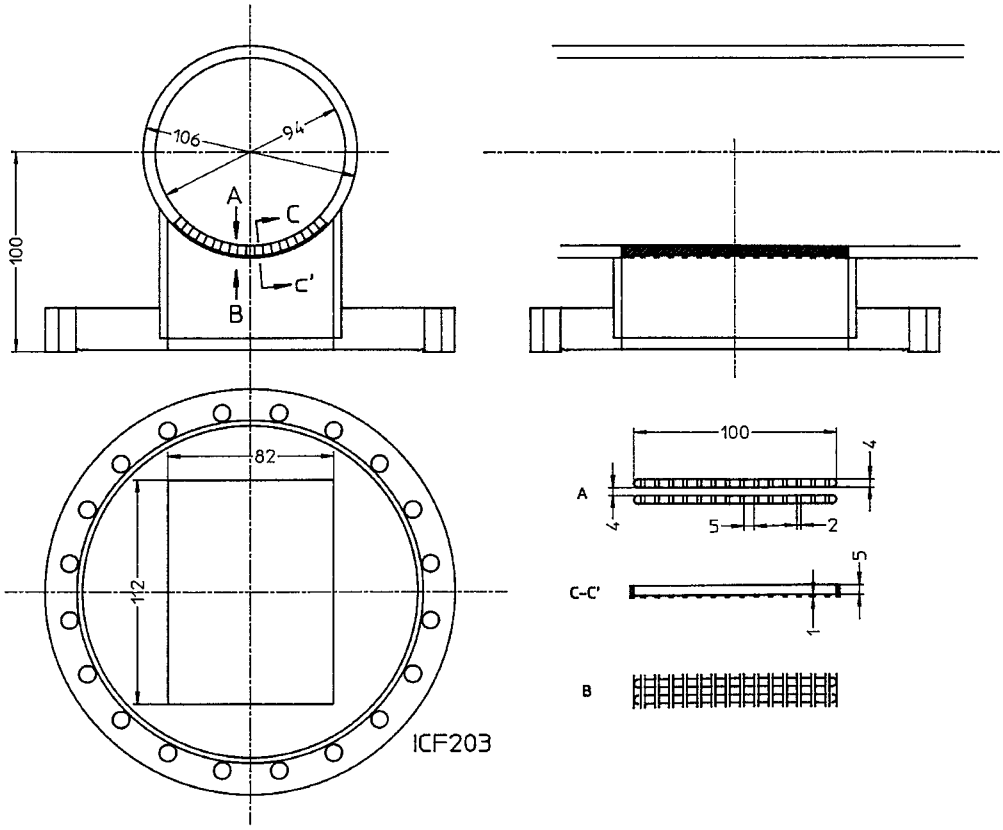

Figure 10.7: Structure of the LER pumping port and slots.

Figure 10.7 shows the structure of a pumping port and slots. The vacuum conductance of the slots of the port has been designed to be greater than 200 ℓs^{-1}. By using a 200 ℓs^{-1} NEG or a 200 ℓs^{-1} ion pump, a pumping speed of 100 ℓs^{-1} per port is expected to be achieved.

While the primary pumps comprise of NEG cartridges, secondary pumping is provided by ion pumps, which are installed every 10 m. Those ion pumps are required for operating the NEGs. They are also expected to bring the pressure down to about 10^{-7} Torr during the initial pump down before the first activation of the NEGs.

An oxide layer on the duct inner surface contains a large amount of carbon compositions, which are released as CO and CO_2 in desorption. To avoid the necessity of frequent conditioning of the NEG during commissioning, it is necessary to remove this first oxide layer and to produce a new oxide layer that is free of carbon. This treatment will be done using a commercially available chemical cleaner containing H_2O_2 and H_2SO_4, or by applying a standard acid etch with H_2SO_4, HNO_3, HCl, and water. The effect of each cleaning is shown in Figure 10.8.

The bellows and flanges must be protected from direct exposure to synchrotron light. For this purpose a mask structure is embedded at one end of each vacuum duct unit. A schematic design diagram of a mask is shown in Figure 10.11. A mask

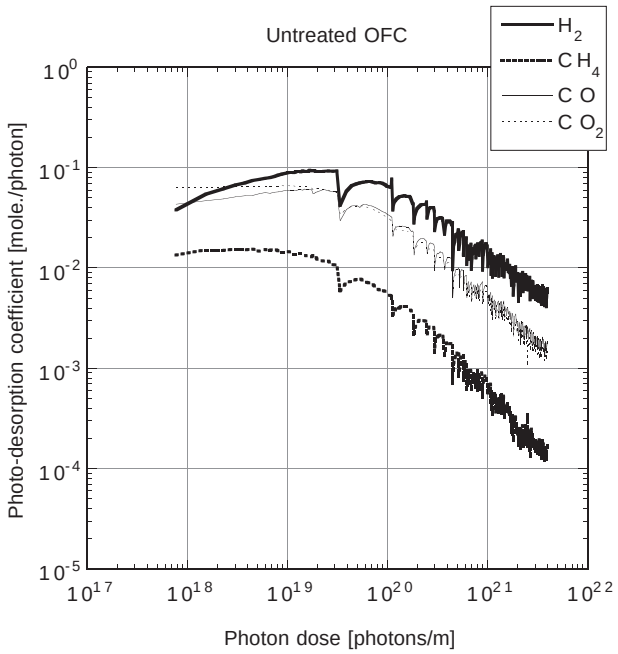

Figure 10.8: Measured photo desorption rate of hydrogen, water, carbon mono oxide and carbon di-oxide as function of accumulated photon doze. In this case, the copper material is not treated by chemical cleaner nor by acid etching.

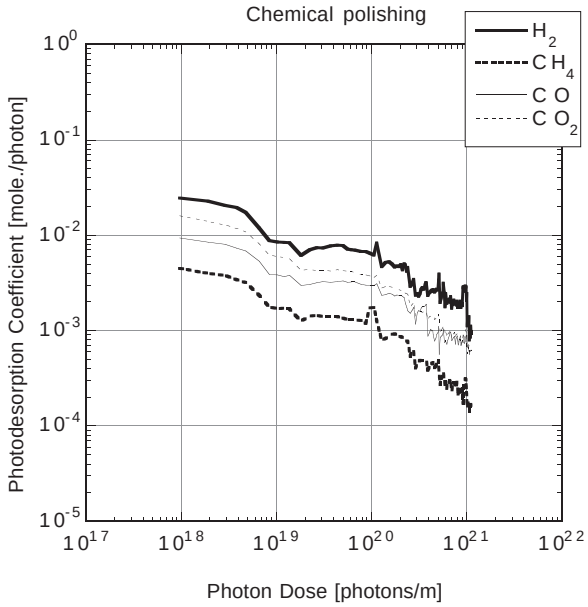

Figure 10.9: Measured photo desorption rate from a copper sample which has been cleaned by chemical cleaner.

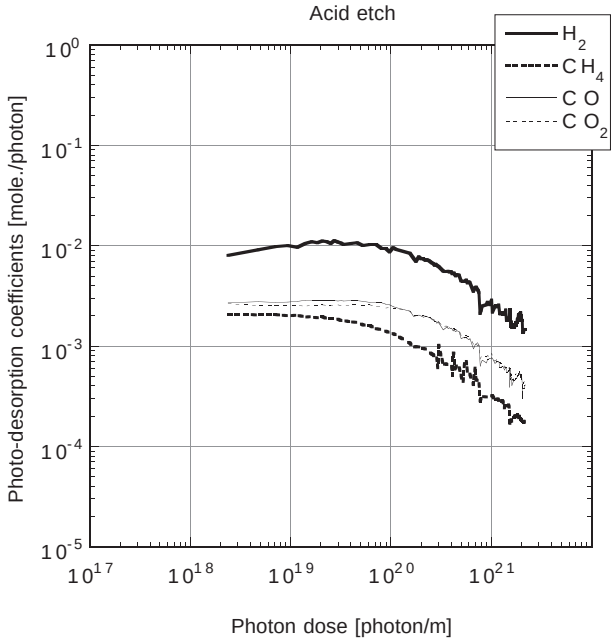

Figure 10.10: Measured photo desorption rate from a copper sample which has been processed by standard acid etching.

receives a larger amount of heat than the surrounding wall. The most stringent case is a 1.41 kW heat load for a 12 cm mask. The maximum temperature will reach about 130° C. This level of temperature rise is not considered to be problematic.

Button electrodes of the beam position monitor (BPM) unit are blazed on a copper block. The locations of the BPMs in a regular cell are shown in Figure 10.1. The design of the BPM blocks is discussed in chapter 11. The heat load due to synchrotron radiation depends on the location of individual BPMs. The heat deformation of the BPM units has been estimated. About one hundred BPMs will have their pickup feed-through assemblies shifted by 10 to 20 μm. However, if the shift of four electrodes in a BPM unit occurs in a symmetric way, the net effect does not cause an apparent shift of measured beam position. It only causes a very small change of the BPM sensitivity.

Bellows of two different designs (Type A and Type B) are being considered for the LER, as shown in Figures 10.12 (Type-A) and 10.13 (Type-B). In a Type-A bellows a tube seal is used as the RF contact. The seal follows the possible deformation of the bellows unit. A Type-B bellows has a finger contact. The loss factor of the Type-B bellows is expected to be smaller than that of Type-A. However, since a Type-B bellows has long slot gaps between the fingers, field penetration through those gaps is a potential problem. It appears to be difficult to plug those gaps while maintaining good mechanical flexibility. A possible design solution is to adopt a Type-B bellows,

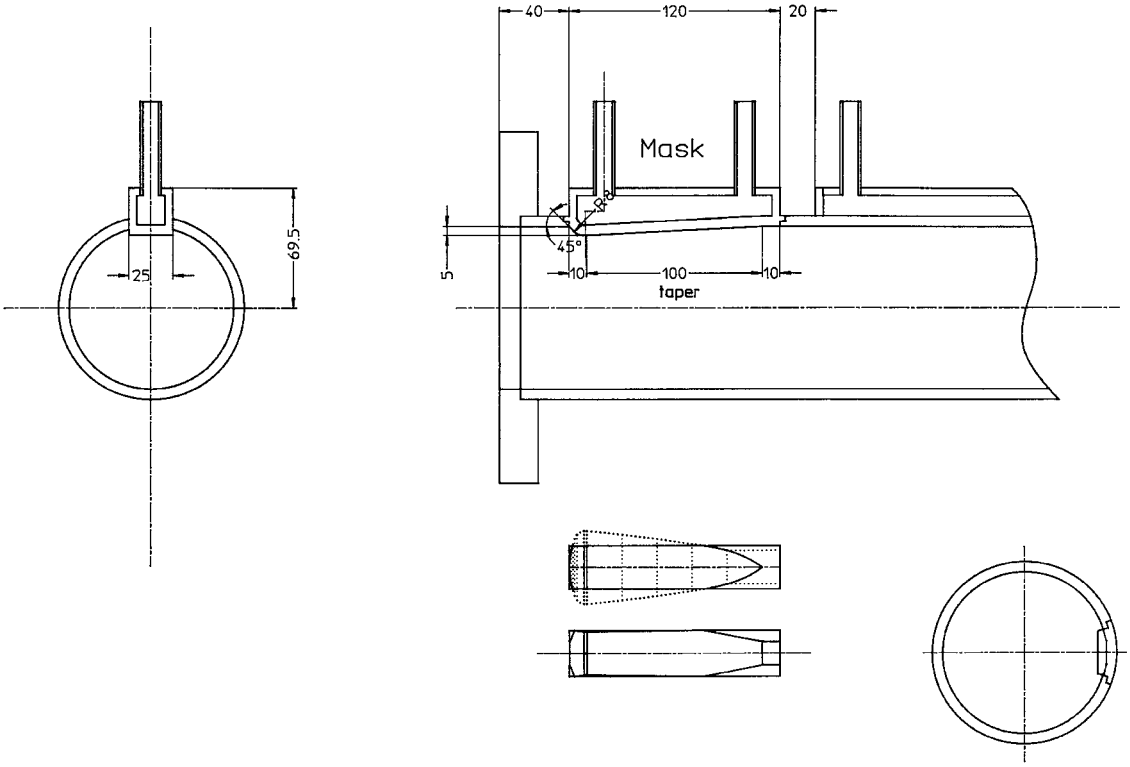

Figure 10.11: Cross section and side view of a synchrotron radiation mask within a LER vacuum duct.

but to limit the slot length exposed to the bunch to be $\sim 1/2$ of the stroke of the bellows.

The connection with standard conflat flanges will leave a gap between the gasket and the flange where the beam field can be trapped. The estimated energy loss at a connection is 635 W. This causes a heating of the flanges. To avoid this situation, beam ducts must be connected without any gaps at the flange. In the proposed design, an aluminum ring is inserted between flange faces to fill the gap. A vacuum seal is made outside of the ring using Helicoflex. The structure based on this idea is shown in Figure 10.14.

10.2 HER Vacuum System

10.2.1 HER System Considerations

Overall, the HER ring has a structure similar to that of the LER. An arc with regular cells has a total length of 2200 m. One straight section is intersecting with LER for collision, two are used for cavities. The last straight section includes a cross-over with the LER as well as an injection complex.

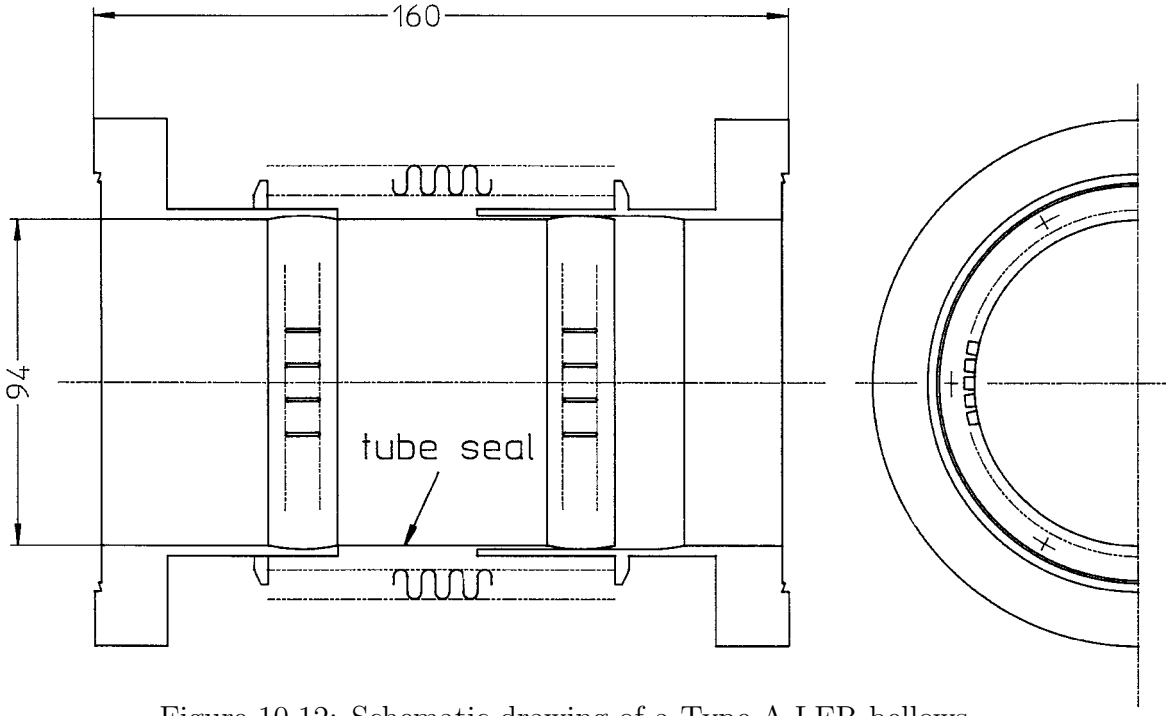

Figure 10.12: Schematic drawing of a Type-A LER bellows.

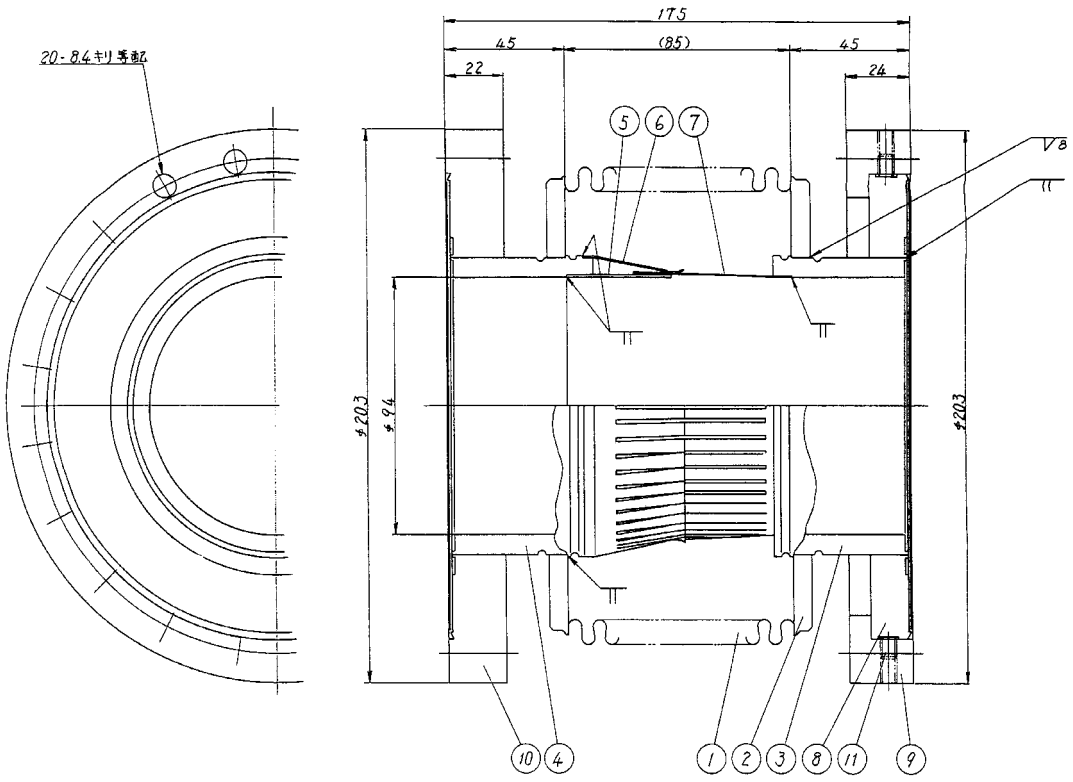

Figure 10.13: A schematic drawing of a Type-B LER bellows.

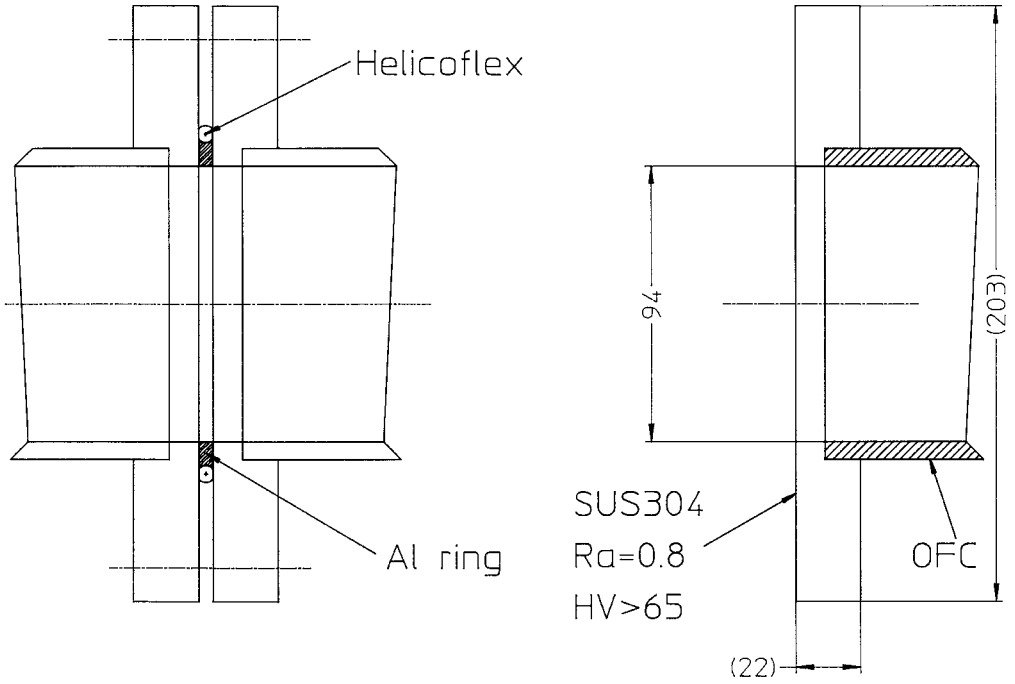

Figure 10.14: Vacuum sealing using Helicoflex.

As shown in Figure 10.15, the cross section of the HER beam duct has a racetrack shape with a 58 mm half width and $r = 31$ mm (outer curvature) with a thickness of 6 mm. The vacuum duct will be made of copper.

The HER stores the electron beam of $E = 8$ GeV at a maximum current of $I = 1.1$ A. The orbit bend radius in a dipole magnet is 104.46 m. The total power of synchrotron radiation is 3817.2 kW with a critical energy of 10.9 keV. Synchrotron radiation will hit the wall of the beam duct within a dipole magnet. The maximum linear heat load on the chamber wall in the arc is 5.8 kW m^{-1}. This heat load allows the use of an aluminum alloy.

The linear photon density in the HER averaged over the arc (2200 m) is expected to be 3.2×10^{18} photons $s^{-1}m^{-1}$. This situation is quite similar to that of the LER. Consequently, the distributed pumping speed in the HER is also 100 ℓ s^{-1} m^{-1}.

Since the beam current is lower than the LER, expected wake field problems at HER are not so serious as in the LER. A beam duct is pumped through side slots (backed up with grid) and NEG strips are used as the distributed pump.

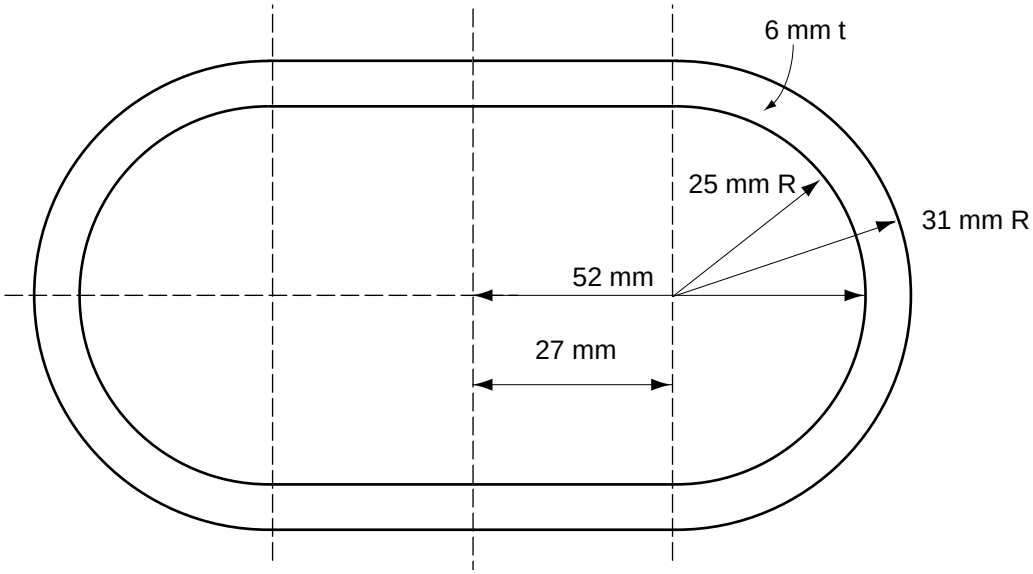

Figure 10.15: Cross section view of the arc vacuum chamber for the HER.

Bibliography

[1] Private communication with Hitachi Works, Co. Ltd.

[2] Private communication with Hitachi Cable, Co. Ltd.

Chapter 11

Beam Instrumentation

11.1 Beam Position Monitor (BPM)

The purpose of the Beam Position Monitor (BPM) system is to measure the beam orbit in the accelerator. The BPM data will be used for correcting closed orbit distortions (COD), and to optimize the operation of the rings. At KEKB the data are also used for analyzing the alignment and strength errors of magnetic components in the rings. The latter purpose requires a BPM system with good stability and high precision. This cannot be easily realized with a "fast" system where the beam positions are measured every turn. Therefore, the system adopted at KEKB is a "slow" system, where measurements are performed for the beam positions averaged over many turns. A similar system has been used at TRISTAN for several years, and its operation has been well proven.

An electrostatic pickup unit at KEKB consists of four disk electrodes. A pickup unit will be installed near every quadrupole magnet in the two rings. There will be about 450 BPMs to be installed in each ring; in total there will be 900 pickup units for the entire KEKB. Since a multi-bunch, high-current beam will be stored at KEKB (LER 2.6 A, HER 1.1 A) special attention must be paid to the design of the pickups, transmission lines, switches and front-end electronics. This section outlines the BPM system design for KEKB.

11.1.1 Pickup unit

The important design considerations of the BPM pickup electrodes are as follows:

- Reduce the pickup beam power by using electrodes with a small cross section (diameter 12 mm).

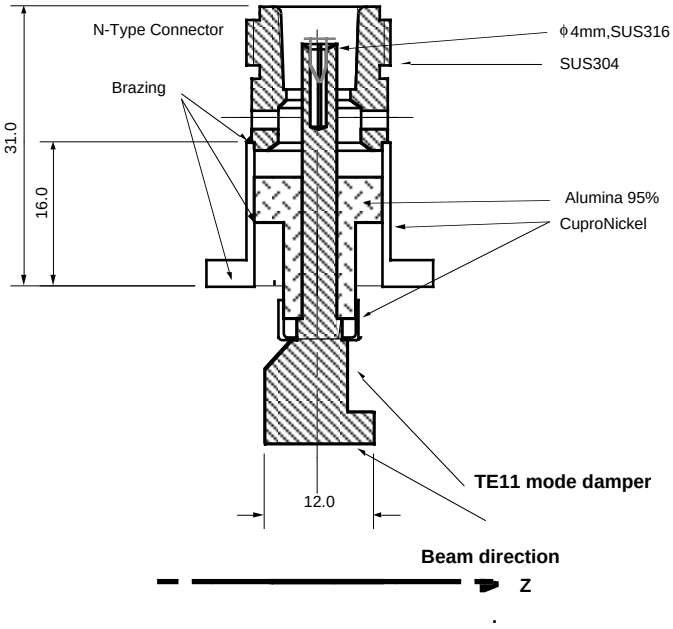

Figure 11.1: BPM electrode for KEKB

- Transfer the beam power safely through feed-throughs with sufficient mechanical strength and power capacity.
- Suppress the higher-order mode resonances in the electrode assembly.
- Minimize the mechanical deformation of the unit in order to improve the measurement precision.
- Unit assembly with reliable brazing processes.
- Precise and mechanically robust installation of the pickup units on the quadrupole magnets.

Figure 11.1 shows a preliminary design of the pickup unit. To realize sufficient mechanical strength and to withstand the expected transmission power, an N-type feed-through with a modified center conductor having a larger diameter, together with a spring contact, will be used.

The BPM block is made from a solid piece of copper. Four feed-throughs with electrodes are brazed onto the block, as shown in Figure 11.2. Two stainless steel frames are brazed to the block, and they prevent a deformation of the unit. The completed BPM assembly is supported firmly and precisely at the end of a quadrupole magnet, as shown in Figure 11.3. The flat surface of the frame also serves as a reference plane for the purpose of an electrical mapping calibration of the BPM.

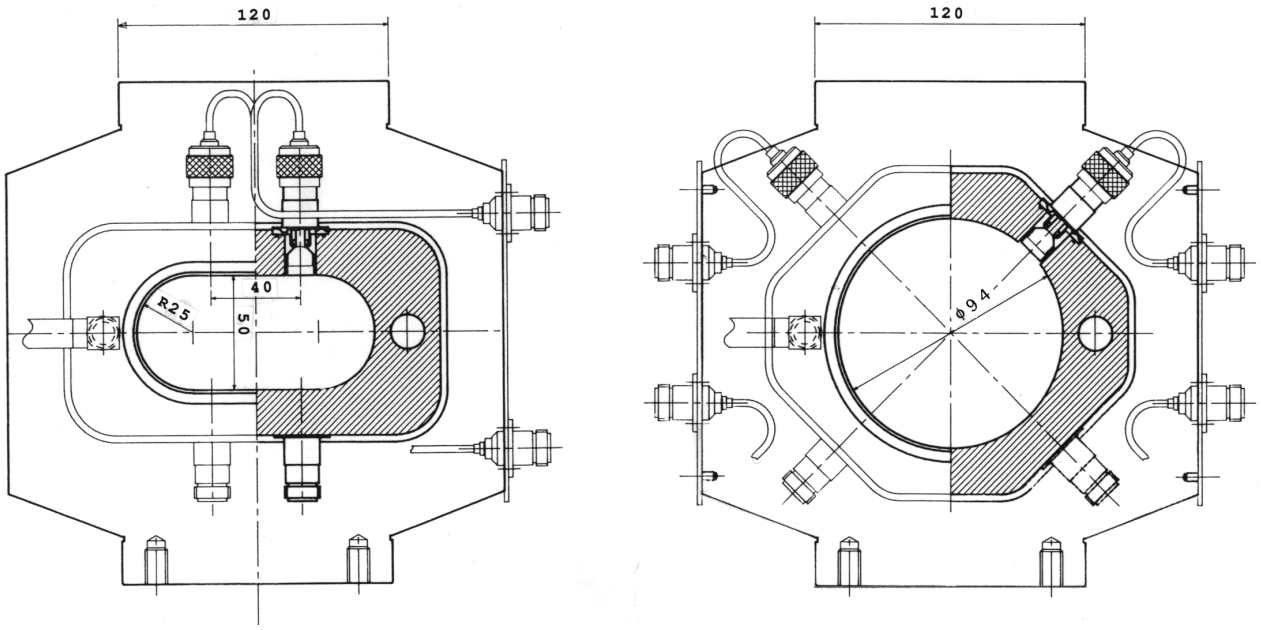

Figure 11.2: BPM blocks for the HER(left) and the LER(right).

All BPMs will be tested at a calibration bench where the electrical center of each BPM will be identified within 20 μm using a movable antenna. During installation, the BPM positions relative to the quadrupole magnets will be measured within several tens of a μm, and the data will be used to correct the measured beam position data.

The frequency response of the BPM electrode impedance has been calculated using a coaxial model. The result is shown in Figure 11.4. Since the 1 GHz component of the signal (i.e. 2nd harmonic of the RF frequency) will be used for beam position measurement, it is not necessary to be very concerned about the VSWR over a wide frequency range.

However, to avoid the growth of coupled bunch instabilities and heating problems of the ceramic seal, close attention must be paid to the resonance impedance of the BPM electrode and the feed-through structure. Design optimization to minimize harmful resonances is in progress. One of the most harmful resonances against beam stability is the TE110 mode, which is expected in the 7.3 $\sim$ 7.9 GHz frequency range. Our calculations indicate that the coupling impedance of the TE110 mode may be sufficiently low, so that the beam instability due to this mode may not be a concern. If this actually becomes a problem, the cross section shapes of the feed-through and the rod electrode may be made non-axially-symmetric to suppress the TE11 mode within the structure. As for the other resonances which may be trapped inside the feed-through structure, it is planned to optimize the size of the ceramic seal, thereby shifting the

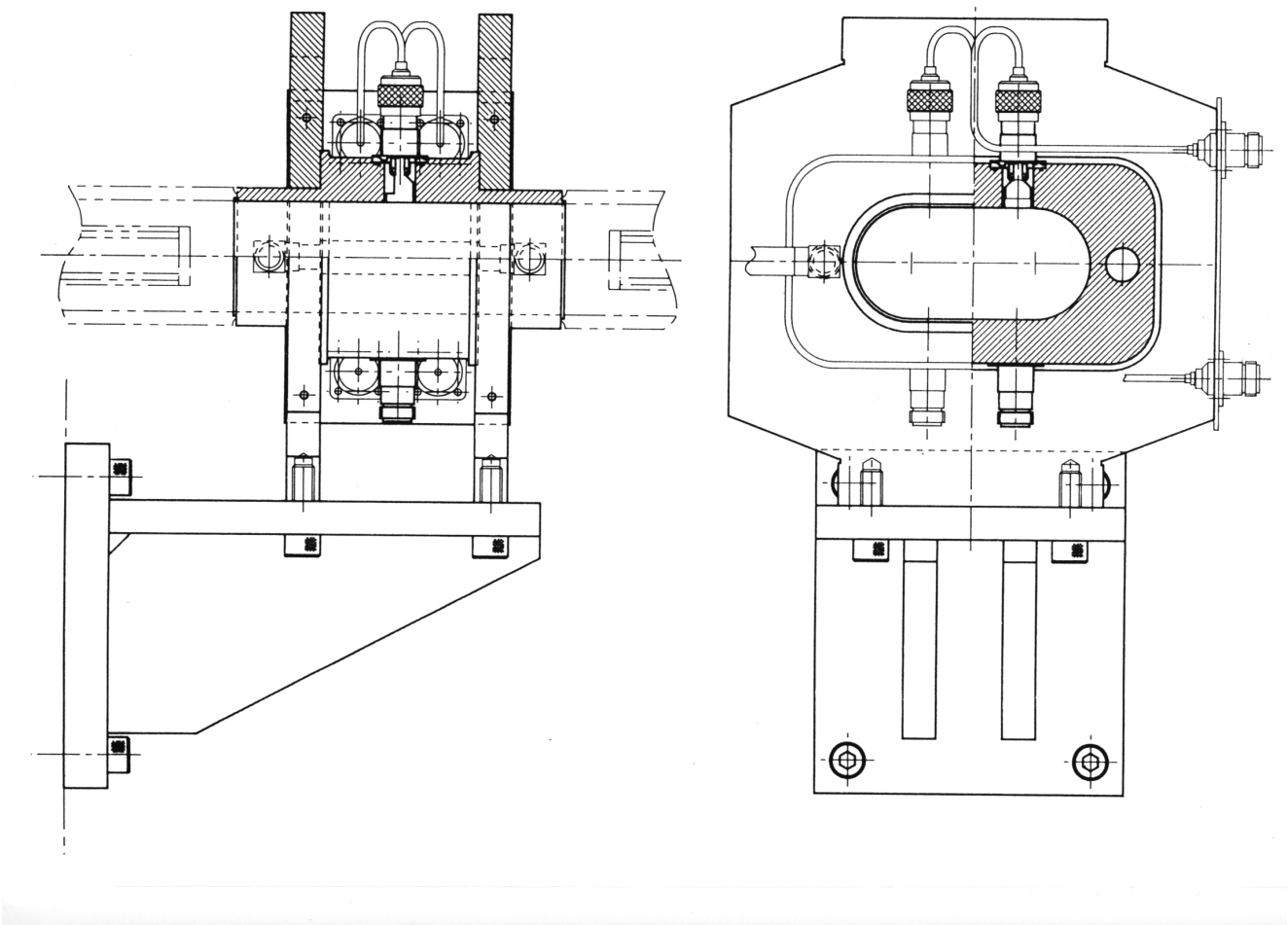

Figure 11.3: Support of the BPM block.

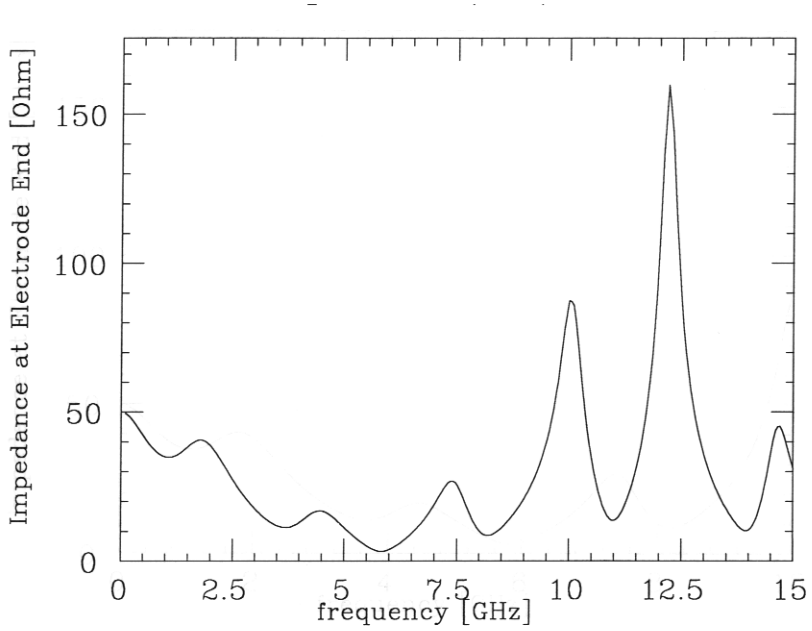

Figure 11.4: Frequency response of the BPM electrode impedance, which has been calculated using a coaxial model.

resonance frequency off the RF harmonics.

11.1.2 Signal processing method

The following performance requirements have been given to the BPM read-out system design:

- The position resolution should be better than 10μm.
- The COD measurement must be completed within a short time of $\sim$1 second.
- The system must function for a beam current range of 10 mA $\sim$ 2.6 A.

In order to satisfy these requirements, we have adopted basically the same signal processing method as of the TRISTAN Main Ring BPM read-out system. Four beam signals from each pickup unit are detected with a common detection circuit, which measures a higher harmonic of the revolution frequency. With narrow band signal processing and by using a common detector we can reduce the measurement errors.

The expected position resolution and the measurable range of the beam signal have been estimated. The calculation assumed that the geometrical sensitivity coefficient K of typically 26 mm, and it includes the effects of the thermal noise of the detection

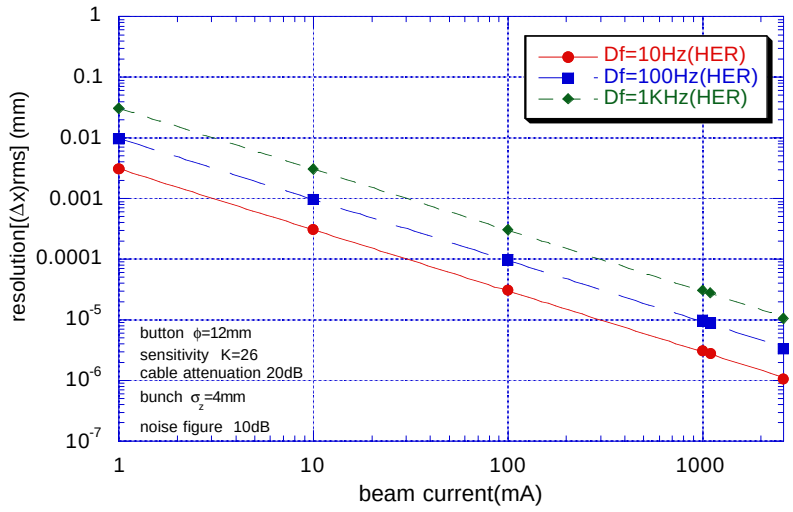

Figure 11.5: Expected position resolution determined by the thermal noise.

circuit, including the signal cable. Figure 11.5 shows the expected position resolution as function of the beam current for a varying frequency band-width (Δf). The resolution improves in proportion to the beam current, and to the inverse of the square root of the band width. This is because the thermal noise power is proportional to the band width. From this study, the bandwidth was chosen to be $\Delta f = 100$ Hz, so that the resolution, including the thermal noises, would be better than 10 μm at the beam current of 10 mA. In the case of the single bunch operation, the bandwidth must be significantly decreased, because the transient signal amplitude limits the dynamic range, and it becomes difficult to keep the noise figure small. Optimization for the single bunch measurement is now under consideration.

11.1.3 Layout of the BPM system

A schematic layout of the signal processing system is shown in Figure 11.6. These circuit units are distributed in 20 local control buildings around the ring. The beam signal from the four pickup electrodes for each BPM are transmitted through independent coaxial cables. A 2 m long radiation-resistant cable, such as a PEEK (poly-ether-ether-keton) insulation cable, will be used between the pickup electrode and the signal transmission cable to overcome possible damage due to radiation. At the input of a detection circuit the signals are selected by RF switches.

The effects of the cable impedance variation during a period of several days have been evaluated for signal cables of the TRISTAN BPMs. It has been found that the equivalent shift of the measured beam position due to such effects is less than 10 μm.

At KEKB the BPM measurements are expected to be conducted much more fre-

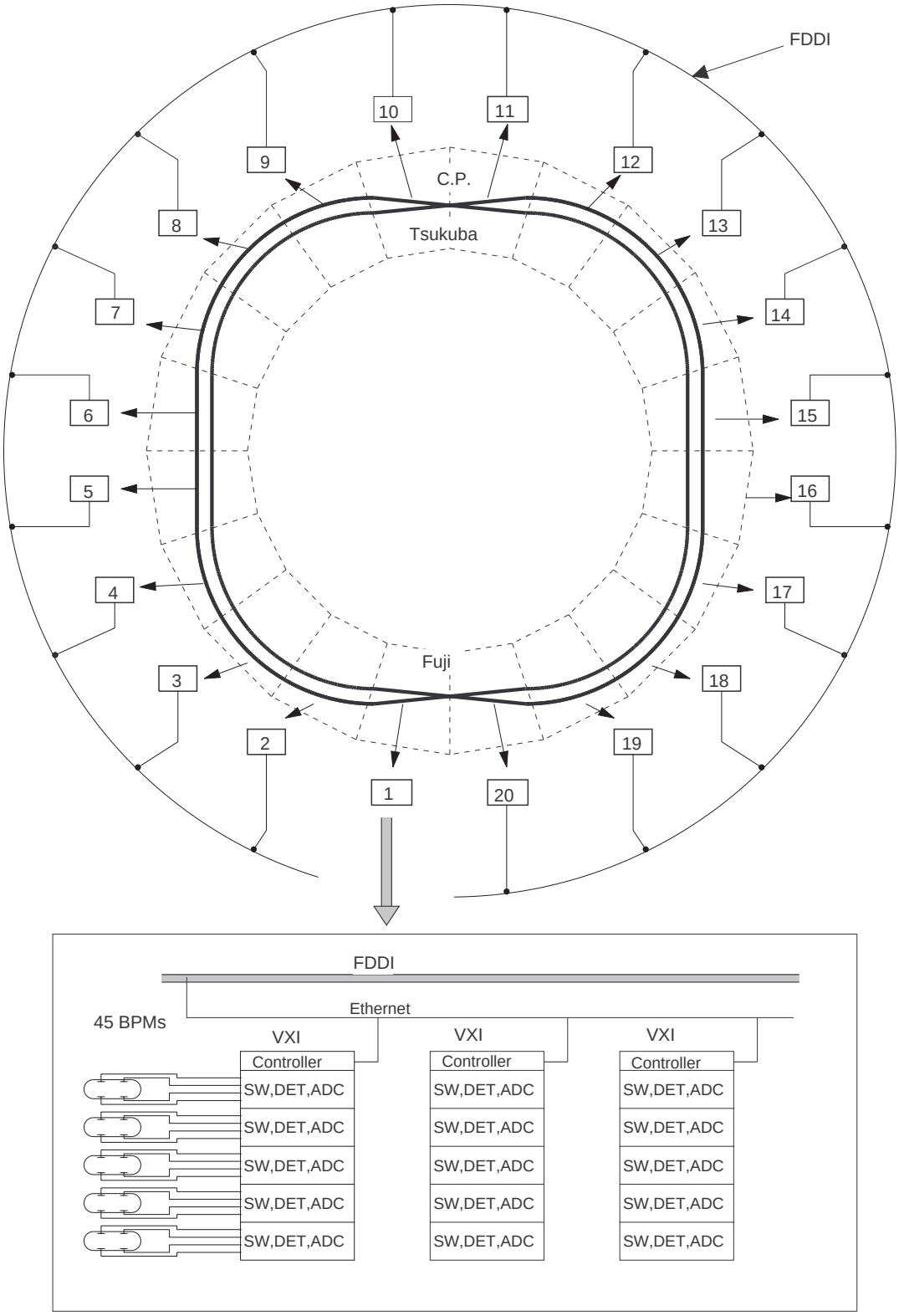

Figure 11.6: Beam position monitor system.

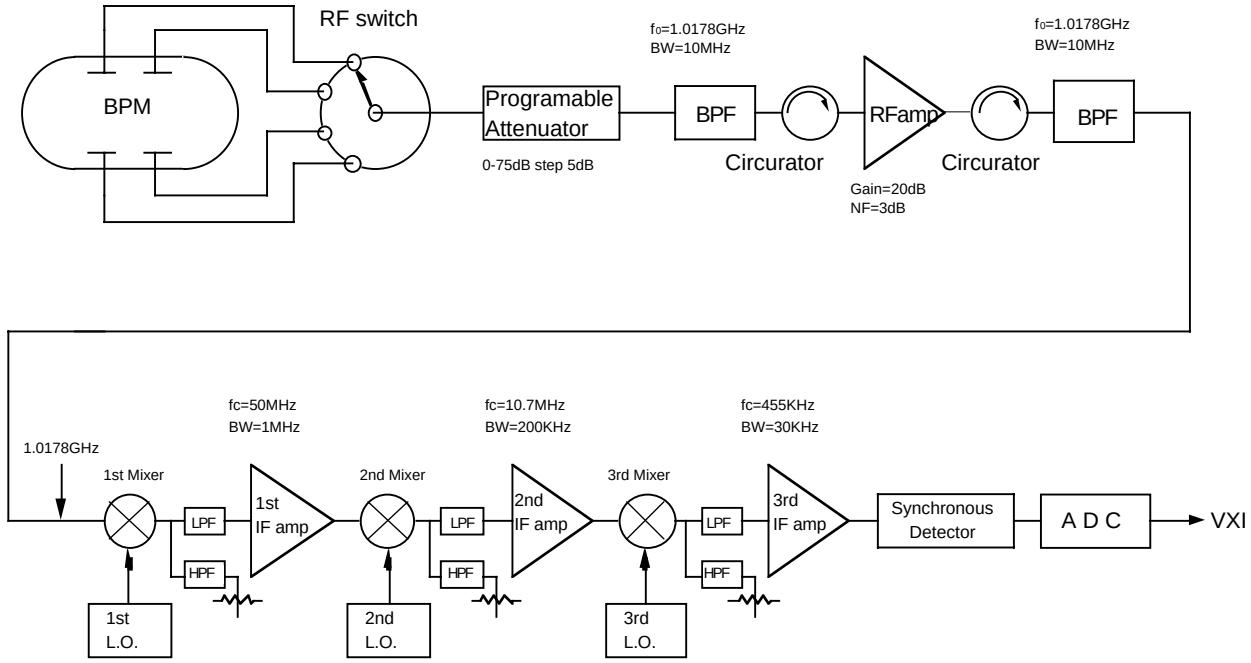

Figure 11.7: Block diagram of the front-end signal processor.

quently than at TRISTAN. For reliability reasons, the use of mechanical switches was abandoned at an early stage of the design studies. Two types of RF switches are currently under consideration: a PIN diode switch and a mercury switch. In our on/off test of $5 \times 10^6 \sim 1.4 \times 10^7$ switching, the measured fluctuation of the insertion loss was less than 1×10^{-4} for both types of switches. This contact fluctuation translates into a measurement error of < 10 μm.

The signal detection circuit consists of a triple-stage super-heterodyne circuit with a synchronous detector. Its concept is similar to that of TRISTAN. Figure 11.7 shows a block diagram of the front-end electronics. In order to measure beams with any multi-bunch configurations, a pickup frequency of 1.016GHz has been chosen. This corresponds to twice the accelerating RF frequency, and the 10240'th harmonic of the revolution frequency (99.9 KHz). To obtain good linearity in a wide signal dynamic range, a synchronous detector is employed to convert the intermediate frequency (IF) signal to the DC signal. The band width for signal detection is determined by the low pass filter in the final stage. The output of the detection circuit is converted to digital data by an A/D converter (ADC). The present plan is to use a 20-bit "Δ/Σ" type ADC with a step-response time of ~ 120 msec to meet the resolution requirement.

The digital data will be sent to a VXI (VME-bus Extensions for Instrumentation) mainframe in each local control room, where they are transformed into beam position data. Each VXI station will be linked to a workstation through a local area network. The shortest possible measurement time is determined by the sum of the switching

time of the RF switch ($\sim 4 \times 2$ ms), the response time of the front-end processor ($\sim 4 \times 15$ ms) and the conversion time of the A/D converter ($\sim 4 \times 120$ ms).

In the present design, each front-end signal processor has an individual A/D converter to minimize the conversion time and the data acquisition time. If each BPM signal is managed by an individual front-end processor including an ADC, a shorter data acquisition time of ~ 0.6 s is expected, thus satisfying the ultimate performance requirement described earlier. In the early stage of operation, signals from the BPMs will be multiplexed to a common circuit to reduce the system cost. For example, if 5 BPMs share a common circuit, the measuring time will be ~ 3 s. However, since the signals from all BPM electrodes are delivered through separate cables, the signal processing time will be shortened by incrementally adding circuits in the electronics house.

11.2 Optical Monitor

The beam profile monitor based on an imaging of the synchrotron radiation will give a visible beam profile, which will greatly improve the efficiency of the commissioning of KEKB. By digitizing the image data, transverse beam sizes can be obtained, and with knowledge of the lattice parameters, various beam parameters, such as the beam emittance and horizontal-vertical coupling, can be deduced. The dependence of the beam size measured with this device on the beam current gives some information concerning collective effects. Furthermore, by using a streak camera or a photon counting system, the longitudinal profile of the beam bunch can be observed. This section presents the basic design of the optical beam profile measurement system at KEKB.

11.2.1 Choice of the Synchrotron Light Source Point

While several choices of the synchrotron light sources are possible, the heat load due to the radiation onto the light extraction mirrors needs to be considered. This is because of the high current operation expected at KEKB. Our design choice is to relax the heat load on the mirror by using a dedicated weak bending magnet as the light source in a zero-dispersion section for both the LER and HER. This offers synchrotron light of manageable power with simple spatial and energy distributions for handling. The parameters of the light source magnets (preliminary) are listed in Table 11.1.

With these parameters the theoretical angular distribution and energy spectrum of the synchrotron light at wavelengths of 480 nm, 550 nm and 634 nm are shown in Figures 11.8 and 11.9. The angular divergence of the synchrotron light is expected to be $2 \sim 3$ mrad at visible light region in both the LER and HER.

	Bend Radius	Dipole Field	Angular Power of SR		Source Size
LER	183 m	0.0638 T	28.86 W/mrad at 2.5 A	σ_x	472 μm
				σ_y	69 μ m*
HER	1172 m	0.0228 T	49.31 W/mrad at 1 A	σ_x	650 μm
				σ_y	120 μm*

Table 11.1: Preliminary parameters of the weak bend magnets that are used as a synchrotron light source for the profile monitors. The theoretical total angular power of the synchrotron light is also listed. *The quoted beam size as the light source assumes an emittance coupling of 2 %.

11.2.2 Extraction of the Visible Synchrotron Light

Since the light focusing system will be placed in an atmospheric environment, which is separated from the accelerator, the visible synchrotron light must be extracted from the ring through a vacuum-tight optical window. To eliminate effects due to unknown light reflection and scattering, the aperture of the vacuum pipe, extraction mirror structure and the optical window must be made sufficiently large. The construction of the light extraction system for the HER and LER are schematically shown in Figure 11.10. A small flat mirror (like a right-angle prism) is located 10 m from the source point, facing the synchrotron light at 45 degrees.

The cross sections of the vacuum pipe in the LER and HER are shown in Figure 11.10. The rectangular apertures allowed for the mirror in the vacuum pipe are 10 mm (horizontal) $\times$ 44 mm (vertical) in the HER and 10 mm(horizontal) $\times$ 50 mm (vertical) in the LER. They lead to an opening angle of 1×4.4 mrad^2 and 1×5 mrad^2. Figure 11.8 indicates that the vertical aperture needs to be 2 mrad in the HER and 4 mrad in the LER. The extraction system is designed to satisfy these conditions. Details concerning the vacuum chamber for the extraction system are currently being designed.

11.2.3 Thermal Deformation of the Extraction Mirror and it's Correction by Use of Corrective Mirror

The extraction mirror must withstand the maximum angular power of the synchrotron light, as given in Table 11.1. The optimum design of a water-cooled mirror system is being worked out. Nonetheless, the thermal deformation of the optical flatness of the mirror can exceed the tolerance of diffraction-limited optics, such as Rayleigh's

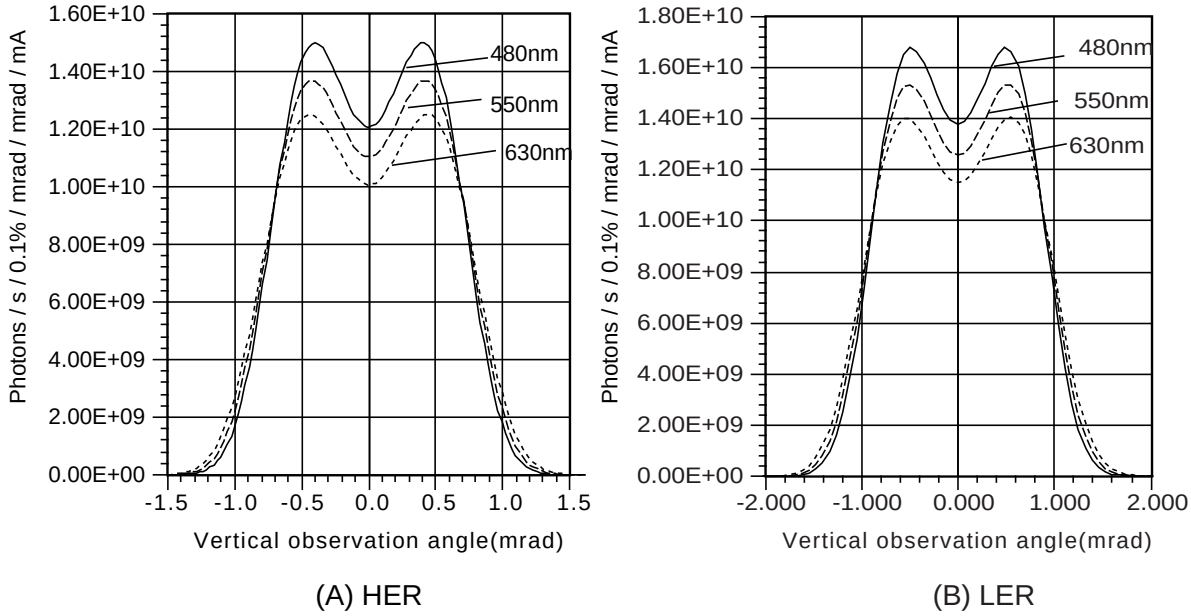

Figure 11.8: Theoretical angular distribution of the synchrotron light in the HER (A) and the LER (B).

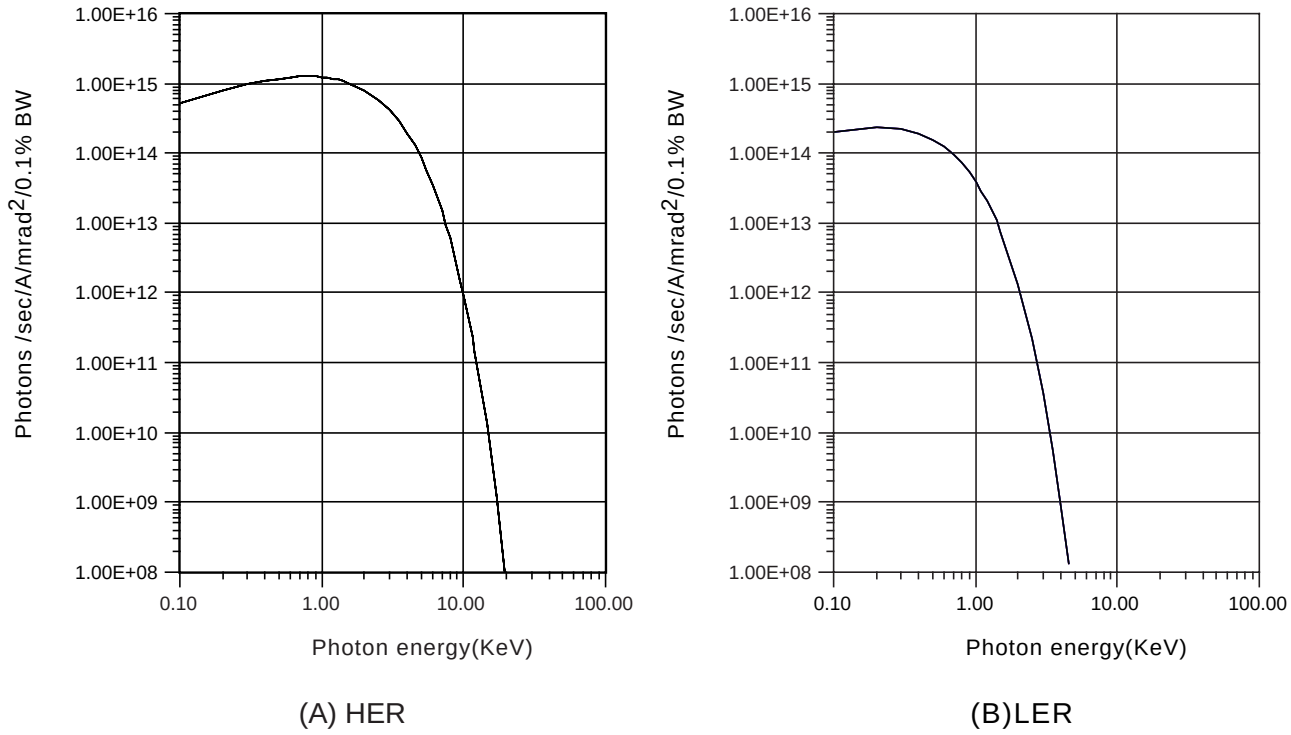

Figure 11.9: Theoretical energy distribution of the synchrotron light in the HER (A) and the LER (B).

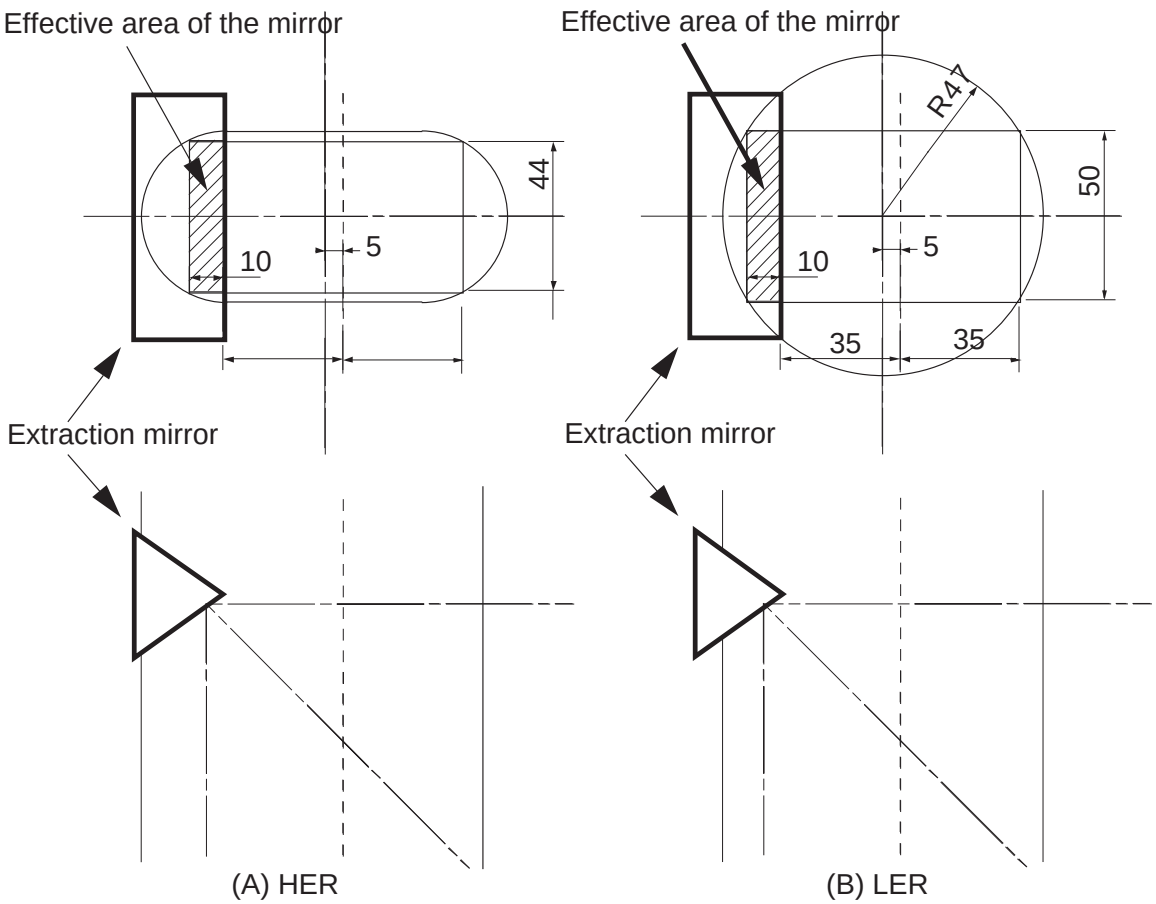

Figure 11.10: Configuration of the extraction system for visible synchrotron light.

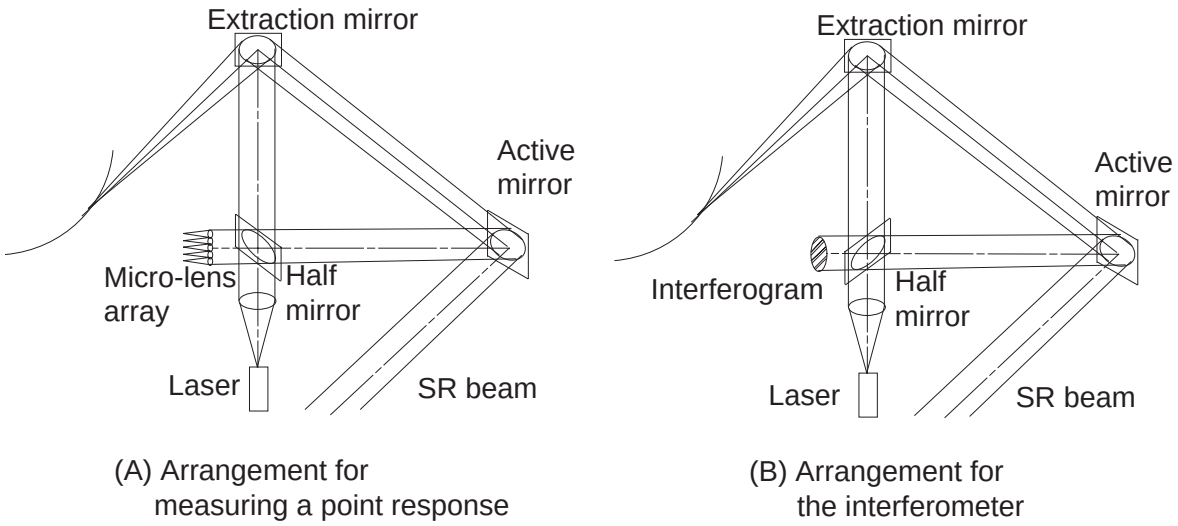

Figure 11.11: Schematic design diagram of the corrective system.

criterion (wave front error $< \lambda/8 \sim 0.07$ μm). There may also be mirror deformation caused by the mechanics of mounting and cooling water tubing. To correct such errors, a corrective optics system will be applied. It is basically a feedback system based on an active mirror that makes the point response function of the two-mirror system as correct as possible. A schematic diagram of the corrective system is shown in Figure 11.11.

An arrangement that is similar to a Tywmann-Green-type interferometer is applied between the extraction mirror and the active mirror, and the point response function of the two mirrors is measured using a collimated laser beam. This arrangement of the extraction mirror and the active mirror can give a Tywmann-Green type interferometer, which can be realized by rotating the half mirror as shown in Figure 11.11(B). If a sufficient space is not available for additional correction mirrors around the extraction mirror, it is possible to construct a corrective optics system in the free space above the ring.

11.2.4 Focusing System

The optical image of the beam must be delivered to the measurement room above the accelerator tunnel, so that sophisticated measurements can be made with streak cameras and photon counting there. The basic design of the focusing system consists of an objective system and a relay system which minimizes the loss of optical information along this long path. The distance between the source point and objective system will be about 15 m. The distance between the objective system and a measurement room at ground level is about 30 m.

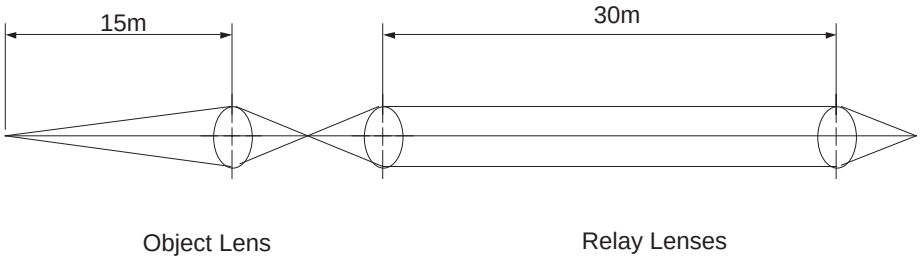

Figure 11.12: Schematic diagram of the focusing system.

Figure 11.12 shows a design diagram of the focusing system which consists of three sets of doublets made of normal optical glass. The first doublet makes up the objective system, and latter two the relay system. The design of the entire system is optimized for a wavelength of 480 nm. The design modulation transfer function (MTF) of the total system and the diffraction-limited MTF (MDMTF) are shown in Figure 11.13. The expected longitudinal aberration is shown in Figure 11.14. By comparing the MTF and the MDMTF, it can be seen that this system is almost aberration-free (diffraction limited) for paraxial use (clear aperture is 0.05 degrees), but is usable only for monochromatic rays. By introducing other kinds of glass, such as ED (extraordinary dispersion) glass, more correction of the aberration will be possible. Since the total magnification of the above mentioned system is set to be 0.0714, the estimated image sizes of the beam on the focusing plane are 33.7 μm (h) $\times$ 4.93 μm (v) in the LER and 46.4 μm (h) x 8.57 μm (v) in the HER. Since this image is too small for direct observation by a CCD camera, it is necessary to apply a final magnification system, such as an eye-piece, in the telescope.

11.2.5 Correction of the Optical Pass Difference by Windows and Filters

Since the components of the focusing system, such as the optical windows and the filters, have the refractive index greater than 1, an optical pass difference (OPD) will appear. It we denote the refractive index and thickness of material i as n_i and t, the OPD relative to the vacuum optical pass is given by

$$\mathrm{OPD} = (n_i - 1) \times t. \tag{11.1}$$

For example, a 20 mm thick optical window made of the typical crown glass creates an OPD of 9.8 mm. If an OPD exists in the image field (after lens), its effect on the magnification is often non-negligible. Consequently, to measure the magnification of

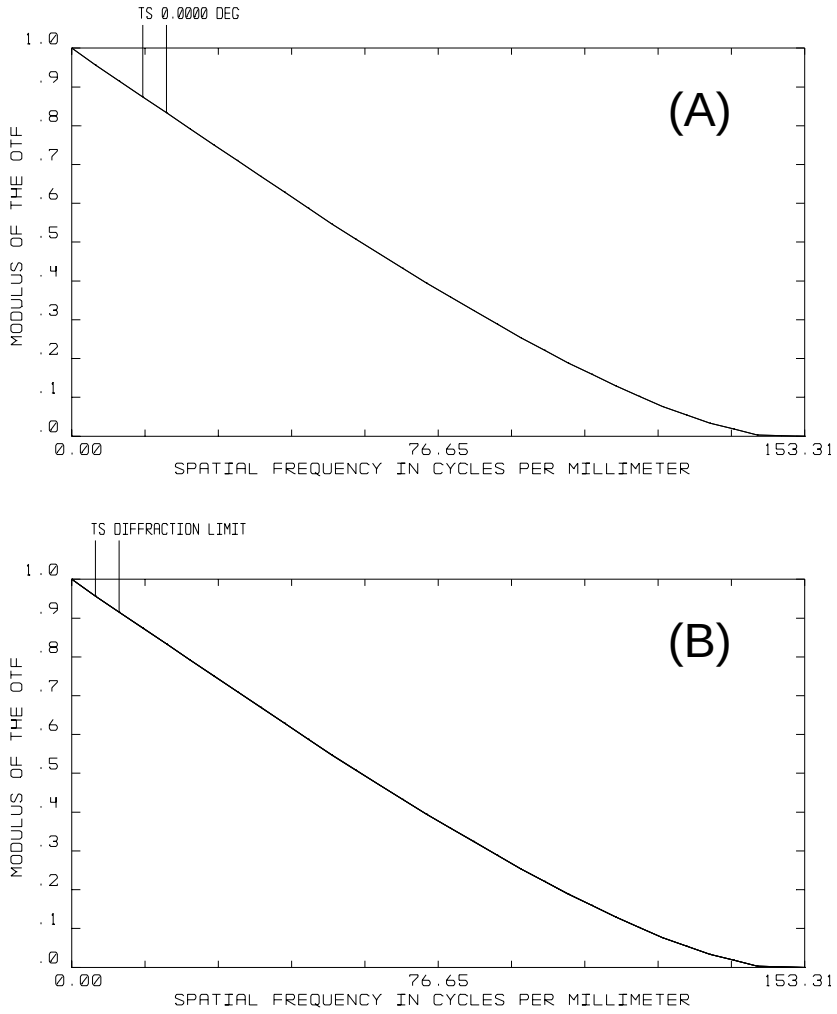

Figure 11.13: Design MTF (A) and MDMTF (B) of the total system.

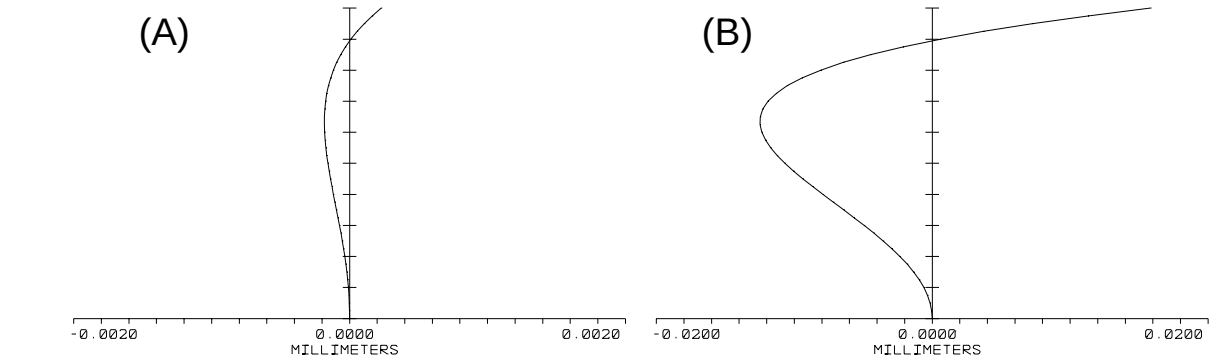

Figure 11.14: Expected longitudinal aberration of the object lens (A) and the total system (B).

a real system, an OPD correction will be required. This correction is important for measuring the absolute beam size.

If we have a material with an unknown refractive index, such as a band-pass filter for monochromatization, it is necessary to measure its OPD in advance. It should be noted that special care is required when applying a variable number of neutral-density filters to regulate the image intensity. If the filters are located in a non-collimated section of the focusing system, the OPD effect will cause a shift of the focal plane.

Also, an OPD by means of a longitudinal aberration (color or spheric aberration) causes a time difference, resulting in a traveling time difference among different optical paths. Therefore, the longitudinal aberration should be corrected for time-sensitive measurements, such as studies of the bunch length.

11.2.6 Transverse Diffraction Effects

The finite aperture of the entrance pupil of the focusing system produces diffraction. With the Fresnel approximation of the diffraction theory and the paraxial lens transfer function, a pupil with a lens produces a Franhofer diffraction on the image plane. The wave front error in these approximation is treated by means of the wave front aberration. With a well optimized focusing system (i.e. diffraction limited), the diffraction pattern is dominated by Franhofer diffraction (paraxial theory). Then a diffraction pattern is given by the Fourier transformation of a generalized pupil function of the focusing system.

The amplitude transmittance of the generalized pupil function is modified by the vertical angular intensity distribution, as shown in Figure 11.8. To create a simple generalized pupil function, an apodization for the entrance pupil of the focusing system is required. The apodization filter must have an anti-amplitude transmittance corresponding to the vertical angular intensity distribution of the synchrotron light beam. This apodization filter will create a flat intensity distribution on the entrance pupil, and the entrance pupil will give a maximum cut-off spatial frequency. The entrance pupil will be the maximum rectangular slit, which has an apodization filter that corresponds to the intensity distribution of the extracted synchrotron light. As mentioned in section 11.2.2, it will be 10 mm in the horizontal direction and 40 mm in the vertical direction at 10 m for the LER, and 10 mm in horizontal and 20 mm in vertical for the HER apart from the source point.

The entrance pupil of the focusing system will be located 15 m from the source point, so the dimensions of slit will be multiplied by a factor of 1.5. The results of a calculation of a point spread function (PSF, i.e. a diffraction pattern) for the system are shown in Figure 11.15.

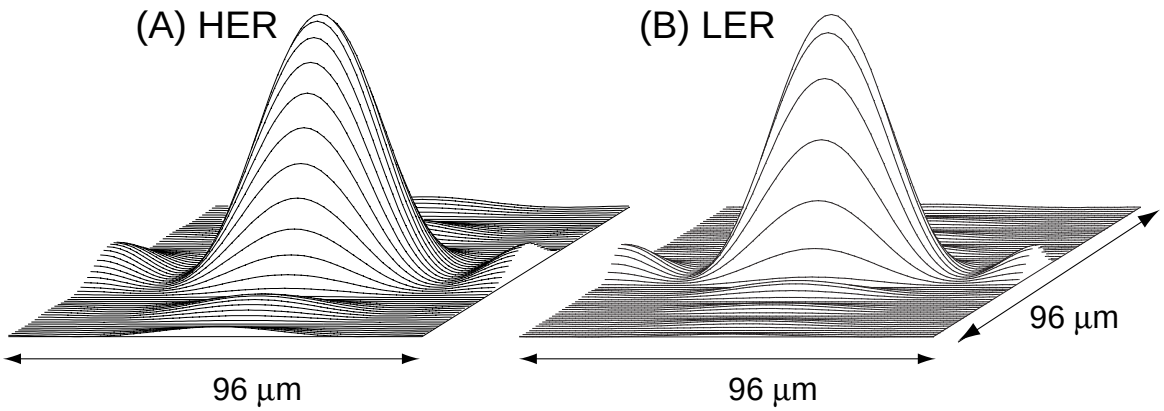

Figure 11.15: Point Spread Function (PSF) of the focusing system. The side length of the 3-dimensional density plots is 96 μm.

The rms width of the central peaks of the PSF are 5.36 μm vertical and 13.1 μm horizontal for the LER and 7.32 μm vertical and 13.1 μm horizontal for the HER. The image of the beam is given by a convolution of the PSF and the geometrical image. Noting the expected beam size in Table 11.1, it is important to apply a correction of the PSF in the beam size observation. The point response of the real focusing system will be measured for the PSF correction.

11.2.7 Longitudinal Diffraction and the Field Depth Effect

The field depth of the diffraction limited focusing system is dominated by longitudinal diffraction along the optical axis. Figure 11.16 shows the calculated longitudinal diffraction pattern of the first doublet lens. The rms of the central peaks are 0.87 mm in the LER and 2.18 mm in the HER. The corresponding field depths on the object point (on the beam) are 171 mm in the LER, and 428 mm in the HER. The effects of the longitudinal aberration, as discussed in section 11.2.3, is sufficiently small for this length. The system also appears to be diffraction-limited in the longitudinal direction. The curvature effect in the horizontal beam size of the beam trajectory due to this field depths will be 14.3 μm in the LER and 81.6 μm in the HER. This effect in the HER is not negligible. Since the curvature effect is mostly proportional to the bending radius, it is better to adopt a smaller bending radius in the HER. The observed horizontal beam sizes including this effect are expected to be 427 μm in the LER and 655 μm in the HER.

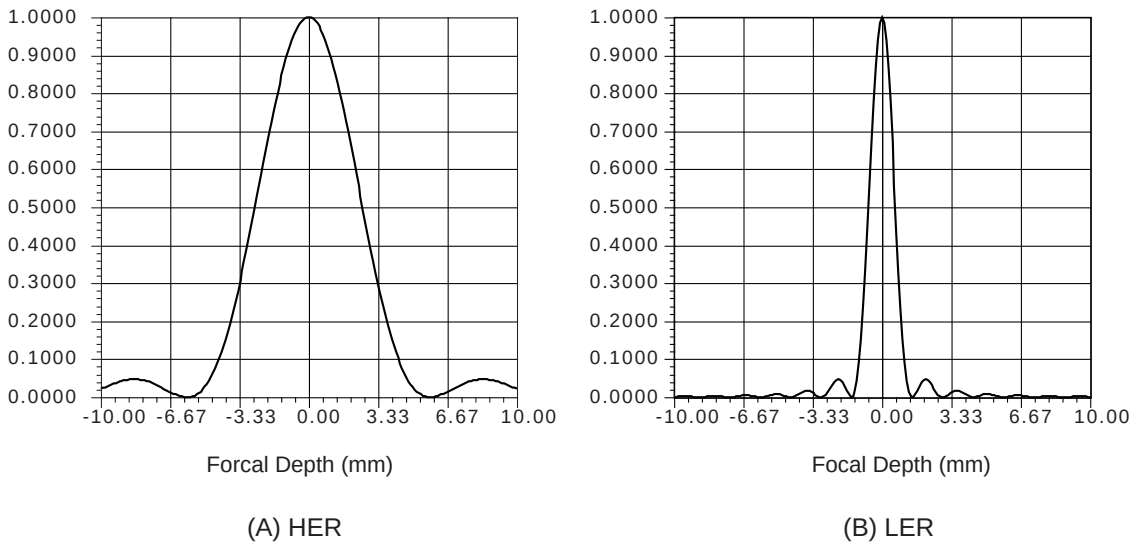

Figure 11.16: Longitudinal diffraction pattern of the focusing system.

11.2.8 Alignment of the system

The total path length of the focusing system will be about 40 m $\sim$ 50 m. To maintain good optical alignment of the entire system, an independent alignment for the lenses needs to be established first. Then, the axis of synchrotron light after the corrective system must align with the optical axis of the focusing system. The alignment of these two axes can be established with a two- or three-mirror system which corrects angular and transverse alignments. It is also very important to suppress fluctuation of air flow, and to eliminate dust in the optical pass. Therefore, an optical pass will be surrounded by a structure which has some irises to eliminate unwanted reflections or scattering. The entire arrangement of the total system, which includes the optical lab hut, is yet to be determined.

11.2.9 Summary

1. An extraction mirror system having a corrective optical system has been preliminary designed.

2. A diffraction-limited focusing system having an object-lens and relay-lens system has been designed.

3. A Fourier analysis of the focusing system is done in both the transverse and the meridional (longitudinal) planes. The expected observed beam sizes are summarized in Table 11.2. Since the diffraction effects are not negligible for a beam size

	LER		HER	
	σ_x	σ_y	σ_x	σ_y
Original	472 μm	69 μm	650 μm	120 μm
With Aberration	472 μm	69 μm	650 μm	120 μm
With transverse diffraction	506 μm	102 μm	675 μm	158 μm
With longitudinal diffraction	471 μm	69 μm	655 μm	120 μm
Total	507 μm	102 μm	680 μm	158 μm

Table 11.2: Expected values of the observed beam sizes which include contributions from effects of aberrations and diffraction.

measurement, it will be necessary to measure the point response of the system and to correct it.

4. The total length of optical pass will be 40 $\sim$ 50 m. An independent alignment will be required for both the focusing system and mirrors.

11.3 Laser Wire Monitor

In addition to the beam profile monitor based on imaged synchrotron light, the use of so-called laser wires is under consideration for better resolution with an ability to measure individual bunches.

The principle of the measurement is illustrated in Figure 11.17. A narrow laser beam ("laser wire") meets a beam bunch perpendicularly, creating a number of Compton-scattered photons. The population of scattered photons is proportional to the overlap area of the laser wire and the particle beam. Therefore, by scanning the laser light horizontally or vertically, and by measuring the flux of Compton-scattered photons, a one-dimensional particle distribution of the bunch is obtained.

The discussions in this section assume that the laser wire is placed at the end of a straight section. However, since the laser wire technique can offer a very high resolution, it may be also used at the collision point. The practical application depends on the availability of adequate space for the measurement ports.

The accuracy of the measurement is determined by the waist size (focused spot size) of the laser beam. As an example, we consider the vertical bunch-size measurement, which requires a better resolution than the horizontal one. In this case, the depth of the focus of the laser beam should be longer than the horizontal bunch size. The Rayleigh length L_R gives a measure for which a laser beam keeps its transverse size

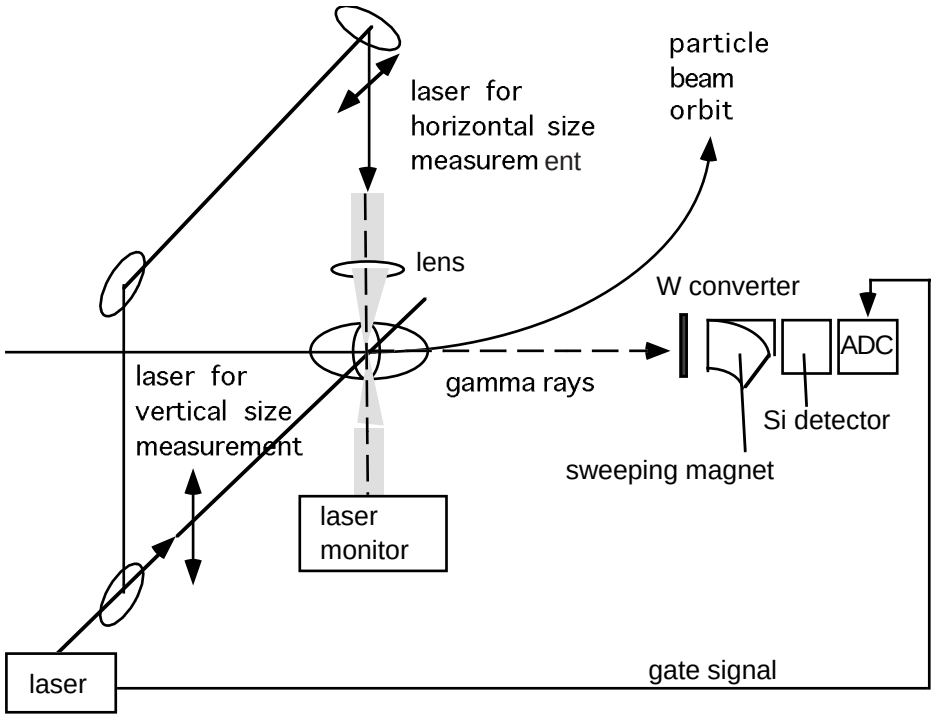

Figure 11.17: Concept of the beam size measurement using laser wires. A lens and laser monitors are necessary for the vertical size measurement as well, although they are not shown in the figure.

nearly constant,

$$L_R = 4\pi\sigma_L^2/\lambda_L, \tag{11.2}$$

where σ_L is the rms spot size at the waist of the laser and λ_L is the laser wavelength. We note here that in the field of laser technology $w = 2\sigma_L$ is conventionally used when giving the size of a light spot.

As stated earlier, we based our laser optics design on the following requirement:

$$L_R = 2\sigma_{ex}, \tag{11.3}$$

where σ_{ex} is the horizontal size of the particle beam. The laser spot size then becomes

$$\sigma_L = [\lambda_L\sigma_{ex}/(2\pi)]^{1/2}. \tag{11.4}$$

The typical particle bunch size in the horizontal direction is around 500 μm, except for the interaction region. The 355 nm third harmonic YAG gives $\sigma_L = 5.3$ μm. The minimum vertical beam size is approximately 30 μm. The measured value of the vertical bunch size by the laser wire will be $(30^2 + 5.3^2)^{1/2} = 30.4\mu$m. Figure 11.18 shows an example of the laser profile at the vertical beam-size measurement, together with the beam particle distributions.

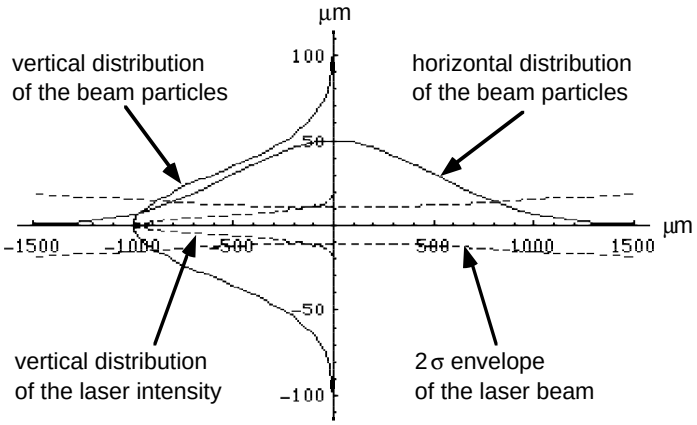

Figure 11.18: Design example of the laser-wire dimensions at a typical vertical beam-size measurement. The assumed beam sizes are 30μm vertically and 500 μm horizontally. Laser wavelength λ_L is 355nm and the minimum rms spot size is 5.3μm.

The statistical resolution of the measurement depends on the counting rate $\langle N_\gamma \rangle$ of the Compton photons,

$$\langle N_\gamma \rangle = \sigma_c L_c, \tag{11.5}$$

where σ_c is the cross section of the Compton scattering and L_c is the luminosity of the Compton scattering. The cross section is given by

$$\sigma_c = 2\pi r_e^2 [\frac{1+\epsilon}{\epsilon^3}\{\frac{2\epsilon(1+\epsilon)}{1+2\epsilon} - \log(1+2\epsilon)\} + \frac{1}{2\epsilon}\log(1+2\epsilon) - \frac{1+3\epsilon}{(1+2\epsilon)^2}], \tag{11.6}$$

where r_e denotes the classical electron radius and $\epsilon = \gamma h\nu_0/(m_e c^2)$ with the laser frequency ν_0 and Lorentz factor of the electron beam γ. This equation gives σ_c =594 mb for the 3.5GeV LER and 527 mb for the 8 GeV HER.

The Compton luminosity is given by

$$L_c[\mathrm{sec}^{-1}\mathrm{mb}^{-1}] = 0.5 \times 10^9 \lambda_L[\mu\mathrm{m}] I[\mathrm{mA}] W[\mathrm{J}] f_L[\mathrm{sec}^{-1}]/\Sigma[\mathrm{mm}^2] f_r[\mathrm{sec}^{-1}], \tag{11.7}$$

where λ_L is the laser wavelength, I the bunch current, W the laser pulse energy, f_L the laser pulse rate, and f_r the revolution frequency. The Σ is maximum when the laser beam passes the center of the particle beam. This maximum Σ is given by

$$\Sigma = (\sigma_{ey}^2 + \sigma_{Ly}^2)^{1/2}[(\sigma_{ex}^2 + \sigma_{Lx}^2)\cos^2(\delta/2) + (\sigma_{ez}^2 + \sigma_{Lz}^2)\sin^2(\delta/2)]^{1/2}, \tag{11.8}$$

where $\delta = \pi/2$ denotes the crossing angle, $\sigma_{ex,ey,ez}$ denotes electron beam sizes and $\sigma_{Lx,Ly,Lz}$ denotes laser beam sizes of the respective directions. If we assume the following pertinent parameters:

$$\lambda_L = 355\mathrm{nm},$$

$$I = 0.1\text{mA}, f_r = 100\text{kHz},$$

$$\sigma_{ex} = 500\mu\text{m}, \sigma_{ey} = 50\mu\text{m}, \sigma_{ez} = 5\text{mm},$$

$$\sigma_{Lx} = \sigma_{Ly} = \sigma_L = 5\mu\text{m}, \sigma_{Lz} = 30\text{mm},$$

$\Sigma = 1.42\text{mm}^2$ is obtained. Here, the beam current assumed in the LER and HER are 0.5 mA and 0.2 mA, respectively. By approximating σ_c =500 mb, we have $L[\text{sec}^{-1}\text{mb}^{-1}] = 165W[\text{J}]f_L[\text{sec}^{-1}]$ and $\langle N_\gamma[\text{sec}^{-1}]\rangle = 82.7W[\text{mJ}]f_L[\text{sec}^{-1}]$. A commercially-available 20 mJ, 100 Hz, 100 ps laser gives 165 kHz γ radiations at the maximum.

The maximum energy of the scattered photons is

$$E_{\gamma max} = \frac{(4\gamma^2 + 1)h\nu_0}{1 + 4\epsilon}, \tag{11.9}$$

which gives 389MeV to the LER and 1.77GeV to the HER. The bremsstrahlung produces noise radiation in this energy range. The bremsstrahlung counting rate caused by the interaction between the particle beams and the residual gas has been estimated to be $\sim$ 50MHz. This estimate is based on the following assumptions: the mean atomic number of the gas is 5, length of the straight section is 100 m, the gas pressure is 10^{-8} Torr, the particle beam current is 2.5 mA and the threshold energy of the gamma radiation detection is 20 MeV.

The photon detector consists of a tungsten converter, which converts gamma radiations to electron-positron pairs, a sweeping magnet to select electrons in a specific energy range and a Si detector, as shown in Figure 11.17. The Analog-Digital converter is controlled by a gate circuit to improve the S/N ratio. Gating of 10 ns width that is synchronized to the 100 Hz laser beam will reduce the bremsstrahlung noise rate to 50 Hz. The S/N ratio will be improved to 165kHz/50Hz=3300. The fluctuation of the laser output power contributes another statistical error. Using a 20 mJ, 100 Hz, 100 ps laser, the beam size measurement will be obtained with a statistical error better than 1% within a few minutes.

A pair of ports are required for each of the vertical and horizontal beam size measurements: one port to introduce the laser beam into the beam duct, and the other to monitor the laser beam transmitted through the duct. These ports may influence the impedance of the beam duct, depending on the size. The size requirement for the measurement is given by

$$w = \frac{4}{3}\frac{\lambda_L f}{\pi(2\sigma_L)}, \tag{11.10}$$

where $w = 2\sigma_p$ is twice the r.m.s. size of the laser beam at the lens with focal length f. This f is nearly equal to the distance between the lens and the particle beam. The 4/3 correction factor is for aberration and diffraction caused by a single lens.

Assuming $f = 100$mm, $\sigma_L = 5\mu$m and $\lambda_L = 355$nm, we obtain $w = 2\sigma_p = 1.50$mm or $\sigma_p = 0.75$mm.

The port size, under the assumption that the particle beam passes through the center of the beam duct, should be determined by the root of the squared sum of the particle beam size $\sigma_e = \sigma_{ex}$ or σ_{ey} and the laser beam size at the port σ_p, i.e. $(\sigma_e^2 + \sigma_p^2)^{1/2}$. The result is 0.901 mm for the horizontal size measurement and 0.751 mm for the vertical size measurement. If we want to cover 6σ at the port, the diameters of the ports for the horizontal and vertical size measurement are 5.4 mm and 4.5 mm, respectively. The port with 10mm diameter is large enough in each case, even if we take account of the variation in the particle beam position. A laser beam expander is commercially available for obtaining a $w = 1.50$mm beam at the final focusing lens.

Design of the laser optics, the timing control and the Compton detectors are being worked out. They are essentially the same as what has been developed for particle-beam polarization measurements at the TRISTAN Main Ring[1].

11.4 Bunch Feedback System

11.4.1 Design Considerations

Required damping time Studies on the acceleration cavities indicate that the growth times of multi-bunch instabilities at KEKB will be on the order of a few ms to 10 ms. The transverse instabilities will generally be stronger than the longitudinal ones. From these considerations, the goal of the bunch feedback system has been set to achieve a damping time of one ms for the transverse and 10 ms for the longitudinal planes.

Feedback systems There are roughly two categories of feedback systems that can be applied at KEKB: the bunch-by-bunch and the mode-by-mode feedback systems.

The bunch-by-bunch feedback systems are designed to deal with any combined oscillations of multi-bunches with or without correlations. For this purpose, such feedback systems should be wide-banded, and must cover up to at least one half of the bunch frequency. At KEKB this frequency is 255 MHz. The mode-by-mode feedback systems are designed for specific coupled-oscillation modes, and their bandwidth does not have to be as wide as the bunch-by-bunch feedback systems. However, a number of identical feedback systems (at least as many as the number of dangerous modes) need to be prepared for stable operation of the storage rings.

At KEKB both technologies will be implemented. For instabilities due to the resistive wall, as well as those due to the fundamental mode of the accelerating cavities, we

will use the mode-by-mode feedback method [2]. This is because for these two cases, the frequencies of the instabilities are predictable and can be known in advance. For those instabilities due to the higher order modes (HOM) of the accelerating cavities, our choice is to use the bunch-by-bunch feedback method. This is because their frequencies and the number of dangerous modes cannot be reliably predicted at this stage. Another reason to prepare bunch-by-bunch feedback systems is that they can deal with transient oscillations of a bunch during the injection process. The mode-by-mode feedback method could be less effective in this case.

Digital signal process The key technique in signal processing for the feedback system is to store information of bunch orbit deviations (transverse or longitudinal) for at least one full revolution period of the ring. At KEKB this is achieved by a pure-hardware digital filter system, which can work in a very high-frequency environment. The reasons for using the digital delay technique are as follows:

1. The digital system is more flexible than an analog delay with optical fiber cables and other devices.

2. The DC offset can be relatively easily eliminated with simple digital filters. We note here that the elimination of the DC offset for an individual bunch is essential for saving power to send to the kicker. This is because, in the longitudinal case, the synchronous phases of individual bunches can vary because of the large beam loading on the cavities introduced by the bunch gap.

3. It is easier to adjust the gain, phase and other parameters with digital systems. This helps the rapid start-up of the system as well as allowing efficient maintenance.

11.4.2 Pickup part

The feedback systems at KEKB consist of three parts: the pickup part, the signal processing part, and the kicker part. Figure 11.19 shows a system block diagram. The design of each of the three parts is described in the following.

Longitudinal

The longitudinal position (timing) of a bunch is converted into the phase difference between the pickup signal and a timing-reference signal as shown in Figure 11.20. The timing-reference signal is generated by multiplying the frequency of the RF signal for accelerating cavities. Hereafter, we call the frequency of the reference signal the

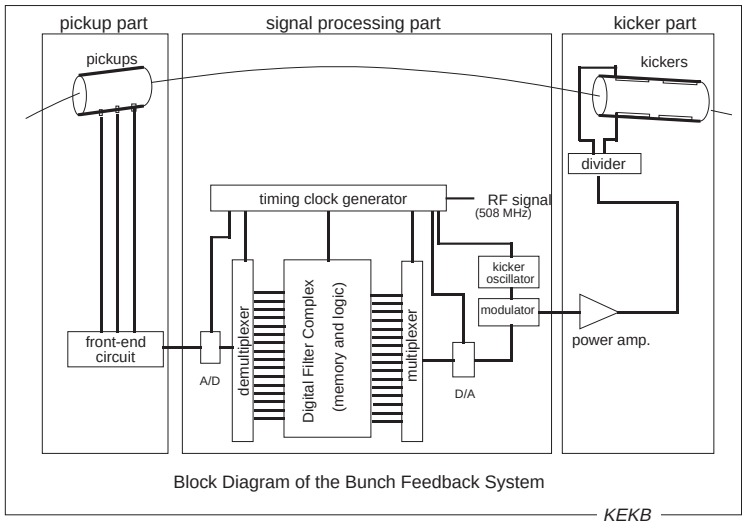

Figure 11.19: Block diagram of the feedback system.

"detection frequency." It is chosen to be 4 times the RF frequency, ∼2 GHz [3]. The pickup signal is created by combining 3 pulses from 3 longitudinally aligned pickup electrodes with a power combiner. The timing differences of these pulses should be adjusted so that the combined signal contains the detection frequency component.

Since the output of this circuit is proportional to the bunch current, the feedback gain will be proportional to the bunch current. However, this gain variation is not considered to be a major problem, since the growth rates of the instabilities are also proportional to the bunch current.

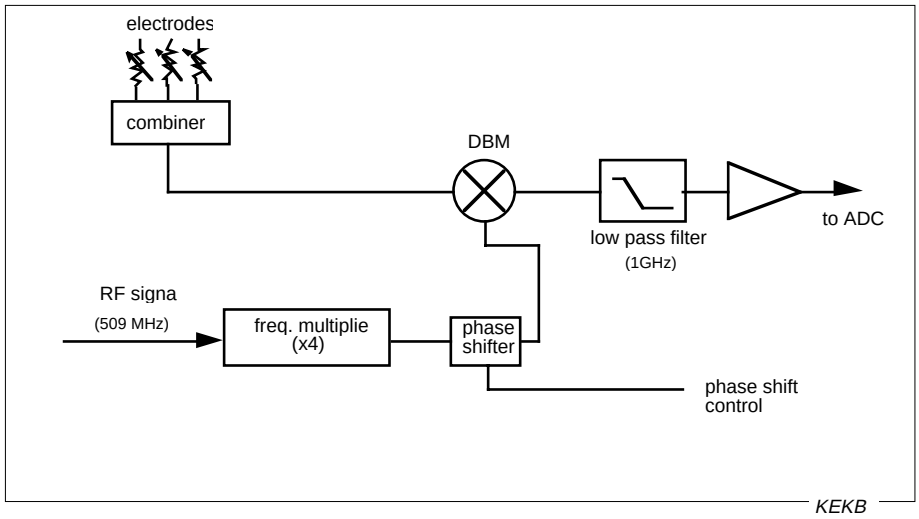

Figure 11.20: Front-end circuit for longitudinal pickup.

Transverse

The transverse position of a bunch is detected by the AM/PM method [4]. Figure 11.21 shows a block diagram of the circuit. Similar to the longitudinal signal pickup technique, the transverse beam signal is created by combining 3 pulses from three pairs of pickup electrodes. It produces the detection frequency component without any extra band-pass filter (BPF) in the front-end stage. By eliminating the BPF, unwanted overlaps of the ringing to the neighboring bunch are avoided, and the phase shift associated with the filter can be reduced.

The detection frequency used in the AM/PM circuit is chosen to be 2 GHz. This is so that the signals can terminate within the time interval that corresponds to a bunch spacing, i.e. 2 ns.

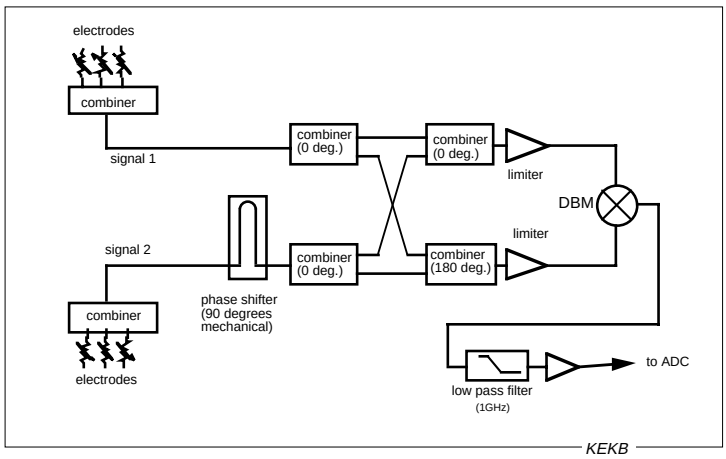

Figure 11.21: Front end circuit for transverse position detection.

11.4.3 Signal Processing

Two-tap filter in the signal processing

The jobs [5] of the signal processing part are: (1) create a signal delay (or phase shift), and (2) eliminate the DC offset.

These jobs are done by a simple 2-tap finite impulse response (FIR) filter. In general, the relation between the inputs (x_i) and the output (y) of an FIR filter is expressed by

$$y = \sum_{j=1} a_j x_j, \tag{11.11}$$

where the a_j's are called the filter coefficients. The 2-tap filters are the simplest ones among these FIR filters, and they will be employed in the KEKB feedback systems.

The output of the filter is a very simple function of the inputs, which can be written as:

$$y = a(x_k - x_j). \tag{11.12}$$

Note that the two coefficients have the same magnitude, but with opposite signs. This ensures that the gain of the filter is 0 in the limit of the frequency near zero. This also means that the calculations required during the operation of the digital filter involves only subtraction operations and, no multiplications. Consequently, the required hardware of the filter calculation is greatly simplified.

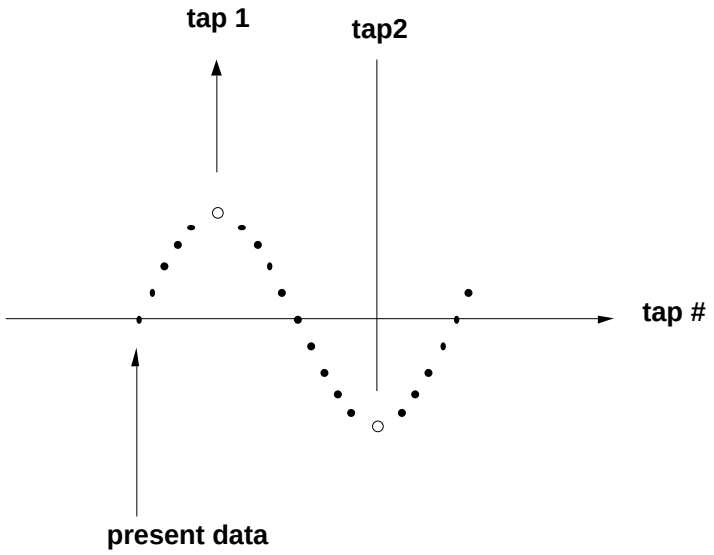

Figure 11.22: Tap positioning for the peak gain mode filter. The distance of two taps is half of one period and tap 1 is positioned at the 1/4 period before the present time to obtain a 90 degree shift.

There is a large difference in the tap positioning in the longitudinal and the transverse cases. For the longitudinal case, since the tune (synchrotron tune) is much smaller than 1, sampling points of the oscillation are relatively dense. In this case peak-gain filters can be applied, in which the positions of two taps should be separated by half of the full period of the oscillation. For efficient feedback purposes the phase shift should be 90 degrees [6]. As shown in Figure 11.22, this is achieved by choosing the taps at the 1/4 (90 degrees) and 3/4 period (270 degrees) positions relative to the timing of applying correction kicks to the beam.

Figure 11.23 gives an example of the frequency characteristics of the peak gain filter. The synchrotron tune is assumed to be 0.015, i.e. one period being about 67 turns. The taps are positioned at the 16-th and 49-th turns. The gain of the filter has peaks

at a tune of 0.015 and at its multiples. The phase shift is 90 degrees at a tune of 0.015 and at its odd multiples.

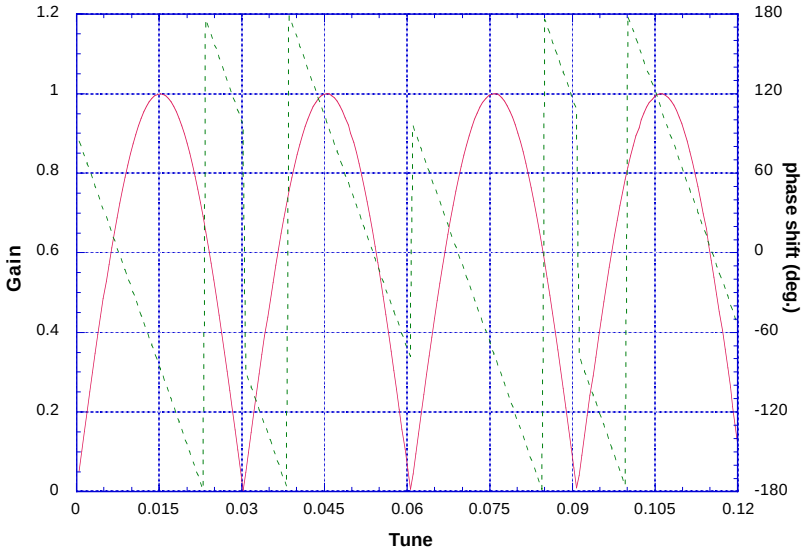

Figure 11.23: Frequency Characteristic of the FIR filter for longitudinal signal processing. The taps are positioned at 16 and 49. The solid and dashed lines show the gain and phase shift of the filter, respectively

For transverse systems, the tap positioning is more complex. The betatron tune is larger than 1 and its fractional part can vary between 0 and 1. The algorithm of the tap positioning is to find the configuration that maximizes the feedback gain for a given betatron tune. The feedback gain, χ, is expressed by

$$\chi = \text{gain}_{filter} \cdot \sin(\nu + \delta\nu), \tag{11.13}$$

where ν is the betatron tune and $\delta\nu$ is the phase advance from the monitor to the kicker. A simple computer program has been written to tabulate suitable tap positions for each tune. This program calculates the gain for all possible combinations of the tap positions. Figure 11.24 shows the result of a calculation for the case $\delta\nu = 90$ degrees with a maximum tap position of 8. Figure 11.24 indicates that for any tune we can find suitable tap positioning. We plan to prepare a few additional signal pickups which correspond to various $\delta\nu$ values, and will select one of them for a given betatron tune. This technique allows us to find a suitable tap positioning more easily with restricted positions of the taps.

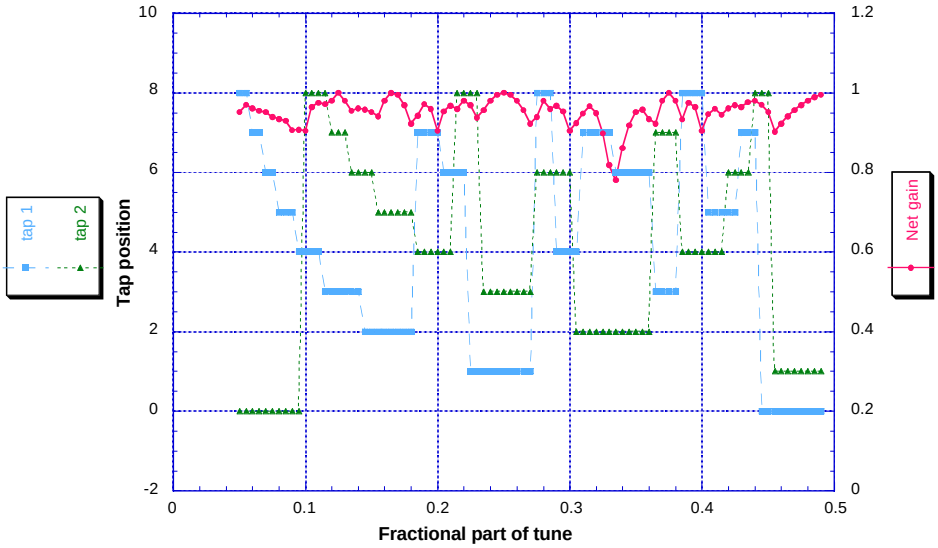

Figure 11.24: Tap positioning of the 2 tap filter for the transverse feedback. The feedback gain corresponding to the tap position is also shown. Note that tap position 0 means that the data of the last turn are used, but not the data of the present turn.

Signal processor

The heart of the signal processing part, which executes the filter calculation, is *the digital filter complex*. It consists of memory units and simple arithmetic units. Since the digital filter complex is a relatively low-speed device, in order to feed/extract data to/from it, two auxiliary devices will be implemented, i.e. fast demultiplexers (FDMUX) and fast multiplexers (FMUX). In addition, the signal processing part must be equipped with an analog-to-digital converter (ADC) and a digital-to-analog converter (DAC) as the interface with external elements. Figure 11.25 shows a block diagram of the system. The same design concept applies to both the longitudinal and the transverse systems.

Digital filter complex Figure 11.26 shows a block diagram of the digital filter complex. The complex consists of 16 identical units, each of which treats the data of 320 bunches (5120/16 = 320). The memory in one unit is aligned in two series. Each series is used for one of two taps. The capacity of one memory series is 32 kbytes, and it can store the data for 100 turns for each bunch. There is one arithmetic logic unit (ALU) in one unit which executes the subtraction of data from two series of memories. The digital filter complex will be assembled with wired logic or a custom IC. It will be capable of processing all of the data within one revolution period of the KEKB rings.

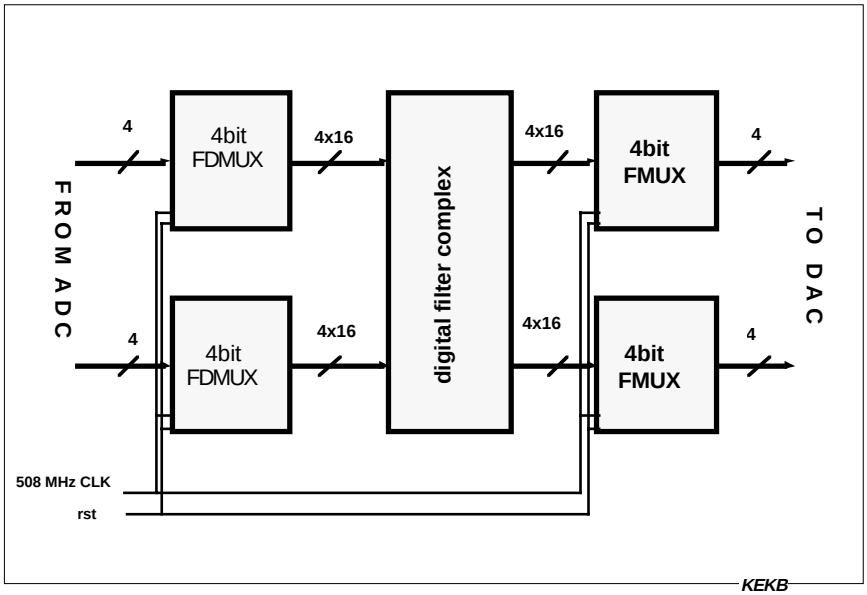

Figure 11.25: Block diagram of the signal processing part. The main part is a digital filter complex, which stores the data and executes the filter calculation. Two fast demultiplexers degrade the signal rate from 509 MHz to 1/16 that value. The processed data is again multiplexed to 509 MHz by a couple of the multiplexers.

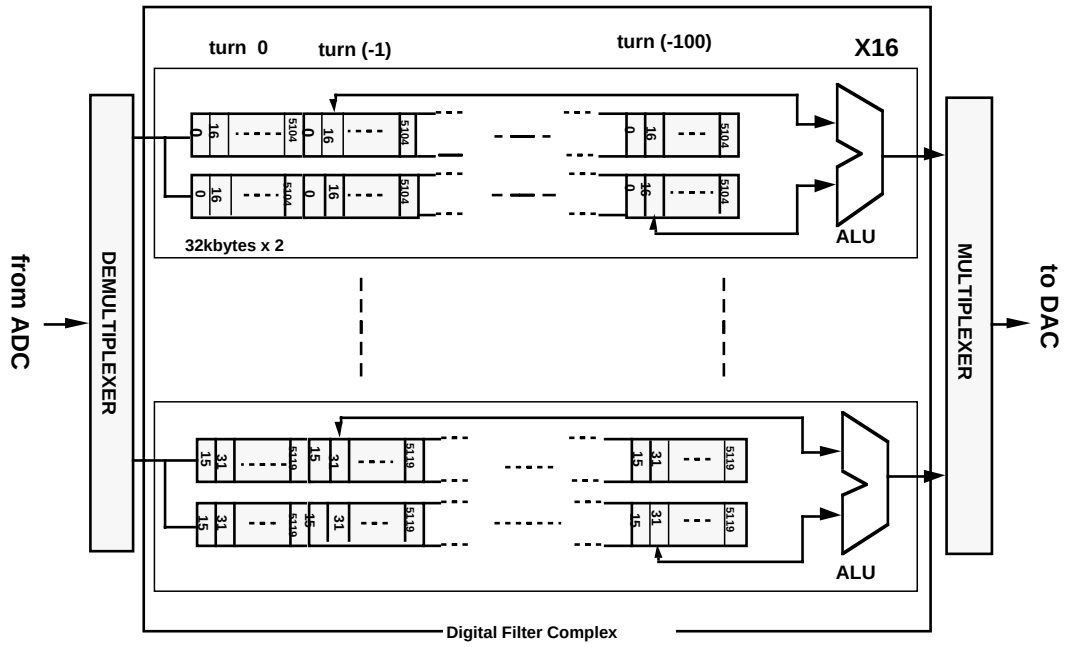

Figure 11.26: Block Diagram of the digital filter complex.

For practical use it must be made possible to rearrange the tap positioning easily and quickly when the working point is changed. This flexibility is particularly important for the transverse feedback systems. For this purpose, this circuit is equipped with tap pointers which can be modified with a relatively slow logic circuit.

A digital gain adjuster is implemented at the back-end of the digital filter complex. This adjuster allows us to easily control the loop gain. In addition, it realizes a saturated feedback loop (i.e. the bang-bang damping).

Demultiplexers and multiplexers Since the bunch frequency is 509 MHz at KEKB, the rate of the signal output from the ADC can be up to 509 MHz. The digital filter complex can not work at such high frequencies. To overcome this difficulty, a high speed demultiplexer will be used to drop the signal rate by a factor of 1/16 (about 32 MHz). Since this demultiplexer needs to handle the original 509 MHz signal, it will be built with custom GaAs gate-array chips. Each chip has 136 connector pins and is packed in a 28 mm×28 mm package. For demultiplexing 8-bit data, two chips are used, where each chip treats 4-bit data. The multiplexer will be built using the same technique. Figure 11.25 shows the connection of these chips as well as the digital filter complex.

ADC and DAC Flash ADC technologies have seen a remarkable progress in recent years. Several vendors have released 8-bit ADC's with a digitization speed of 500 Mega samples/second. Such devices can be used in the front end of the signal processing system. DAC's with similar speed and accuracies are less difficult to design than ADC's, and are also available.

11.4.4 Power Amplifiers and Kickers

Longitudinal

Kicker design The kicker for the bunch feedback system must support wide-band operation while maintaining a reasonable shunt impedance. At KEKB the band-width of the kicker required for the bunch by bunch feedback is 255 MHz. This is not a trivial requirement. Although a resonator structure similar to an accelerating cavity can be a good longitudinal kicker from the view point of the shut impedance, its frequency band width is too narrow for this purpose. While a structure which guides the TEM wave offers adequate wide-band characteristics, the shut impedance is sacrificed there.

The R & D for KEKB has been centered on a wide-band device based on TEM waveguides (so-called the drift tube type). Figure 11.27 schematically shows the structure

of the TEM wave guide [7] for the longitudinal case. A combination of the beam pipe and the inner electrodes creates a co-axial structure of the characteristic impedance of 25Ω. An RF power fed by power amplifiers propagates as a TEM wave along the structure. The RF to the kicker is created by modulating a sinusoidal carrier signal with the feedback signal. The frequency of the carrier is chosen to be 1016 MHz, which is twice the bunch frequency. Between adjacent inner electrodes, delay lines are inserted to shift the phase of this RF power by 180 degrees in the carrier frequency. This phase shift creates a longitudinal electric field between the neighboring electrodes.

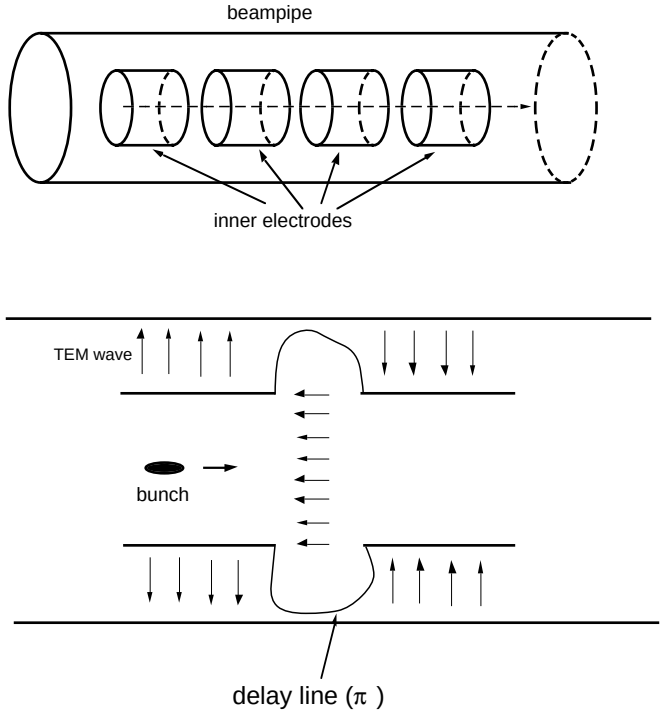

Figure 11.27: Principle of the longitudinal kicker

Since the RF power propagates in the direction opposite to the bunch in the kicker structure, the number of electrodes (N) in a kicker is limited by the condition that it must give an individual kick to each bunch. With the carrier frequency of 1016 MHz the largest number of electrodes, N_{max}, is given by

$$N_{max} = 2 \times \frac{\text{rf frequency}}{\text{bunch frequency}}. \tag{11.14}$$

Thus, for KEKB, the largest number of the electrodes is 2. The longitudinal length of a unit kicker is approximately 20 cm. The shunt impedance of the kicker is given by

$$Z_s = 4N^2 Z_c, \tag{11.15}$$

where Z_c is the characteristic impedance of the co-axial structure. Then, the expected shunt impedance for $Z_c = 25\Omega$ and $N = 2$ is

$$Z_s = 400\Omega. \tag{11.16}$$

Amplifier power and the number of the kickers One unit of the kicker has two input connectors. Each connector receives RF signals from a 500 W power amplifier. Thus the total power per kicker is 1000 W. The maximum kick voltage available from this kicker unit is

$$V_{max}/\text{unit} = \sqrt{2Z_s P_{max}} = \sqrt{2 \cdot 400 \cdot 1000} \simeq 900^{(\text{V})}. \tag{11.17}$$

The number of required kicker-units in the case of the LER is evaluated as follows[8]. The required kick voltage per turn, V_{turn}, is given by

$$V_{turn} = 2gT_0(\Delta E/e), \tag{11.18}$$

where g is the available damping rate, T_0 the revolution period and $\Delta E/e$ an energy deviation. If the required exponential damping rate is 100s^{-1} (damping time=10 ms) up to the energy deviation of 0.1%, the required kick per turn is

$$V_{turn} = 2 \cdot 100 \cdot 1 \times 10^{-5} \cdot 3.5 \times 10^9 \cdot 0.001 = 7000^{(Volts)}. \tag{11.19}$$

Therefore, 8∼9 kicker units will be required. The total length of the kickers will be about 1.8 m.

Transverse

The strip-line kickers For the transverse kickers we use standard strip-lines. The shunt impedance, $Z_\perp$, of the transverse kicker is given by

$$Z_\perp = 2Z_c \left(g_\perp \frac{l}{a} \frac{\sin kl}{kl} \right)^2, \tag{11.20}$$

where,

- a : radius of the strip-line (distance of the strip-line from the pipe center),
- Z_c : characteristic impedance of the strip-line,
- k : the wave number of the rf power,
- $g_\perp$: a geometrical factor (usually close to 1),
- l : length of the strip-line of the kicker.

From this expression, it is seen that the shunt impedance at the lower frequency limit is proportional to the square of strip-line length. Therefore, for the lower frequency the longer one is preferable. However, at a higher frequency, the sine factor in Equation 11.20, contributes with an opposite sign. Two kinds of the strip-line kickers will be prepared: a broad-band type, and a relatively narrow-band one with higher shunt impedance at lower frequencies. The wide-band type is 30 cm long and its shunt impedance at around 125 MHz is about 6 kΩ, assuming a=3cm, Z_c=50 Ω, $g_\perp$=0.9. The narrow-band type, which will suppress instabilities due to the resistive wall impedance and some HOM instabilities which have very low mode numbers, is 3 m long. The shunt impedance at the low-frequency limit is 200kΩ.

Estimation of the required power A formula corresponding to (11.18) for the transverse case is

$$V_{turn} = 2gT_0(E/e)x_{max}/\sqrt{\beta_m\beta_k}, \tag{11.21}$$

where E/e is the energy of the beam in electron-Volts, $\beta_{m,k}$ the beta function at the monitor and the kicker, and x_{max} the maximum amplitude of the oscillation. Assuming the beta function at the kicker is 10 m and the maximum beam orbit amplitude is 1 mm, the voltage required to bring the damping time to 4 ms is obtained as

$$V_{turn} = 2 \cdot 250 \cdot 1 \times 10^{-5} \cdot 3.5 \times 10^9 \cdot 0.001/10 = 1750^{(Volts)}. \tag{11.22}$$

Using the shunt impedance of 6 kΩ of the wide-bad type, the required power is approximately 250 W. To fulfill this requirement, two 200 W-amplifiers will be prepared. They must cover a frequency range from 20 MHz to 250 MHz.

For the narrow-band type, the required voltage for obtaining a damping time of 1 ms is 7 kV. The required power will be 120 W. For this purpose two 120 W amplifiers need to be prepared. They must cover a frequency range from 10kHz to 20MHz.

Bibliography

[1] K. Nakajima *et al.*, Phys. Rev. Lett. **66**, 1697(1991); TRISTAN Polarization Study Group, Proc. 10th Int. Symp. High Energy Spin Physics, 1992, Nagoya, (University Academy Press, Inc., Tokyo, 1993) p.919.

[2] The instability due to the fundamental mode of the accelerating cavities can be fatal without any damping techniques. The RF cavities are very carefully designed so as to decrease the growth rate of this instability. Nonetheless, there is some possibility left that the growth time is shorter than the radiation damping time.

[3] The detection frequency must be lower than the cut-off frequency of the beam pipe. Typically, the radius of the beam pipe at KEKB is about 50 mm, or a somewhat smaller. The cut-off frequency in this case is 1.7 GHz. We will prepare a special beam pipe with the radius of 35 mm for the oscillation pickup.

[4] The principle and characteristics of the AM/PM method is explained in detail in the paper by R.E. Shafer. (AIP Conference Proceedings 212).

[5] One may think that noise reduction must be one of the tasks of the signal processing part. However, according to our beam studies the noise is very low and its is not necessary.

[6] Strictly speaking, this 90 degrees should be the sum of the phase shift of the filter and the synchrotron phase advance within one revolution. Because the synchrotron tune is very small compared with 1, one turn delay is very small.

[7] This structure of the longitudinal kicker was originally proposed in the PEP-II Design Report.

[8] A rough estimation shows that the growth rate of the coupled bunch instabilities is proportional to the factor, $R = I_{beam}/E_{beam} \times$ (# of cavities). The ratio of this factor for LER and HER, R(LER)/R(HER), is about 3. Then the instabilities will be stronger in LER.

Chapter 12

Injection

12.1 Linac

12.1.1 Overview

To allow for the smooth operation of KEKB, a major upgrade program is under way for the 2.5 GeV injector linac, which was formerly used to inject beams to the Tristan accelerator complex and the Photon Factory (PF) ring. Two main goals of the upgrade are:

- Increase the energies of electrons and positrons to 8 GeV and 3.5 GeV, so that they can be injected into HER and LER of KEKB at full energies.
- Increase the bunch intensities of positrons by a factor of ~ 20 for efficient fills.

Tables 12.1(1) through (4) compare the parameters of the injector before and after the upgrade. The upgrade program includes tasks in the following three areas:

1. Successive replacement of the RF power sources by higher-power klystrons with RF pulse compressors.
2. Small extension of the linac total length.
3. Relocation of the positron production target, so that positrons are produced by incident electrons of 3.7 GeV instead of the former 0.25 GeV.

The pre-upgrade linac consists of six sectors called P, 1, 2, 3, 4 and 5. A regular sector consists of eight accelerator units, which include four 2-m accelerator sections. The accelerator sections in each unit are driven by one klystron. In the upgrade, two sectors will be added to the linac, and they will be renamed A, B, C, 1, 2, 3, 4 and 5, as shown in Figure 12.1.

Sectors A, B and C are those to be newly built. Sector A will have a pre-injector, which will produce intense single bunches. It will include double sub-harmonic bunchers (SHB's), followed by three accelerator units. Sectors B and C are regular accelerating sectors. Sector 2 will be rebuilt so as to include a positron generator by moving Sector P to this location. In Sectors 1, 3, 4 and 5, the component layout will not be changed, or changed only slightly.

The pulse energy of the pulse modulators will be increased by a factor of two. This will be achieved by increasing the total capacitance of PFN while maintaining the same charging voltage. All of the 30-MW klystrons will be replaced by 50-MW types. RF pulse-compressors will be installed at the klystron output with a small modification to the waveguide system and improvements to the vacuum system.

The number of accelerator units is to be increased from 46 to 57. The average energy gain of one unit will be 160 MeV. The full linac energy without beam loading will reach about 9 GeV. An extra energy gain of over 8 GeV(13%) will be used to compensate for any gain loss due to defective units, energy-spread adjustment, or energy tuning.

In the pre-upgrade linac the positrons were produced with primary electrons of 0.25 GeV. The positron production yield has been measured to be $N^+/(N^-E^-) = 1.8$ % GeV^{-1}. The expected positron charge after the upgrade is 0.67 nC for a primary electron pulse of 0 nC at 3.7 GeV.

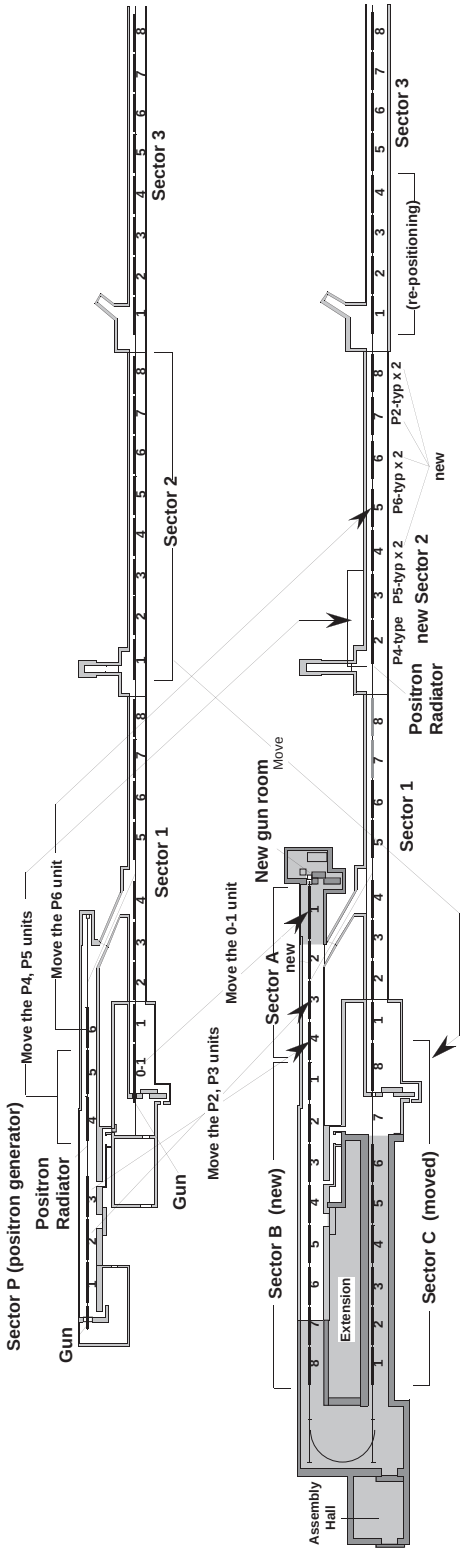

Figure 12.1: Linac re-formation from the 2.5 GeV linac (upper) to the KEKB 8 GeV injector (lower).

		PRESENT	KEKB	
[INJECTION BEAM]				
energy	(e^-)	2.5	8.0	GeV
	(e^+)	2.5	3.5	GeV
pulse length		<2	single bunch	ns
bunch width (σ_z)		∼5	∼5	ps
particle (charge)/pulse	(e^-)	2×10^9(0.32)	8×10^9(1.28)	(nC)
	(e^+)	2×10^8(0.032)	4×10^9(0.64)	(nC)
pulse repetition		25	50	
emittance	(e^-)	4×10^{-8}	6.4×10^{-8}	m
	(e^+)	8×10^{-7}	8.8×10^{-7}	m
energy width	(e^-)	0.2	0.125	%
	(e^+)	0.22	0.25	%
[MAIN ACCELERATOR]				
Accelerator section				
type of structure		T.W., $\frac{2}{3}\pi$-mode, semi-C.G.		
frequency		2856		MHz
disk aperture diameter		24.85∼ (75 μm step)		mm
length (with vacuum flanges)		2040		mm
filling time		0.5		μs
energy gain (no-load)		7.4		$MeV/MW^{1/2}$
total number		162	230	
Accelerator unit[*2]				
length (regular unit)		9.6		m
number (total)		46	57	
(before e^+ radiator)		3	26	
(stand-by and energy-tuning)		∼3+1	4+2	
energy gain (with RF compressor)			160	MV/unit
(without RF compressor)		62.5 (@20 MW)	90 (@40 MW)	MV/unit
energy multiplication			1.8	

Table 12.1(1): Changes in the major parameters of the linac from the present to KEKB.

	PRESENT	KEKB	
[PRE-INJECTOR]			
Gun			
type	triode		
cathode	BI-cathode (EIMACY796)		
high-voltage/width	200 kV/1μs		
grid-voltage/width	200 V/4 ns		
normalized emittance	$\sim 5 \times 10^{-6}$		m
1st-subharmonic buncher			
type of structure	re-entrant cavity		
frequency	119.000	114.2	MHz
field-strength	4	4	MV/m
2nd-subharmonic buncher			
type of structure	re-entrant cavity		
frequency		571.27	MHz
field-strength		4	MV/m
1st-prebuncher			
type of structure	T.W., $\frac{2}{3}\pi$, C.I.		
frequency	2856		MHz
cell number	7		
disk-aperture diameter	35.74		mm
phase velocity	0.7c		
shunt impedance	16.0		MΩ/m
2nd-prebuncher			
type of structure	T.W., $\frac{2}{3}\pi$, C.I.		
frequency	2856		MHz
cell number	5		
disk-aperture diameter	36.89		mm
phase velocity	0.7c		
shunt impedance	15.0		MΩ/m
Buncher			
type of structure	T.W., $\frac{2}{3}\pi$, C.G.		
frequency	2856		MHz
cell number	35		
disk-aperture diameter	35.0$\sim$19.3		mm
phase velocity	0.7c$\sim$1c		
shunt impedance	15.0		MΩ/m
Output beam			
energy	50	50	MeV
energy spread (σ_E/E)	0.6	0.6	%
normalized emittance	$\sim 6 \times 10^{-5}$		m

Table 12.1(2): Changes in the major parameters of the linac from the present to KEKB.

	PRESENT	KEKB	
[POSITRON PRODUCTION]			
Radiator			
material	Ta		
thickness (radiation length)	8 ($2X_0$)	16($4X_0$)	mm
diameter	8	8	mm
Primary electron			
energy	0.25	3.7	GeV
particle (charge)/pulse	1×10^{11}(16)	6×10^{10}(10)	(nC)
emittance (1σ)			m
energy with (σ_E/E)		0.45	%
Positron production rate			
after the solenoid (100 MeV)	6.5%		
at the 30° -transport (250 MeV)	4.2%		$\frac{e^+}{e^-GeV}$
final (2.5 GeV)	1.8%	>1.8%	
Focusing system			
type	QWT		
pulsed solenoid (strength×length)	2.3T×45 mm	2.3T×45 mm	
D.C. solenoid (strength×length)	0.4T×8 m		
normalized acceptance	6×10^{-3}		m

Table 12.1(3): Changes in the linac major parameters from the present to KEKB.

	PRESENT	KEKB	
[RF SOURCE]			
Modulator			
PFN charging voltage	45		kV
PFN total capacitance	0.3	0.6	μF
energy stored in PFN	300	600	J
pulse repetition rate	50		pps
PFN impedance	6.4	4.7	Ω
pulse width	3.5	5.6	μs
pulse output voltage	22.5		kV
pulse output power	80	107	MW
Pulse transformer			
step-up ratio	1:12	1:13.5	
2nd. voltage×width	0.95	1.7	Vs
core bias	none	necessary	
Klystron			
beam voltage	270	304	kV
beam current	295	352	A
rf power peak	33	46	MW
rf power average	3.3	9.3	kW
rf pulse width	2	4	μs
Pulse compression	none	SLED	
multiplication factor	1	$\sim$2	
Energy gain/unit	65	$\sim$160	MeV
[BEAM TRANSPORT]			
solenoids (injection)			
solenoids (e^+ generator)			
quadrupole triplets			
doublets			
singlets			
betatron wavelength			
[BEAM MONITORS]			
wall current monitor			
profile monitor (Ceramic)			
beam position monitor			
wire scanner			
core monitor			

Table 12.1(4): Changes in the major parameters of the linac from the present to KEKB.

12.1.2 RF Power Sources

The pulse modulators will be upgraded as indicated in Table 12.1(4). Ten new modulators will be added, while the existing units will be upgraded by replacing the IVRs, charging choke transformers, PFNs and thyratrons. To produce 4 μs pulses, two arrays of 20-section PFNs are used for each modulator. A schematic drawing of a modulator unit is shown in Fig. 12.2.

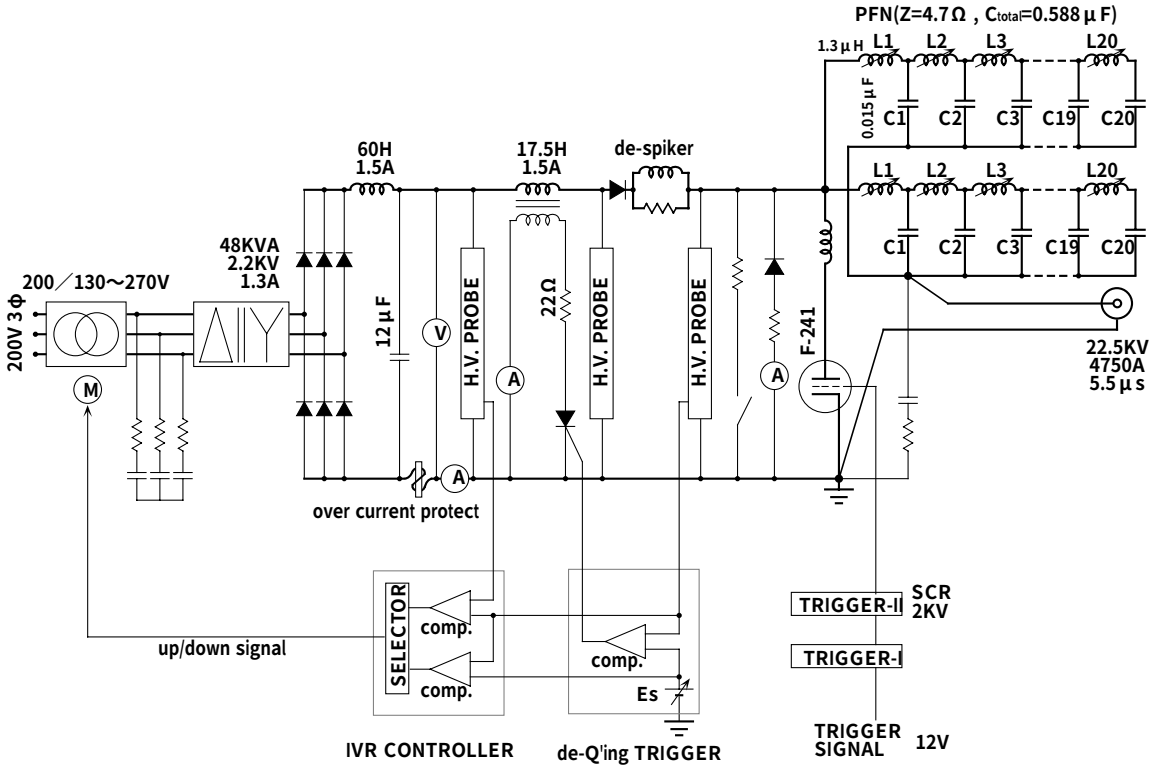

Figure 12.2: Modulator for the KEKB injector linac.

To produce the required 50 MW output power, an upgrade program of PV3030 klystron (30 MW type) is under way. The new klystron is called PV3030A3. Some of the specific features are:

1. The dimensions of the RF interaction region (cavity) are kept the same as those of PV3030, and hence, the same as SLAC XK-5 tubes.

2. The cathode diameter is increased from 80 mm to 85 mm, and the average pulse-current density from the cathode has been reduced.

3. A larger ceramic-seal is employed on the gun, in order to improve the high voltage capability.

4. The dimensions of the new klystron are similar to those of the original 30 MW type. This allows focusing magnets of previous types to be used with only minor modifications.

5. The distance between the anode and the 1st cavity was increased by 4 cm for stable microwave operations.

6. The space between the collector and its outer spool is increased, and a thicker X-ray shielding is inserted.

A test of PV3030A3 at a beam voltage of 310 kV has produced an output power of 51.5 MW with an efficiency of 44%.

In addition, a totally new 50 MW type klystron is under development. Figure 12.3 shows a comparison of cut-away views of the old and new tubes with an optimum magnetic field. Table 12.2 gives a comparison of the existing klystron and the new tubes.

	Unit	existing(PV3030)	PV3030A3	50MW
Beam voltage	kV	270	285(310)	315
Beam current	A	295	319(362)	370
Beam power	MW	80	91(112)	117
Beam pulse width	μs	3.5	5.5	5.5
Repetition rate	pps	50	50	50
RF output power peak	MW	33	40(50)	50
RF output power av.	kW	3.3	8.0	10
RF pulse width	μs	2	4	4
Efficiency	%	42	44	44
Perveance	$\mu A/V^{3/2}$	2.1	2.1	2.1
Overall length	mm	1317	1317	<1400
Number of cavity		5	5	5
RF window		single	single	single

Table 12.2: Parameters of the high power klystrons

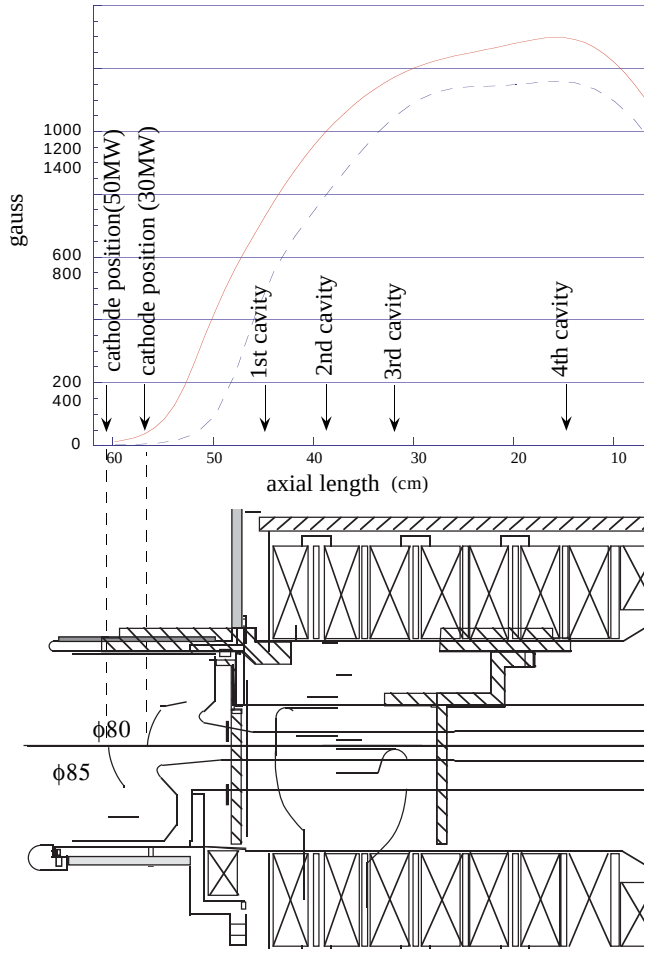

Figure 12.3: Comparison of a cut-away view of the old and new tubes with an optimum magnetic field.

The pulse transformers are being upgraded to provide a step-up ratio of 1 : 13.5 instead of the former 1 : 12. This is done by changing the winding ratio of the primary and secondary coils. To continue using the existing cores, which are rather large, a core-reset bias current to the primary windings will be applied. The insulation of the transformer will be improved to withstand a high voltage of over 310 kV during operation.

The existing pulse-transformer oil tanks will be reused. However, extension adapter tanks (10 cm high) will be added for mounting new klystrons with long gun insulators. All other parts, such as the feeder sockets, cooling pipes, klystron socket, heater transformer, and wave-form monitors, will be reused without modifications.

12.1.3 RF Pulse Compressor

The design of a SLED-type RF compressor has been developed to meet the specifications for KEKB. Table 12.3 summarizes its parameters. Five units have been fabricated so far. During an initial testing the RF power up to 48 MW was fed, and the energy gain was measured with and without the SLED to be 179 MeV and 97 MeV, respectively. The amplification of the accelerating energy was found to be > 1.85, as shown in Figure 12.4. The theoretically expected energy gain is 1.96 (see Figures 12.5(a)-(d)). A new RF-drive system is also being tested (Fig. 12.6).

Resonant mode	TE015
Q (theoretical)	105000
Q (measured)	100000
Coupling (type)	two-hole, side-wall
(β)	6.4
tuner	$<$ 2kHz/step (manual)
detuner (type)	solenoid-drive, needle (ϕ2mm, stroke 168mm)
(separation)	$>$20MHz
gain-shift	0.1%/5kHz(0.1°C)

Table 12.3: SLED specifications for the KEKB linac

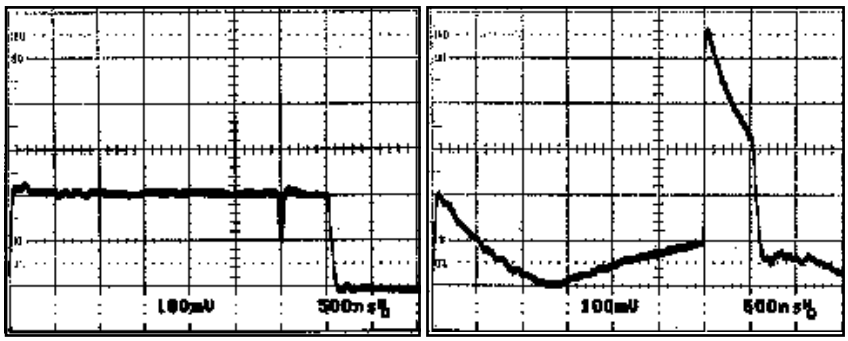

Figure 12.4: RF-pulse waveforms observed at an output port of the SLED.

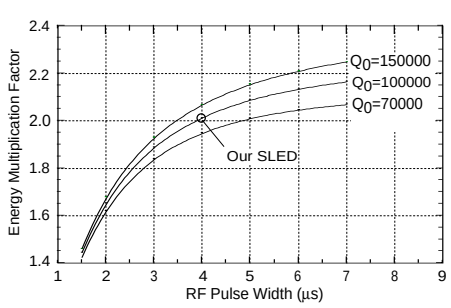

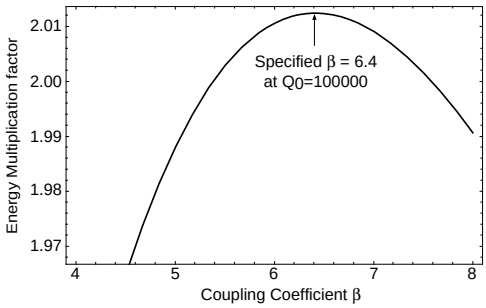

Figure 12.5(a): Energy multiplication factor as a function of the RF pulse width and the Q-value of the cavity.

Figure 12.5(b): Energy multiplication factor as a function of the coupling coefficient β.

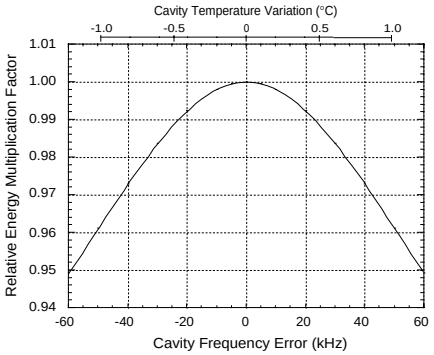

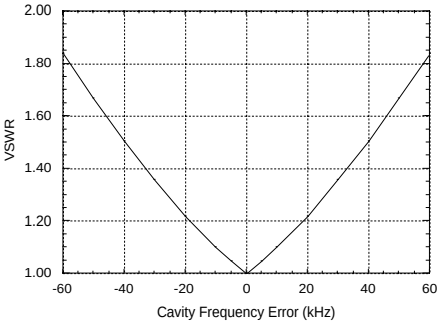

Figure 12.5(c): Relative energy multiplication factor as a function of the frequency error and temperature variation.

Figure 12.5(d): VSWR as a function of the frequency difference of the SLED cavities.

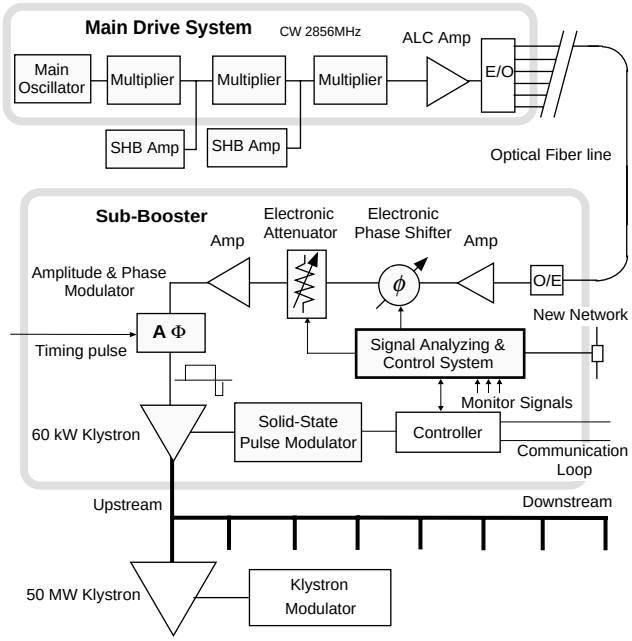

Figure 12.6: New rf drive system for the KEKB injector linac.

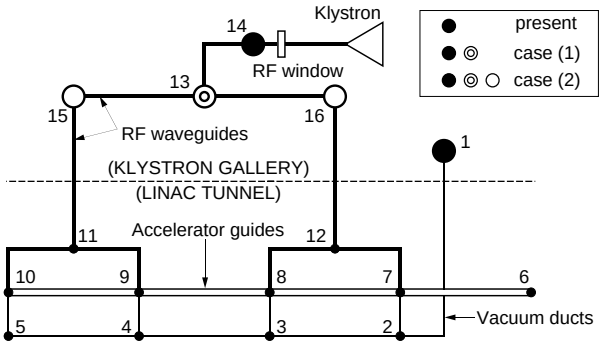

Figure 12.7: Schematic diagram of the vacuum network in an accelerator unit.

12.1.4 Vacuum Improvement for High-power Operation

To stably operate the linac under a very high-field strength (20 MeV/m) condition in the linac, the rf-conditioning may take a long time period. Also, electrical breakdown phenomena at the accelerator guides and the rf window are a concern.

The breakdown phenomena depend not only on the strength of the electric (accelerating) and magnetic (focusing) fields, but also on the surface and bulk conditions of the materials. Such surface conditions as contamination and adsorbed water molecules are generally correlated to the vacuum pressure. Therefore, the breakdown phenomena are often related to the vacuum quality in the system. For instance, klystron window breakdown is scarcely initiated from the inside of a klystron, where the pressure is lower than 1×10^{-6} Pa; window breakdown usually occurs on the waveguide side, where the pressure is typically $\sim 10^{-5}$ Pa. It is thus expected that a pressure reduction is one of the possible measures for suppressing various breakdown problems. A new method, which uses characteristic matrices of the vacuum network geometry, has been developed, and is used to analyze the pressure profile of the system.

We have investigated the changes of the pressure profile when some new pumps are added to the present system. Figures 12.7 shows the layout of the vacuum system. Two configurations have been tested initially: (1) A pump is added at node 13, and (2) three pumps are added at nodes 13, 15 and 16. Figure 12.8 shows the resultant pressure distribution.

Other configurations were then examined for a further reduction of the pressure (Figure 12.9). The configuration for case (3) is slightly different from that of case (2). A 500 ℓ/s pump is moved from the klystron gallery to the neighborhood of the accelerator guides in the tunnel; the length of the penetrating vacuum duct is shortened from 6 m to 1 m. In case (4), eleven pumps having an effective pumping speed of 10 ℓ/s are mounted at every node. The pressures at both ends of the accelerator guide are noticeably reduced in these configurations, as shown in Figure 12.10. Among these

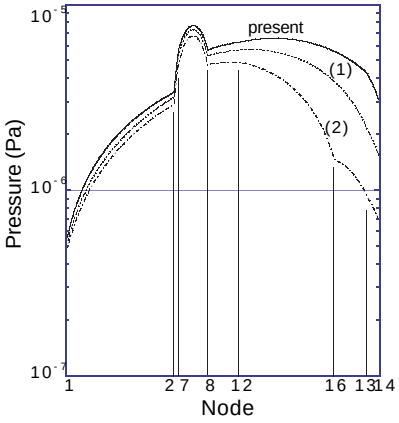

Figure 12.8: Pressure distributions calculated for the present configuration and for cases (1) and (2).

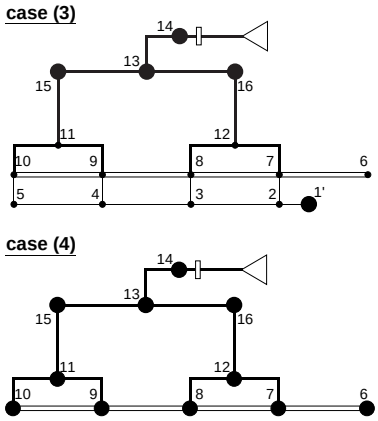

Figure 12.9: Configuration of the additionally installed pumps in the linac tunnel.

configurations, cases (2) and (3) are being tested in Sectors 4 and 2, respectively.

12.1.5 Beam Dynamics Issues

Longitudinal and Transverse Wakefields

To produce the required positron bunch population, intense electron bunches (10 nC with $\sigma_z = 1.5$ mm) need to be delivered on the positron production target at 3.7 GeV. With an accelerating gradient of 20 MV/m and a betatron wavelength of 40 m, the expected electron beam envelope in the upstream part of the injector is as shown in Figure 12.11(a),(b).

Due to the longitudinal wakefield, the energy broadening (σ_E/E) of the electron bunch for producing positrons is 1.2% when the bunch is on crest, and 0.45% when 7 degrees off crest (see Figure 12.12(a) and (b)). The average energy loss is 4 % as shown in Figure 12.13.

For stable operation of the system, the electron spot size on the positron production target needs to be less than 0.6 mm. Evaluations on the transverse wakefields indicate that to meet this requirement the beam displacement from the accelerator axis has

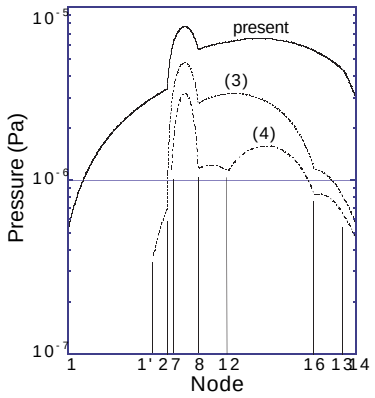

Figure 12.10: Pressure distributions calculated for cases (3) and (4).

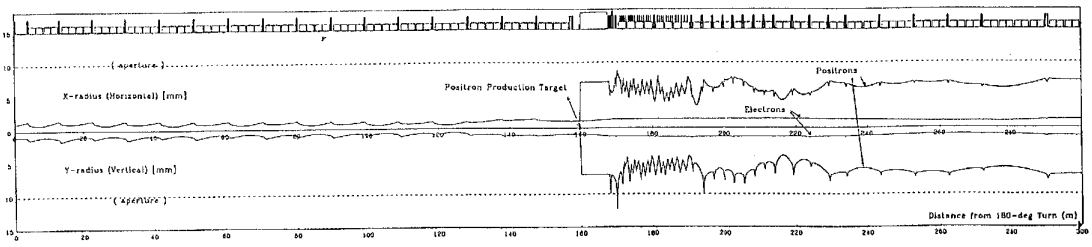

Figure 12.11(a): Calculated electron beam envelopes from the pre-injector (right side) to the 180° arc (left side).

Figure 12.11(b): Calculated electron beam envelopes after the 180° arc (left side) and positron beam envelopes after the positron production target (center).

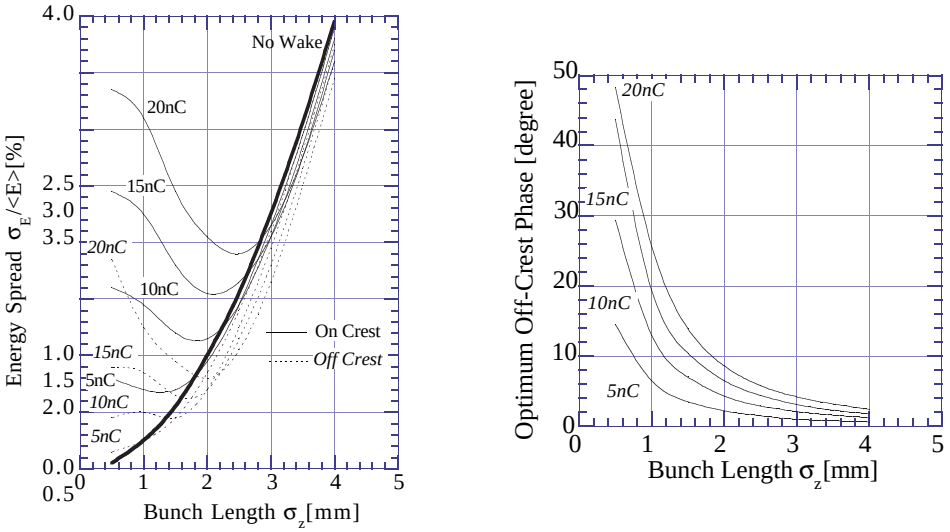

Figure 12.12(a): Bunch-length dependence of the energy spread.

Figure 12.12(b): Optimum off-crest phase as a function of the bunch length.

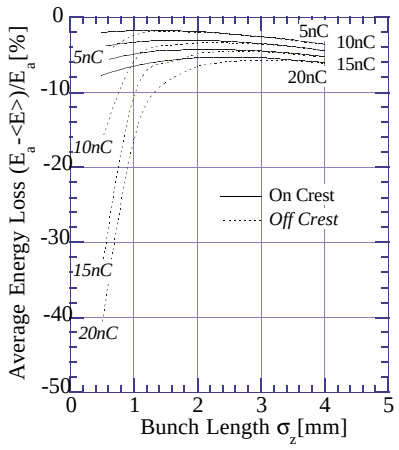

Figure 12.13: Average energy as a function of the bunch length.

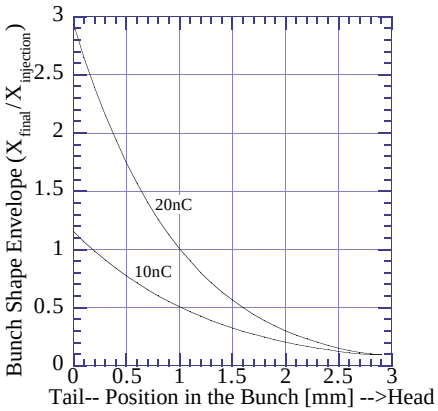

Figure 12.14: Bunch-shape deformation due to injection errors.

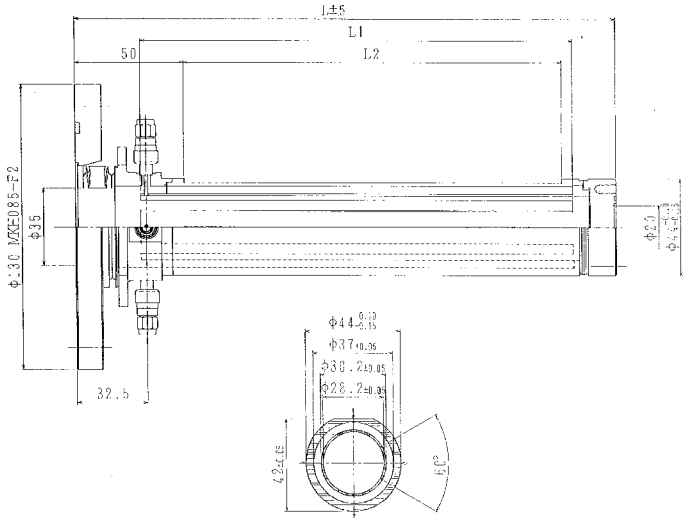

Figure 12.15: Beam position monitor (BPM) to be used in the KEKB injector linac.

to be kept below 0.5 mm. Good accelerator alignment and the beam position control must achieve and maintain this requirement.

Beam Position Measurement

From the discussion above, the accuracy of beam-position monitors (BPMs) is required to be ±0.1mm. Conventional strip-line monitors have been developed to be used at each quadrupole magnet. An electrode length of 130 mm has been tentatively chosen for testing, as shown in Figure 12.15.

The read-out electronics consists of the front-end, the detector and an external ADC, as shown in Figure 12.16. At the front-end the signal from an electrode is stretched in time by a band-pass filter (BPF), and is then amplified. At the detector the signal is split into the RF mixer port and the limiting amplifiers (L/A) to generate a local oscillator (LO). The peak value of the low-pass filtered intermediate-frequency (IF) signal is proportional to the beam-charge density and the beam position. The signal is captured by the sample-and-hold, and is digitized for computer processing where the horizontal and vertical displacements of the beam are calculated.

The required dynamic range of the signal processing circuit is 60 dB. Out of this, 35 dB is for the beam intensity measurement, and the remaining ±12 dB is for position measurements. This dynamic range covers the signal levels expected during regular operation, as well as during the commissioning period. A linearity better than 2% needs to be maintained. The measurements of test circuits indicate that those specifications can be met.

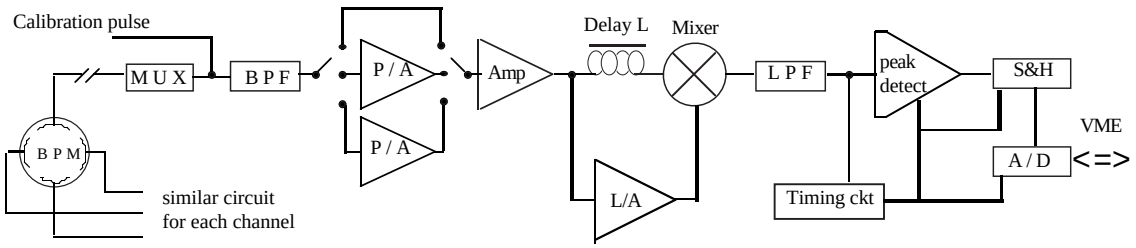

Figure 12.16: BPM circuit block diagram.

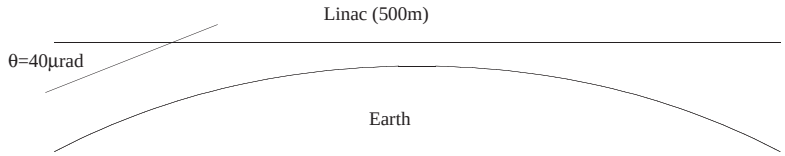

Figure 12.17: The linac is to be aligned tangential to the earth at its center.

Alignment of the J-shaped Linac Using a Laser System

The injector consists of two parallel linacs and a 180° bend arc section, as shown in Figure 12.1. A high-current beam from the upstream linac needs to be transported to the positron-production target without degradation of the beam quality. The alignment tolerance in the linac, according to beam dynamics calculations, is 0.1 mm. The downstream linac has a total length of 500 m, and the effect of the curvature of the earth is not negligible. The gravity observed at the center of the downstream linac defines its horizontal alignment, and, consequently, at its upstream end the linac has an angle of 40 μrad relative to the local horizontal plane defined by gravity. Figure 12.17 illustrates this fact.

Two methods for the injector alignment have been evaluated. The first method treats the three parts of the injector independently. In the second method a single common plane for the two linacs and the arc part is created as a reference. However, in this second method whenever the alignment of the downstream linac is changed, the rest of the system also must be changed. Therefore, the first method is favored and will be adopted. Although two vertical translation optics are required to join the entire injector, it is considered possible to achieve the required alignment accuracy.

The practical procedure for realizing this alignment is as follows. First, one must

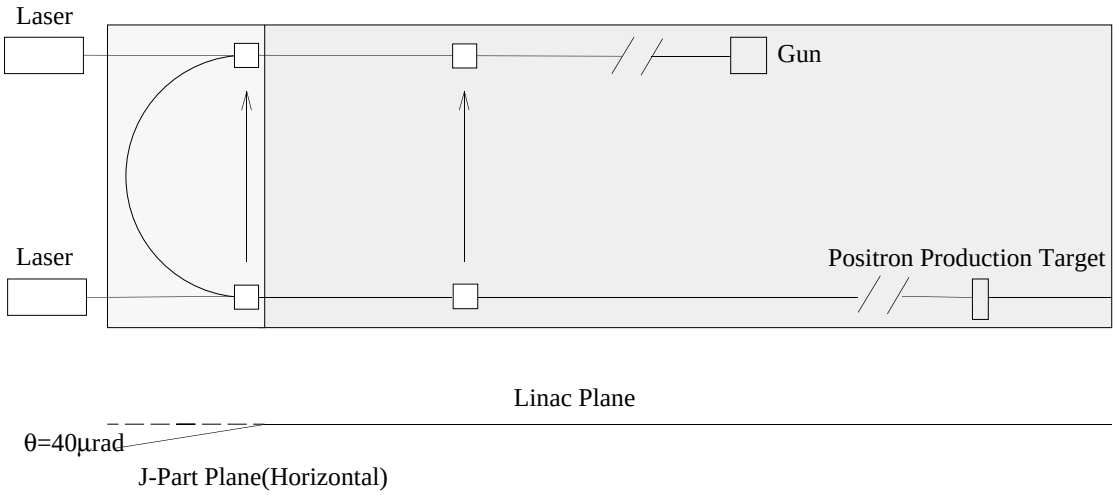

Figure 12.18: Alignment of two long linacs to be built parallel to each other.

establish a reference plane determined by the downstream linac by using the existing alignment system. A diffraction-limited laser beam defines the precise alignment axis along the entire downstream linac. Quadruple-type photo detectors placed on two ends of each support frame of the accelerator can detect vertical and horizontal position deviations with an accuracy better than 0.1 mm. All of the accelerator components are put on the support frames with a mechanical precision within 0.1 mm.

We then transfer two points of the downstream linac to the corresponding points of the upstream linac, as shown in Figure 12.18. This is done by using a laser beam, while using the usual levels for the direction perpendicular to the beam line. Based on these two points in the upstream linac as a reference, the laser alignment system is used in the same way as that of the downstream linac. Thus, one realizes the same plane for the two linacs with the same alignment precision.

Finally, the arc part is aligned in the horizontal plane by using levels. Because of the way that the "horizontal" alignment is defined for the upstream and downstream linacs, the plane of the arc part is inclined to that of the linac plane by 40 μrad.

After an initial alignment is carried out, continuous monitoring of the alignment status will be carried out by two sets of level-comparing systems for the upstream and downstream linacs. Clinometers will be installed at key locations, including the arc part.

12.1.6 Beam Control

Linac Operation Mode Regarding Electron and Positron Injection

Several schemes are being studied concerning the acceleration of electrons and positrons.

In the most straightforward scheme, the operating conditions for the electrons and

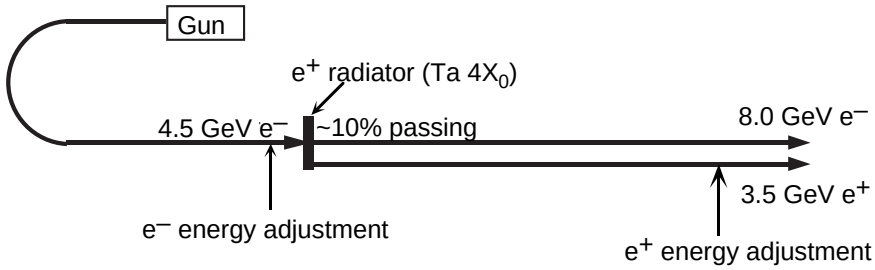

Figure 12.19: Simultaneous acceleration scheme of the electron and positron beams.

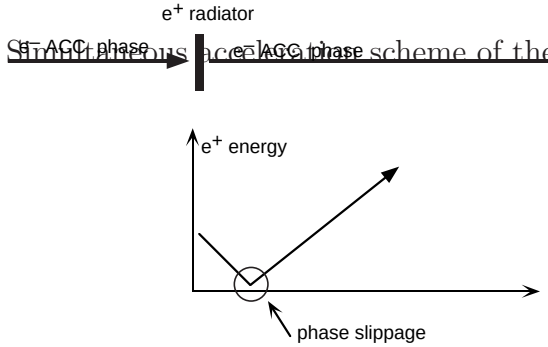

Figure 12.20: Acceleration phase adjustment of the electron/positron beams (Op.1), using phase slipping of the positrons in deceleration phase.

positrons are completely switched, and they are separately injected to HER and LER. This scheme provides optimized lattice focusing for the accelerated particles. However, many parameters, such as the RF timing and phases, need to be re-adjusted for both the upstream and downstream linacs.

In another scheme both the electron and positron beams are simultaneously accelerated and injected into the rings, as shown in Figure 12.19. The electrons are accelerated to 4.5 GeV by the first part of the injector. They then hit the positron production target. The emerging positrons are accelerated to 3.5 GeV. The target is built so as to have a small aperture which allows 10% of the electrons to pass through. Those electrons are accelerated in the downstream part up to 8 GeV. The electron and positron energies are adjusted at the end of the first and second parts, respectively.

In downstream part of the injector, the acceleration phases of the electrons and positrons should be 180° apart. This can be achieved by two methods. The first case is schematically shown in Figure 12.20: emerging positrons are first focused during their deceleration phase, but soon come to be accelerated because of phase-slippage. Figures 12.21(a) and 12.21(b) show a simulation of the capture rate and the longitudinal phase space of these positrons. Calculations indicate that 80% of the produced positrons can be accelerated; however, the energy spread will be larger than in the case with an optimum phase configuration.

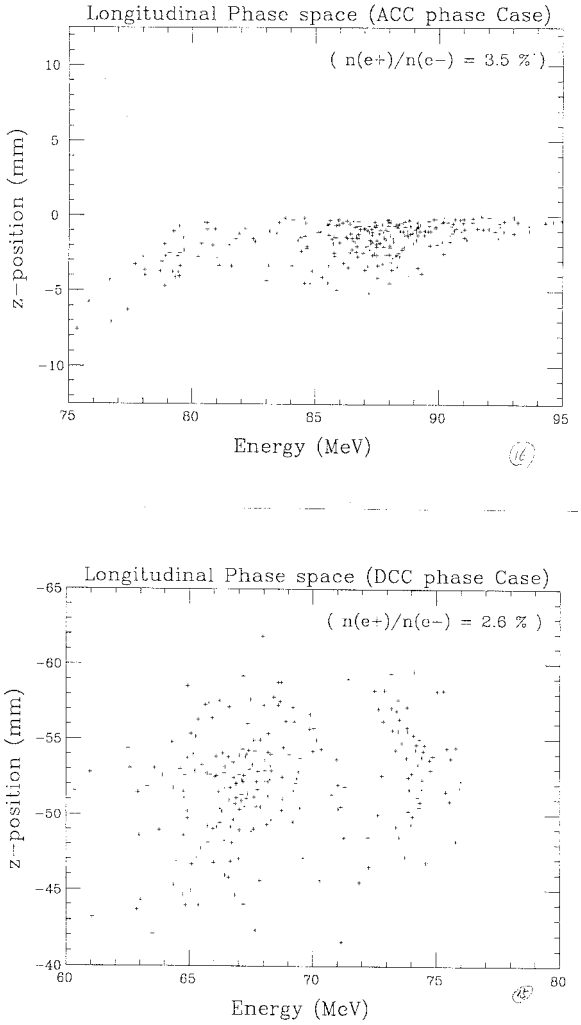

Figure 12.21(a): Longitudinal phase-space of the accepted positron beam (positron-acceleration phase).

Figure 12.21(b): Longitudinal phase-space of the accepted positron beam (positron-deceleration phase at first).

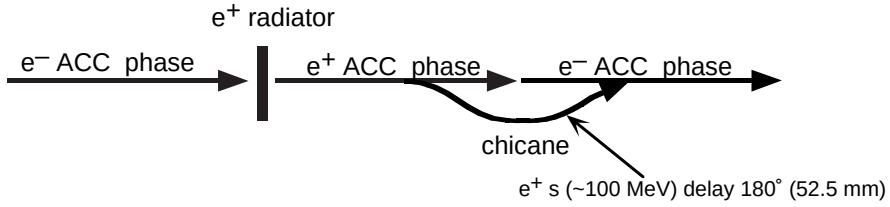

Figure 12.22: Acceleration phase adjustment of the electron/positron beams (Op.2), using a chicane to make phase-delay of positrons.

In the second case (shown in Figure 12.22) positrons are first focused in their acceleration phase, then their phase is shifted by 180° by separating them with a chicane. In the interval between the positron production target and the chicane, the electrons are slightly decelerated. However, its effect is negligible since the electron energy is larger than the positron energy there by a factor > 50.

If the two beam are co-accelerated, naturally the early part of the beam transport beam line needs to simultaneously deliver two beams of different energies. Studies are being prepared, regarding these issues as well as the bunching process during the phase-slippage.

Feedback to the Linac Beam Parameter

The beam energy in the injector is monitored at two locations: one in the arc section and the other after the linac.

In the arc section the nominal beam energy is 1.6 GeV. The energy fluctuation is detected with BPMs having a resolution of 0.03%. The beam energy there will be controlled by adjusting the phase of the last two klystrons of the upstream linac. Details of the correction algorithm are being considered.

At the end of the linac, electron and positron beams will be separated and transported independently. At the beam switch yard, the energies of both the electron and positron beams will be controlled in the same manner as in the arc section.

12.1.7 Schedule

The schedule for the upgrade is shown in Table 12.4. An important constraint is that injection to the PF ring has to be maintained during the upgrade project. Invasive work has to be done during the annual shutdown period each year. The upgrade of the present linac (from sector 1 to 5) and the construction of new sections (A, B, C and the arc section) will be conducted independently before June, 1998. After each portion is sufficiently tested, it will be connected during the summer shutdown of 1998. Commissioning of the 8 GeV linac will start in November, 1998.

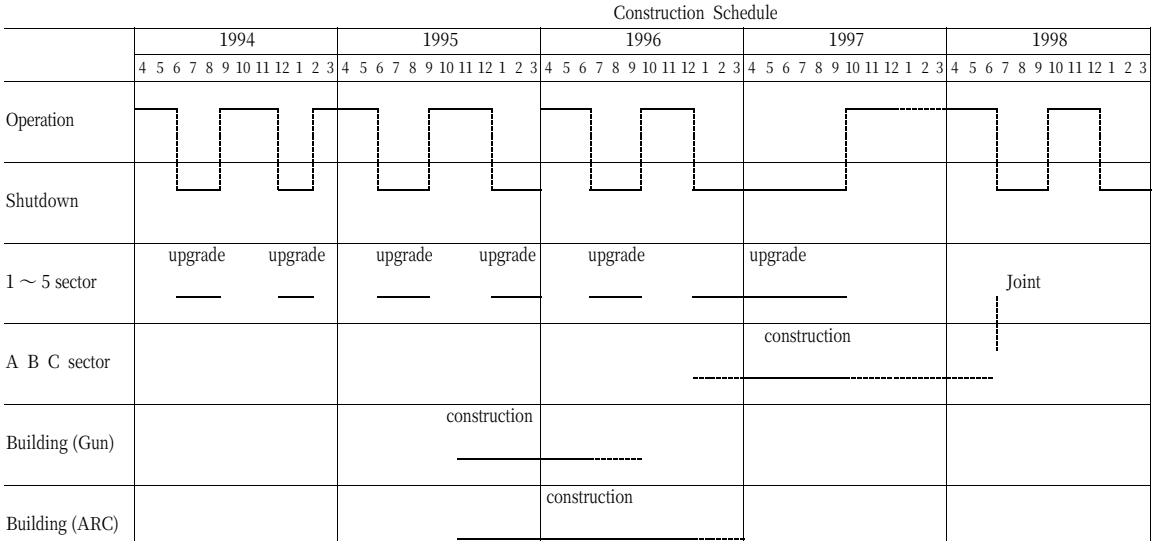

Table 12.4: The schedule of the injector upgrade program.

12.2 Average Luminosity

12.2.1 Beam Lifetime

In this section we evaluate the beam lifetime, which will be useful for simulating the optimum operation and the beam fill patterns of KEKB. The dominant sources of particle loss, which is responsible for the finite beam lifetime at KEKB, are the following three: the beam-beam bremsstrahlung in the beam collision, the beam-gas scattering and the Touschek effect.

The beam lifetime due to beam collisions depends on the energy acceptance $\Delta E/E$ of the ring. However, the dependence on $\Delta E/E$ is relatively small for $\Delta E/E$ >0.5%. For example, if the energy acceptance is increased from 1% to 2%, the lifetime varies from 8.8 hours to 10.7 in the LER, and from 20.9 hours to 25.3 in the HER. Since an optics study has shown the feasibility of an energy acceptance which exceeds 1% in both rings, it is reasonable to take the lifetime at the 1% acceptance.

The lifetime due to beam-gas scattering depends on the vacuum pressure, and again weakly on the energy acceptance. Assuming a design value pressure of 1×10^{-9} Torr and a 1% energy acceptance, the lifetime would be 45 hours in both rings.

The Touschek effect plays an important role in causing a beam loss in the LER. In this case, the lifetime depends strongly on the energy acceptance, as well as on the transverse acceptance. The expected acceptance of LER leads a Touschek lifetime of more than 15 hours. At this moment the LER lattice has not been completely finalized, and complete calculations of the expected acceptance, which include effects of machine errors, are not yet available. Consequently, the estimated Touschek lifetime should be considered to be a variable parameter for simulating the operation. It is noted that this effect does not contribute to the lifetime of the HER. Table 12.5 summarizes the beam lifetime estimation.

Table 12.5: Beam lifetime estimation for KEKB

	Beam-Beam	Beam-Gas	Touschek	Total
LER	20.9	45	5	3.7 h
			10	5.9 h
			15	7.3 h
HER	8.8	45	–	7.4 h

12.2.2 Operation Pattern

First, we estimate the initial fill time for KEKB. In what follows, the calculations are made based on the assumption that the positron and electron charges from the linac are 0.64 nC/pulse and 1.28 nC/pulse at 50 Hz, and that the injection efficiency to the KEKB rings is 50%. Then, for full-bunch operation the required injection time for the LER and HER will be 0.5 hours and 0.1 hours, respectively.

It should be noted that the beam intensity in the rings does not necessarily decay as an exponential function of time. Under stationary operation, the stored current will not decay very much before the next topping. Therefore, we use a simple model where the intensity decays exponentially with the estimated lifetime. Then the luminosity itself decays exponentially with a lifetime, τ_L, given by

$$\frac{1}{\tau_L} = \frac{1}{\tau_1} + \frac{1}{\tau_2},$$

where τ_1 and τ_2 are the lifetime for the LER and HER. With the refilling time T_F, and the experiment time T_E, the average luminosity would be

$$\overline{\mathcal{L}} = \frac{1}{T_F + T_E} \int_0^{T_E} \mathcal{L}_0 e^{-\frac{t}{\tau_L}} dt = \frac{\tau_L \mathcal{L}_0}{T_F + T_E} [1 - e^{-\frac{T_E}{\tau_L}}],$$

where $\mathcal{L}_0$ is the peak luminosity. The beam loss during the refill time has been neglected. The refill time is a sum of the injection time for the positrons and electrons, and the time that is needed for switching the operation mode between the injection and the physics run.

Figure 12.23 shows the average luminosity for three cases with the varying Touschek lifetime in LER. A mode switch time of 2 minutes is assumed. With a 10-hour Touschek lifetime, the average luminosity and the injection time would be as shown in Figure 12.24. Taking account of the number of bunches (5120) and the repetition rate of 50 Hz of the linac, we can see that at least 1.7 minutes are required to refill each bunch. The injection time will be a multiple of the minimum refilling time. We define the optimum operation pattern to be what gives an average luminosity to be $> 75\%$ of the peak luminosity. In Figure 12.24, such an optimum operation pattern would consist of a 40-minute physics data acquisition time and a 7-minute refill time, including both electrons and positrons. Each positron bunch would be recharged with two shots from the linac. Under this condition the operation pattern would look like the time chart in Figure 12.25.

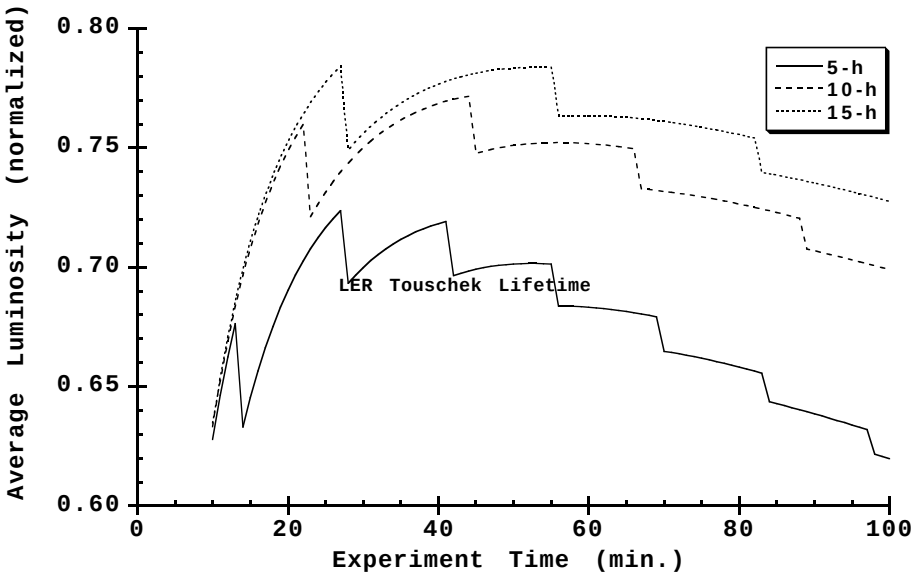

Figure 12.23: Average luminosity for different LER Touschek lifetimes.

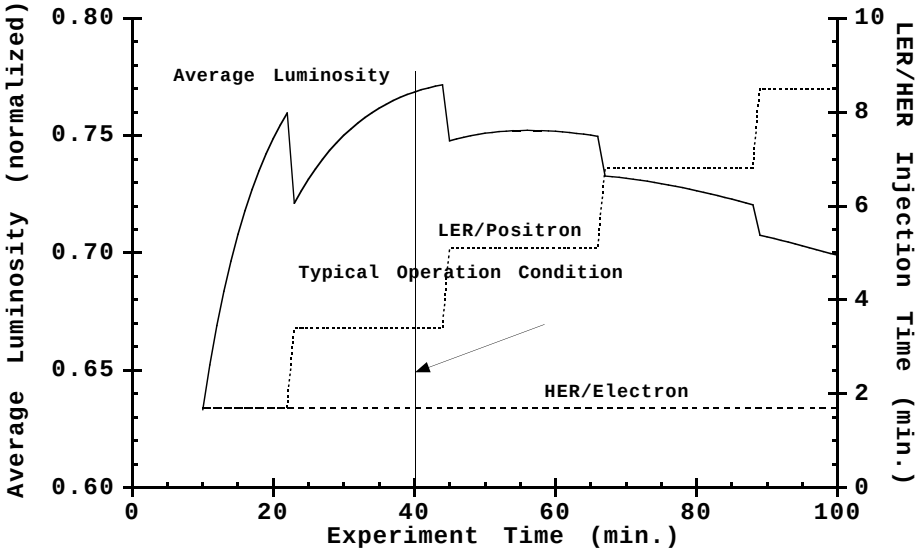

Figure 12.24: Average luminosity and injection times for the case of a 10-hour LER Touschek lifetime. The vertical line indicates a typical operation condition.

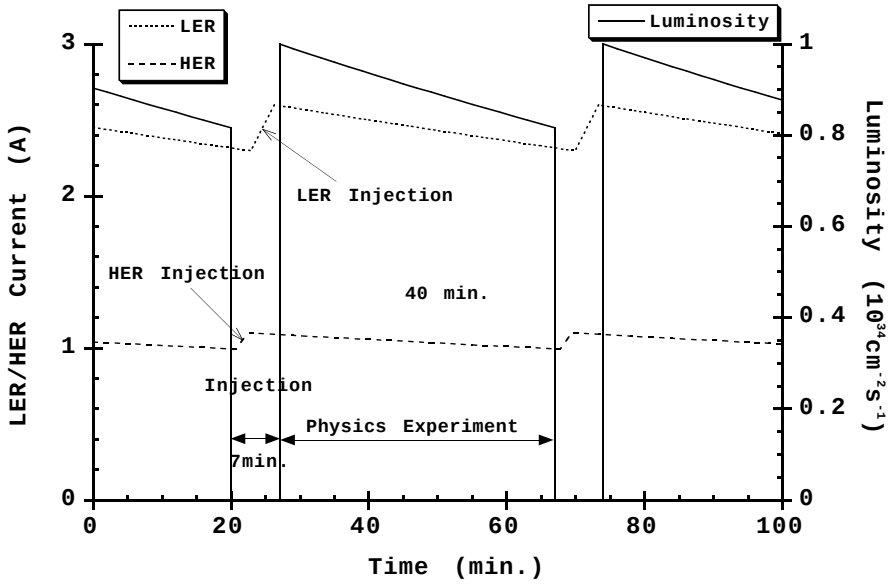

Figure 12.25: Luminosity and the LER/HER currents on the typical operation condition. The injection time includes the LER/HER topping times and the time period for changing the operation mode.

12.3 Beam Transport

12.3.1 Design Considerations

The parameters related to the beam transport (BT) between the linac and the KEKB rings are summarized in Table 12.6.

To minimize the construction cost, maximum use will be made of the existing tunnels for TRISTAN injection; the tunnels for both the TRISTAN accumulation ring (AR) injection and the TRISTAN main ring (MR) injection will be used. For injecting beams to the KEKB rings, the route as shown in Figure 12.26 has been chosen. This route is designed to avoid interference with the existing buildings for the AR.

Another important design consideration is operational simplicity. If a single beam line is used for both electrons and positrons having different energies, the need to re-adjust the magnet excitations or to switch their polarities tends to create various operational complications. Thus, in the BT design for KEKB, two beam lines will be implemented separately for the electrons and positrons. The beam lines have no common magnets nor common magnet power supplies, except for the first magnet that separates the two beams from the linac.

	e^-	e^+
Maximum energy [GeV]	8.4	3.7
Emittance(2σ) [m]	6.4×10^{-8}	8.8×10^{-7}
Energy Spread(2σ) [%]	±0.3	±0.5
with ECS		±0.25
Bunch length (σ_z) [mm]	1.5	1.5
with ECS		3.0
Time jitter $\Delta z_{max}/c$ (ps)	±30	±30
Momentum acceptance of Rings [%]	0.5†	0.5†

† 30 to 50 % degradation are assumed compared to the ideal case.

Table 12.6: Parameters relevant to the beam transport system. In the table, "ECS" means the energy compressor system for the positrons in the early part of the beam transport. See the text for details.

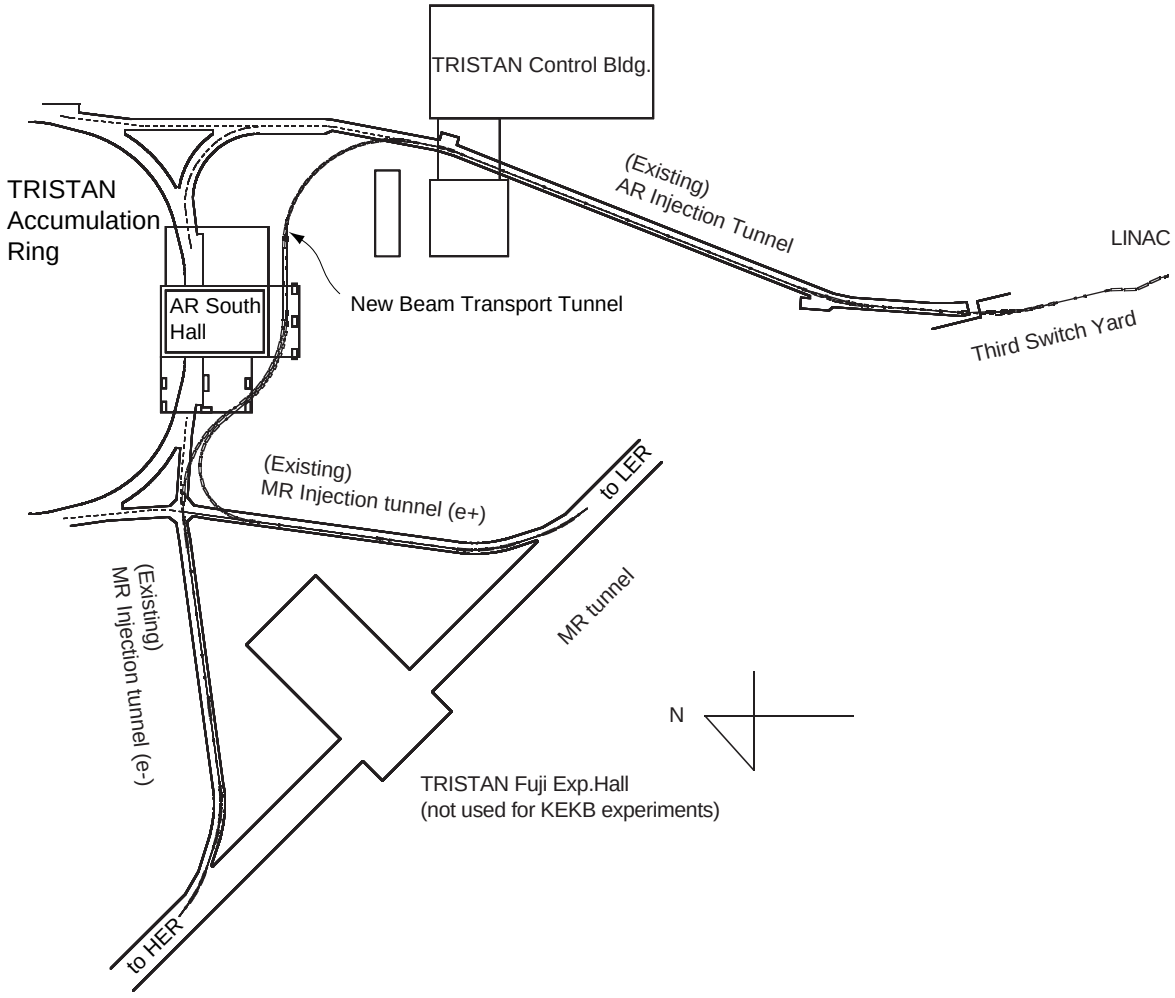

Figure 12.26: Layout of the beam transport lines.

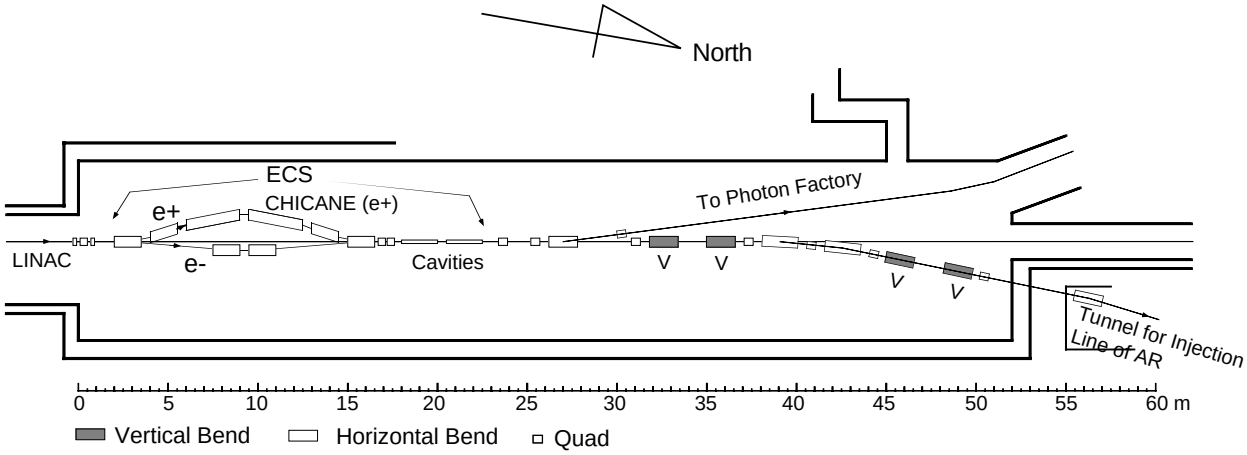

Figure 12.27: Layout of the Third Switch Yard.

12.3.2 Routing of the electron and positron beams

Figure 12.27 shows a part of the beam line which is immediately downstream of the linac exit before reaching the AR injection tunnel. This area is called the 3rd switch yard

In the upstream end of the 3rd switch yard, an energy compression system (ECS) will be implemented. Its purpose is to reduce the energy spread of the positrons from the linac by a factor of 1/2, and to relax the energy acceptance requirement for the LER. The ECS consists of a series of chicane dipole bends and two 2 m-long S-band accelerating structures. There will be no ECS specifically for electrons. The electrons are simply separated from the positrons, bypassing the positron ECS, and are brought back to the original line by two dipole magnets.

The AR injection tunnel does not have sufficient width to accommodate the two beam lines horizontally. The lines will be stacked vertically, with the positron line on top of the electron line in the AR injection tunnel. For this purpose, the two beams are separated by vertical dipole magnets in the downstream part of the 3rd switch yard. As shown in Figure 12.27, four dipole magnets will be used to make the vertical dispersion closed. With this manipulation, the vertical separation of two beams will be 0.6 m. The horizontal dipole magnets between the vertical ones will guide the beams to the new transport lines through the AR injection tunnel.

As shown in Figure 12.26, immediately after the first arc in the middle of the new tunnel the two lines are separated horizontally. The elevation of the positron line is reduced in the subsequent straight section to meet the MR injection tunnel at an appropriate point in the middle of the downward slope. The electron line maintains its level up to the entrance of the MR injection line. After passing the downward slopes, only minor modifications to the injection lines are required, since the injection points to the KEKB rings are at nearly the same position as those of the TRISTAN MR.

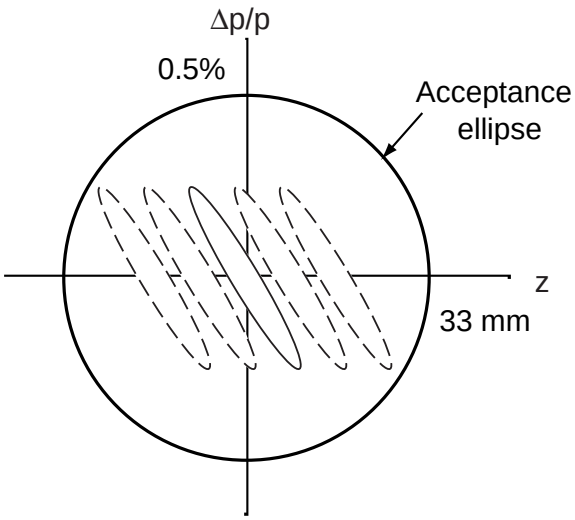

Figure 12.28: Acceptance of the LER and incoming beam. The large circle indicates the acceptance ellipse in the longitudinal plane of the LER. The rotated ellipse with a solid line represents the incoming positron beam with ECS, while the ellipses with broken lines indicate incoming beams with a timing jitter. The outermost ellipse corresponds to the maximum allowable jitter. R_{56} is assumed to be 4 m.

12.3.3 Constraints to R_{56} and the tolerance of timing jitter

The ECS may not be operational in the initial KEKB operation. In that case, the positron beam will have a large energy spread ($\sigma_\epsilon = 0.25\%$ without ECS). While the original bunch length expected from the linac is 1.5 mm, a bunch lengthening effect through the $\sigma_\epsilon R_{56}$ term needs to be considered. Here, the R_{56} refers to the (5, 6) component of the transfer matrix, i.e. the path length dependence on the momentum. For example, if the R_{56} term of the BT exceeds 5 m, the bunch length will be larger than 12.5 mm. The beam with a large bunch length induces a large quadrupole synchrotron oscillation after injection. Similarly, any timing jitter of the injected beam also induces (dipole) synchrotron oscillations. Figure 12.28 illustrates the acceptance ellipse for injection and possible patterns of a mismatch.

The largest amplitude of the induced bunch oscillation immediately after injection thus depends on R_{56}. Figure 12.29(a) shows the largest amplitude of energy oscillation as a function of R_{56}. Figure 12.29(b) shows the timing jitter tolerances as a function of R_{56}, which was defined as the largest longitudinal position shift that makes the beam ellipse cross with the acceptance boundary.

It is seen that the timing jitter tolerance is zero for the case of positrons without ECS. For positrons with ECS, a jitter tolerance of 30 ps (9 mm) demands that R_{56} be less than 7.5 m. For electrons, R_{56} should be less than 6 m. The optics design of BT

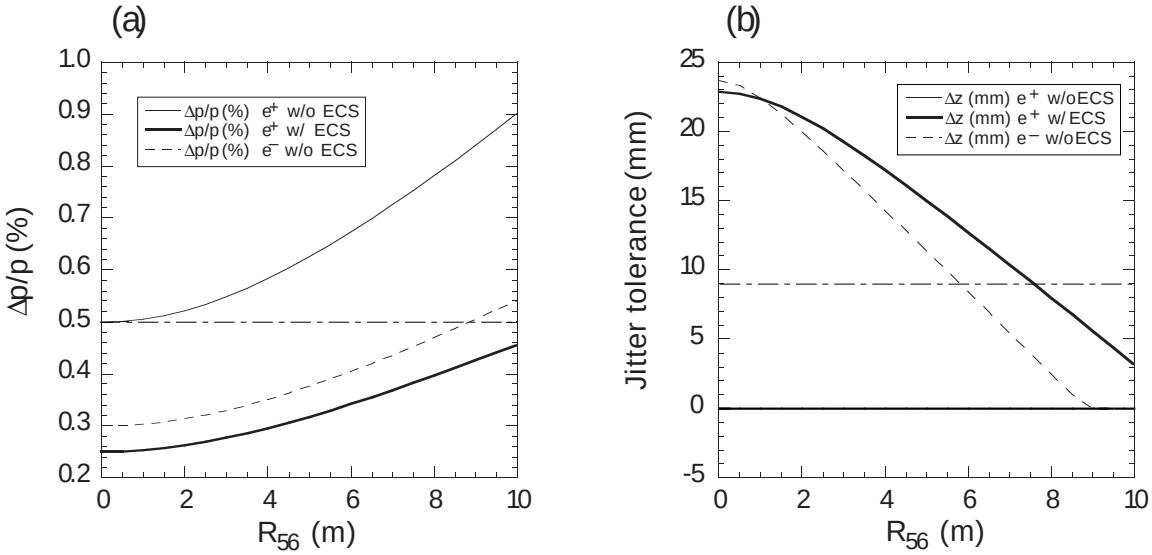

Figure 12.29: (a) Largest amplitude of energy oscillation as a function of R_{56}. The dash-dot line shows a momentum acceptance of 0.5%. (b) the timing jitter tolerances as a function of R_{56}. The broken line shows a tolerance of 9 mm (30 ps).

has been made such that the value of R_{56} will be 4 m.

It should be noted that R_{56} can be written as

$$R_{56} = \Theta\bar{\eta}, \tag{12.1}$$

where Θ is the total bending angle and $\bar{\eta}$ is the average dispersion in the dipole magnets. From this it is found that $\bar{\eta}$ needs to be smaller than 1.2 m for the positron line to satisfy $R_{56} = 4$ m.

Since the BT arc is occupied by strong dipole magnets of 1.5 T, there is no room to make the dispersion below 1.2 m for each arc. Consequently, another approach to suppress the R_{56} has been taken for this BT design: the optics around the three arcs in the new BT tunnel are arranged such that the arcs in the upstream generate negative dispersion at the downstream arcs so that R_{56} of the downstream arcs is decreased.

In the current design the electron line will require 54 dipole and 62 quadrupole magnets; the positron line will require 57 dipole and 64 quadrupole magnets. Some of the magnets, particularly the magnets in the downward slopes, may be recycled from the TRISTAN injection beam line.

Chapter 13

Accelerator Control System

13.1 System Requirements

The KEKB accelerator complex has more than 50,000 control points along the 3 km circumference of the two rings, the LER and HER. Some control data must be updated at a high rate up to 100 Hz. A fast and powerful control system is required to implement sophisticated tuning procedures and feedback loops for the stable operation of KEKB. In addition, such a control system has to be readied in a timely fashion, *i.e.* it has to be operational at the first commissioning time of KEKB, which is expected to begin near the end of 1998. The schedule for the control system development is summarized in Table 13.1.

13.1.1 Functional Requirements

The functional requirements for the KEKB accelerator control system can be categorized into three groups as follows. Some of the important issues are itemized below:

1. *Hardware Control*:

   (a) It should be that the graphical user interface (GUI) to read/set/monitor the status of a hardware device can be constructed without resorting to complicated programming.

   (b) It should be that the data logging can be configured without complicated programming.

   (c) The low level access to individual hardware components should be supported for developing and debugging the hardware interface. The interface of this low level access should be user-friendly and flexible.

FY1995	April	Decision to use EPICS.
		Start development of software tools.
		Start user education on EPICS.
	July	Complete First stage of Relational Database Design.
	December	Complete Steering Power supply/ BPM interface design.
FY1996		Develop Application programs for AR/KEKB.
	December	System test of new TRISTAN AR control system.
FY1997	July	New TRISTAN-AR control system commissioning
		New TRISTAN/KEKB beam transport line control system
	December	Starts installation of KEKB accelerator control system equipment.
FY1998		
	December	Commissioning of KEKB.

Table 13.1: Schedule of the KEKB accelerator control system development.

(d) A powerful yet easy-to-handle development system should be provided for the device driver level software.

(e) Stand-alone operation of the hardware subsystem should be allowed, without depending on other part of the accelerator.

2. *Accelerator Operation*:

Application programs required for this category include: automated machine operation software, monitors of the machine performance, feedback loops to optimize the machine performance, alarm notification system and others.

(a) The user interface of these programs should be operator-friendly.

(b) Operator interfaces should have a quick response; typically less than a few seconds.

(c) An alarm notification system should be included.

(d) All key operations should be recorded for later inspection.

(e) Powerful yet easy-to-handle development system for the development of application programs with GUI.

3. *Accelerator Development*:

Accelerator development refers to activities where various machine errors are identified and fixed, new tuning techniques are attempted, better operating conditions are searched for, or unresolved accelerator physics issues are investigated, and so on. Its guiding principles may be summarized as:

(a) All data that can possibly be collected should be collected.

(b) All collected data should be saved for later analyses.

(c) All operations should be recorded for later inspection.

The requirements on the data analysis tools are:

(d) Stored data can be easily retrieved.

(e) The data can be easily analyzed.

(f) The data analysis tools should be able to handle both data from the accelerators and the results from computer simulation in a similar way.

(g) The development system for application programs should be programmer-friendly.

In a particle accelerator for high energy physics, hardware modifications and upgrades to the machine configuration are common events in its life cycle. The following features should be incorporated so that the control system will be able to keep pace with the changes of the accelerator.

1. All machine parameters and data of individual machine components should be saved in a database. This is so that changes in the accelerators are automatically reflected in the control system.

2. Incremental upgrades and the replacement of components of the control system should be allowed.

3. Integration of control sub-systems within the accelerator control system should be done in a easy and seamless way.

13.1.2 Design Guideline

With the requirements stated above, the design considerations for the KEKB accelerator control system are summarized as follows. The keywords of the guidelines are "Openness", "Standard" and "Scalability":

1. For future maintenance and upgrades, the control system should have a layered structure. The layers described here refer to such concepts as: the device interface layer, the equipment control layer and the presentation layer. The interface protocol between these layers should be a well-defined one based on international standards. This layered structure will allow us to modify components in one layer without affecting other layers.

2. As the interface between the control system and the equipment, international standards such as CAMAC, VME, VXI and GP-IB should be used where their performance is found adequate.

3. To maintain good responsiveness of the control system, a high-speed network should be used to connect the computers. The network architecture should be chosen from well established, standard technologies.

4. To reduce the man-power requirement and efforts to build the control system, international collaboration and/or commercially available products should be taken advantage of.

5. At times, adopting object-oriented techniques or data abstraction for hiding the details of the hardware helps in the development of application programs

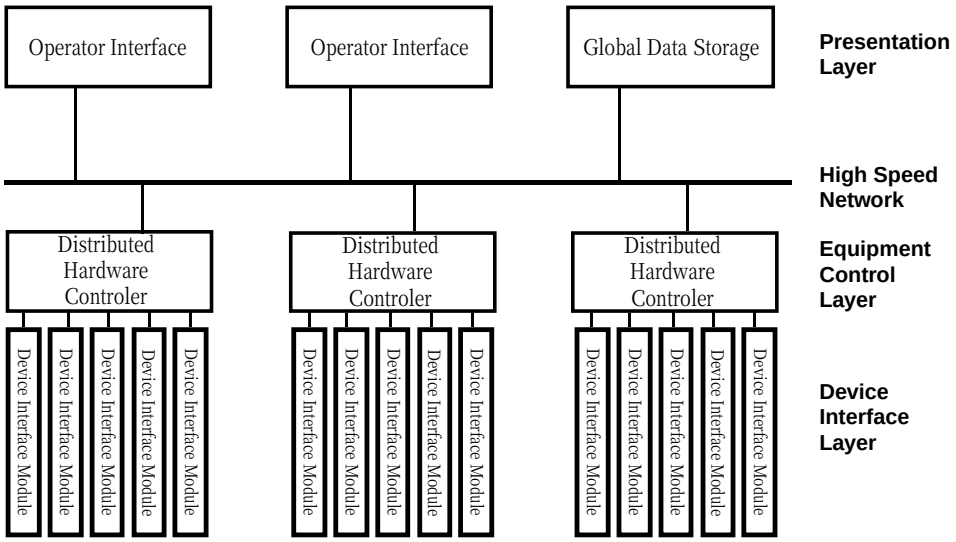

Figure 13.1: Schematic view of the KEKB accelerator control system.

13.2 System Architecture

The KEKB accelerator control system will be built based on the EPICS[2] toolbox. The control system is divided into three layers:

- Presentation layer,
- Equipment control layer, and
- Device interface layer,

as shown in Figure 13.1. The network system which connects the first two layers is another key component of the control system. In EPICS terminology, a computer in the presentation layer is called an OPI (Operator Interface) and one in the equipment control layer is called an IOC (Input/Output Controller).

13.2.1 Device Interface Layer

The device interface layer, which sits at the lowest level of the three, sends and receives signals from or to individual hardware equipment. This layer communicates such signals and data with computers in the equipment control layer. A schematic view of the device interface layer is shown in Figure 13.2.

KEK has a large inventory of CAMAC modules from the TRISTAN control system. The CAMAC crates and modules inside them are used as a device interface layer of the KEKB control system. The CAMAC crates are connected by CAMAC serial highways or CAMAC branch highways, depending on specific requirements. An equipment

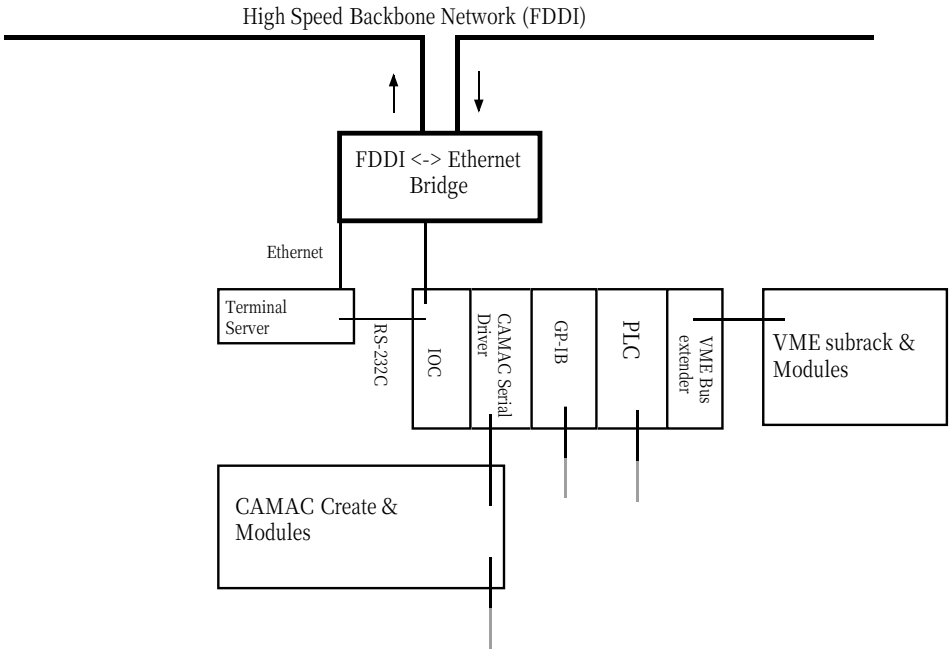

Figure 13.2: Schematic of the device interface layer

control computer in the VME sub-rack controls the serial/branch CAMAC highway driver in the same VME sub-rack .

The standard CAMAC modules used in TRISTAN are supported by the KEKB accelerator control group, i.e. the control group takes the responsibility for maintaining proper functionality of these modules. It is considered that standard CAMAC modules can cover most of the needs for the device interface modules.

However, CAMAC is not the only field bus that is used in the device interface layer for KEKB. Drivers of other field bus architecture, such as GP-IB, can be placed in a VME sub-rack . Another example of the field bus used in the KEKB accelerator control system is a multi-drop serial line, with which about 1600 power supplies for steering correction magnets are controlled. A device interface using a multi-drop serial line for magnet power supplies is now being studied in collaboration with the magnet group and the beam transport group for KEKB. The high-speed BPM electronics system will be implemented on VXI. The VXI is yet another example of the field bus to be used at KEKB. In this case, it will be natural to control these modules directly from IOC through the VME/VXI bus .

13.2.2 Equipment Control Layer

The equipment control layer consists of computers that functionally control the equipment in each hardware group, e.g. magnet, RF systems, beam monitor and others. The

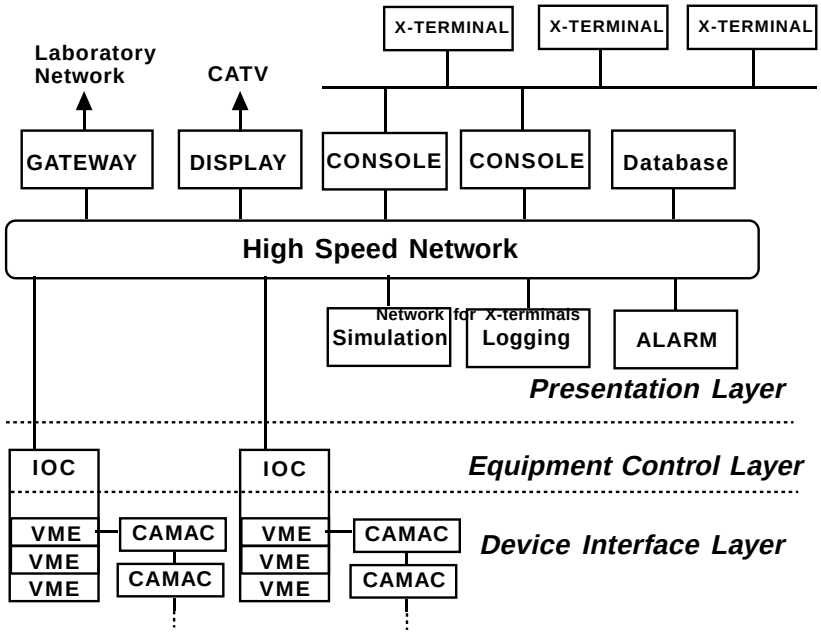

Figure 13.3: KEKB Accelerator Control System Architecture

equipment control computer, IOC, is a VME board-computer. The current version of EPICS system supports VxWorks as the real-time operating system for IOC.

One of the core elements in EPICS is the distributed runtime database, which resides in IOC. A database record (also called a process variable) in the runtime database corresponds to each channel in the device interface layer. Those records include all the device-specific information, such as hardware address, calibration table, upper/lower limits of action variables, and others.

Software components to support CAMAC are already included in EPICS. To simplify the use of standard CAMAC modules for KEKB, device support routines for these standard CAMAC modules will be developed.

Although EPICS supports a rich collection of VME modules, some modules that are introduced for KEKB may not be readily supported by EPICS at the moment. For these modules, it is necessary to develop a set of software, device driver, device support and record support. This task will be carried out by personnel from the control group and the hardware group which uses such modules.

13.2.3 Network

The equipment control layer and the presentation layer are connected through a high-speed network, such as FDDI. To separate the network traffic between these layers from the traffic between console computers and X-terminals, another network and/or

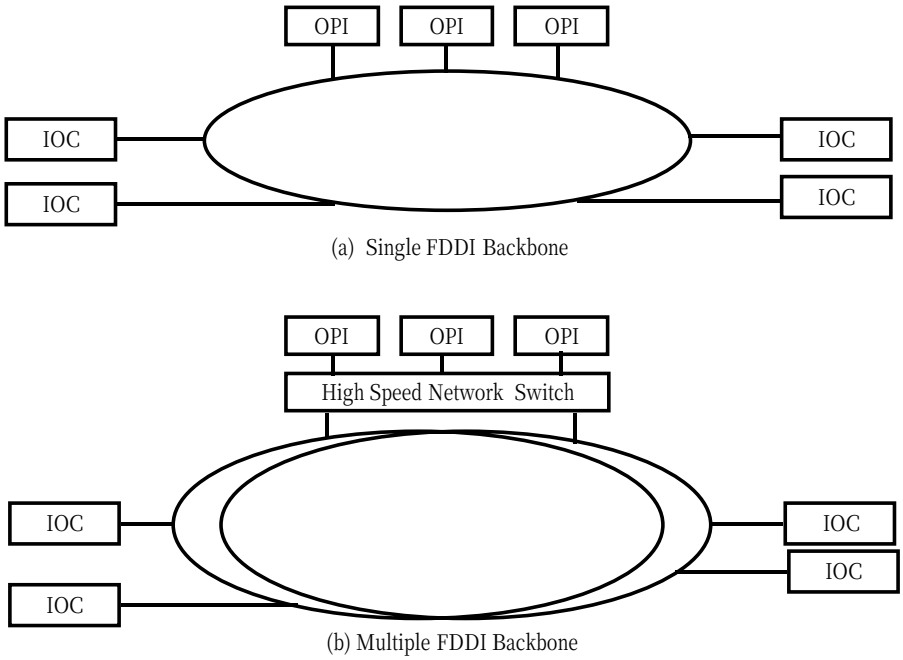

Figure 13.4: Throughput of the network will be enhanced by duplicating the FDDI backbone.

a network switch will be used, as shown in Figure 13.3.

In EPICS, the OPI and IOC communicate through a protocol called "Channel Access" (CA). The CA protocol hides the detail of physical configuration of lower layers from the application program on OPI. The CA protocol is built on the standard TCP/IP network protocol.

If the network system is not scalable as other parts of the system, the network can become a bottleneck when the system grows. When the backbone FDDI is saturated by the network traffic, a high-speed network switch and multi FDDI backbones will be introduced, as shown in Figure 13.4. It enhances the network throughput up to the speed of network switch, which is currently ~ 1 GBit/sec.

There is also the possibility of adopting a distributed shared-memory network to obtain fast data transfer and event transmission among computers. The high-speed orbit feedback is a candidate to utilize this technology.

13.2.4 Presentation Layer

The presentation layer includes the operator's consoles, database manager, simulation computer, alarm generation/recording, data logging, displays, and a gateway to the KEK local-area network. Workstations and/or CPU servers running UNIX[1] operating

[1]UNIX is a trademark of Unix Lab.

systems are used in this layer. The X-window system is used as the graphical user interface standard.

The software environment used in this layer is very important for the whole system. The fundamental functions that have to be supported from the beginning of the installation include: the controls of each hardware equipment and graphical displays of the hardware status and various monitor values from the accelerator. Programmer-friendly interfaces must be provided for the accelerator physicists to develop application programs painlessly. It is also important to have very efficient data retrieval tools and analysis tools. The use of EPICS solves some of these problems as discussed later.

Operator's console

X-terminals with multiple displays will be used as operator consoles. The X-terminals are connected to the UNIX machines in the presentation layer. By using the tools in EPICS, personnel who are not from the control group will be able to create graphical operator interfaces without difficulties. Tcl/Tk and other languages which support CA access can also be used to develop application programs.

Database manager

The database manager keeps all information concerning the KEKB accelerator complex, such as machine parameters, equipment specifications, component locations, and others. Logged data, archived data and configuration data should also be accessible from a database system with the same interface. Commercially available DBMS(Database Management System) will be used as a framework of the database manager. Two commercial relational database management software, ORACLE[2] and SYBASE[3], are currently being evaluated. Recent progress in OODB(Object Oriented Database) technology should be also taken into account for the choice of DBMS.

Each runtime database record in EPICS has a unique name in the system. This unique name may not be easy enough to decipher for application programmers. The database manager also works as a channel name server. An application program can send a query on channel names and get a list of the channel names from the database manager.

[2]ORACLE is a registered trademark of ORACLE Corporation.

[3]SYBASE is a registered trademark of SYBASE,Inc.

Simulation computer

The simulation computer is used for accelerator physics calculations for such purposes as orbit correction and optical matching optimization. Computer code SAD[4] has been heavily used in the design work of KEKB, and will be used as a modeling/simulation program in the KEKB control system as well.

The ultimate goal of the development of SAD is to build a virtual accelerator on a digital computer. The KEKB control system will be built such that the SAD users should be able to control this virtual accelerator through the *same* operator interface that is used for the real accelerator, like a "flight simulator." To realize this idea, an interface program between SAD and a portable CA server will be developed, which will run on UNIX workstations. The CA clients can access the virtual accelerator through this CA server using an ordinary CA protocol.

The concept of a virtual accelerator is also useful in the development of application programs. Application programmers can test their software without risking operation of the real machine. It is even possible to develop an application program without a real machine.

System Alarm/Data logging

Equipment failures are monitored by each IOC and are reported to the alarm computer for broadcasting and recording purposes. The alarm computer notifies such conditions to the operator with various methods including: alarm sound, flashing or pop-up display, automatic pocket-beeper calls, and so on. The data logging computer collects and saves data from IOCs for later analyses.

System status broadcast and the local network gateway

The display computer broadcasts and displays data and information throughout the KEK site through the CATV network and other media. There is also a gateway computer which connects the KEKB control computer network with the KEK laboratory network. Through the KEK lab network, users who are away from the control room can monitor the status of each device and the status of KEKB overall. Privileged users are allowed to control their equipment from their office. To avoid a network jam caused by access through the laboratory network, a proxy channel access (CA) server will be used on the gateway computer. It will intercept and bundle CA requests from the laboratory network.

13.2.5 Timing system

Magnet synchronization

Since the magnet setting in the KEKB rings needs to be changed without loosing the beam, the control system has to change the strength of the magnets step by step in a synchronized way. For this operation, a timing system will be used to send a "heart beat" to the entire system. A dedicated signal line will be used to send a timing signal. A module in a device interface layer receives this signal and triggers an action.

Synchronized data acquisition

The beam orbit in the beam transport line are measured by using one-pass beam position monitors (BPMs). The KEKB control system needs to be able to associate this data with data from the injector linac BPMs or from the beam loss monitors and others within KEKB. This is important for studying and optimizing the beam injection setup.

When orbit distortions are intentionally introduced at KEKB for studying magnet misalignment and other effects, the BPM data need to be tagged appropriately such that sensible analyses are made possible.

Bibliography

[1] W-D. Klotz et al., "Experience with a *Standard Model '91* based Control System at the ESRF", ICALEPCS '93, Berlin(FRG), 1993.

[2] L.R. Dalesio, et al., "EPICS Architecture", ICALEPCS 91, KEK Proceedings 92-15, (1992) pp.278-282., Dalesio, L., et al. "The Experimental Physics and Industrial Control System Architecture," ICALEPCS, Berlin,Germany, Oct. 18-22, 1993.

[3] "Vsystem" is a product of Vista Control Systems Inc., Los Alamos, NM.

[4] SAD is the accelerator design tool program developed at KEK.

[5] Shin-ichi Kurokawa, et al., "The TRISTAN Control System", Nucl. Instr. and Meth., A247, (1986) pp. 29-36.

[6] Shin-ichi Kurokawa, " Status of TRISTAN-II Project", Proceedings of the 1993 Particle Accelerator Conf, pp. 2004-2006, S-I Kurokawa, "KEKB status and Plans", 1995 Particle Accelerator Conference, Dallas, Texas.